

Exploring the Structural Complexity of Compartmentalized Nanostructures of Triblock Terpolymers

DISSERTATION

zur Erlangung des akademischen Grades eines
Doktors der Naturwissenschaften (Dr. rer. nat.)
im Fach Chemie
an der Bayreuther Graduiertenschule
für Mathematik und Naturwissenschaften
der Universität Bayreuth

vorgelegt von

Tina I. Löbling

Geboren in Lichtenfels

Bayreuth, 2015

Die vorliegende Arbeit wurde in der Zeit von Februar 2012 bis März 2015 am Lehrstuhl Makromolekulare Chemie II unter der Betreuung von Prof. Dr. Axel H. E. Müller angefertigt.

Vollständiger Abdruck der von der Bayreuther Graduiertenschule für Mathematik und Naturwissenschaften (BayNAT) der Universität Bayreuth genehmigten Dissertation zur Erlangung des akademischen Grades eines Doktors der Naturwissenschaften (Dr. rer. nat.).

Dissertation eingereicht am: 01.04.2015

Zulassung durch die Prüfungskommission: 28.04.2015

Wissenschaftliches Kolloquium: 17.07.2015

Amtierender Direktor: Prof. Dr. Franz Xaver Schmid

Prüfungsausschuss:

Prof. Dr. Axel H. E. Müller (Erstgutachter)

Prof. Dr. Stephan Förster (Zweitgutachter)

Prof. Dr. Volker Altstädt (Vorsitz)

Prof. Dr. Andreas Fery

(Drittgutachter: Prof. Dr. Alexander Böker)

*“Success is the ability to go from one failure to another
with no loss of enthusiasm”*

(Winston Churchill)

meinen Eltern

meiner Familie

André

Table of Contents

Summary	1
Zusammenfassung	3
List of Abbreviations	7
1. Introduction	11
1.1. Block Copolymer Self-Assembly in Bulk	12
1.1.1. Self-Assembly of AB Diblock Copolymers in Bulk	12
1.1.2. Self-Assembly of ABC Triblock Terpolymers in Bulk	14
1.2. Block Copolymer Self-Assembly in Solution	15
1.2.1. Self-Assembly of AB Diblock Copolymers in Solution	16
1.2.2. Self-Assembly of ABC Triblock Terpolymers in Solution	23
1.2.2.1. Spherical Multicompartment Micelles	24
1.2.2.2. Cylindrical Multicompartment Micelles	27
1.2.2.3. Compartmentalized Sheets and Vesicles	29
1.3. Aim of This Thesis	32
1.4. References	33
2. Thesis Overview	47
2.1. Micellar Interpolyelectrolyte Complexes with a Compartmentalized Shell	48
2.2. Cryogenic Transmission Electron Tomography Reveals Hidden Features in Compartmentalized Particles	51
2.3. Self-Assembly of Triblock Terpolymer Towards Complex Micellar Superstructures	54
2.4. Tuning Multicompartment Nanostructures	57
2.5. Bulk Phase Behavior of Polystyrene- <i>block</i> -Polybutadiene- <i>block</i> -Poly(<i>tert</i> -butyl methacrylate) Triblock Terpolymers	58
2.6. Janus Nanoparticles Compatibilize Immiscible Polymer Blends under Technologically Relevant Conditions	59
2.7. Individual Contributions to Joint Publications	62

Table of Contents

3.	Micellar Interpoelectrolyte Complexes with a Compartmentalized Shell	65
4.	Hidden Structural Features of Multicompartment Micelles Revealed by Cryogenic Transmission Electron Tomography	93
5.	Rational Design of ABC Triblock Terpolymer Solution Nanostructures with Controlled Patch Morphology	129
6.	Control of Multicompartment Nanostructures of Linear Triblock Terpolymers by Post-Polymerization Processes	179
7.	Bulk Morphologies of Polystyrene-<i>block</i>-Polybutadiene-<i>block</i>-Poly(<i>tert</i>-butyl methacrylate) Triblock Terpolymers	203
8.	The Impact of Janus Nanoparticles on the Compatibilization of Immiscible Polymer Blends under Technologically Relevant Conditions	227
	List of Publications	255
	List of Conference Contributions	257
	Danksagung	259
	Erklärung	263

Summary

Within this work, complex compartmentalized nanostructures were created *via* the self-assembly of linear ABC triblock terpolymers in selective solvents. Thoroughly chosen block sequences and lengths combined with precisely tuned self-assembly pathways enable the controlled formation of novel compartmentalized nanoparticles with so far unprecedented complexity. This thesis is divided in three main topics. Two of them focus on the fabrication of complex nanostructures and their comprehensive characterization to elucidate underlying formation mechanisms, while the third subject deals with synthesis and application of nanoparticles in industrial relevant amounts.

The first topic within this thesis is the fabrication of complex patchy nanoparticles *via* a combination of solution-based self-assembly of a charged amphiphilic polybutadiene-*block*-poly(1-methyl-2-vinyl pyridinium)-*block*-poly(methacrylic acid) (BVqMAA) triblock terpolymer followed by interpolyelectrolyte complexation with oppositely charged polymers. The BVqMAA triblock terpolymer with a hydrophobic PB, a polycationic PVq and a polyanionic PMAA block self-assembles in aqueous solution into multicompartiment micelles (MCMs) with a PB core, compartments of an *intra*-micellar interpolyelectrolyte complex (IPEC) between PVq and PMAA while excess PMAA forms the stabilizing corona. These polyanionic MCMs were used as precursor micelles for complexation reaction with polycationic homopolymers as well as bishydrophilic diblock copolymers. Instead of forming a continuous IPEC shell, addition of a polycationic homopolymer forms distinct IPEC patches on top of the micellar core when complexed with the polyanionic PMAA chains. This behavior was ascribed to the fact that long corona chains allow the IPEC to form thick patches lowering the total interfacial area towards the micellar core compared to a continuous shell. An unfavorable interface with the aqueous medium is thereby prevented through the long corona of the precursor micelles. In case of polycationic bishydrophilic diblock copolymers, carefully chosen block length mismatch between the negatively charged corona chains and the polycationic block results in a dense packing of the ionically grafted diblock copolymer chains within the corona of the precursor MCMs. The collapse of newly formed hydrophobic IPEC from solution is hindered due to steric stabilization through the water-swollen but non-ionic part of the diblock copolymer. Cryogenic transmission electron tomography and computational 3D reconstruction reveal novel “sea-urchin” and “paddle-wheel” like IPEC structures.

The formation of core-compartmentalized nanoparticles through hierarchical self-assembly of linear ABC triblock terpolymers was the second main aspect within this thesis. The structuring concept is based on consecutive precipitation of the two hydrophobic blocks. This method, developed in our group to form spherical MCMs, was expanded in this work towards other particle geometries as well as patch morphologies. On the basis of diblock copolymer solution morphologies, ranging from spherical micelles to cylinders, sheets and vesicles, a synthetic library of terpolymers was established with proper choice of corona block length to screen all these particle geome-

tries. The investigated terpolymer system was polystyrene-*block*-polybutadiene-*block*-poly(*tert*-butyl methacrylate) (SBT) and the final solvent mixture for the self-assembly was acetone/isopropanol. This solvent mixture is a good solvent for the T corona over all solvent compositions, while it is a non-solvent for B and S. It was proven that S is plasticized to a certain extent by acetone allowing sufficient chain rearrangement preventing kinetically trapped structures. Spherical MCMs, compartmentalized cylinders, sheets and vesicles were achieved with decreasing the T corona block length and/or swelling of the S block with acetone. Following the theory of block copolymer self-assembly in bulk, we hypothesized that the S and B blocks phase-separate analogously within the confined geometry of the particle core. The library of SBT triblock terpolymers was systematically expanded through synthetic variation of the S/B volume ratio, while adjusting the T corona to gain different particle geometries. A myriad of complex compartmentalized superstructures was studied with so far unprecedented detail applying transmission electron tomography to reveal the internal phase separation of the hydrophobic blocks in the final aggregate. Besides rather simple sphere-on-sphere and core-shell-corona structures, complex helix-on-cylinder and unprecedented cylinder-on-sheet, cylinder-on-vesicle as well as sheets and vesicles with a bicontinuous membrane were realized. A consecutive work deals with parameters influencing the resultant compartmentalized nanostructures apart from synthetic encoding block volume fractions. Tuning the solvent conditions allows swelling or contraction of core and corona blocks and induces morphological transitions from spherical MCMs towards vesicles including cylinders and sheets as intermediate states. These transitions were also obtained through controlled blending with solvophobic homopolymers or post-modification of the B block. To complete the systematic investigation of as synthesized SBT triblock terpolymers, the phase behavior in bulk was investigated and a phase diagram established. The bulk morphologies comprise core-shell cylinder, lamella-lamella, core-shell gyroid and a rarely observed cylinder-in-lamella morphology.

Within the third section, polystyrene-*block*-polybutadiene-*block*-poly(methyl methacrylate) (SBM) Janus particles were obtained through crosslinking of the B compartments and subsequent dissolution of spherical MCMs. The Janus particle synthesis was upscaled to fabricate 100 g of Janus particles per batch. They were used as efficient compatibilizers for immiscible polymer blends under technologically relevant conditions using industry scale blending equipment. The blend morphology was changed from a co-continuous to small droplet morphology upon compatibilization with Janus particles. The Pickering effect contributes to the particle adsorption at the interface between the two blend components and sufficient droplet stabilization was achieved between a content of 2-5 wt.-% of Janus particles within the blend mixture.

Zusammenfassung

Die vorliegende Arbeit befasst sich mit der Herstellung von kompartmentierten Nanostrukturen durch die Selbstassemblierung von linearen ABC-Triblock-Terpolymeren in Lösung. Gezielte Auswahl von Blocksequenzen und –längen in Kombination mit einem genau einstellbaren Selbstassemblierungspfad erlauben die Herstellung von neuen kompartmentierten Nanopartikeln mit bisher noch nie gezeigter Komplexität. Die Dissertation ist dabei in drei Hauptkapitel unterteilt, wobei sich die ersten zwei Themenblöcke mit der Synthese von neuartigen und komplexen Nanostrukturen sowie deren gründlicher Charakterisierung und Strukturaufklärung befassen. Gegenstand des letzten Kapitels ist die Herstellung und Anwendung von Nanopartikeln in industriell interessanten Mengen.

Der erste Themenblock beschäftigt sich mit der Synthese von komplexen Partikeln, die durch eine Kombination aus Selbstassemblierung und anschließender Interpolyelektrolyt-Komplexierung hergestellt werden. Hierfür wird ein geladenes, amphiphiles Polybutadien-*block*-poly(1-methyl-2-vinyl pyridinium)-*block*-polymethacrylsäure (BVqMAA) Triblock Terpolymer mit einem hydrophoben PB-Block, einem polykationischen PVq-Block und einem negativ geladenen PMAA-Block in wässrige Lösung gegeben was zu sogenannten Multikompartiment-Mizellen (*multicompartment micelles*, MCMs) führt. Diese besitzen einen weichen PB-Kern, eine strukturierte Oberfläche (Patches) aus dem gebildeten Interpolyelektrolyt-Komplex (IPEK) zwischen PVq/PMAA und eine negativ geladene PMAA-Korona aufgrund der höheren Kettenlänge von PMAA im Vergleich zu PVq. Diese polyanionischen MCMs wurden als Startmaterial genutzt, um polykationische Homopolymere sowie polykationische-*block*-neutrale Diblock-Copolymere zu komplexieren. Die Zugabe von polykationischen Homopolymeren führt dabei zu der Entstehung von diskreten IPEK-Patches anstelle einer homogenen IPEK-Schale auf der Oberfläche des Mizellkerns. Dieses Verhalten kann damit erklärt werden, dass die langen Korona-Ketten den neu geformten IPEK gut genug von der wässrigen Lösung abschirmt und so dickere Patches geformt werden können, die im Gegenzug eine kleinere (ungünstige) Grenzfläche mit der Mizellkernoberfläche einnehmen können ohne dabei gleichzeitig eine noch ungünstigere Grenzfläche mit dem umgebenden Lösungsmittel anzunehmen. Unter Verwendung von bishydrophilen polykationische Diblock-Copolymeren zur Komplexierung, kann durch gezielte Wahl der Blocklänge des polykationischen Blocks eine hohen Kettenpackung innerhalb der Korona der MCMs erreicht werden. Die sterische Stabilisierung des nicht-ionischen Blocks hindert den entstehenden IPEK vor dem Kollabieren und anisotrope IPEK-Strukturen entstehen. Unter Zuhilfenahme von kryogener Transmissionselektrentomographie und computer-gestützter 3D Rekonstruktion konnten neuartige „Seeigel“ und „Schaufelrad“ IPEK-Mizellen aufgelöst werden.

Ein weiterer Hauptaspekt dieser Dissertation ist die Herstellung neuartiger Kernkompartimentierter Nanostrukturen durch hierarchische Selbstassemblierung von linearen Triblock-Terpolymeren. Das gewählte Strukturierungskonzept basiert auf einer in

unserer Arbeitsgruppe entwickelten Methode, bei der die beiden hydrophoben Blöcke nacheinander ausgefällt und dadurch sehr homogene sphärische MCMs erhalten werden. Im Rahmen meiner Arbeit wurde dieses Konzept auf andere Partikelgeometrien erweitert. In Anlehnung an die bekannten Diblock-Copolymer-Morphologien Kugeln, Zylinder, Sheets und Vesikel, wurde synthetisch eine Reihe an Triblock-Terpolymeren hergestellt bei der die Koronalänge entsprechend variiert wurde. Das dabei untersuchte Terpolymersystem bestand aus Polystyrol-*block*-polybutadien-*block*-poly(*tert*-butylmethacrylat) (SBT) und als finales Lösungsmittel wurden Aceton/Isopropanol-Gemische benutzt. Dieses Lösungsmittelgemisch ist in allen Zusammensetzungen ein gutes Lösungsmittel für die T-Korona, jedoch es ein Nichtlösungsmittel für S und B. Der S-Block wird durch Aceton zu einem bestimmten Grad gequollen, was eine ausreichende Kettenmobilität gewährleistet um kinetisch gefangene Strukturen zu verhindern. Sphärische MCMs, kompartmentierte Zylinder, Sheets und Vesikel konnten durch Verringerung der Koronalänge und/oder durch gezielte Quellung des S-Blocks erreicht werden. Inspiriert durch das Bulk-Verhalten von Diblock-Copolymeren wurde die Hypothese aufgestellt, dass innerhalb der resultierenden Nanostrukturen die beiden hydrophoben S- und B-Blöcke analog zum Bulk phasenseparieren. Die Reihe an SBT-Terpolymeren wurde mit unterschiedlichen S/B-Volumenverhältnissen erweitert, wobei die Koronalänge entsprechend der angestrebten Geometrie in Lösung eingestellt wurde. Durch dieses systematische Vorgehen konnten eine Vielzahl an komplexen kompartmentierten Strukturen hergestellt und detailliert mittels Transmissionselektronen-tomographie hinsichtlich der Phasenseparation der hydrophoben Blöcke untersucht werden. Neben eher simplen Kugel-auf-Kugel- und Kern-Schale-Strukturen konnten auch komplexere Helix-auf-Zylinder, Zylinder-auf-Sheet, Zylinder-auf-Vesikel sowie perforierte Sheets und Vesikel erreicht werden. Eine weiterführende Arbeit beschäftigt sich mit der Untersuchung von verschiedenen Einflussfaktoren auf die entstehenden kompartmentierten Nanostrukturen. Dabei wurde der Einfluss des gewählten Lösungsmittels untersucht und morphologische Übergänge von sphärischen MCMs zu Zylindern, Sheets und Vesikeln gefunden, je nachdem wie stark das gewählte Lösungsmittel den Mizellkern quillt oder die Korona kontrahieren lässt. Der solvophobe Volumenanteil innerhalb des Triblock-Terpolymers lässt sich des Weiteren auch durch die Zugabe von solvophobem Homopolymer oder Nachfunktionalisierung des B-Blocks erreichen, was ebenfalls eine Änderung der resultierenden Morphologie zur Folge hat. Um die tiefgreifende Untersuchung der SBT-Triblock-Terpolymere noch zu vervollständigen, wurde das Phasenverhalten im Festzustand untersucht und ein ternäres Phasendiagramm erstellt. Die Bulk-Morphologien umfassen dabei Kern-Schale-Zylinder, Lamelle-Lamelle- und Kern-Schale-Gyroid-Strukturen sowie eine weniger bekannte Zylinder-in-Lamelle-Morphologie.

Ein anderer Kernpunkt dieser Arbeit ist die Synthese von Polystyrol-*block*-polybutadien-*block*-polymethylmethacrylat (SBM) Janus-Mizellen durch Vernetzen der B-Kompartimente in sphärischen SBM MCMs. Im Rahmen dieser Arbeit wurde eine Methode entwickelt die Menge an Janus-Partikeln vom Labormaßstab auf 100 g pro

Herstellungsprozess zu erhöhen. Mehrere 100 g dieser Partikel wurden im Anschluss erfolgreich als Phasenvermittler unter technologisch relevanten Bedingungen in einem industriellen Extruder für Blend-Experimente von nicht mischbaren Polymeren eingesetzt. Die Blend-Morphologie änderte sich von einer nicht kontrollierten co-kontinuierlichen hin zu einer kleinen Tröpfchen-Morphologie. Der Pickering-Effekt trägt zu einer erhöhten Grenzflächenaffinität der Partikel bei und eine erfolgreiche Stabilisierung der Polymertröpfchen wird auch bei Einsatz relativ geringer Mengen von 2-5 Gew.-% an Janus Partikeln gewährleistet.

List of Abbreviations

1D, 2D, 3D	one-, two-, three-dimensional
$^1\text{H-NMR}$	proton nuclear magnetic resonance
AAO	anodized aluminium oxide
AFM	atomic force microscopy
ATRP	atom transfer radical polymerization
Au	gold
BuLi	<i>sec</i> -butyl lithium
BVqMAA	polybutadiene- <i>block</i> -poly(1-methyl-2-vinylpyridinium)- <i>block</i> -poly(methacrylic acid)
BVT	polybutadiene- <i>block</i> -poly(2-vinylpyridine)- <i>block</i> -poly(<i>tert</i> -butyl methacrylate)
CaCl₂	calcium chloride
CdSe	cadmium selenide
Cryo-ET	cryogenic transmission electron tomography
Cryo-TEM	cryogenic transmission electron microscopy
CTA	chain transfer agent
CWC	critical water concentration
DLS	dynamic light scattering
DMAc	<i>N,N</i> -dimethylacetamide
DMF	dimethylformamide
DNA	deoxyribonucleic acid
E_{bend}	bending energy
E_{disk}	line energy
ET	transmission electron tomography
H	interfacial mean curvature
HCl	hydrogen chloride
HPMA	hydroxypropylmethacrylate

IPEC	interpolyelectrolyte complex
JP(s)	Janus particle(s)
K	Gaussian curvature
MCM(s)	multicompartment micelle(s)
M_n	number average molecular weight
M_w	weight average molecular weight
MWCO	molecular weight cut-off
MWD	molecular weight distribution
N	degree of polymerization
NaCl	sodium chloride
N_{agg}	aggregation number
NaOH	sodium hydroxide
ODT	order-disorder transition
OSBO	poly(ethylene oxide)- <i>block</i> -polystyrene- <i>block</i> -polybutadiene- <i>block</i> -poly-(ethylene oxide)
OsO₄	osmium tetroxide
p	packing parameter
PB	polybutadiene
PBA	poly(butyl methacrylate)
PCEMA	poly(2-(cinnamoyloxy)ethyl methacrylate)
PD	poly(3-butenyl (dodecyl)sulphane)
PDEA	poly(2-diethylaminoethyl methacrylate)
PDI	polydispersity index
PEG	polyethylene glycol
PEO	polyethylene oxide
PFS	poly(ferrocenyldimethyl silane)
PI	polyisoprene
PISA	polymerization induced self-assembly

PMA	poly(methyl acrylate)
PMAA	poly(methacrylic acid)
PMMA	poly(methyl methacrylate)
PS	polystyrene
PSGMA	poly(succinated glyceryl monomethacrylate)
PtBA	poly(<i>tert</i> -butyl acrylate)
PtBMA	poly(<i>tert</i> -butyl methacrylate)
PtBS	poly(4- <i>tert</i> -butoxy-styrene)
PVBFP	poly(pentafluorophenyl 4-vinylbenzyl ether)
PVBM	poly(4-methyl-4-(4-vinylbenzyl)morpholin-4-ium chloride)
P2VP	poly(2-vinylpyridine)
P2VPq	poly(1-methyl-2-vinylpyridinium)
<i>R</i>	gas constant
RAFT	reversible addition fragmentation transfer polymerization
$R_{h,app}$	apparent hydrodynamic radius
RI	refractive index
S	polystyrene
SAXS	small angle X-ray scattering
SBM	PS- <i>b</i> -PB- <i>b</i> -PMMA
SBMAA	PS- <i>b</i> -PB- <i>b</i> -PMAA
SCFT	self consistent field theory
SEC	size exclusion chromatography
SEM	scanning electron microscopy
<i>T</i>	absolute temperature
TEM	transmission electron microscopy
T_g	glass transition temperature
THF	tetrahydrofuran

List of Abbreviations

V_X	molar volume of block X
Z	aggregation number
χ_{XY}	Flory-Huggins-interaction parameter between blocks X and Y
ϕ_X	block volume fraction of block X

1. Introduction

Self-assembly is the ability of building blocks to spontaneously organize into highly defined superstructures through non-covalent interactions without external intervention.¹⁻³ Sculpturing complex patterns from simple starting materials attracted great attention in the scientific world, yet nature has made this bottom-up structuring perfect. To name only two out of many exquisite examples how nature acts as an archetype for self-assembly, nanometer-sized building blocks such as proteins, hydroxyapatite and aragonite are combined in a stepwise hierarchical procedure to form bones and nacre with excellent mechanical properties.^{4,5} Inspired by that, materials scientists try to develop new materials on the basis of building blocks that are able to undergo self-assembly, bridging several levels of hierarchy. Particularly, self-assembly on the nano- and mesoscale evolved to be very promising with regard to future applications like drug delivery,^{6,7} sensors^{8,9} or for materials with unique electronic or optical properties.¹⁰⁻¹² Several intriguing examples for self-assembly on this scale have been demonstrated like DNA-origami^{13,14} or the self-assembly of cellulose nanocrystals,¹⁵ proteins¹⁶ and viruses.¹⁷ Beyond these bio-based building blocks, hard colloidal particles raised interest due to straightforward synthetic methods and their great potential to arrange into colloidal crystals with unique photonic properties.^{10,18-23} However, self-assembly into such crystals of infinite size and domain orientation is a result of the isotropic particles that have no restricting or directing forces that allow assembly into a preferred direction. Hence, directionality within building blocks is desirable to control and predict final superstructures.

One possibility of colloids to gain directionality is through anisotropy or distinct shapes as in polyhedra.²⁴⁻²⁷ Theoretical predictions of the latter show self-assembly into highly complex superstructures with structural diversity,²⁸ yet experimentally it still remains challenging to synthesize particles with narrow enough size dispersity to qualify as building block for self-assembly into higher hierarchies without defect propagation.²⁹⁻³⁴ Equipping colloids with valences to form so-called colloidal molecules is another way to control the self-assembly direction.^{35,36} The interparticle interaction is thereby guided by, *e.g.* DNA linkers attached to the surface of the colloids.^{37,38} Encoding directionality to isotropic particles with surface patches proved to be an elegant way to achieve predictable self-assembly and several top-down methods are accessible, like stamping methods,³⁹⁻⁴¹ glancing angle deposition⁴² or lithography.^{43,44} The self-assembly of these colloidal building blocks comprises clusters of defined size, but also complex arrangements ranging from helices to colloidal kagome lattices.⁴⁵⁻⁴⁷ However, top-down approaches reach their limits on the nanoscale and bottom-up approaches are promising to build superstructures from nanometer-sized building blocks. Downsizing of building blocks is of particular interest as final superstructures have feature sizes on the scale of the underlying units.

Especially block copolymers give rise to sophisticated nanomaterials with tunable chemical and physical properties as well as periodicities within the sub 100 nm range. Their properties are easy to tailor towards the final application through proper choice of monomers while the minimum feature size of the final assembly is influenced by the over-

all molecular weight of the block copolymer. Block copolymers have proven to be applicable in everyday life, *e.g.*, as surfactants, in materials science as compatibilizer in blends, and in nanotechnology for the fabrication of nanostructured materials with complex shape and functionality. The intrinsic incompatibility of the blocks leads to phase-separation and enables the template-free formation of distinct structures in bulk and in selective solvents.⁴⁸ Various controlled polymerization methods allow tailored fabrication of diblock, triblock or even multiblock copolymers. Already the addition of one block from diblock copolymers to triblock terpolymers considerably increases the spectrum of accessible morphologies in bulk as well as in solution.⁴⁹ Complex self-assembled patchy and compartmentalized superstructures in solution are of particular interest for, *e.g.* drug delivery applications as chemically different compartments allow simultaneous storage of different compounds within one particle.^{50,51} However, the prediction and controlled fabrication of these supramolecular assemblies challenges theoreticians and experimentalists alike. The development towards evermore complex block co-/terpolymer based self-assembled structures can encompass length scales from nano- to micron size and give rise to unique materials with precisely tunable properties. In the following chapters, the structural diversity of diblock co- and triblock terpolymers will be briefly addressed giving an overview of fundamental theory as well as recent developments in self-assembly of more complex particles.

1.1. Block Copolymer Self-Assembly in Bulk

Block copolymers consist of two or more covalently linked blocks with distinct chemical and physical properties. In the bulk phase the immiscibility of the blocks leads to the microphase separation on the molecular scale, as macroscopic phase separation is prevented due to the covalent connectivity. The resulting phase behavior is governed by three parameters: the overall degree of polymerization, N , the volume fraction, ϕ , of the blocks ($\phi_A=1-\phi_B$) and the Flory-Huggins-Parameter, χ . The first two parameters can be tuned through synthetic protocols, whereas the latter describes the segment-segment-incompatibility between the blocks and depends on the selection of monomers.⁵²

1.1.1. Self-Assembly of AB Diblock Copolymers in Bulk

The phase behavior of simple AB diblock copolymers has been subject of both theoreticians and experimentalists. Controlled polymerization techniques such as atom transfer radical polymerization (ATRP), radical addition-fragmentation chain-transfer polymerization (RAFT) or living anionic polymerization opened the door towards narrowly distributed, tailor-made block copolymers.⁴⁸ The segregation of block copolymers is a compromise between enthalpic (interfacial energy) and entropic (chain stretching) contributions; the system tries to minimize the interfacial area between the blocks to lower the total interfacial energy. In contrast to low molecular weight compounds, mixing of covalently linked polymer chains of a block copolymer gives only a small entropy gain and the

unfavorable mixing enthalpy promotes self-assembly into distinct thermodynamically stable nanostructures which will be discussed in the following section.^{53–55}

Helfand already established fundamentals of block copolymer self-assembly in strong segregation in 1978⁵⁶ while for the weak segregation, Leibler described for the first time the transition from a disordered to an ordered, microphase-separated state of AB block copolymers in dependence of the volume fraction, ϕ , of the blocks and the product χN , where N is the total number of monomer segments.⁵⁷ Calculated with self-consistent field theory (SCFT), the established phase diagram by Matsen *et al.* includes all thermodynamically stable phases: spheres, cylinders, lamellae and gyroids (Figure 1.1).^{58,59}

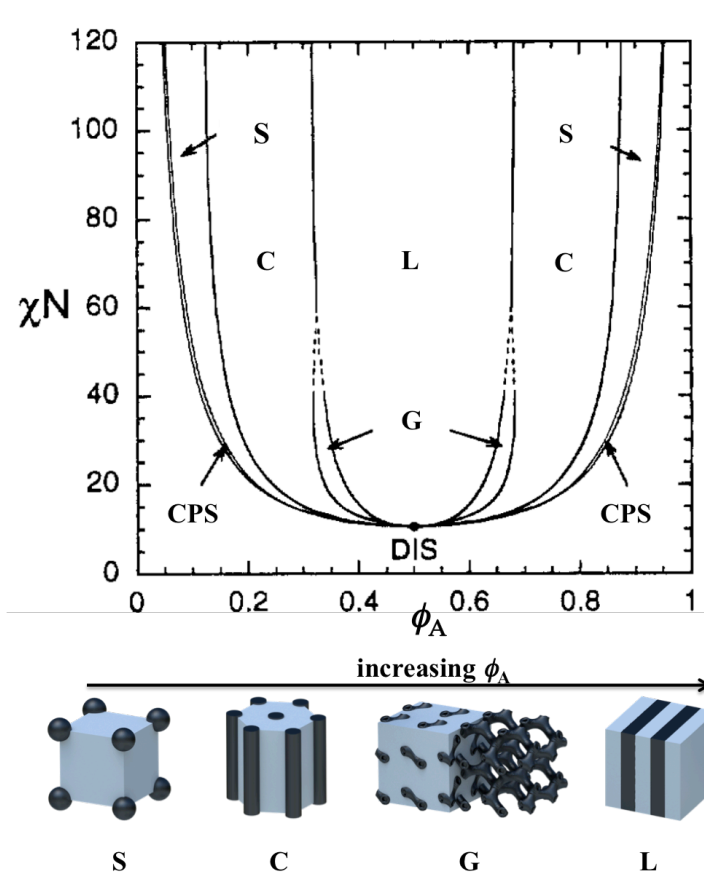


Figure 1.1: Thermodynamically stable phases in AB diblock copolymers. Theoretical phase diagram calculated with SCFT. Adapted from [59]. Reprinted with permission from American Chemical Society. The morphologies comprise spheres (CPS, S), cylinders (C), gyroids (G) and lamellae (L). The schematics represent the morphologies in dependence of increasing ϕ_A (black) from $\phi_A=0.1$ (sphere) to $\phi_A=0.5$ (lamellar). For higher ϕ_A the inverse morphologies occur.

The order-disorder transition (ODT) from an unperturbed, disordered state, which is dominated by entropic terms, towards microphase separation directed by enthalpic terms has been calculated to occur at $\chi N > 10.5$ for equal volume fractions.⁶⁰ The bulk behavior is experimentally well understood and mostly governed by two parameters, the interaction parameter, χ_{AB} , and the volume composition, ϕ_A .^{61–63} The gyroid morphology, although only observed in a narrow composition window, attracted considerable attention as template material to fabricate nanohybrid or nanoporous materials as the gyroid morphology is

bicontinuous and hence has a high surface area.^{64–66} Besides synthetic control of morphology (block length and choice of monomers), several post polymerization methods are commonly used to manipulate the phase behavior of diblock copolymers. The volume fraction of one of the blocks can be influenced *via* blending with homo- and copolymers,^{67,68} nanoparticles⁶⁹ or *via* hydrogen-bonding.^{70–73} Also thermally induced order-order transitions,^{74,75} shear alignment^{76,77} and alignment in electrical fields^{78–80} have evolved to state-of-the art techniques to induce, alter and optimize long-range order or to switch between morphologies.

In contrast to the straightforward phase behavior giving four thermodynamically stable phases, introducing a third block to the AB system to form ABC triblock terpolymers greatly increases the parameter space. Consequently, the complexity of the resulting phase behavior increases and gives rise to a myriad of morphologies not possible to be generated with simple AB diblock copolymers.

1.1.2. Self-Assembly of ABC Triblock Terpolymers in Bulk

While AB diblock copolymers adopt four different nanophases, the complexity dramatically increases in ABC triblock terpolymers.^{49,81,82} While only two parameters govern the phase behaviour of diblock copolymers, in ABC triblock terpolymers there are already five parameters that influence the final morphology: χ_{AB} , χ_{AC} , χ_{BC} , ϕ_A and ϕ_B .^{55,83} Additionally, variations in the block sequence (ABC, ACB, BAC)^{84,85} and the architecture (linear or miktoarm)^{86–88} contribute to the complexity of the bulk behaviour. Focusing on linear ABC triblock terpolymers, Stadler *et al.* pioneered this field of bulk self-assembly of polystyrene-*block*-polybutadiene-*block*-poly(methyl methacrylate) (SBM). Besides core-shell analogues of cylindrical and gyroid diblock copolymer morphologies, they revealed diverse complex structures, *e.g.* the spheres-on-sphere, spheres-on-cylinder, helix-on-cylinder and (after hydrogenation of the PB block) a “knitting pattern” morphology.^{89–92} Figure 1.2 shows the ternary phase diagram for the SBM triblock terpolymer, intriguingly demonstrating the high complexity of arranging three blocks, going far beyond the ability of arranging AB diblock copolymers.⁹³

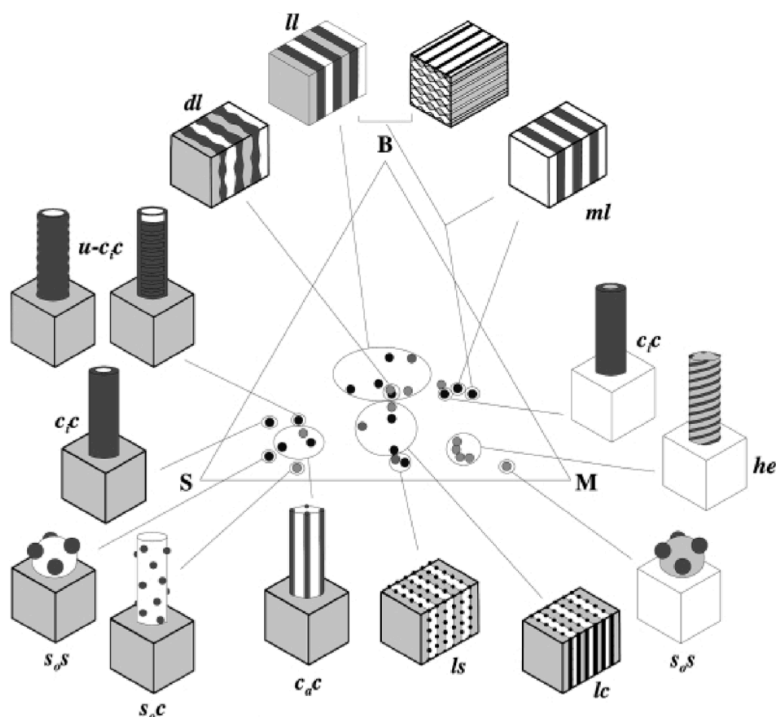


Figure 1.2: Ternary phase diagram of SBM. The ternary phase diagram of SBM established by Stadler *et al.* demonstrates the structural complexity of bulk morphologies that SBM triblock terpolymers can adopt, showing more than 10 different morphologies. The colours of the schematics represent polystyrene (gray), polybutadiene (black) and poly(methyl methacrylate) (white). Adapted from [93]. Reprinted with permission from Wiley-VCH Verlag GmbH & Co. KGaA.

Since then, much efforts have been put into in-depth understanding of the phase behaviour of various linear ABC triblock terpolymers comprising polyisoprene-*block*-polystyrene-*block*-poly(ethylene oxide),^{94–96} polystyrene-*block*-poly(2-vinylpyridine)-*block*-poly(*tert*-butyl methacrylate)⁹⁷ or polybutadiene-*block*-poly(2-vinylpyridine)-*block*-poly(*tert*-butyl methacrylate).⁹⁸ Distinct morphologies like lamella-sphere, lamella-cylinder or lamella-lamella (Figure 1.2 *ls*, *lc*, *ll*) are suitable to synthesize Janus particles, *i.e.* particles with two hemispheres, through crosslinking of the middle block (black) and subsequent dissolution of the bulk phase.^{99–102}

In addition to bulk microphases, the distinct properties of individual blocks make them ideal candidates for structuring in solution when introduced into a selective solvent. In the following sections, the solution self-assembly of diblock copolymers and ABC triblock terpolymers is addressed to give an overview of basic solution morphologies of diblock copolymers and more complex assemblies of triblock terpolymers.

1.2. Block Copolymer Self-Assembly in Solution

If a good solvent is added to a homopolymer in bulk, the solvent molecules start to interpenetrate to the bulk polymer, swell it and finally a homogeneous solution exists with single distributed polymer chains. This is the case when the interaction energy between the polymer segments is comparable to the interaction energy of a polymer segment with the solvent molecules or, in other words, when the solubility parameters of polymer and sol-

vent are similar (“like dissolves like”). However, the homogeneous distribution of single polymer chains in a good solvent is hindered, if this polymer is covalently linked to another, insoluble block and distinct nanostructures emerge that will be discussed in the following sections.

1.2.1. Self-Assembly of AB Diblock Copolymers in Solution

Addition of a selective solvent to an amphiphilic AB diblock copolymer leads to micellar aggregates similar to those known for lipids. Hence, diblock copolymers can be seen as macromolecular surfactants that assemble into distinct nanostructures with a core consisting of the insoluble block and a stabilizing corona of the soluble block. Depending on the ratio of hydrophobic/hydrophilic blocks, or more general solvophobic/solvophilic blocks, the geometry of the aggregates can range from spherical micelles and cylinders to bilayer sheets that roll up to vesicles (Figure 1.3a). Two decades ago, Eisenberg was the first to characterize multiple morphologies from asymmetric polystyrene-*block*-poly(acrylic acid) (PS-PAA) block copolymers in DMF/water mixtures.¹⁰³ In aqueous solution, the morphological change from micelles to vesicles with polybutadiene-*b*-poly(ethylene oxide) (PB-PEO) diblock copolymers was intensely studied by Bates *et al.* (Figure 1.3b).^{104–106} They observed micelle to cylinder to vesicle transitions with increasing PEO block length and additionally, they found worm-like micelles with Y-junctions and network-formation at a certain PEO block length between the cylinder and the final vesicle state.¹⁰⁶

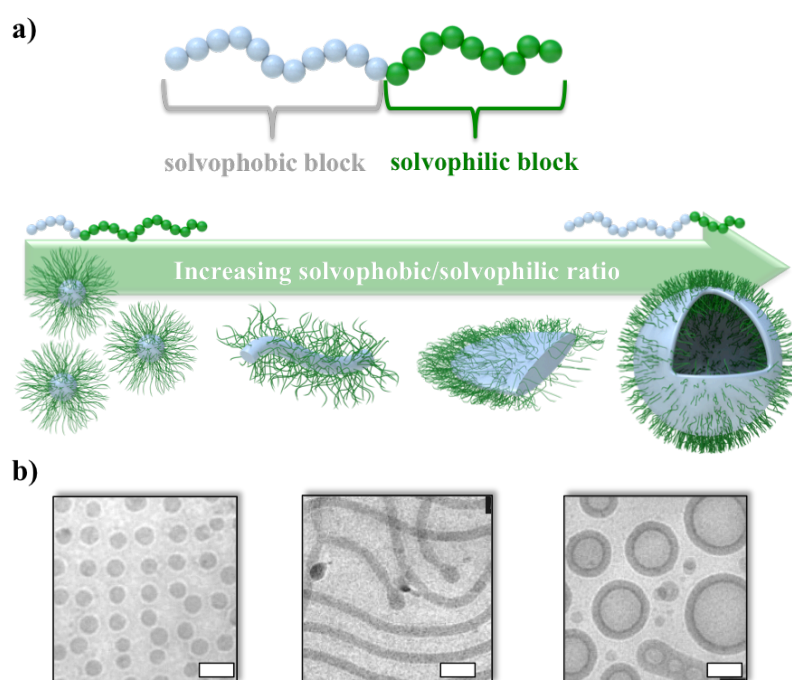


Figure 1.3: Overview of AB diblock copolymer solution structures. **a)** The diblock copolymer consists of a solvophobic (gray) and a solvophilic (green) block. Depending on the solvophobic/solvophilic ratio, spherical micelles, cylinders, bilayer sheets or vesicles occur. **b)** With decreasing corona block length, spheres, cylinders and vesicles form from PB-PEO in aqueous solution. The scale bar corresponds to 100 nm. Adapted from [106]. Reprinted with permission from the American Association for the Advancement of Sciences.

Bates *et al.* used a system comprising polybutadiene as the hydrophobic block with a low glass transition temperature ($T_g \ll$ room temperature) that is able to rearrange in the collapsed state to form the thermodynamically preferred geometry (spheres, cylinders, vesicles). If a high T_g block like polystyrene is used instead, kinetically trapped structures easily occur due to freezing of the hydrophobic chains in the core without the possibility of rearrangement and equilibration. In that case usually a co-solvent is added to plasticise the hydrophobic core facilitating chain mobility to reach equilibrium conditions.^{103,107,108}

A frequently used approach aiding to predict the overall geometry of micellar structures is the packing parameter, p . This parameter was developed by Israelachvili to describe the packing behaviour of lipids based on geometrical considerations.¹⁰⁹ The packing parameter is defined in Figure 1.4a, where V is the volume of the solvophobic part, l is the length of the solvophobic chain normal to the interface and a is the area at the solvophobic-solvophilic/solvent interface. Beyond that, the packing parameter p can be described by means of the interfacial mean curvature, H , and the Gaussian curvature, K , (Figure 1.4a). Depending on the value of p the resulting micellar geometry from spheres to cylinders and bilayers can be estimated (Figure 1.4b).^{106,110–112}

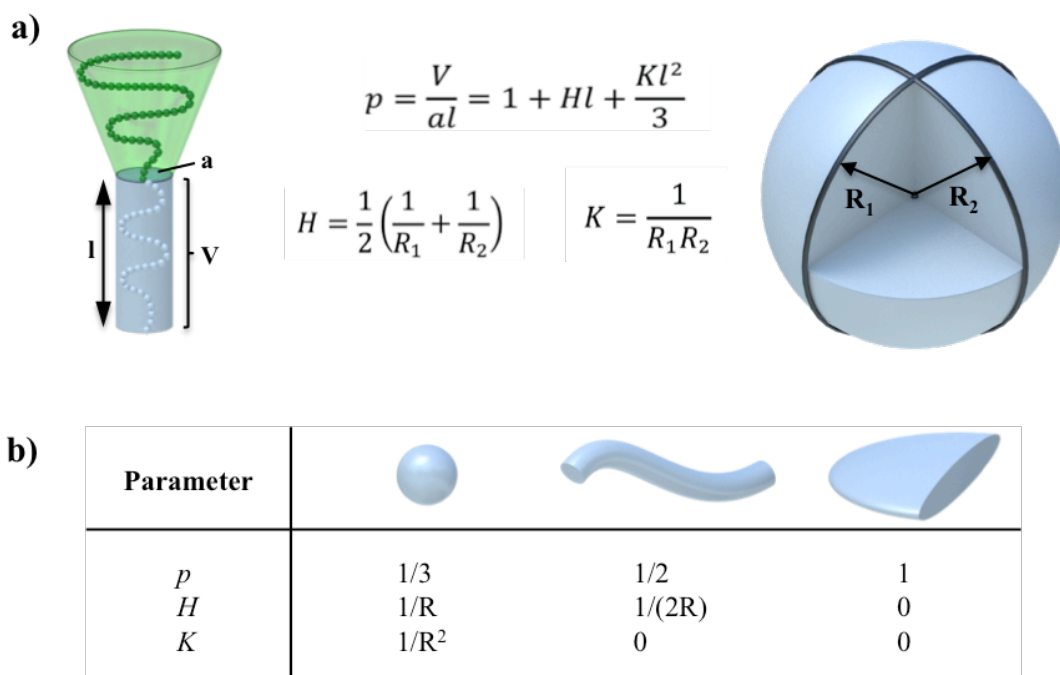


Figure 1.4: Packing parameter p and its relation to the geometry of the resulting assembly. a) Based on geometrical considerations, the packing parameter describes the packing behaviour of amphiphilic particles exemplified for a block copolymer chain. The packing behaviour can be described also through the interfacial mean and Gaussian curvature H and K . b) Particle shape and corresponding values for p , H and K .¹¹¹

The packing parameter, p , is solely based on geometric considerations of the core forming block carrying a hydrophilic headgroup, hence predicting micellar structures of diblock copolymers by means of p reaches its limit as the chain length of the corona block is not taken into account. Other models proved to be suitable to describe the self-assembly of *e.g.* neutral-*block*-amorphous diblock copolymers into distinct equilibrium structures and are in

good agreement with experimental results. The calculations are based on the free energies per chain of the core, its surface and of the corona. The free energy per chain in dependence of the molar fractions x_A of the solvophilic block provide stability regions of distinct micellar structures. In case of $x_A > 0.36$ spherical micelles occur and shift to cylinders for $0.36 > x_A > 0.27$ and vesicles for $x_A < 0.27$.¹¹³

Since the first report on multiple solution morphologies of block copolymers in 1995¹⁰³, Eisenberg *et al.* thoroughly screened the phase behaviour of PS-PAA in solution and achieved more than 20 different morphologies. These aggregates comprise, spherical micelles, cylinders and vesicles but also more complex bicontinuous rods and hexagonally packed hollow hoops among others (Figure 1.5a).⁵³ Additionally to water, the high T_g of the hydrophobic, core-forming PS block requires a co-solvent (*e.g.* DMF) to ensure chain mobility and formation of equilibrium structures. In a typical procedure, the PS-PAA diblock copolymer is dissolved in a common solvent for both blocks and the PS block is subsequently precipitated by addition of water. Eisenberg intensely studied the influence of compounds such as HCl, NaOH, NaCl, or CaCl₂, in the aqueous phase.^{114,115} In presence of HCl, PAA is partially protonated and the chain repulsion decreases, which leads to a morphological transition from spheres to vesicles (Figure 1.5b). Analogously, NaCl or CaCl₂ promote a morphological transition towards cylindrical and vesicular structures, due to ion-binding (NaCl) or ion-bridging (divalent Ca²⁺), resulting in a decreased steric repulsion of corona chains. However, if NaOH is added instead, PAA is deprotonated and the morphology changes from vesicular particles towards spherical micelles due to an increase in chain repulsion.

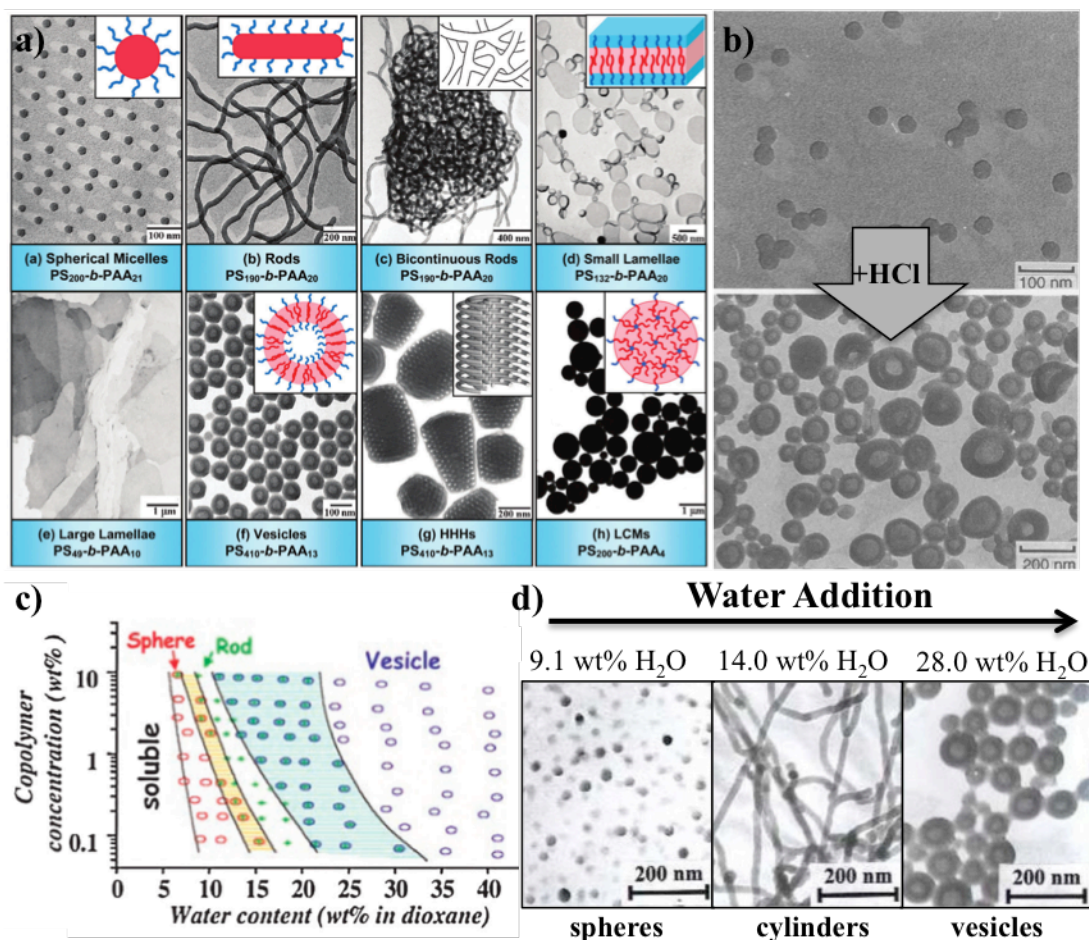


Figure 1.5: Morphologies of diblock copolymers. **a)** Various morphologies of PS-PAA diblock copolymers of different block length ratios in solvent/non-solvent mixtures. Adapted from [53]. Reprinted with permission from The Royal Society of Chemistry. **b)** Morphological transition of spherical micelles towards vesicles upon addition of HCl. **c)** Phase diagram of PS₃₁₀-PAA₅₂ in water-dioxane mixtures as a function of copolymer concentration and water content. Adapted from [114] and [116]. Reprinted with permission from the American Association for the Advancement of Sciences. **d)** Morphological change from micelles to vesicles upon water addition to a PS₃₁₀-PAA₅₂ in dioxane. Adapted from [117]. Reprinted with permission from American Chemical Society. The subscripts denote degree of polymerization, N .

Besides the nature of the common solvent^{107,108} and concentration of the diblock copolymer, the water content within the system has a crucial influence on morphology that develops.¹¹⁷ At the beginning, the block copolymer is unimolecularly dissolved in the common solvent. Upon addition of water above a critical water concentration (CWC), the polymer chains form spherical micelles. Further increase of water content subsequently leads to a morphological shift towards cylinders and vesicles (Figure 1.5c,d).^{116,117} They proved that the structures are under thermodynamic control as the system is fully reversible and does not change even after one year of ageing. The morphological transition from spheres to cylinders and vesicles can be explained as follows. Upon addition of water, the hydrophobic PS block starts to collapse and spherical micelles are formed. At the same time the interfacial tension increases and the system tries to minimize the total interfacial area of the core with the surrounding solvent. At first, larger micelles with a higher aggre-

gation number, Z , form, leading to an unfavourable core-chain stretching and more chains per micelles lead to a higher repulsion of coronal chains. As a consequence, the system minimizes the total free energy of the system by changing the morphology from spheres towards cylinders, thereby decreasing core-chain stretching and the total surface area of the PS core.^{117,118}

The work of Armes *et al.* tremendously contributed to the understanding of morphological transitions within block copolymers employing polymerization-induced self-assembly (PISA) *via* RAFT dispersion polymerization in aqueous media.^{119–121} They use *e.g.* poly(2-(methacryloyloxy)ethyl phosphorylcholine)¹¹⁹ or poly(ethylene glycol)¹²¹ as water-soluble macro-chain transfer agent (macro-CTA) and polymerize 2-hydroxypropyl methacrylate (HPMA). The emerging polymer block is hydrophobic and induces *in-situ* morphological transitions from spheres to cylinders and vesicles. With progressing polymerization – as illustrated in Figure 1.6a – the volume of the hydrophobic block volume increases and shifts the hydrophobic/hydrophilic ratio towards higher values. This PISA process gives an intriguing insight into morphological transitions from cylinders to bilayers and finally vesicles, which otherwise are challenging to capture when analysing fixed block copolymer compositions in solution.¹²²

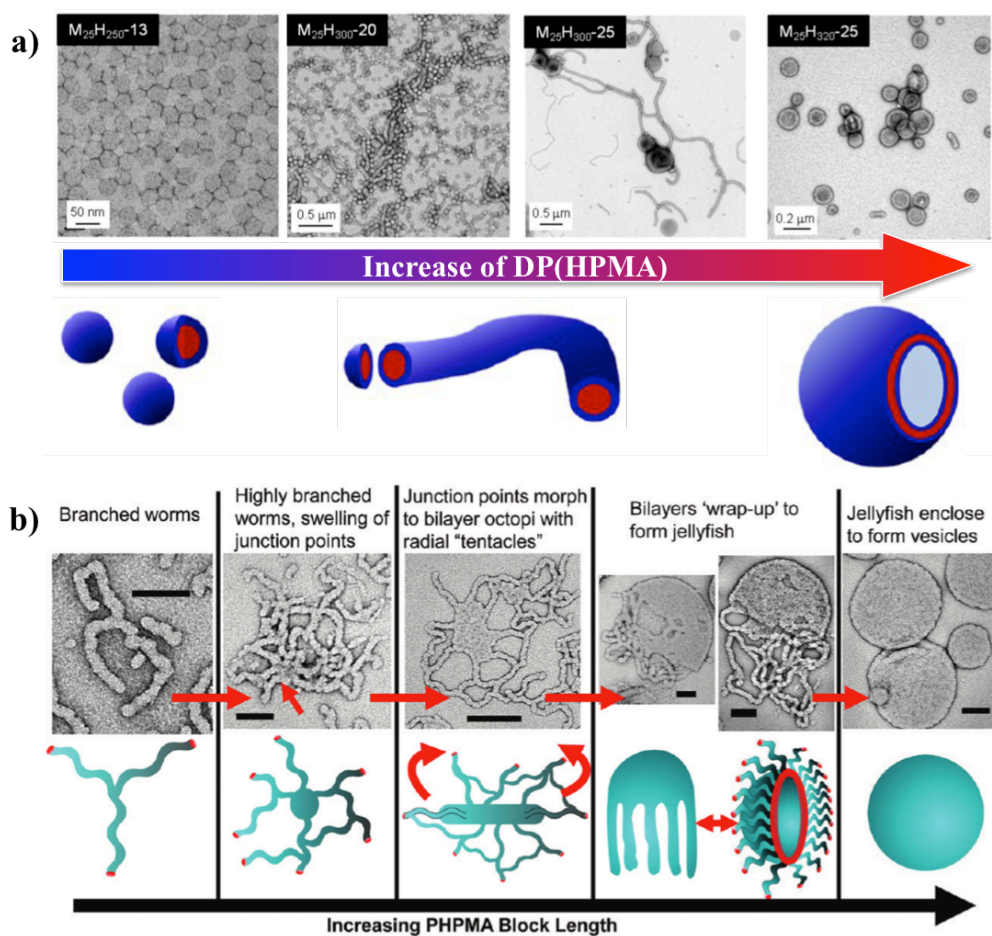


Figure 1.6: Polymerization-induced self-assembly. a) RAFT dispersion polymerization of HPMA from a water soluble macro-initiator leads to the morphological transition from spheres to vesicles upon progression of polymerization. Adapted from [119,121]. b) Mechanistic insight in

the formation of vesicles from cylindrical micelles. The cylinders first start to branch and fuse to sheets with tentacles that in the final state roll up and close to form vesicles. Adapted from [122]. Reprinted with permission from American Chemical Society.

Armes *et al.* revealed that the cylinder-to-bilayer transition proceeds *via* “octopus”- and “jellyfish”-like intermediate structures that finally roll-up to form vesicles (Figure 1.6b). Upon polymerization they first observed spherical micelles that start to fuse into worm-like micelles upon polymerization. With increasing block length of the hydrophobic block the cylindrical micelles first form branches and then start to cluster and fuse to the octopus-like structures. After wrapping of these “octopi” they progress through a “jellyfish”-like intermediate structure before they close-up through tentacle-fusion to form closed vesicles.

Vesicles built from block copolymers attracted attention due to their potential to encapsulate guest compounds, at the same time having better mechanical properties as compared to low molecular weight (*e.g.*, lipid) analogues. In 1995, Meijer *et al.* contributed one of the first reports about block copolymer vesicles using polystyrene coupled with poly(propylene imine) dendrimers as macromolecular amphiphilic analogue to lipids.¹²³ Later, Discher *et al.* coined the term “polymersome” for block copolymer vesicles in analogy to liposomes.¹²⁴ The self-assembly of block copolymers to vesicles in selective solvents is also called solvent replacement technique in contrast to solvent-free methods like electroformation or bulk film rehydration.^{125–127} Block copolymer vesicles form when a bilayer sheet (Figure 1.7a) rolls-up to a closed capsule. The roll-up occurs if the bending energy E_{bend} that is required to close a vesicle is lower than the line energy E_{disk} that exists because of the circular border of the bilayer sheet (Figure 1.7b).^{111,128}

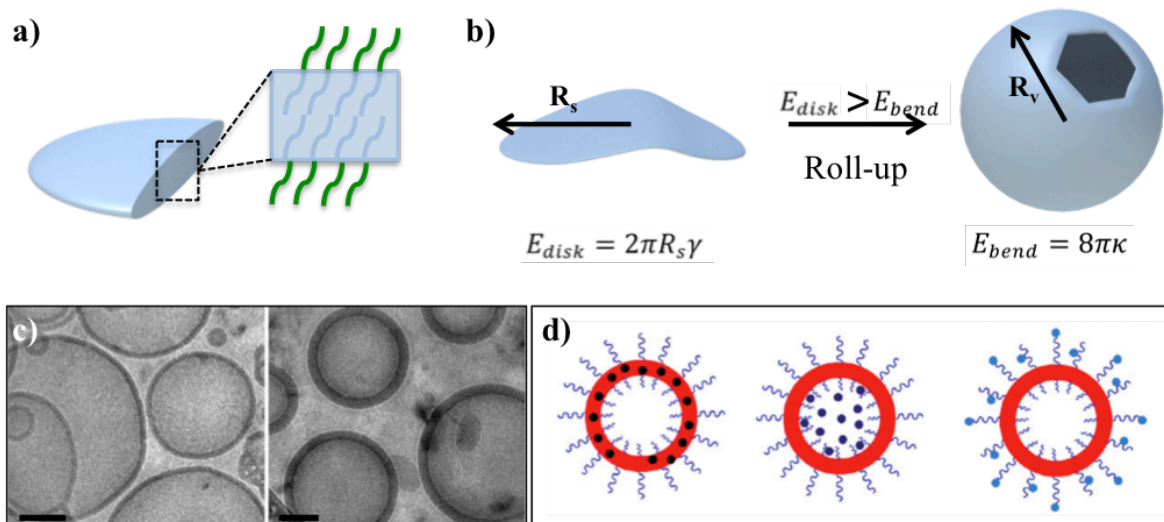


Figure 1.7: Vesicle formation. **a)** Schematic block copolymer chain arrangement within a bilayer sheet. **b)** Formation of vesicles from bilayer sheets. γ is the line tension and κ the bending modulus.¹¹¹ **c)** Examples of PB-PEO vesicles in aqueous solution. The membrane thickness increases with increasing molecular weight of PB (from left to right). The scale bar is 100 nm. Adapted from [129]. Reprinted with permission from American Chemical Society. **d)** Possible functionalization methods making polymersomes attractive for various potential applications: Incorporation of hydrophobic compounds into the membrane, hydrophilic particles can be entrapped in the interior and the corona may be post-functionalized. Adapted from [130]. Reprinted with permission from The Royal Society of Chemistry.

Vesicles have been intensely studied with respect to the formation mechanisms and applications and the gained knowledge is summarized in various review articles.^{111,116,125,126,131-134} The molecular weight can be modified synthetically and vesicles with tuneable membrane thicknesses (Figure 1.7c) typically in the range of 2-30 nm are achieved exceeding that of lipid bilayers (3-5 nm).¹²⁶ In contrast to lipid bilayers, the increased membrane thickness is causal for the enhanced toughness of polymersomes and the reduced permeability of the membrane.¹²⁴ The toughness increases even further when vesicles with a cross-linked membrane are used.¹³⁵ The reduced permeability and higher mechanical stability makes them ideal candidates for controlled release applications. There are three different ways to make polymersomes accessible for possible application: the hydrophobic membrane, solvent/water filled cavity, and the corona chains (Figure 1.7d). Closure of bilayer sheets to vesicles allows encapsulation of hydrophilic compounds such as proteins or drugs.¹³⁶ These compounds are released through various stimuli where the hydrophobic, membrane-forming block either is degraded,^{137,138} molecularly dissolved through pH- and/or temperature change¹³⁹⁻¹⁴² or irradiation with light.¹⁴³ Hydrophobic guests can be incorporated into the vesicle membrane as demonstrated for hydrophobic dyes, iron oxide^{144,145}, Au,¹⁴⁶ CdSe¹⁴⁷ or silica nanoparticles¹⁴⁸. The corona chains of polymersomes are responsible for stabilization and to prevent the particles from aggregation, yet also the corona is accessible for post-functionalization. Synthesis of Au nanoparticles¹⁴⁸ within a corona carrying amino groups or click reactions of biotin to an azide-functionalized corona were demonstrated as modification methods.¹⁴⁹

Although the main focus of this chapter was to introduce the self-assembly behaviour of coil-coil diblock copolymers, there exists other types of blocks that lead to controlled solution morphologies and some examples should be briefly mentioned. Manners, Winnik *et al.* for example use a crystalline-coil diblock copolymer system with a crystallisable polyferrocenylsilane block to form cylindrical micelles (Figure 1.8a)¹⁵⁰⁻¹⁵², but also two dimensional sheet-like (Figure 1.8b)¹⁵³⁻¹⁵⁵ and hybrid structures¹⁵⁶ or recently, more complex assemblies bridging several levels of hierarchy.¹⁵⁷ PS-*b*-PEO is able to form narrowly distributed rectangular platelets in methylcyclohexane through crystallization of the PEO block¹⁵⁸ (Figure 1.8c) and block copolymers bearing a liquid crystalline block can form smectic polymer vesicles (Figure 1.8d).^{159,160} Sommerdijk *et al.* used double comb or semicrystalline amphiphilic block copolymers to assemble them into complex bicontinuous nanostructures (Figure 8e) and reveal them in detail with the method of cryo-transmission electron tomography (cryo-ET).^{161,162} This method provides a tomographic 3D reconstruction of the studied particles and allows resolution of internal features with high precision and nanometre scale resolution. This is an advantage especially for complex particles as in 2D imaging techniques features may overlap, complicating a reliable characterization.¹⁶³ Cryo-ET is used in this thesis as a powerful method to reveal structural features of multi-compartment micelles which otherwise are hidden when analyzed with conventional 2D imaging techniques like cryo-TEM.

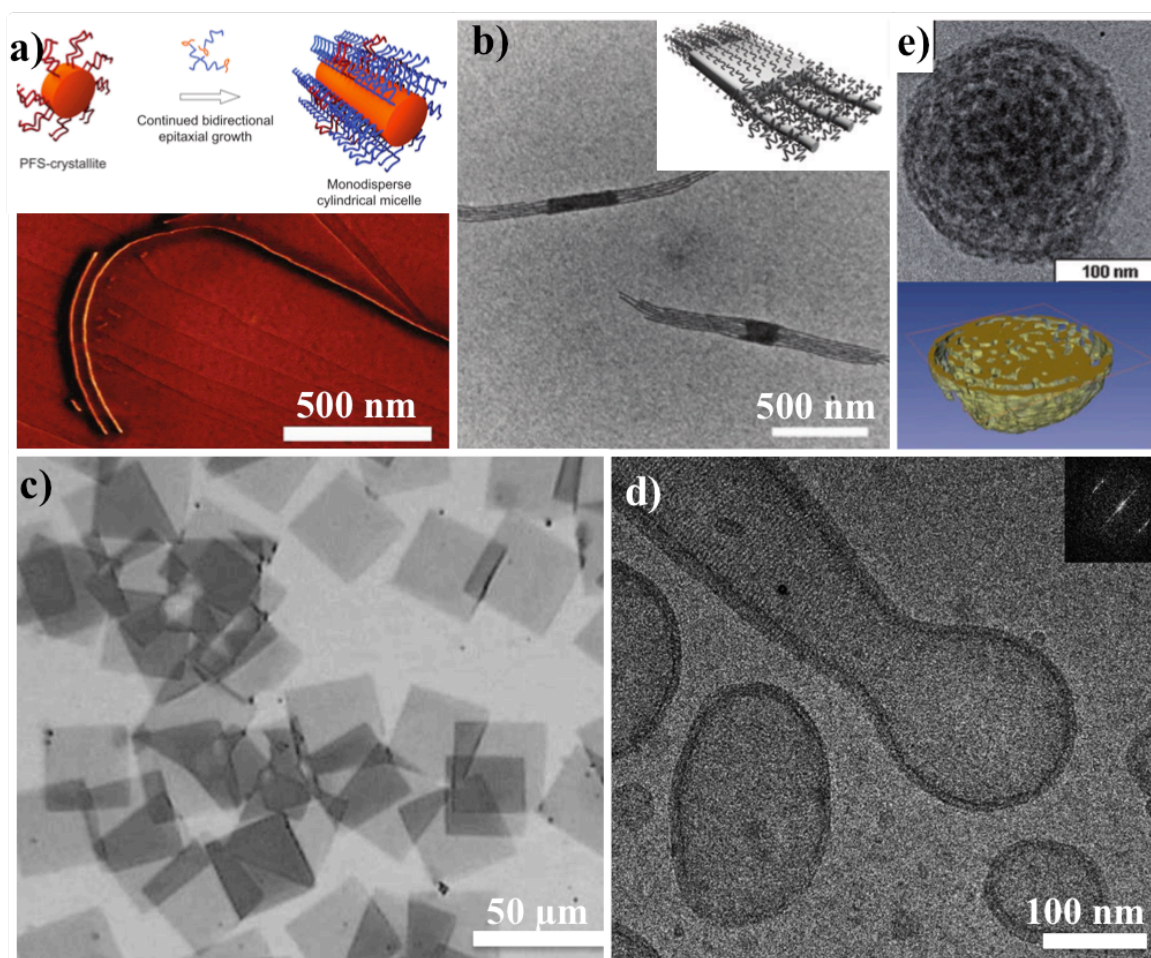


Figure 1.8: Self-Assembly of rod-crystalline, rod-liquid-crystalline and double comb diblock copolymers. Crystallization driven self-assembly of diblock copolymers can lead to (a) cylindrical micelles, (b) scarf-like nanostructures or (c) platelets. Adapted from [150], [154] and [158]. Reprinted with permission from Nature Publishing Group and Elsevier. (d) Smectic vesicles are achieved using a diblock copolymer that contains a liquid-crystalline block and (e) complex bicontinuous nanostructures were revealed with cryo-ET for a double comb diblock copolymer. Adapted from [159] and [161]. Reprinted with permission from The Royal Society of Chemistry and Wiley-VCH Verlag GmbH & Co. KGaA.

Analogous to the differences in bulk behavior of diblock copolymers and ABC triblock terpolymers, one can imagine that solution morphologies likewise evolve in complexity through addition of a third block. The self-assembly behavior of ABC triblock terpolymers in solution will be discussed in the following chapter.

1.2.2. Self-Assembly of ABC Triblock Terpolymers in Solution

The self-assembly of linear ABC triblock terpolymers in selective solvents may lead to either core-corona-corona⁸⁸ structures if the solvent is selective for the middle and one end block or to mixed or corona-compartmentalized structures also referred to as “patchy” if the solvent is selective for the two end blocks.¹⁶⁴ In case of vesicles it is also found, that the corona chains are entirely separated from each other as one block preferably points towards the solvent filled cavity while the other block points towards the surrounding medium.^{165,166} There exist only few examples for patchy nanostructures where the immis-

cibility of the corona chains lead to the formation of distinct patches on the surface. This was demonstrated *e.g.* for crystalline-core micelles with a PE core and distinct patches of PMMA and PS in spherical as well as cylindrical micelles.^{167–169} Frequently, co-assembly of two block copolymers is employed to obtain mixed, patchy or Janus structures.¹⁷⁰ Janus micelles with a core and a corona divided in two hemispheres are of particular interest due to their interfacial properties, yet gaining sufficient phase separation of corona chains within self-assemblies of ABC triblock terpolymers is challenging and usually achieved through bulk-templating as already described in section 1.1.2.¹⁷¹

Beyond the above mentioned patchy nanostructures, ABC triblock terpolymers with two solvophobic blocks are known to form core-compartmentalized - so-called multicompartment - nanostructures when dispersed in a selective solvent for only one of the blocks. The incompatibility of the solvophobic blocks induces microphase separation within the confined space of the micellar core. The focus of the following sections is drawn to ABC triblock terpolymers with two solvophobic block A and B and a solvophilic endblock C, although there exist also the case where the solvent is selective for the middle block.^{172,173} It has to be mentioned that miktoarm star terpolymers, *i.e.* terpolymers where all blocks are covalently connected in one junction, form a plethora of compartmentalized particles in solution due to the unique block arrangement which forces them to form interfaces of all three immiscible blocks. This field was pioneered by the groups of Hillmyer and Lodge who explored spherical, cylindrical, bilayer and vesicular structures in aqueous solution,^{174–177} yet the focus of this section is pointed towards linear ABC triblock terpolymers. This chapter is organized in a way that the single particle geometries, *i.e.* spheres, cylinders, bilayer and vesicles are discussed one after another to give an overview of recent literature in the field of compartmentalized nanostructures from linear ABC triblock terpolymers.

1.2.2.1. Spherical Multicompartment Micelles

Ringsdorf was among the first who proposed multicompartment micelles (MCMs) based on block copolymers.^{178,179} Dispersing an ABC triblock terpolymer in a selective solvent for only one of the outer blocks, leads to micelles where distinct core-compartments are formed through intrinsic phase separation of the two immiscible core-forming blocks. One of the first examples of MCMs was demonstrated by Laschewsky *et al.* who analyzed MCMs in aqueous solution from a poly(4-methyl-4-(4-vinylbenzyl)morpholin-4-ium chloride)-*block*-polystyrene-*block*-poly(pentafluorophenyl 4-vinylbenzyl ether) (PVBM-PS-PVBFP) triblock terpolymer (Figure 1.9a).¹⁸⁰ They suggested micelles with a PS core and patches of the fluorinated block, which was later confirmed by cryo-transmission electron tomography (cryo-ET).¹⁸¹ Onset of hamburger-like micelles was found by Liu *et al.* for poly(*tert*-butyl acrylate)-*block*-poly(2-cinnamoyloxyethyl methacrylate)-*block*-poly(succinylated glyceryl monomethacrylate) (PtBA-PCEMA-PSGMA) as shown in Figure 1.9b.¹⁸² A mixture of THF and 1-propanol in combination with a diamine was employed to directly disperse the triblock terpolymer with subsequent annealing for two days. MCMs occur as the PCEMA block is insoluble in the solvent mixture while the

PSGMA block becomes solvophobic due to binding of the diamine to the carboxylic acid moieties of the block. *Pt*BA is soluble and acts as the stabilizing corona. If only a minor fraction of the PSGMA is coordinated with the diamine, hamburger-like MCMs occur, whereas longer chains arise if the degree of complexation increases.

Direct dispersion of a polybutadiene-*block*-poly(2-vinyl pyridine)-*block*-poly(*tert*-butyl methacrylate) (PB-P2VP-*Pt*BMA) triblock terpolymer in acetone produces MCMs with a PB core decorated with P2VP patches stabilized by *Pt*BMA.¹⁸³ Quaternization of the P2VP block and deprotection of *Pt*BMA block to poly(methacrylic acid) (PMAA) gives PB-P2VPq-PMAA. If this triblock terpolymer is introduced into aqueous solution, MCMs form with a PB core carrying patches of an interpolyelectrolyte complex (IPEC) that forms between the positively charged P2VPq and the negatively charged PMAA, stabilized by a corona of excess PMAA.¹⁸⁴ This polyanionic corona is accessible for further complexation with polycationic homopolymers and diblock copolymers to form an additional IPEC layer continuously surrounding the micellar core and the first IPEC.^{185,186} Comparable structures were found for polybutadiene-*block*-poly(sodium methacrylate)-*block*-poly{2-[(methacryloyloxy)-ethyl]trimethylammonium methylsulfate} (PB-PMANa-PDMAEMAq) triblock terpolymers in aqueous solution. This terpolymer forms positively charged MCMs with can further be complexed with polyanionic homopolymers or polyanionic/neutral diblock copolymers.^{187,188}

Gröschel *et al.* were the first to prepare MCMs with a defined number of patches in high purity (Figure 1.9d).¹⁸⁹ A series of polystyrene-*block*-polybutadiene-*block*-poly(methyl methacrylate) (PS-PB-PMMA, SBM) allowed systematic screening of the factors influencing the patch-number and size. The self-assembly pathway is thereby crucial to gain highly monodisperse MCMs. Compared to the widely used method of direct dispersion of triblock terpolymers in the final solvent, Gröschel *et al.* employed a two-step procedure to consecutively collapse the solvophobic blocks. First the SBM triblock terpolymer is dispersed in *N,N*-dimethylacetamide (DMAc) to create micelles with a PB core and a mixed or patchy PS/PMMA corona. Subsequent dialysis against acetone/isopropanol mixtures induces the collapse of the PS block that phase separates from the PMMA corona chains. The intrinsically formed Janus particles *i.e.* a particle with two hemispheres,¹⁹⁰ are not stable and aggregate over the PS patch to form the final MCM. The amount of patches in the final MCMs is thereby equivalent to the number of aggregated Janus micelles needed to form a MCMs sufficiently stabilized by the solvophilic PMMA corona. The solvent mixture acetone/isopropanol is chosen, as acetone is a non-solvent for PB, a near θ -solvent for PS and a good solvent for PMMA while isopropanol is a near θ -solvent for PMMA and a non-solvent for both PB and PS blocks. The PB remains insoluble during all steps of self-assembly, yet its low T_g allows sufficient chain rearrangement. Acetone as co-solvent in the solvent mixture is furthermore assumed to plasticise the glassy PS block preventing kinetically trapped morphologies. It was demonstrated, that the volume ratio of PS/PB determines the amount of patches per MCM. If $V_S/V_B \approx 1.46$, hamburger-like MCMs occur, while clover and football micelles arise when $V_S/V_B \approx 1.78$ and 4.20 respectively (see Figure 1.9d). This behaviour is ascribed to the increasing hydrophobic PS patch, which

requires more transient Janus micelles to cluster in order to gain a stable MCM homogeneously surrounded by the corona chains.

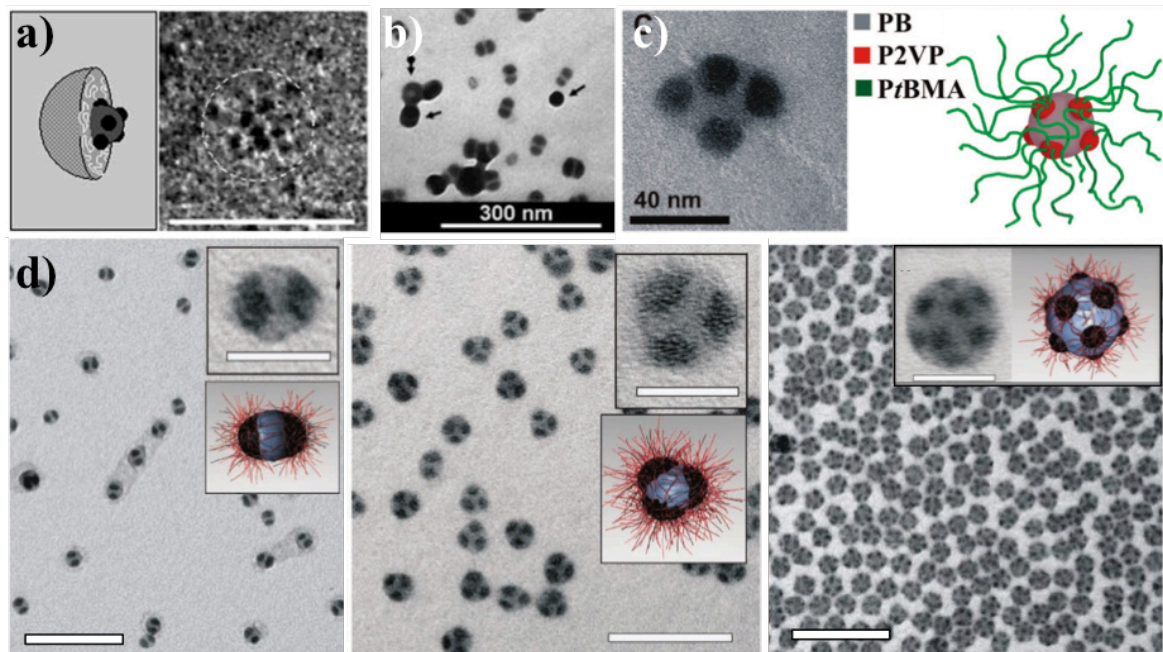


Figure 1.9: Spherical Multicompartmental Micelles (MCMs). **a)** Schematic and TEM image of a spherical MCM of a ABC triblock terpolymer carrying a fluorocarbon block in aqueous solution. Adapted from [180]. Reprinted with permission from Wiley-VCH Verlag GmbH & Co. KGaA. **b)** Hamburger-like MCMs from PtBA-PCEMA-PSGMA in THF/(-)-sparteine/1-propanol. Adapted from [182]. Reprinted with permission from The Royal Society of Chemistry. **c)** Formation of MCMs from PB-P2VP-PtBMA through direct dispersion in acetone. Adapted from [183]. Reprinted with permission from American Chemical Society. **d)** A two-step dialysis procedure leads to MCMs from PS-PB-PMMA with controlled number of patches (black, PB) depending on the block volume ratio of the hydrophobic blocks. From left to right: ‘hamburger’, ‘clover’ and ‘football’ micelles. The scale bars are 200 nm in the overview images and 50 nm in the insets. Adapted from [189]. Reprinted with permission from Nature Publishing Group.

The final MCMs contain a defined number of PB patches, accessible for cross-linking to permanently fix the structure that is otherwise only held together by non-covalent supramolecular forces. After dissolution of the MCMs with crosslinked PB patches in THF, single distributed Janus nanoparticles are obtained.¹⁹¹ This self-templating process allows the fabrication of Janus micelles with adjustable core sizes and precisely tuneable Janus balance, only depending on the molecular weight and block volume fractions of the involved triblock terpolymer. This solution-based production offers an alternative route to the commonly used method of cross-linking bulk morphologies.⁹⁹ Cross-linking a PS-PB-PMMA bulk morphology for instance, requires a sphere morphology of the PB phase; consequently, the PB block should not exceed a volume fractions of $\phi_B \approx 0.10$. If the blocks are in the weak segregation limit, an entire phase-separation may not occur and also an increase in the asymmetry of the end blocks may alter the bulk-morphology. All factors can be excluded with the solution-based approach. The permanently fixed Janus particles can be dried, stored and easily reused for various applications as they show enhanced inter-

facial activity.^{192,193} They have been successfully used as interfacial stabilizers in emulsion polymerization,¹⁹⁴ as dispersants for carbon nanotubes¹⁹⁵ and compatibilizers for polymer blends.¹⁹⁶

1.2.2.2. Cylindrical Multicompartment Micelles

Up to now, only few groups have reported the synthesis of cylindrical MCMs from linear ABC triblock terpolymers. The work of Wooley *et al.* comprises the self-assembly of poly(acrylic acid)-*block*-poly(methyl acrylate)-*block*-polystyrene (PAA-PMA-PS) in THF/water mixtures in combination with organic diamines. After complexation of the PAA chains with a diamine in THF, addition of water induces aggregation of the two hydrophobic blocks PS and PMA and spherical micelles form. After a specific amount of THF was added to the THF/water mixture the formation of a partially ordered lamellar phase of the hydrophobic blocks occurs, driving the overall micellar shape towards a disk-like structure. The attractive electrostatic interaction of the PAA-diamine coronas results in a one-dimensional growth to form several hundred nanometre long undulated cylindrical micelles (Figure 1.10a).

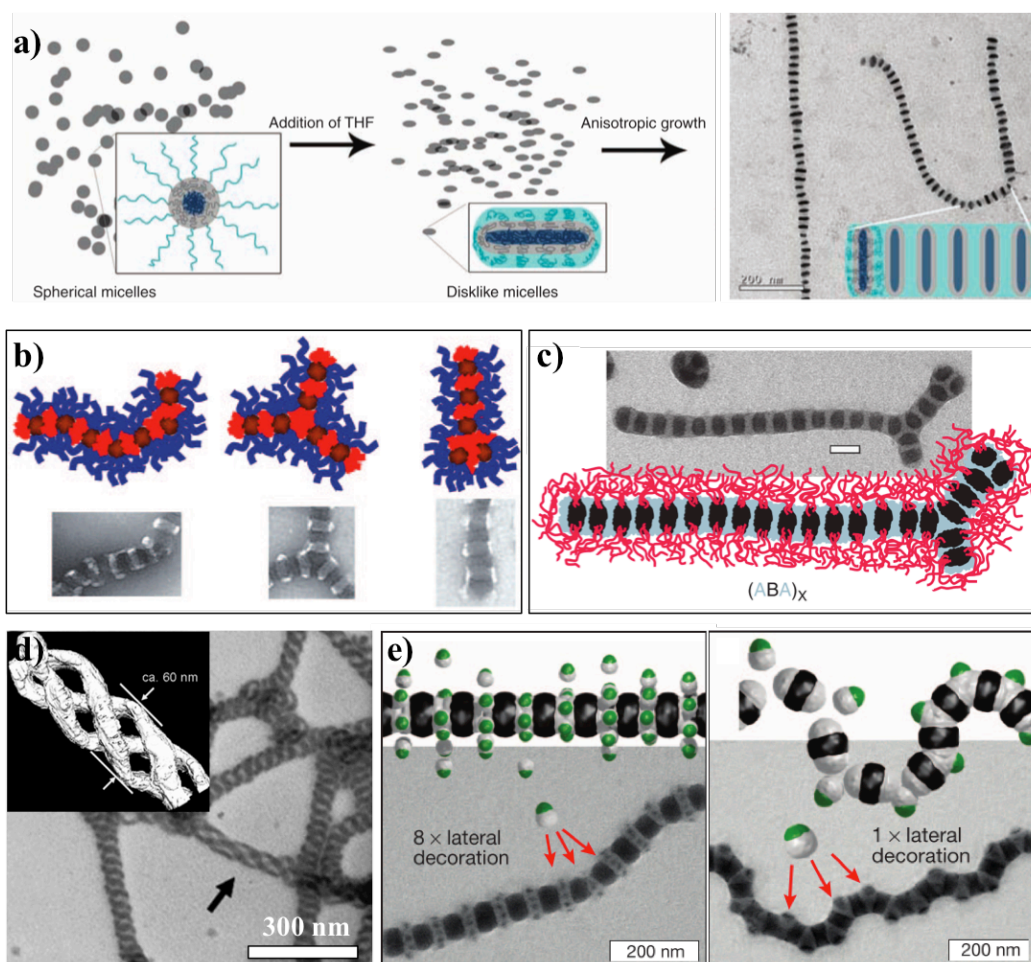


Figure 1.10: Cylindrical Multicompartment Micelles. **a)** Self-assembly of PAA-PMA-PS triblock terpolymer from spherical into undulated cylindrical micelles through stacking of disc-like intermediate micelles in THF/water mixture in the presence of an organic diamine. Adapted from [197]. Reprinted with permission from the American Association for the Advancement of Sciences. **b)** Undulated cylinders in ethanol from the self-assembly of a *PtBS*-PB-*PtBMA* triblock terpolymer after modification of the PB with a perfluoroalkyl-moiety. Adapted from [198]. Reprinted with permission from Wiley-VCH Verlag GmbH & Co. KGaA. **c)** Undulated cylinders from a PS-PB-PMMA in acetone/isopropanol mixtures. The scale bar corresponds to 100 nm. Adapted from [189]. Reprinted with permission from Nature Publishing Group. **d)** More complex double and triple helices are formed from PDMA-PCEMA-*PtBA* sprayed from DCM/methanol after 90 days of ageing. Adapted from [199]. Reprinted with permission from Wiley-VCH Verlag GmbH & Co. KGaA. **e)** Complex segmented cylinders decorated with spherical patches are achieved from the co-assembly of different types of patchy particles. Adapted from [201]. Reprinted with permission from Nature Publishing Group.

Fang *et al.* used a poly(4-*tert*-butoxystyrene)-*block*-polybutadiene-*block*-poly(*tert*-butyl methacrylate) (*PtBS*-PB-*PtBMA*) and modified the double bonds of the PB middle block with 1-mercapto-1H,1H,2H,2H-perfluorooctane via thiol-ene addition.¹⁹⁸ The perfluorinated middle block is insoluble in dioxane and micelles with a patchy corona of *PtBS* and *PtBMA* form after annealing for 48h. Dialysis from dioxane to ethanol, which is a selective solvent for *PtBMA*, induces the collapse of the *PtBS* block and undulated cylindrical micelles with branchpoints and endcaps form as a direct result of the patch distribution within the segregated corona of the micelles in dioxane (Figure 1.10b). If two corona patches of *PtBS* were present in the micellar state upon collapse a linear growth is promoted, whereas a Janus-like corona phase separation (one *PtBS* patch) forms terminal endcaps.

Gröschel *et al.* thoroughly investigated the system SBM and found that in case of a volume ratio of PS to PB of $V_S/V_B > 1$ spherical MCMs with a distinct number of patches occur as already reported in section 1.2.2.1, however, a volume ratio of $V_S/V_B < 1$ results in a linear growth to form segmented worm-like MCMs (Figure 1.10c).¹⁸⁹ This is explained by two different transient building blocks that form upon dialysis from a non-solvent for only the PB block to acetone/isopropanol, which induces the collapse of the PS block. While for $V_S/V_B > 1$ the transient building blocks are Janus micelles that subsequently aggregate *via* the PS patch into spherical MCMs, the situation changes for $V_S/V_B < 1$. In that case SBS “inverse hamburger” particles form that carry two S patches on exactly opposite sides of the PB core, while the PB core is surrounded by the emanating PMMA corona. Hence, the aggregation over the PS patches results in a linear growth, if the solubilizing corona is not long enough to fully protect the solvophobic PS patches. The reversibility of this process was demonstrated by using SBS micelles with a long corona that first fully covers the building blocks. After addition of non-solvent for the corona (*i.e.* isopropanol), contraction of the corona leads to a dimerization and subsequent colloidal polymerization of the SBS segments because of the ineffective shielding of SBS subunits by the PMMA corona.

Besides the undulated cylindrical micelles, Liu *et al.* found double and triple helices formed from poly(butyl methacrylate)-*block*-poly(2-cinnamoyloxyethyl methacrylate)-*block*-poly(*tert*-butyl acrylate) (PBA-PCEMA-*PtBA*) in a dichloromethane/methanol solvent mixture (18:82 v:v) (Figure 1.10d).^{199,200} The hydrophobic PCEMA forms cylindrical

micelles in solution with PtBA and PBA as stabilizing corona. However, at a high methanol content the PBA chains become marginally soluble causing the helices to intertwine in order to decrease the total interfacial area of the PBA with the solvent. Although demixing of the corona chains may occur a compartmentalized character in the final structure is absent and a core-shell-corona structure is suggested. The formation of single-stranded helices was further reported by Wooley and Pochan *et al.* using PAA-PMA-PS in combination with multiamines.²⁰² The polymer is first dissolved in THF and mixed with the multiamine in a ratio of 1:10 or 1:15 of acid:amino groups. Then water is added dropwise to induce the formation of cylindrical core-shell-corona micelles through precipitation of the hydrophobic PS and PMA blocks while the PAA/amine complexes form the corona. At high water contents the samples were aged for 20 days prior to cryo-TEM analysis. The formed helices were explained through electrostatic and hydrogen-bonding interactions occurring between the PAA corona chains. Complexation of PAA with multiamines contracts the PAA chains and produces a uniaxial compression force along the cylinder inducing buckling into a helix while collapse of the helices is prevented due to electrostatic repulsion from excess surface charges along the cylinders. Although these works are intriguing examples to create cylindrical nanostructures from linear ABC triblock terpolymer, the formed helices are based on core-shell-corona cylinders and do not exhibit observable compartmentalized character.

Recently, Gröschel *et al.* reported on the formation of complex one-dimensional supracolloidal assemblies.²⁰¹ Using a combination of the monofunctional Janus-like AB and bifunctional “inverse hamburger” ABA building blocks, segmented cylindrical micelles form where every second compartment is decorated with a specific number of AB particles. The co-assembly of triblock terpolymers bridges several levels of hierarchy and results in peculiar nanostructures shown in Figure 1.10e. The ABA particles are thereby achieved from a PS-PB-PMMA triblock terpolymer where the PB block was modified with dodecane-thiol giving PS-PD-PMMA. The high volume of the PD block drives the V_S/V_D ratio below unity and thus colloidal ABA building blocks with two “sticky” PS patches occur that can polymerize into multicompartiment cylinders. PS-PB-PMMA triblock terpolymers with $V_S/V_B > 1$ form the AB building blocks. Both building blocks were mixed in DMAc and dialyzed into the final solvent mixture. Upon dialysis, the SDS units polymerize into a supracolloidal chain. At the same time, the AB particles start to aggregate, but instead of forming spherical clusters, they attach to the PS surface of the segmented cylindrical micelles thereby decreasing the unfavourable PS/solvent interface. The overall size of the SB building blocks determines the amount of particles fitting in one PS-compartment of the cylinder micelles. If the aggregating S patch is small, approximately 8 AB particles decorate one S compartment, but when the S patch increases in size the number is reduced to only one particle inducing a kink in the cylinder (Figure 1.10e). A further increase of AB size results in the exclusive attachment to the ends of the multicompartiment cylinders due to steric reasons. These particles act as chain stoppers to adjust the overall length of the cylinders by the amount of added AB particles compared to SBS building blocks.

1.2.2.3 Compartmentalized Sheets and Vesicles

While miktoarm star terpolymers form multicompartments more easily due to their frustrated architecture^{176,177}, there are only a handful of examples for the formation of compartmentalized vesicles. The precursor of vesicles *i.e.* bilayer sheets are even more challenging to capture as they usually roll-up to vesicles.

Russell *et al.* used anodized aluminium oxide (AAO) membranes as a template to control the formation of polymersomes from polyisoprene-*block*-polystyrene-*block*-poly(2-vinylpyridine) (PI-PS-P2VP).²⁰³ The approach and resulting compartmentalized vesicles are schematically shown in Figure 1.11a. First, the AAO membrane is filled with the polymer solution (in toluene) and after solvent evaporation the AAO membranes with the polymer film were immersed in ethylene glycol and heated to 150 °C for 5 min to achieve vesicle formation. After quenching to room temperature and dissolution of the AAO membrane the vesicles were recovered by filtration and subsequent drying. The phase-separation of PI and PS within the vesicle membrane gives them a mesh-like morphology that can be visualized in TEM (Figure 1.11a).

A template-free method towards compartmentalized polymersomes was shown by Eisenberg *et al.* in aqueous solution with poly(ethylene oxide)-*block*-polystyrene-*block*-poly(2-diethylaminoethyl methacrylate) (PEO-PS-PDEA).²⁰⁴ At high pH > 10, the vesicle membrane consists of a core-shell-corona structure with PDEA in the core covered by a thin PS layer and stabilized by the water-soluble PEO corona. A decrease in pH successively protonates the PDEA block that swells at first and finally disrupts the closed PS layer. Thereby the polymersomes adopt a reversibly compartmentalized character, and the permeability of the membrane at low pH values was further confirmed with the aid of a fluorescent, water-soluble dye encapsulated at high pH and released at low pH.

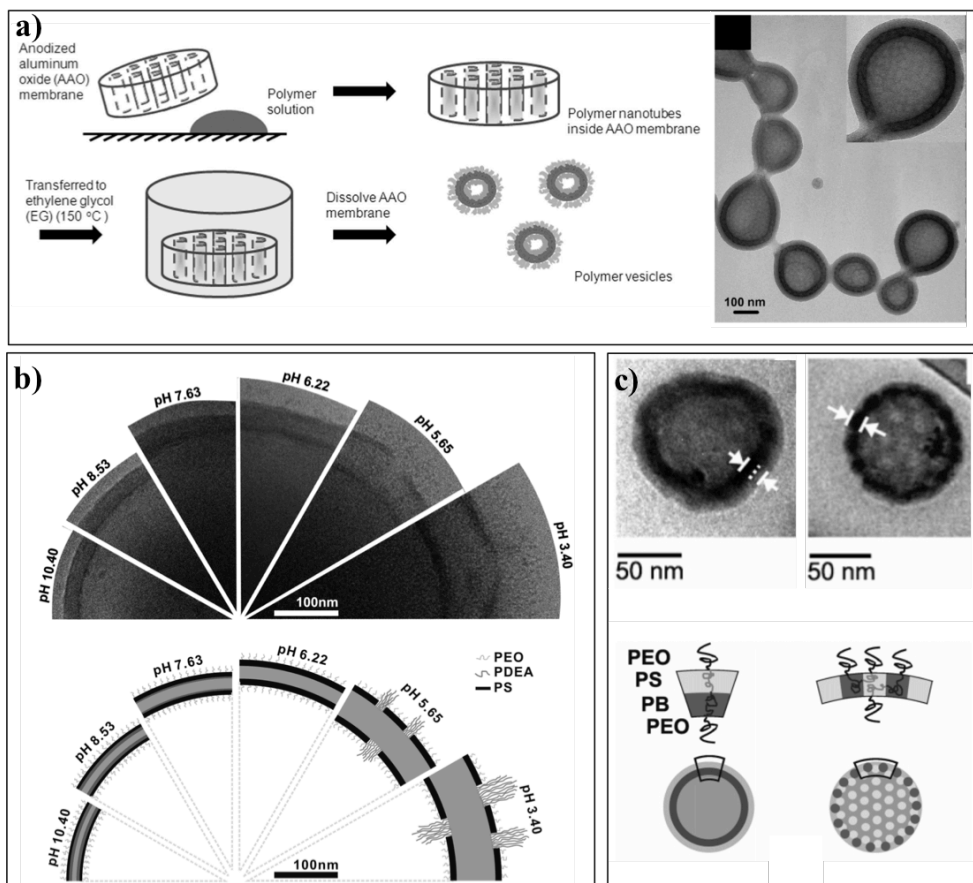


Figure 1.11: Multicompartment Polymersomes. **a)** AAO-templated PI-PS-P2VP assembly into vesicles with a mesh-like membrane. Adapted from [203]. **b)** “Breathing” vesicles from PEO-PS-PDEA. At high pH values, the PDEA block is insoluble, yet becomes soluble with decreasing pH. The fractured PS membrane gives the vesicles a compartmentalized appearance. Adapted from [204]. **c)** An OSBO tetrablock terpolymer forms vesicles with either an inner shell of PB and a outer shell of PS or a perforated membrane if the PEO block exceeds 50 wt.-%. Adapted from [205]. Reprinted with permission from American Chemical Society.

Bates *et al.* showed nanostructured vesicles, by use of a poly(ethylene oxide)-*block*-polystyrene-*block*-polybutadiene-*block*-poly(ethylene oxide) (OSBO) tetrablock terpolymer.²⁰⁵ After casting a bulk film from methylene chloride, water was added followed by stirring at room temperature and several weeks annealing at 40-50 °C. It was found that if the overall weight fraction of the PEO is below 50 wt.-%, vesicles occur with an inner layer of PB and an outer layer of PS, stabilized by the two PEO blocks. This was explained by the minimization of interfacial area of PB with the aqueous phase, because PB and water have a higher interfacial tension than PS and water. However, if the fraction of PEO exceeds 50 wt.-% they observed nanostructured polymersomes with a membrane where the arrangement of the PS and PB blocks is reminiscent of the perforated-lamella structure found for block copolymers in bulk.^{61,206} The corresponding cryo-TEM images as well as a schematic drawing of the block arrangement are shown in Figure 1.11c.

1.3. Aim of This Thesis

The aim of this thesis is to explore and characterize novel compartmentalized nanostructures in solution through self-assembly of linear ABC triblock terpolymers. Gaining knowledge about the correlation between block compositions of the triblock terpolymer and the resulting self-assembly behavior is the basis to controllably produce superstructures with so far unprecedented complexity. This work is divided into three main parts, with the aim to expand the library of compartmentalized nanoparticles of ABC triblock terpolymers and to gain basic knowledge about underlying formation mechanisms, which is important with respect to possible future applications.

One part comprises the use of multicompartment micelles with a charged corona that is accessible for complexation reactions with oppositely charged polymers *via* electrostatic, non-covalent interactions. The formed interpolyelectrolyte complex (IPEC) is hydrophobic and phase separates from the surrounding solvent. As the corona chains are covalently bound to the micellar core, the confined space in which the IPEC formation takes place is assumed to influence the resulting patch geometry of the hydrophobic IPEC on top of the micellar core.

The second part of this work is based on the hierarchical self-assembly of linear ABC triblock terpolymers with the aim to achieve compartmentalized nanostructures in solution beyond known spherical multicompartment micelles (MCMs). Inspired by concepts from the solution and bulk theory of diblock copolymers, it is hypothesized that equipping a linear ABC triblock terpolymer with two solvophobic blocks and one solvophilic block according to parameters known from diblock copolymers should give rise to a myriad of so far unknown compartmentalized nanostructures in solution. Adjusting the corona length should thereby influence the particle geometry, while the two solvophobic blocks should phase-separate within this confined space according to diblock copolymers in bulk.

Spherical MCMs are applied in the third part, to form the simplest type of corona-compartmentalized nanoparticles, *i.e.* Janus micelles, through selective cross-linking of the compartments. The scaling from the lab- towards large-scale preparation is thereby an important step to make Janus micelles attractive for various applications. Their particulate character makes them, *e.g.*, ideal candidates for the compatibilization of immiscible polymer blends on an industrial relevant scale when achieved in sufficient amounts.

1.4 References

1. Whitesides, G. M.; Grzybowski, B. Self-Assembly at All Scales. *Science* **2002**, *295*, 2418–2421.
2. Bishop, K. J. M.; Wilmer, C. E.; Soh, S.; Grzybowski, B. A. Nanoscale Forces and Their Uses in Self-Assembly. *Small* **2009**, *5*, 1600–1630.
3. Brinker, C. J.; Lu, Y.; Sellinger, A.; Fan, H. Evaporation-Induced Self-Assembly: Nanostructures Made Easy. *Adv. Mater.* **1999**, *11*, 579–585.
4. Meyers, M. A.; Chen, P.-Y.; Lin, A. Y.-M.; Seki, Y. Biological Materials: Structure and Mechanical Properties. *Prog. Mater. Sci.* **2008**, *53*, 1–206.
5. Fratzl, P.; Weinkamer, R. Nature's Hierarchical Materials. *Prog. Mater. Sci.* **2007**, *52*, 1263–1334.
6. Ferrari, M. Cancer Nanotechnology: Opportunities and Challenges. *Nat. Rev. Cancer* **2005**, *5*, 161–171.
7. Ferrari, M. Nanogeometry: Beyond Drug Delivery. *Nat. Nanotechnol.* **2008**, *3*, 131–132.
8. Kneipp, K.; Kneipp, H.; Itzkan, I.; Dasari, R. R.; Feld, M. S. Ultrasensitive Chemical Analysis by Raman Spectroscopy. *Chem. Rev.* **1999**, *99*, 2957–2976.
9. Nam, J.-M.; Thaxton, C. S.; Mirkin, C. A. Nanoparticle-Based Bio-Bar Codes for the Ultrasensitive Detection of Proteins. *Science* **2003**, *301*, 1884–1886.
10. Shevchenko, E. V; Talapin, D. V; Kotov, N. A.; O'Brien, S.; Murray, C. B. Structural Diversity in Binary Nanoparticle Superlattices. *Nature* **2006**, *439*, 55–59.
11. Graham-Rowe, D. Tunable Structural Colour. *Nat. Photonics* **2009**, *3*, 551–553.
12. Smith, A. M.; Mohs, A. M.; Nie, S. Tuning the Optical and Electronic Properties of Colloidal Nanocrystals by Lattice Strain. *Nat. Nanotechnol.* **2009**, *4*, 56–63.
13. Wei, B.; Dai, M.; Yin, P. Complex Shapes Self-Assembled from Single-Stranded DNA Tiles. *Nature* **2012**, *485*, 623–626.
14. Han, D.; Pal, S.; Nangreave, J.; Deng, Z.; Liu, Y.; Yan, H. DNA Origami with Complex Curvatures in Three-Dimensional Space. *Science* **2011**, *332*, 342–346.
15. Habibi, Y.; Lucia, L. A.; Rojas, O. J. Cellulose Nanocrystals: Chemistry, Self-Assembly, and Applications. *Chem. Rev.* **2010**, *110*, 3479–3500.
16. Knowles, T. P. J.; Oppenheim, T. W.; Buell, A. K.; Chirgadze, D. Y.; Welland, M. E. Nanostructured Films from Hierarchical Self-Assembly of Amyloidogenic Proteins. *Nat. Nanotechnol.* **2010**, *5*, 204–207.
17. Kostianen, M. A.; Kasyutich, O.; Cornelissen, J. J. L. M.; Nolte, R. J. M. Self-Assembly and Optically Triggered Disassembly of Hierarchical Dendron–virus Complexes. *Nat. Chem.* **2010**, *2*, 394–399.
18. Pusey, P. N.; von Meegen, W. Phase Behaviour of Concentrated Suspensions of Nearly Hard Colloidal Spheres. *Nature* **1986**, *320*, 340–342.
19. Cheng, Z.; Russel, W. B.; Chaikin, P. M. Controlled Growth of Hard-Sphere Colloidal Crystals. *Nature* **1999**, *401*, 893–895.

20. Redl, F. X.; Cho, K.-S.; Murray, C. B.; O'Brien, S. Three-Dimensional Binary Superlattices of Magnetic Nanocrystals and Semiconductor Quantum Dots. *Nature* **2003**, *423*, 968–971.
21. Macfarlane, R. J.; Jones, M. R.; Lee, B.; Auyeung, E.; Mirkin, C. A. Topotactic Interconversion of Nanoparticle Superlattices. *Science* **2013**, *341*, 1222–1225.
22. Leunissen, M. E.; Christova, C. G.; Hynninen, A.-P.; Royall, C. P.; Campbell, A. I.; Imhof, A.; Dijkstra, M.; van Roij, R.; van Blaaderen, A. Ionic Colloidal Crystals of Oppositely Charged Particles. *Nature* **2005**, *437*, 235–240.
23. Li, F.; Josephson, D. P.; Stein, A. Colloidal Assembly: The Road from Particles to Colloidal Molecules and Crystals. *Angew. Chemie Int. Ed.* **2011**, *50*, 360–388.
24. Van Blaaderen, A. Colloids Get Complex. *Nature* **2006**, *439*, 545–546.
25. Glotzer, S. C.; Solomon, M. J. Anisotropy of Building Blocks and Their Assembly into Complex Structures. *Nat. Mater.* **2007**, *6*, 557–562.
26. Sacanna, S.; Pine, D. J.; Yi, G.-R. Engineering Shape: The Novel Geometries of Colloidal Self-Assembly. *Soft Matter* **2013**, *9*, 8096.
27. Sacanna, S.; Korpics, M.; Rodriguez, K.; Colón-Meléndez, L.; Kim, S.-H.; Pine, D. J.; Yi, G.-R. Shaping Colloids for Self-Assembly. *Nat. Commun.* **2013**, *4*, 1688.
28. Damasceno, P. F.; Engel, M.; Glotzer, S. C. Predictive Self-Assembly of Polyhedra into Complex Structures. *Science* **2012**, *337*, 453–457.
29. Rossi, L.; Sacanna, S.; Irvine, W. T. M.; Chaikin, P. M.; Pine, D. J.; Philipse, A. P. Cubic Crystals from Cubic Colloids. *Soft Matter* **2011**, *7*, 4139–4142.
30. Liu, K.; Nie, Z.; Zhao, N.; Li, W.; Rubinstein, M.; Kumacheva, E. Step-Growth Polymerization of Inorganic Nanoparticles. *Science* **2010**, *329*, 197–200.
31. Klinkova, A.; Thérien-Aubin, H.; Choueiri, R. M.; Rubinstein, M.; Kumacheva, E. Colloidal Analogs of Molecular Chain Stoppers. *PNAS* **2013**, *110*, 18775–18779.
32. Wang, Y.; Hollingsworth, A. D.; Yang, S. K.; Patel, S.; Pine, D. J.; Weck, M. Patchy Particle Self-Assembly via Metal Coordination. *J. Am. Chem. Soc.* **2013**, *135*, 14064–14067.
33. Chaudhary, K.; Chen, Q.; Juárez, J. J.; Granick, S.; Lewis, J. A. Janus Colloidal Matchsticks. *J. Am. Chem. Soc.* **2012**, *134*, 12901–12903.
34. Miszta, K.; de Graaf, J.; Bertoni, G.; Dorfs, D.; Brescia, R.; Marras, S.; Ceseracciu, L.; Cingolani, R.; van Roij, R.; Dijkstra, M.; *et al.* Hierarchical Self-Assembly of Suspended Branched Colloidal Nanocrystals into Superlattice Structures. *Nat. Mater.* **2011**, *10*, 872–876.
35. Kraft, D. J.; Groenewold, J.; Kegel, W. K. Colloidal Molecules with Well-Controlled Bond Angles. *Soft Matter* **2009**, *5*, 3823–3826.
36. Kraft, D. J.; Vlug, W. S.; van Kats, C. M.; van Blaaderen, A.; Imhof, A.; Kegel, W. K. Self-Assembly of Colloids with Liquid Protrusions. *J. Am. Chem. Soc.* **2009**, *131*, 1182–1186.
37. Manoharan, V. N.; Elsesser, M. T.; Pine, D. J. Dense Packing and Symmetry in Small Clusters of Microspheres. *Science* **2003**, *301*, 483–487.

38. Wang, Y.; Wang, Y.; Breed, D. R.; Manoharan, V. N.; Feng, L.; Hollingsworth, A. D.; Weck, M.; Pine, D. J. Colloids with Valence and Specific Directional Bonding. *Nature* **2012**, *490*, 51–55.
39. Kumar, A.; Whitesides, G. M. Features of Gold Having Micrometer to Centimeter Dimensions Can Be Formed through a Combination of Stamping with an Elastomeric Stamp and an Alkanethiol “Ink” Followed by Chemical Etching. *Appl. Phys. Lett.* **1993**, *63*, 2002–2004.
40. Cui, J.-Q.; Kretzschmar, I. Surface-Anisotropic Polystyrene Spheres by Electroless Deposition. *Langmuir* **2006**, *22*, 8281–8284.
41. Hong, L.; Jiang, S.; Granick, S. Simple Method to Produce Janus Colloidal Particles in Large Quantity. *Langmuir* **2006**, *22*, 9495–9499.
42. Pawar, A. B.; Kretzschmar, I. Multifunctional Patchy Particles by Glancing Angle Deposition. *Langmuir* **2009**, *25*, 9057–9063.
43. Zhang, G.; Wang, D.; Möhwald, H. Patterning Microsphere Surfaces by Templating Colloidal Crystals. *Nano Lett.* **2005**, *5*, 143–146.
44. Yake, A. M.; Snyder, C. E.; Velegol, D. Site-Specific Functionalization on Individual Colloids: Size Control, Stability, and Multilayers. *Langmuir* **2007**, *23*, 9069–9075.
45. Feng, L.; Dreyfus, R.; Sha, R.; Seeman, N. C.; Chaikin, P. M. DNA Patchy Particles. *Adv. Mater.* **2013**, *25*, 2779–2783.
46. Chen, Q.; Whitmer, J. K.; Jiang, S.; Bae, S. C.; Luijten, E.; Granick, S. Supracolloidal Reaction Kinetics of Janus Spheres. *Science* **2011**, *331*, 199–202.
47. Chen, Q.; Bae, S. C.; Granick, S. Directed Self-Assembly of a Colloidal Kagome Lattice. *Nature* **2011**, *469*, 381–384.
48. Müller, A. H. E.; Matyjaszewski, K. Controlled and Living Polymerizations. **2009**, Weinheim Wiley – VCH Verlag.
49. Bates, F. S.; Hillmyer, M. A.; Lodge, T. P.; Bates, C. M.; Delaney, K. T.; Fredrickson, G. H. Multiblock Polymers: Panacea or Pandora’s Box? *Science* **2012**, *336*, 434–440.
50. Lodge, T. P.; Rasdal, A.; Li, Z.; Hillmyer, M. A. Simultaneous, Segregated Storage of Two Agents in a Multicompartment Micelle. *J. Am. Chem. Soc.* **2005**, *127*, 17608–17609.
51. Synatschke, C. V.; Nomoto, T.; Cabral, H.; Förtsch, M.; Toh, K.; Matsumoto, Y.; Miyazaki, K.; Hanisch, A.; Schacher, F. H.; Kishimura, A.; *et al.* Multicompartment Micelles with Adjustable Poly (Ethylene Glycol) Shell for Efficient in Vivo Photodynamic Therapy. *ACS Nano* **2014**, *8*, 1161–1172.
52. Bates, F. S.; Fredrickson, G. H. Block Copolymer Thermodynamics: Theory and Experiment. *Annu. Rev. Phys. Chem.* **1990**, *41*, 525–557.
53. Mai, Y.; Eisenberg, A. Self-Assembly of Block Copolymers. *Chem. Soc. Rev.* **2012**, *41*, 5969–5985.
54. Orilall, M. C.; Wiesner, U. Block Copolymer Based Composition and Morphology Control in Nanostructured Hybrid Materials for Energy Conversion and Storage: Solar Cells, Batteries, and Fuel Cells. *Chem. Soc. Rev.* **2011**, *40*, 520–535.

55. Bates, F. S.; Fredrickson, G. H. Block Copolymers—Designer Soft Materials. *Phys. Today* **1999**, *52*, 32–38.
56. Helfand, E. Proposed Experiment to Estimate the Mixing Free Energy of Polymers. *Macromolecules* **1978**, *11*, 682–685.
57. Leiblert, L. Theory of Microphase Separation in Block Copolymers. **1980**, *1617*, 1602–1617.
58. Matsen, M.; Schick, M. Stable and Unstable Phases of a Diblock Copolymer Melt. *Phys. Rev. Lett.* **1994**, *72*, 2660–2663.
59. Matsen, M. W.; Bates, F. S. Unifying Weak- and Strong-Segregation Block Copolymer Theories. *Macromolecules* **1996**, *29*, 1091–1098.
60. Bates, F.; Fredrickson, G. H. Block Copolymer Thermodynamics: Theory And Experiment. *Annu. Rev. Phys. Chem.* **1990**, *41*, 525–557.
61. Khandpur, A. K.; Förster, S.; Bates, F. S.; Hamley, I. W.; Ryan, A. J.; Bras, W.; Almdal, K.; Mortensen, K. Polyisoprene-Polystyrene Diblock Copolymer Phase Diagram near the Order-Disorder Transition. *Macromolecules* **1995**, 8796–8806.
62. Schulz, M. F.; Khandpur, A. K.; Bates, F. S.; Almdal, K.; Mortensen, K.; Hajduk, D. a.; Gruner, S. M. Phase Behavior of Polystyrene–Poly(2-Vinylpyridine) Diblock Copolymers. *Macromolecules* **1996**, *29*, 2857–2867.
63. Floudas, G.; Vazaiou, B.; Schipper, F.; Ulrich, R.; Wiesner, U.; Iatrou, H.; Hadjichristidis, N. Poly (ethylene Oxide-B-Isoprene) Diblock Copolymer Phase Diagram. *Macromolecules* **2001**, *34*, 2947–2957.
64. Hsueh, H.-Y.; Chen, H.-Y.; She, M.-S.; Chen, C.-K.; Ho, R.-M.; Gwo, S.; Hasegawa, H.; Thomas, E. L. Inorganic Gyroid with Exceptionally Low Refractive Index from Block Copolymer Templating. *Nano Lett.* **2010**, *10*, 4994–5000.
65. Hsueh, H.-Y.; Yao, C.-T.; Ho, R.-M. Well-Ordered Nanohybrids and Nanoporous Materials from Gyroid Block Copolymer Templates. *Chem. Soc. Rev.* **2015**.
66. Vukovic, I.; Brinke, G. Ten; Loos, K. Block Copolymer Template-Directed Synthesis of Well-Ordered Metallic Nanostructures. *Polymer* **2013**, *54*, 2591–2605.
67. Hashimoto, T.; Tanaka, H.; Hasegawa, H. Ordered Structure in Mixtures of a Block Copolymer and Homopolymers. 2. Effects of Molecular Weights of Homopolymers. *Macromolecules* **1990**, *23*, 4378–4386.
68. Abetz, V.; Goldacker, T. Formation of Superlattices via Blending of Block Copolymers. *Macromol. Rapid Commun.* **2000**, *21*, 16–34.
69. Warren, S. C.; Messina, L. C.; Slaughter, L. S.; Kamperman, M.; Zhou, Q.; Gruner, S. M.; DiSalvo, F. J.; Wiesner, U. Ordered Mesoporous Materials from Metal Nanoparticle-Block Copolymer Self-Assembly. *Science* **2008**, *320*, 1748–1752.
70. Ruokolainen, J.; Mäkinen, R.; Torkkeli, M.; Mäkelä, T.; Serimaa, R.; ten Brinke, G.; Ikkala, O. Switching Supramolecular Polymeric Materials with Multiple Length Scales. *Science* **1998**, *280*, 557–560.
71. Ruokolainen, J.; Brinke, G. Ten; Ikkala, O. Supramolecular Polymeric Materials with Hierarchical Structure-Within-Structure Morphologies. *Adv. Mater.* **1999**, *11*, 777–780.

72. Valkama, S.; Kosonen, H.; Ruokolainen, J.; Haatainen, T.; Torkkeli, M.; Serimaa, R.; ten Brinke, G.; Ikkala, O. Self-Assembled Polymeric Solid Films with Temperature-Induced Large and Reversible Photonic-Bandgap Switching. *Nat. Mater.* **2004**, *3*, 872–876.
73. Vukovic, I.; ten Brinke, G.; Loos, K. Hexagonally Perforated Layer Morphology in PS-B-P4VP(PDP) Supramolecules. *Macromolecules* **2012**, *45*, 9409–9418.
74. Kimishima, K.; Koga, T.; Hashimoto, T. Order-Order Phase Transition between Spherical and Cylindrical Microdomain Structures of Block Copolymer. I. Mechanism of the Transition. *Macromolecules* **2000**, *33*, 968–977.
75. Shi, L.-Y.; Hsieh, I.-F.; Zhou, Y.; Yu, X.; Tian, H.-J.; Pan, Y.; Fan, X.-H.; Shen, Z. Thermoreversible Order–Order Transition of a Diblock Copolymer Induced by the Unusual Coil–Rod Conformational Change of One Block. *Macromolecules* **2012**, *45*, 9719–9726.
76. Fredrickson, G. H. Steady Shear Alignment of Block Copolymers near the Isotropic–lamellar Transition. *J. Rheol.* **1994**, *38*, 1045–1067.
77. Gupta, V. K.; Krishnamoorti, R.; Chen, Z.-R.; Kornfield, J. A.; Smith, S. D.; Satkowski, M. M.; Grothaus, J. T. Dynamics of Shear Alignment in a Lamellar Diblock Copolymer : Interplay of Frequency , Strain Amplitude , and Temperature. *Macromolecules* **1996**, *29*, 875–884.
78. Morkved, T. L.; Lu, M.; Urbas, A. M.; Ehrichs, E. E.; Jaeger, H. M.; Mansky, P.; Russell, T. P. Local Control of Microdomain Orientation in Diblock Copolymer Thin Films with Electric Fields. *Science* **1996**, *273*, 931–933.
79. Schmidt, K.; Schoberth, H. G.; Ruppel, M.; Zettl, H.; Hänsel, H.; Weiss, T. M.; Urban, V.; Krausch, G.; Böker, A. Reversible Tuning of a Block-Copolymer Nanostructure via Electric Fields. *Nat. Mater.* **2008**, *7*, 142–145.
80. Böker, a.; Elbs, H.; Hänsel, H.; Knoll, a.; Ludwigs, S.; Zettl, H.; Urban, V.; Abetz, V.; Müller, a.; Krausch, G. Microscopic Mechanisms of Electric-Field-Induced Alignment of Block Copolymer Microdomains. *Phys. Rev. Lett.* **2002**, *89*, 135502.
81. Stadler, R.; Auschra, C.; Beckmann, J.; Krappe, U.; Voigt-Martin, I.; Leibler, L. Morphology and Thermodynamics of Symmetric Poly (A-Block-B-Block-C) Triblock Copolymers. *Macromolecules* **1995**, *28*, 3080–3091.
82. Zheng, W.; Wang, Z. Morphology of ABC Triblock Copolymers. *Macromolecules* **1995**, *28*, 7215–7223.
83. Ruzette, A.-V.; Leibler, L. Block Copolymers in Tomorrow ' S Plastics. *Nat. Mater.* **2005**, *4*, 19–31.
84. Hückstädt, H.; Göpfert, A.; Abetz, V. Influence of the Block Sequence on the Morphological Behavior of ABC Triblock Copolymers. *Polymer* **2000**, *41*, 9089–9094.
85. Hirao, A.; Matsuo, Y.; Oie, T.; Goseki, R.; Ishizone, T.; Sugiyama, K.; Gröschel, A. H.; Müller, A. H. E. Facile Synthesis of Triblock Co- and Terpolymers of Styrene, 2-Vinylpyridine, and Methyl Methacrylate by a New Methodology Combining Living Anionic Diblock Copolymers with a Specially Designed Linking Reaction. *Macromolecules* **2011**, *44*, 6345–6355.

86. Hückstädt, H.; Abetz, V.; Stadler, R. Synthesis of a Polystyrene-Arm-Polybutadiene-Arm-Poly(methyl Methacrylate) Triarm Star Copolymer. *Macromol. Rapid Commun.* **1996**, *17*, 599–606.
87. Hückstädt, H.; Göpfert, A.; Abetz, V. Synthesis and Morphology of ABC Heteroarm Star Terpolymers of Polystyrene, Polybutadiene and poly(2-Vinylpyridine). *Macromol. Chem. Phys.* **2000**, *201*, 296–307.
88. Hadjichristidis, N.; Iatrou, H.; Pitsikalis, M.; Pispas, S.; Avgeropoulos, A. Linear and Non-Linear Triblock Terpolymers. Synthesis, Self-Assembly in Selective Solvents and in Bulk. *Prog. Polym. Sci.* **2005**, *30*, 725–782.
89. Breiner, U.; Krappe, U.; Jakob, T.; Abetz, V.; Stadler, R. Spheres on Spheres - a Novel Spherical Multiphase Morphology in Polystyrene-Block-Polybutadiene-Block-Poly(methyl Methacrylate) Triblock Copolymers. *Polym. Bull.* **1998**, *40*, 219–226.
90. Krappe, U.; Stadler, R.; Voigt-Martin, I. Chiral Assembly in Amorphous ABC Triblock Copolymers. Formation of a Helical Morphology in Polystyrene-Block-Polybutadiene-Block-Poly(methyl Methacrylate) Block Copolymers. *Macromolecules* **1995**, *28*, 4558–4561.
91. Breiner, U.; Krappe, U.; Abetz, V.; Stadler, R. Cylindrical Morphologies in Asymmetric ABC Triblock Copolymers. *Macromol. Chem. Phys.* **1997**, *198*, 1051–1083.
92. Breiner, U.; Krappe, U.; Stadler, R. Evolution of the “knitting Pattern” Morphology in ABC Triblock Copolymers. *Macromol. Rapid Commun.* **1996**, *17*, 567–575.
93. Abetz, V.; Goldacker, T. Formation of Superlattices via Blending of Block Copolymers. *Macromol. Rapid Commun.* **2000**, *21*, 16–34.
94. Epps, T. H.; Cochran, E. W.; Bailey, T. S.; Waletzko, R. S.; Hardy, C. M.; Bates, F. S. Ordered Network Phases in Linear Poly (isoprene-B-Styrene-B-Ethylene Oxide) Triblock Copolymers. *Macromolecules* **2004**, *37*, 8325–8341.
95. Chatterjee, J.; Jain, S.; Bates, F. S. Comprehensive Phase Behavior of Poly (isoprene-B-Styrene-B-Ethylene Oxide) Triblock Copolymers. *Macromolecules* **2007**, *40*, 2882–2896.
96. Qin, J.; Bates, F. S.; Morse, D. C. Phase Behavior of Nonfrustrated ABC Triblock Copolymers: Weak and Intermediate Segregation. *Macromolecules* **2010**, *43*, 5128–5136.
97. Ludwigs, S.; Böker, A.; Abetz, V.; Müller, A. H. E.; Krausch, G. Phase Behavior of Linear Polystyrene-Block-poly(2-Vinylpyridine)-Block-Poly(tert-Butyl Methacrylate) Triblock Terpolymers. *Polymer* **2003**, *44*, 6815–6823.
98. Schacher, F.; Yuan, J.; Schoberth, H. G.; Müller, A. H. E. Synthesis, Characterization, and Bulk Crosslinking of Polybutadiene-Block-poly(2-Vinyl Pyridine)-Block-Poly(tert-Butyl Methacrylate) Block Terpolymers. *Polymer* **2010**, *51*, 2021–2032.
99. Erhardt, R.; Böker, A.; Zettl, H.; Kaya, H.; Pyckhout-Hintzen, W.; Krausch, G.; Abetz, V.; Müller, A. H. E. Janus Micelles. *Macromolecules* **2001**, *34*, 1069–1075.
100. Liu, Y.; Abetz, V.; Müller, A. H. E. Janus Cylinders. *Macromolecules* **2003**, 7894–7898.

101. Walther, A.; André, X.; Drechsler, M.; Abetz, V.; Müller, A. H. E. Janus Discs. *J. Am. Chem. Soc.* **2007**, *129*, 6187–6198.
102. Walther, A.; Müller, A. H. E. Janus Particles. *Soft Matter* **2008**, *4*, 663–668.
103. Zhang, L.; Eisenberg, A. Multiple Morphologies of “Crew-Cut ”Aggregates of Polystyrene-B-Poly(acrylic Acid) Block Copolymers. *Science* **1995**, *268*, 1728–1731.
104. Won, Y.; Davis, H. T.; Bates, F. S. Giant Wormlike Rubber Micelles. *Science* **1999**, *283*, 960–963.
105. Won, Y. Y.; Brannan, A. K.; Davis, H. T.; Bates, F. S. Cryogenic Transmission Electron Microscopy (cryo-TEM) of Micelles and Vesicles Formed in Water by Poly(ethylene Oxide)-Based Block Copolymers. *J. Phys. Chem. B* **2002**, *106*, 3354–3364.
106. Jain, S.; Bates, F. S. On the Origins of Morphological Complexity in Block Copolymer Surfactants. *Science* **2003**, *300*, 460–464.
107. Yu, Y.; Zhang, L.; Eisenberg, A. Morphogenic Effect of Solvent on Crew-Cut Aggregates of Amphiphilic Diblock Copolymers. *Macromolecules* **1998**, *31*, 1144–1154.
108. Yu, Y.; Eisenberg, A. Control of Morphology through Polymer - Solvent Interactions in Crew-Cut Aggregates of Amphiphilic Block Copolymers. *JACS* **1997**, *119*, 8383–8384.
109. Israelachvili, J. N.; Mitchell, D. J.; Ninham, W. Theory of Self-Assembly of Hydrocarbon Amphiphiles into Micelles and Bilayers. *J. Chem. Soc. Faraday Trans. 2* **1976**, *72*, 1525–1568.
110. Israelachvili, J. N.; Ninham, B. W. Theory of Self-Assembly of Lipid Bilayers and Vesicles. *Biochim. Biophys. Acte* **1977**, *470*, 185–201.
111. Antonietti, M.; Förster, S. Vesicles and Liposomes: A Self-Assembly Principle Beyond Lipids. *Adv. Mater.* **2003**, *15*, 1323–1333.
112. Holder, S. J.; Sommerdijk, N. A. J. M. New Micellar Morphologies from Amphiphilic Block Copolymers: Disks, Toroids and Bicontinuous Micelles. *Polym. Chem.* **2011**, *2*, 1018–1028.
113. Zhulina, E. B.; Adam, M.; Larue, I.; Sheiko, S. S.; Rubinstein, M. Diblock Copolymer Micelles in a Dilute Solution. *Macromolecules* **2005**, *38*, 5330–5351.
114. Zhang, L.; Yu, K.; Eisenberg, A. Ion-Induced Morphological Changes in “Crew-Cut” Aggregates of Amphiphilic Block Copolymers. *Science* **1996**, *272*, 1777–1779.
115. Zhang, L.; Eisenberg, A. Morphogenic Effect of Added Ions on Crew-Cut Aggregates of Polystyrene- B -Poly(acrylic Acid) Block Copolymers in Solutions. *Macromolecules* **1996**, *29*, 8805–8815.
116. Discher, D. E.; Eisenberg, A. Polymer Vesicles. *Science* **2002**, *297*, 967–973.
117. Shen, H.; Eisenberg, A. Morphological Phase Diagram for a Ternary System of Block Copolymer PS₃₁₀-*b*-PAA₅₂/Dioxane/H₂O. *J. Phys. Chem. B* **1999**, *103*, 9473–9487.

118. Choucair, A.; Eisenberg, A. Control of Amphiphilic Block Copolymer Morphologies Using Solution Conditions. *Eur. Phys. J. E. Soft Matter* **2003**, *10*, 37–44.
119. Sugihara, S.; Blanazs, A.; Armes, S. P.; Ryan, A. J.; Lewis, A. L. Aqueous Dispersion Polymerization: A New Paradigm for in Situ Block Copolymer Self-Assembly in Concentrated Solution. *J. Am. Chem. Soc.* **2011**, *133*, 15707–15713.
120. Yang, P.; Ratcli, L. P. D.; Armes, S. P. Efficient Synthesis of Poly(methacrylic Acid)-*block*-Poly(styrene-*alt*-*N*-phenylmaleimide) Diblock Copolymer Lamellae Using RAFT Dispersion Polymerization. *Macromolecules* **2013**, *46*, 8545–8556.
121. Warren, N. J.; Mykhaylyk, O. O.; Mahmood, D.; Ryan, A. J.; Armes, S. P. RAFT Aqueous Dispersion Polymerization Yields Poly(ethylene Glycol)-Based Diblock Copolymer Nano-Objects with Predictable Single Phase Morphologies. *J. Am. Chem. Soc.* **2014**, *136*, 1023–1033.
122. Blanazs, A.; Madsen, J.; Battaglia, G.; Ryan, A. J.; Armes, S. P. Mechanistic Insights for Block Copolymer Morphologies: How Do Worms Form Vesicles? *J. Am. Chem. Soc.* **2011**, *133*, 16581–16587.
123. Van Hest, J. C.; Delnoye, D. a; Baars, M. W.; van Genderen, M. H.; Meijer, E. W. Polystyrene-Dendrimer Amphiphilic Block Copolymers with a Generation-Dependent Aggregation. *Science* **1995**, *268*, 1592–1595.
124. Discher, B. M.; Won, Y.-Y.; Ege, D. S.; Lee, J. C.-M.; Bates, F. S.; Discher, D. E.; Hammer, D. A. Polymersomes: Tough Vesicles Made from Diblock Copolymers. *Science* **1999**, *284*, 1143–1146.
125. Kita-Tokarczyk, K.; Grumelard, J.; Haeefe, T.; Meier, W. Block Copolymer Vesicles—using Concepts from Polymer Chemistry to Mimic Biomembranes. *Polymer* **2005**, *46*, 3540–3563.
126. LoPresti, C.; Lomas, H.; Massignani, M.; Smart, T.; Battaglia, G. Polymersomes: Nature Inspired Nanometer Sized Compartments. *J. Mater. Chem.* **2009**, *19*, 3576–3590.
127. Howse, J. R.; Jones, R. a L.; Battaglia, G.; Ducker, R. E.; Leggett, G. J.; Ryan, A. J. Templated Formation of Giant Polymer Vesicles with Controlled Size Distributions. *Nat. Mater.* **2009**, *8*, 507–511.
128. Sackmann, E. Membrane Bending Energy Concept of Vesicle- and Cell-Shapes and Shape-Transitions. *FEBS Lett.* **1994**, *346*, 3–16.
129. Davis, K. P.; Lodge, T. P.; Bates, F. S. Vesicle Membrane Thickness in Aqueous Dispersions of Block Copolymer Blends. *Macromolecules* **2008**, *41*, 8289–8291.
130. Du, J.; O'Reilly, R. K. Advances and Challenges in Smart and Functional Polymer Vesicles. *Soft Matter* **2009**, *5*, 3544–3561.
131. Soo, P. L.; Eisenberg, A. Preparation of Block Copolymer Vesicles in Solution. *J. Polym. Sci. Part B Polym. Phys.* **2004**, *42*, 923–938.
132. Lazzari, M.; Liu, G.; Lecommandoux, S. Block Copolymers in Nanoscience. **2006**.
133. Fuks, G.; Mayap Talom, R.; Gauffre, F. Biohybrid Block Copolymers: Towards Functional Micelles and Vesicles. *Chem. Soc. Rev.* **2011**, *40*, 2475–2493.

134. Brinkhuis, R. P.; Rutjes, F. P. J. T.; van Hest, J. C. M. Polymeric Vesicles in Biomedical Applications. *Polym. Chem.* **2011**, *2*, 1449–1462.
135. Discher, B. M.; Bermudez, H.; Hammer, D. a.; Discher, D. E.; Won, Y. Y.; Bates, F. S. Cross-Linked Polymersome Membranes: Vesicles with Broadly Adjustable Properties. *J. Phys. Chem. B* **2002**, *106*, 2848–2854.
136. Kishimura, A.; Koide, A.; Osada, K.; Yamasaki, Y.; Kataoka, K. Encapsulation of Myoglobin in PEGylated Polyion Complex Vesicles Made from a Pair of Oppositely Charged Block Ionomers: A Physiologically Available Oxygen Carrier. *Angew. Chemie - Int. Ed.* **2007**, *46*, 6085–6088.
137. Ahmed, F.; Discher, D. E. Self-Porting Polymersomes of PEG-PLA and PEG-PCL: Hydrolysis-Triggered Controlled Release Vesicles. *J. Control. Release* **2004**, *96*, 37–53.
138. Sui, X.; Kujala, P.; Janssen, G.-J.; de Jong, E.; Zuhorn, I. S.; van Hest, J. C. M. Robust Formation of Biodegradable Polymersomes by Direct Hydration. *Polym. Chem.* **2015**, *6*, 691–696.
139. Du, J.; Tang, Y.; Lewis, A. L.; Armes, S. P. pH-Sensitive Vesicles Based on a Biocompatible Zwitterionic Diblock Copolymer. *J. Am. Chem. Soc.* **2005**, *127*, 17982–17983.
140. Borchert, U.; Lipprandt, U.; Bilanz, M.; Kimpfler, A.; Rank, A.; Peschka-Süss, R.; Schubert, R.; Lindner, P.; Förster, S. pH-Induced Release from P2VP-PEO Block Copolymer Vesicles. *Langmuir* **2006**, *22*, 5843–5847.
141. Li, Y.; Lokitz, B. S.; McCormick, C. L. Thermally Responsive Vesicles and Their Structural “Locking” through Polyelectrolyte Complex Formation. *Angew. Chemie - Int. Ed.* **2006**, *45*, 5792–5795.
142. Chen, X.; Ding, X.; Zheng, Z.; Peng, Y. Thermosensitive Cross-Linked Polymer Vesicles for Controlled Release System. *New J. Chem.* **2006**, *30*, 577–582.
143. Zhao, Y. Rational Design of Light-Controllable Polymer Micelles. *Chem. Rec.* **2007**, *7*, 286–294.
144. Lecommandoux, S.; Sandre, O.; Chécot, F.; Rodriguez-Hernandez, J.; Perzynski, R. Magnetic Nanocomposite Micelles and Vesicles. *Adv. Mater.* **2005**, *17*, 712–718.
145. Krack, M.; Hohenberg, H.; Kornowski, A.; Lindner, P.; Weller, H.; Förster, S. Nanoparticle-Loaded Magnetophoretic Vesicles. *J. Am. Chem. Soc.* **2008**, *130*, 7315–7320.
146. Mai, Y.; Eisenberg, A. Controlled Incorporation of Particles into the Central Portion of Vesicle Walls. *JACS* **2010**, 10078–10084.
147. Binder, W. H.; Sachsenhofer, R.; Farnik, D.; Blaas, D. Guiding the Location of Nanoparticles into Vesicular Structures: A Morphological Study. *Phys. Chem. Chem. Phys.* **2007**, *9*, 6313–6318.
148. Du, J.; Armes, S. P. Preparation of Primary Amine-Based Block Copolymer Vesicles by Direct Dissolution in Water and Subsequent Stabilization by Sol-Gel Chemistry. *Langmuir* **2008**, *24*, 13710–13716.
149. Opsteen, J. A.; Brinkhuis, R. P.; Teeuwen, R. L. M.; Löwik, D. W. P. M.; Van Hest, J. C. M. Clickable Polymersomes. *Chem. Commun.* **2007**, *49*, 3136–3138.

150. Gilroy, J. B.; Gädt, T.; Whittell, G. R.; Chabanne, L.; Mitchels, J. M.; Richardson, R. M.; Winnik, M. A.; Manners, I. Monodisperse Cylindrical Micelles by Crystallization-Driven Living Self-Assembly. *Nat. Chem.* **2010**, *2*, 566–570.
151. Rugar, P. A.; Chabanne, L.; Winnik, M. A.; Manners, I. Non-Centrosymmetric Cylindrical Micelles by Unidirectional Growth. *Science* **2012**, *337*, 559–562.
152. Hudson, Z. M.; Lunn, D. J.; Winnik, M. A.; Manners, I. Colour-Tunable Fluorescent Multiblock Micelles. *Nat. Commun.* **2014**, *5*, 3372.
153. Cao, L.; Manners, I.; Winnik, M. A. Influence of the Interplay of Crystallization and Chain Stretching on Micellar Morphologies: Solution Self-Assembly of Coil-Crystalline Poly(isoprene-Block-Ferrocenylsilane). *Macromolecules* **2002**, *35*, 8258–8260.
154. Gädt, T.; Jeong, N. S.; Cambridge, G.; Winnik, M. A.; Manners, I. Complex and Hierarchical Micelle Architectures from Diblock Copolymers Using Living, Crystallization-Driven Polymerizations. *Nat. Mater.* **2009**, *8*, 144–150.
155. Hudson, Z. M.; Boott, C. E.; Robinson, M. E.; Rugar, P. A.; Winnik, M. A.; Manners, I. Tailored Hierarchical Micelle Architectures Using Living Crystallization-Driven Self-Assembly in Two Dimensions. *Nat. Chem.* **2014**, *6*, 893–898.
156. Jia, L.; Zhao, G.; Shi, W.; Coombs, N.; Gourevich, I.; Walker, G. C.; Guerin, G.; Manners, I.; Winnik, M. a. A Design Strategy for the Hierarchical Fabrication of Colloidal Hybrid Mesostructures. *Nat. Commun.* **2014**, *5*, 3882.
157. Qiu, H.; Hudson, Z. M.; Winnik, M. A.; Manners, I. Multidimensional Hierarchical Self-Assembly of Amphiphilic Cylindrical Block Comicelles. *Science* **2015**, *347*, 1329–1332.
158. Riess, G. Micellization of Block Copolymers. *Prog. Polym. Sci.* **2003**, *28*, 1107–1170.
159. Jia, L.; Cao, A.; Lévy, D.; Xu, B.; Albouy, P.-A.; Xing, X.; Bowick, M. J.; Li, M.-H. Smectic Polymer Vesicles. *Soft Matter* **2009**, *5*, 3446–3451.
160. Xing, X.; Shin, H.; Bowick, M. J.; Yao, Z.; Jia, L.; Li, M.-H. Morphology of Nematic and Smectic Vesicles. *PNAS* **2012**, *109*, 5202–5206.
161. Parry, A. L.; Bomans, P. H. H.; Holder, S. J.; Sommerdijk, N. A. J. M.; Biagini, S. C. G. Cryo Electron Tomography Reveals Confined Complex Morphologies of Tripeptide-Containing Amphiphilic Double-Comb Diblock Copolymers. *Angew. Chemie Int. Ed.* **2008**, *47*, 8859–8862.
162. McKenzie, B. E.; Nudelman, F.; Bomans, P. H. H.; Holder, S. J.; Sommerdijk, N. A. J. M. Temperature-Responsive Nanospheres with Bicontinuous Internal Structures from a Semicrystalline Amphiphilic Block Copolymer. *J. Am. Chem. Soc.* **2010**, *132*, 10256–10259.
163. McKenzie, B. E.; Holder, S. J.; Sommerdijk, N. A. J. M. Assessing Internal Structure of Polymer Assemblies from 2D to 3D CryoTEM: Bicontinuous Micelles. *Curr. Opin. Colloid Interface Sci.* **2012**, *17*, 343–349.
164. Du, J.; O'Reilly, R. K. Anisotropic Particles with Patchy, Multicompartment and Janus Architectures: Preparation and Application. *Chem. Soc. Rev.* **2011**, *40*, 2402–2416.

165. Liu, F.; Eisenberg, A. Preparation and pH Triggered Inversion of Vesicles from Poly(acrylic Acid)-Block-Polystyrene-Block-poly(4-Vinyl Pyridine). *J. Am. Chem. Soc.* **2003**, *125*, 15059–15064.
166. Stoenescu, R.; Meier, W. Vesicles with Asymmetric Membranes from Amphiphilic ABC Triblock Copolymers. *Chem. Commun.* **2002**, 3016–3017.
167. Schmelz, J.; Karg, M.; Hellweg, T.; Schmalz, H. General Pathway toward Crystalline-Core Micelles with Tunable Morphology and Corona Segregation. *ACS Nano* **2011**, *5*, 9523–9534.
168. Gegenhuber, T.; Gröschel, A. H.; Löbbling, T. I.; Drechsler, M.; Ehlert, S.; Förster, S.; Schmalz, H. Noncovalent Grafting of Carbon Nanotubes with Triblock Terpolymers: Toward Patchy 1D Hybrids. *Macromolecules* **2015**, *48*, 1767–1776.
169. Schmelz, J.; Schacher, F. H.; Schmalz, H. Cylindrical Crystalline-Core Micelles: Pushing the Limits of Solution Self-Assembly. *Soft Matter* **2013**, *9*, 2101–2107.
170. Voets, I. K.; Leermakers, F. A.; Keizer, A. De; Charlaganov, M.; Stuart, M. A. C. Co-Assembly Towards Janus Micelles. *Adv. Polym. Sci.* **2011**, *241*, 163–185.
171. Walther, A.; Müller, A. H. E. Janus Particles: Synthesis, Self-Assembly, Physical Properties, and Applications. *Chem. Rev.* **2013**, *113*, 5194–5261.
172. Wang, L.; Lin, J. Discovering Multicore Micelles: Insights into the Self-Assembly of Linear ABC Terpolymers in Midblock-Selective Solvents. *Soft Matter* **2011**, *7*, 3383–3391.
173. Skrabania, K.; Berlepsch, H. V.; Böttcher, C.; Laschewsky, A. Synthesis of Ternary, Hydrophilic–Lipophilic–Fluorophilic Block Copolymers by Consecutive RAFT Polymerizations and Their Self-Assembly into Multicompartment Micelles. *Macromolecules* **2010**, *43*, 271–281.
174. Li, Z.; Kesselman, E.; Talmon, Y.; Hillmyer, M. A.; Lodge, T. P. Multicompartment Micelles from ABC Miktoarm Stars in Water. *Science* **2004**, *306*, 98–101.
175. Edmonds, W. F.; Li, Z.; Hillmyer, M. A.; Lodge, T. P. Disk Micelles from Nonionic Coil-Coil Diblock Copolymers. *Macromolecules* **2006**, *39*, 4526–4530.
176. Li, Z.; Hillmyer, M. A.; Lodge, T. P. Laterally Nanostructured Vesicles, Polygonal Bilayer Sheets, and Segmented Wormlike Micelles. *Nano Lett.* **2006**.
177. Li, Z.; Hillmyer, M. A.; Lodge, T. P. Morphologies of Multicompartment Micelles Formed by ABC Miktoarm Star Terpolymers. *Langmuir* **2006**, *22*, 9409–9417.
178. Weberskirch, R.; Ringsdorf, H. Functional, Photoreactive and Polymerizable Amphiphilic Systems in Organized Media. In *Meeting of HCM Network*; 1995; p. Greece.
179. Ringsdorf, H.; Lehmann, R.; Weberskirch, R. Book of Abstracts. In *217th ACS National Meeting*; 1999.
180. Kubowicz, S.; Baussard, J.-F.; Lutz, J.-F.; Thünemann, A. F.; von Berlepsch, H.; Laschewsky, A. Multicompartment Micelles Formed by Self-Assembly of Linear ABC Triblock Copolymers in Aqueous Medium. *Angew. Chem. Int. Ed.* **2005**, *44*, 5262–5265.
181. Berlepsch, H. V.; Böttcher, C.; Skrabania, K.; Laschewsky, A. Complex Domain Architecture of Multicompartment Micelles from a Linear ABC Triblock

- Copolymer Revealed by Cryogenic Electron Tomography. *Chem. Commun.* **2009**, 2290–2292.
182. Dupont, J.; Liu, G. ABC Triblock Copolymer Hamburger-like Micelles, Segmented Cylinders, and Janus Particles. *Soft Matter* **2010**, *6*, 3654–3661.
183. Schacher, F.; Walther, A.; Ruppel, M.; Drechsler, M.; Müller, A. H. E. Multicompartment Core Micelles of Triblock Terpolymers in Organic Media. *Macromolecules* **2009**, 3540–3548.
184. Schacher, F.; Walther, A.; Müller, A. H. E. Dynamic Multicompartment-Core Micelles in Aqueous Media. *Langmuir* **2009**, *25*, 10962–10969.
185. Schacher, F.; Betthausen, E.; Walther, A.; Schmalz, H.; Pergushov, D. V.; Müller, A. H. E. Interpolyelectrolyte Complexes of Dynamic Multicompartment Micelles. *ACS Nano* **2009**, *3*, 2095–2102.
186. Synatschke, C. V.; Schacher, F. H.; Förtsch, M.; Drechsler, M.; Müller, A. H. E. Double-Layered Micellar Interpolyelectrolyte Complexes—How Many Shells to a Core? *Soft Matter* **2011**, *7*, 1714–1725.
187. Betthausen, E.; Drechsler, M.; Förtsch, M.; Schacher, F. H.; Müller, A. H. E. Dual Stimuli-Responsive Multicompartment Micelles from Triblock Terpolymers with Tunable Hydrophilicity. *Soft Matter* **2011**, *7*, 8880–8891.
188. Betthausen, E.; Drechsler, M.; Förtsch, M.; Pergushov, D. V.; Schacher, F. H.; Müller, A. H. E. Stimuli-Responsive Micellar Interpolyelectrolyte Complexes – Control of Micelle Dynamics via Core Crosslinking. *Soft Matter* **2012**, *8*, 10167–10177.
189. Gröschel, A. H.; Schacher, F. H.; Schmalz, H.; Borisov, O. V.; Zhulina, E. B.; Walther, A.; Müller, A. H. E. Precise Hierarchical Self-Assembly of Multicompartment Micelles. *Nat. Commun.* **2012**, *3*, 710.
190. Walther, A.; Müller, A. H. E. Janus Particles : Synthesis, Self-Assembly, Physical Properties, and Applications. *Chem. Rev.* **2013**.
191. Gröschel, A. H.; Walther, A.; Löbbling, T. I.; Schmelz, J.; Hanisch, A.; Schmalz, H.; Müller, A. H. E. Facile, Solution-Based Synthesis of Soft, Nanoscale Janus Particles with Tunable Janus Balance. *J. Am. Chem. Soc.* **2012**, *134*, 13850–13860.
192. Ruhland, T. M.; Gröschel, A. H.; Walther, A.; Müller, A. H. E. Janus Cylinders at Liquid-Liquid Interfaces. *Langmuir* **2011**, *27*, 9807–9814.
193. Ruhland, T. M.; Gröschel, A. H.; Ballard, N.; Skelton, T. S.; Walther, A.; Müller, A. H. E.; Bon, S. a F. Influence of Janus Particle Shape on Their Interfacial Behavior at Liquid-Liquid Interfaces. *Langmuir* **2013**, *29*, 1388–1394.
194. Walther, A.; Hoffmann, M.; Müller, A. H. E. Emulsion Polymerization Using Janus Particles as Stabilizers. *Angew. Chemie Int. Ed.* **2008**, *47*, 711–714.
195. Gröschel, A. H.; Löbbling, T. I.; Petrov, P. D.; Müllner, M.; Kuttner, C.; Wieberger, F.; Müller, A. H. E. Janus Micelles as Effective Supracolloidal Dispersants for Carbon Nanotubes. *Angew. Chemie Int. Ed.* **2013**, *52*, 3602–3606.
196. Walther, A.; Matussek, K.; Müller, A. H. E. Engineering Nanostructured Polymer Blends with Controlled Nanoparticle Location Using Janus Particles. *ACS Nano* **2008**, *2*, 1167–1178.

197. Cui, H.; Chen, Z.; Zhong, S.; Wooley, K. L.; Pochan, D. J. Block Copolymer Assembly via Kinetic Control. *Science* **2007**, *317*, 647–650.
198. Fang, B.; Walther, A.; Wolf, A.; Xu, Y.; Yuan, J.; Müller, A. H. E. Undulated Multicompartment Cylinders by the Controlled and Directed Stacking of Polymer Micelles with a Compartmentalized Corona. *Angew. Chemie Int. Ed.* **2009**, *48*, 2877–2880.
199. Dupont, J.; Liu, G.; Niihara, K.; Kimoto, R.; Jinnai, H. Self-Assembled ABC Triblock Copolymer Double and Triple Helices. *Angew. Chemie Int. Ed.* **2009**, *48*, 6144–6147.
200. Dou, H.; Liu, G.; Dupont, J.; Hong, L. Triblock Terpolymer Helices Self-Assembled under Special Solvation Conditions. *Soft Matter* **2010**, *6*, 4214–4222.
201. Gröschel, A. H.; Walther, A.; Löblich, T. I.; Schacher, F. H.; Schmalz, H.; Müller, A. H. E. Guided Hierarchical Co-Assembly of Soft Patchy Nanoparticles. *Nature* **2013**, *503*, 247–251.
202. Zhong, S.; Cui, H.; Chen, Z.; Wooley, K. L.; Pochan, D. J. Helix Self-Assembly through the Coiling of Cylindrical Micelles. *Soft Matter* **2008**, *4*, 90–93.
203. Zhao, W.; Chen, D.; Hu, Y.; Grason, G. M.; Russell, T. P. ABC Triblock Copolymer Vesicles with Mesh-Like Morphology. *ACS Nano* **2011**, *5*, 486–492.
204. Yu, S.; Azzam, T.; Rouiller, I.; Eisenberg, A. “Breathing” Vesicles. *J. Am. Chem. Soc.* **2009**, *131*, 10557–10566.
205. Brannan, A. K.; Bates, F. S. ABCA Tetrablock Copolymer Vesicles. *Macromolecules* **2004**, *37*, 8816–8819.
206. Ludwigs, S.; Böker, A.; Voronov, A.; Rehse, N.; Magerle, R.; Krausch, G. Self-Assembly of Functional Nanostructures from ABC Triblock Copolymers. *Nat. Mater.* **2003**, *2*, 744–747.

2. Thesis Overview

This dissertation contains 6 articles presented from chapter 3-8.

The common topic that connects all chapters is the fabrication of highly complex compartmentalized nanoparticles with the aim to expand the library of accessible structures from triblock terpolymers in solution. Connected to this, the in-depth characterization is a key element in this work, which becomes challenging with downsizing while simultaneously increasing the complexity of the system with features in the sub-100 nm range. Throughout this thesis, anionic polymerization is the method of choice for the synthesis of narrowly distributed triblock terpolymers, and electron microscopy and tomography techniques are applied for characterization and elucidating underlying formation mechanisms of as synthesized particles.

In chapters 3 and 4 an ampholytic triblock terpolymer is self-assembled in aqueous solution to form negatively charged multicompartment micelles (MCMs). The charged corona of the particles is accessible to form interpolyelectrolyte complexes (IPECs) if mixed with polycationic homopolymers or bishydrophilic cationic/neutral diblock copolymers. Large, negatively charged corona chains in combination with high ionic grafting of the polycations results in the formation of anisotropic hydrophobic IPECs on top of the micellar core. These intricate, purely organic nanoparticles were thoroughly characterized by means of cryogenic transmission electron microscopy and tomography.

The self-assembly of triblock terpolymers from spherical MCMs towards more complex nanostructures is described in chapters 5 and 6. Up to now the solution self-assembly of triblock terpolymers into spherical MCMs is well described, however the assembly into multicompartment cylinders, sheets and vesicles remained challenging. During this thesis synthetic design strategies were developed to encode information into triblock terpolymers to access these novel compartmentalized particle geometries. Inspired by the bulk and solution behaviour of diblock copolymers, we hypothesized that ABC triblock terpolymers with two solvophobic blocks should be able to form a myriad of nanostructures. The particle geometry is thereby guided by the corona block length (*i.e.* spheres, cylinders, vesicles), while the two solvophobic blocks should phase separate within the confined space of the particle core in analogy to bulk. Systematic screening of block compositions of the triblock terpolymers allows establishing a broad library of novel compartmentalized superstructures with so far unprecedented complexity. Not only all particle geometries from spheres, cylinders, sheets to vesicles, but also the internal phase separation of the solvophobic blocks was precisely tuned in analogy to bulk morphologies from spheres cylinders to gyroids and lamellae. In chapter 6 parameters are screened that govern morphological transitions of ABC triblock terpolymers from multicompartment micelles to cylinders and vesicles apart from synthetic manipulation of the terpolymers. Morphological transitions were induced *via* solvent conditions, blending with homopolymers or polymer analogous reactions. Connected to that, and to complete the investigation of structure-morphology relationship of the synthesized triblock terpolymers, chapter 7 presents a comprehensive study on the respective bulk morphologies. Within this article, the triblock

terpolymers were investigated in the bulk state, giving lamella-lamella, core-shell cylinder, core-shell gyroid and a cylinder-in-lamella morphology. All phases are thoroughly characterized with transmission electron microscopy (TEM) and small angle X-ray scattering (SAXS).

In chapter 8, polymeric Janus micelles are used for the first time to compatibilize immiscible polymer blends in an industry scale extruder. This work is based on a self-assembly protocol developed in our group to synthesize Janus micelles from triblock terpolymers in solution *via* MCMs. During my work, this process was upscaled to create 100 g of Janus micelles in one batch and used in an extruder with a throughput of 1 kg/h to compatibilize a blend of immiscible polymers. The Janus micelles show extraordinary interfacial activity leading to a small droplet size of less than 300 nm in the final polymer blend, significantly smaller than by the use of the precursor triblock terpolymer.

2.1. Micellar Interpolyelectrolyte Complexes with a Compartmentalized Shell

A combination of self-assembly of ampholytic triblock terpolymers with interpolyelectrolyte complexation of polycationic homopolymers is employed to achieve novel patchy particles. First a triblock terpolymer polybutadiene-*block*-poly(2-vinylpyridine)-*block*-poly(*tert*-butyl methacrylate) (BVT) is synthesized *via* sequential living anionic polymerization and converted to polybutadiene-*block*-poly(1-methyl-2-vinylpyridinium)-*block*-poly(methacrylic acid) (BVqMAA) through quaternization of the P2VP block and hydrolysis of the *Pt*BMA block. Transfer of BVqMAA to aqueous pH 10 buffer solution gives multicompartment micelles (MCMs) with a hydrophobic PB core, patches of a hydrophobic intramicellar interpolyelectrolyte complex (*im*-IPEC) of P2Vq with PMAA stabilized by a negatively charged PMAA corona as the degree of polymerization of PMAA is higher than that of P2VPq. Two different MCMs, BVqMAA₄₀₀ and BVqMAA₁₃₅₀, were synthesized differing only in the length of the negatively charged corona block. The characteristics of the triblock terpolymer, a schematic of the formed MCMs as well as cryo-TEM images are shown in Figure 2.1.

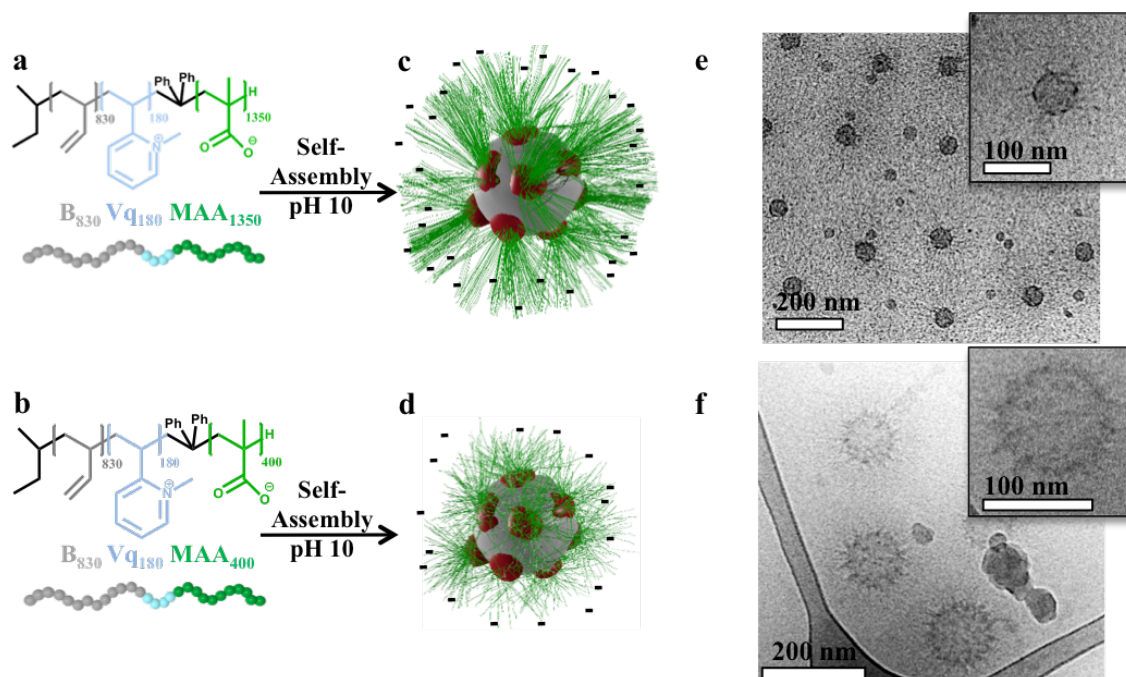


Figure 2.1: Synthesis of BVqMAA precursor micelles. a-b) Characteristics of used BVqMAA triblock terpolymers for the BVqMAA₁₃₅₀ (a) and BVqMAA₄₀₀ (b) precursor micelles. c-d) Schematics of the formed precursor micelles with PB core (grey), the *im*-IPEC between P2Vq/PMAA (red) and the stabilizing PMAA corona (green). e-f) Representative cryo-TEM images of the BVqMAA₁₃₅₀ (e) and BVqMAA₄₀₀ (f) multicompartment micelles.

The negatively charged MCMs are used as precursor micelles to undergo further complexation reactions with polycationic homopolymers thereby creating a new hydrophobic IPEC. In this work, we chose poly(2-((2-(dimethylamino)ethyl)methylamino)ethyl methacrylate) (PDAMAq) as polycation, synthesized for the first time *via* RAFT polymerization, and quaternized with methyl iodide. The two charges per monomeric unit lead to a dense IPEC when complexed with the remaining PMAA corona of the precursor micelles. The short BVqMAA₄₀₀ and the long BVqMAA₁₃₅₀ precursor micelles were mixed with the polycations to induce IPEC formation. Figure 2.2 shows the resulting patchy nanoparticles, where the newly formed hydrophobic PDAMAq/PMAA IPEC forms a homogeneous shell in case of the short BVqMAA₄₀₀ micelles and IPEC large patches in case of the long BVqMAA₁₃₅₀ precursor micelles.

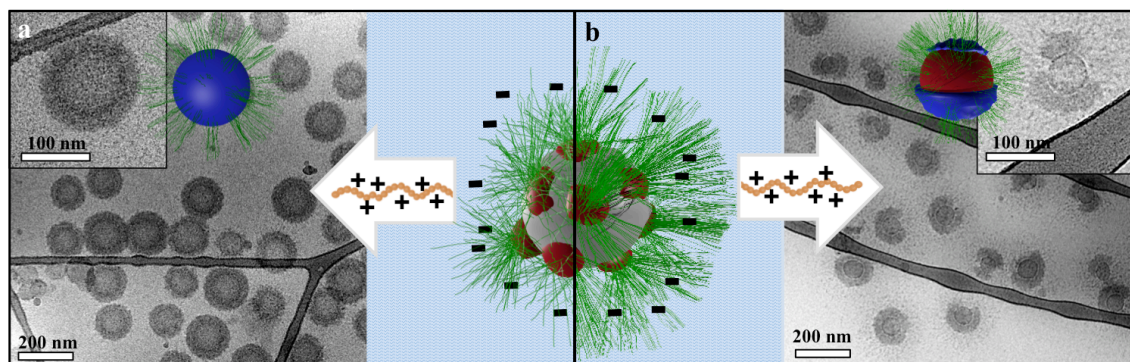


Figure 2.2: Complexation of BVqMAA precursor micelles with polycationic PDAMAq. **a)** The complexation of PDAMAq with BVqMAA₄₀₀ micelles leads to the formation of a homogeneous PDAMAq/PMAA IPEC shell. The schematic shows the homogeneous newly formed IPEC as blue shell. **b)** BVqMAA₁₃₅₀ complexed with PDAMAq forms irregular IPEC patches (blue) on top of the micellar core.

The formation of these rather unusual patchy IPECs with the long BVqMAA₁₃₅₀ was thoroughly studied. We performed experiments to exclude that the structure is kinetically trapped due to fast IPEC formation upon mixing the components. We increased the salinity of the system to screen the charges of the polyelectrolytes inducing the break-up of the IPEC. After dialyzing particles back to the original pH 10 buffer solution, the IPEC can slowly form again. The increased chain mobility gives the energetically favoured structure, which again is the patchy IPEC. Also the polycation can be changed to *e.g.* quaternized poly(2-(dimethylamino)ethyl methacrylate) (PDMAEMAq) leading to these peculiar structures, which led us to the assumption that the nature of polycation does not influence the resulting structure, but the corona chain length of the precursor micelles is responsible for the formation of either a continuous or a patchy IPEC. In more detail, we assume different favourable interfaces of the participating components responsible for the IPEC formation. Figure 2.3 shows different interfaces of the newly formed PDAMAq/PMAA IPEC and the surrounding medium for both BVqMAA micelles for a homogeneous and patchy IPEC. The new IPEC forms an interface with the micellar core consisting of PB and the *im*-IPEC (interface IF-1, yellow dashed line), with the PMAA corona chains (IF-2, red dashed line) and may also form an interface with water (IF-3, purple dashed line).

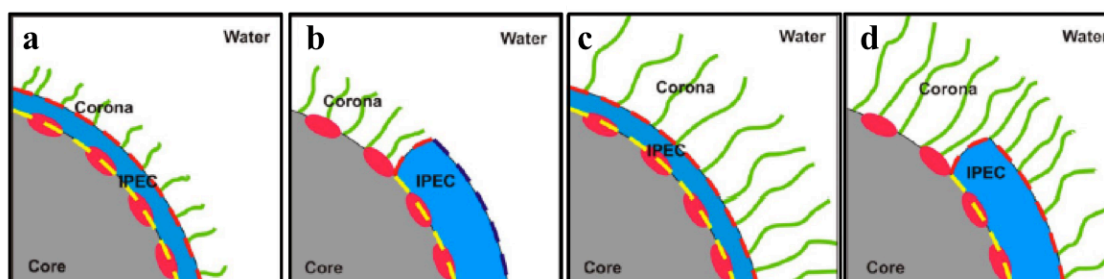


Figure 2.3. Schematic illustration of the potentially relevant interfaces. The formation of an additional IPEC shell in BVqMAA micelles with a short (**a, b**) or long (**c, d**) corona, leading to either continuous (**a, c**) or patchy (**b, d**) IPECs. The relevant interfaces of the newly formed IPEC are highlighted as dashed lines and are between the IPEC and the core (IF-1, yellow), the corona (IF-2, red), or water as the selective solvent (IF-3, purple).

Different cases can now be considered. When a continuous new IPEC shell is formed, the interfaces IF-1 and IF-2 are maximized, while IF-3 is absent (Figure 2.3a,c). IF-1 is minimized in case of the formation of a patchy IPEC, but in turn would lead to the generation of a significant interface IF-3 (Figure 2.3b) and potentially, a loss of colloidal stability in case of the BVqMAA₄₀₀ micelles. In contrast, the BVqMAA₁₃₅₀ micelles minimize IF-1 without creating an additional IF-3 (Figure 2.3d). Although this explanation is solely based on simple considerations and does not include effects like chain entropy or partial dissociation of IPEC domains, we assume that micelles with a very long ionic corona preferentially form patchy IPEC compartments when complexed with oppositely charged polycations.

2.2. Cryogenic Transmission Electron Tomography Reveals Hidden Features in Compartmentalized Particles

Cryogenic Transmission Electron Tomography (cryo-ET) is a valuable tool for the *in-situ* characterization of nanostructures, commonly used in biological science, but only slowly progressing to the field of materials science. In contrast to conventional cryogenic transmission electron microscopy (cryo-TEM), which is a 2D imaging technique, the advantage of cryo-ET is the generation of a 3D reconstruction of one particle computationally calculated from a series of 2D images captured at varying tilt angles. Especially the ongoing progress towards ever more complex structures in the field of materials- and soft matter nanoscience requires elaborate characterization tools to visualize such complex materials often with internal features on the nanoscale. 2D imaging techniques reach their limits when a 2D projection of a 3D object is captured, as overlapping internal features of complex structures complicates a reliable characterization of the underlying structure or structure forming mechanisms. In this chapter we address two main aspects, the synthetic concept to form complex patchy nanoparticles as well as the use of cryo-ET to resolve all internal features of the synthesized, purely organic nanoparticles.

Analogous to the previous chapter, a B₈₃₀V₁₈₀T₁₃₅₀ triblock terpolymer (subscripts denote degree of polymerization) was converted to B₈₃₀Vq₁₈₀MAA₁₃₅₀. After transferring to aqueous solution, multicompartment micelles with a PB core, patches of the intramicellar IPEC (*im*-IPEC) and a negatively charged PMAA corona arise. The anionic corona of these precursor micelles is then complexed with bishydrophilic polycationic/neutral diblock copolymers to form a new hydrophobic IPEC that phase-separates from the aqueous solution. The neutral and solvent swollen block of the densely grafted diblock copolymer within the corona of the precursor micelles suppresses the collapse of the newly formed IPEC leading to nanoparticles with complex anisotropic IPEC morphologies (Figure 2.4). The diblock copolymers used in this work contain one polycationic block, poly(L-lysine) (PLL) or quaternized poly(2-(dimethylamino)ethyl methacrylate) (PDq), and poly(ethylene oxide) (PEO) as the neutral, water-soluble block.

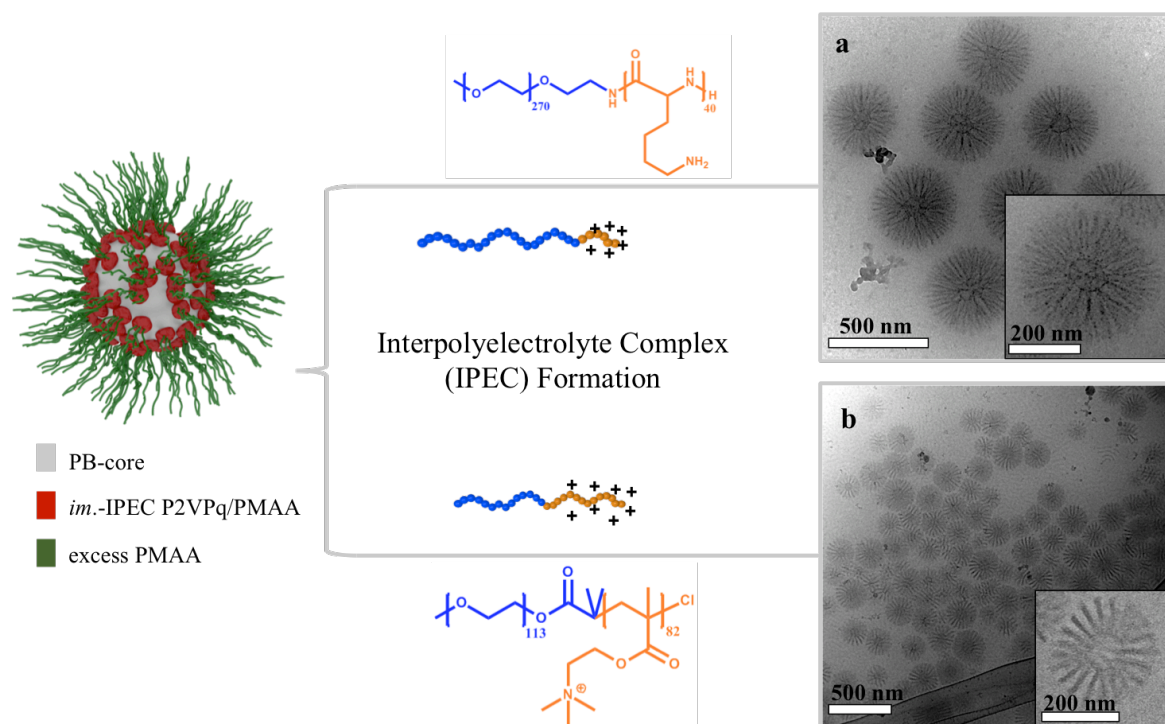


Figure 2.4: Complexation of B₈₃₀Vq₁₈₀MAA₁₃₅₀ precursor micelle with polycationic/neutral block copolymers. a) cryo-TEM image of B₈₃₀Vq₁₈₀MAA₁₃₅₀/LL₄₀EO₂₇₀ IPEC and (b) cryo-TEM image of B₈₃₀Vq₁₈₀MAA₁₃₅₀/Dq₈₂EO₁₁₄ after full complexation. The insets show a higher magnification of a corresponding particle.

The influence of the polycationic block and the stabilizing non-ionic PEO block on the resulting IPEC morphology is investigated by using LL₄₀EO₂₇₀ (Figure 2.4a) and Dq₈₂EO₁₁₄ (Figure 2.4b), having comparable molecular weight but differing in the length of the polycationic as well as PEO block. The precursor micelles are mixed with the respective diblock copolymer to achieve full complexation (charge neutrality) gaining stability through the new PEO corona. Figure 2.4a shows the resulting micellar IPECs after complexation of B₈₃₀Vq₁₈₀MAA₁₃₅₀ with LL₄₀EO₂₇₀. The chain length of the polycationic block determines the amount of diblock copolymer chains that are grafted per PMAA chain (here 29 diblock copolymer chains/PMAA chain). This massive overcrowding with diblock copolymer chains in the confined space of the precursor micelle corona suppresses the collapse of the newly formed, hydrophobic IPEC as a continuous shell on top of the micellar core, but instead, ray-like protrusions are emanating from the core, visible in the cryo-TEM image (Figure 2.5a). This particle was subjected to cryo-ET and a 3D reconstruction was calculated using the maximum entropy iterative method (Figure 2.5b). The reconstruction and computer-aided calculation of the isosurface model (in ET it is a surface that represents points of equal electron density within a volume) show a particle with compartmentalized corona structure reminiscent of a sea urchin (Figure 2.5c). There, the newly formed IPEC adopts a cylindrical brush shape, intercalated by the solvent swollen PEO chains providing steric stabilization for the IPEC brushes as well as stabilize the nanoparticles as new hydrophilic, non-ionic corona.

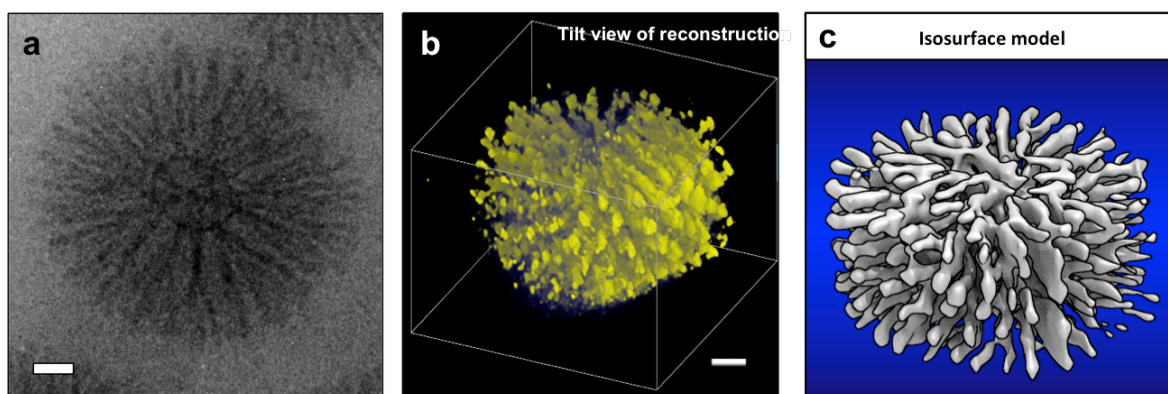


Figure 2.5. Cryo-ET of $B_{830}Vq_{180}MAA_{1350}/LL_{40}EO_{270}$. **a)** Cryo-TEM image of one micelle subjected to cryo-ET. **b)** 3D reconstruction and **(c)** isosurface model of the respective micelle. Scale bars denote 50 nm.

The corona-compartmentalized particles resulting from complexation of $B_{830}Vq_{180}MAA_{1350}$ with $Dq_{82}EO_{114}$ on a first glimpse look similar to the IPECs discussed before, however the rays protruding from the micellar core are thicker and less in number (Figure 2.6a). The diblock copolymer $Dq_{82}EO_{114}$ has a polycationic block that is twice as long as compared to $LL_{40}EO_{270}$, while the PEO block is only half the length. Here, the number of diblock copolymer chains grafted to one PMAA chain is only 14 to reach charge neutral conditions. Surprisingly, cryo-ET reveals that the newly formed IPECs do not appear as rays, but form a complex construct of lamellae on top of the spherical micellar core giving the particles an appearance reminiscent of a turbine (Figure 2.6b,c).

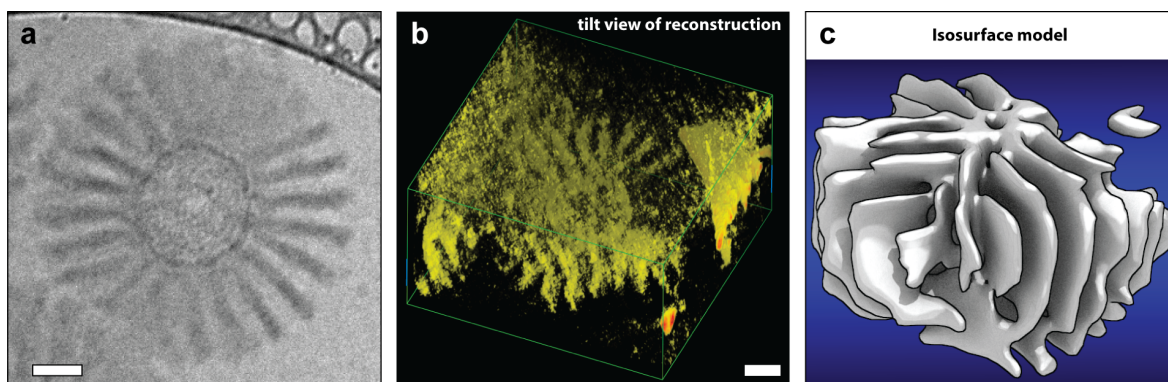


Figure 2.6. Cryo-ET of $B_{830}Vq_{180}MAA_{1350}/Dq_{82}EO_{114}$. **a)** Cryo-TEM image of one micelle subjected to cryo-ET. **b)** 3D reconstruction and **(c)** isosurface model of the respective micelle. Scale bars denote 50 nm.

The two types of micellar IPECs have in common that both particles exhibit the same micellar core and first intramicellar IPEC between Vq/MAA , a second inter-micellar anisotropic IPEC and a surrounding PEO corona. To understand the different appearances of the newly formed IPECs, the volume fractions of the hydrophobic IPEC, f_{IPEC} , and the solvent-swollen PEO corona were calculated from the isosurface reconstructions. In case of the cylindrical IPECs, a volume fraction of $f_{IPEC1} \approx 0.21$ was calculated whereas the lamellar IPEC has a volume fraction of $f_{IPEC2} \approx 0.43$. These values are close to typical values for

the cylinder and lamellar bulk morphology of highly incompatible block copolymers. We assume, that the resulting IPEC morphology originates from the volume ratio of the hydrophobic IPEC to the solvent swollen PEO corona and is an intriguing example of structuring particle corona peripheries by steric control with feature sizes in the sub 100 nm regime, predetermined by the block length and composition of the used polymers.

2.3. Self-Assembly of Triblock Terpolymers Towards Complex Micellar Superstructures

The ability of ABC triblock terpolymers to self-assemble into a myriad of complex nanostructures was studied beyond state-of-the art spherical multicompartment micelles (MCMs) or undulated cylinders. The aim was to expand the library of accessible compartmentalized nanostructures by proper choice of block volume fractions and self-assembly pathways. Inspired by diblock copolymer assembly in bulk and in solution, we hypothesize that unifying both concepts into one triblock terpolymer might give rise to a series of novel multicompartment nanostructures. A library of polystyrene-*block*-polybutadiene-*block*-poly(*tert*-butyl methacrylate) triblock terpolymers (SBT, Figure 2.7a) was synthesized to systematically screen parameters influencing the final solution structure. Comparable to diblock copolymers in solution, the T corona block length controls the overall micellar geometry (Figure 2.7b) while the two hydrophobic blocks S and B intrinsically phase separate within the confined geometry comparable to diblock copolymers in bulk (Figure 2.7c). The self-assembly pathway comprises a two-step procedure where the polymer is first dissolved in a non-solvent for the B block to induce micelle formation with a B core and S/T corona. Upon dialysis into the final solvent mixture the S block starts to aggregate and phase-separate from the soluble T block. The as-formed transient Janus micelles are not stable and aggregate over the S patch to the final multicompartment structure as exemplified in Figure 2.7d. An example of SBT spherical multicompartment micelles with S core, B patches and T as stabilizing corona is shown in Figure 2.7e. The final solvent mixture is chosen to be acetone/isopropanol as it is a good solvent for the T corona over all solvent compositions and a non-solvent for S and B. However, S is plasticized by acetone and proper solvent conditions can be used to (fine-) tune the resulting morphology by swelling or contracting the S block.

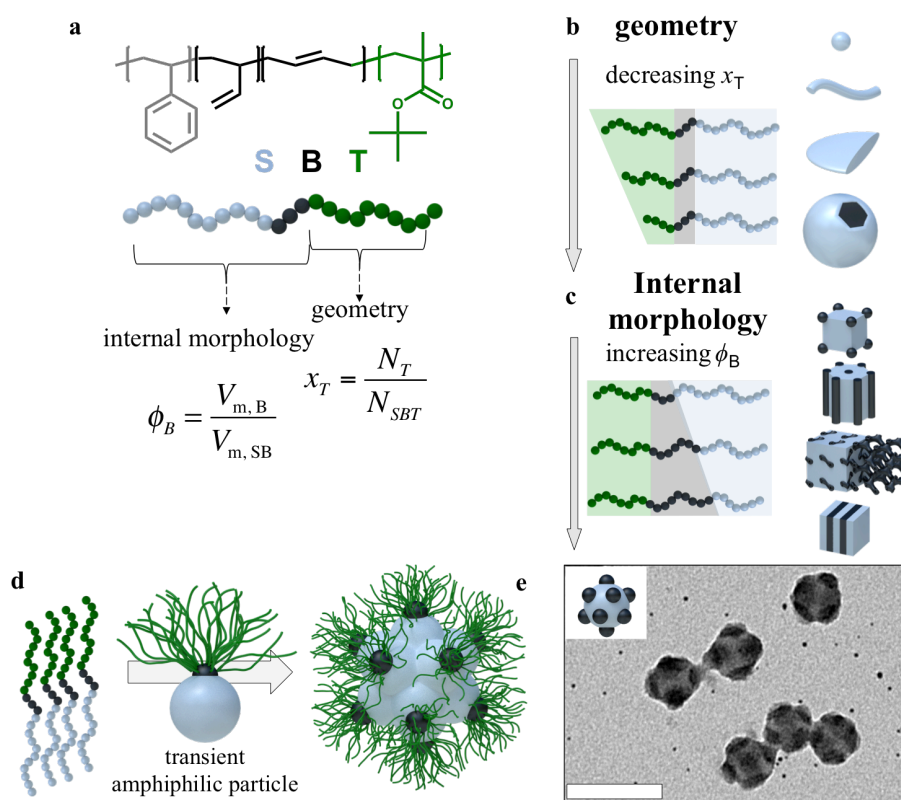


Figure 2.7. Design and Self-Assembly Concept. **a)** Chemical structure of the used SBT triblock terpolymer. The hydrophilic T block determines the overall geometry and the two hydrophobic blocks the internal morphology in the final assembly. **b)** The Geometry of the superstructure is determined by the molar fraction x_T , which is schematically shown for polymer chains with constant S/B ratios (light grey/black) and decreasing x_T (green) to give spheres, cylinders, sheets and vesicles. **c)** The morphology within the respective geometry is determined by the ratio of S/B and is supposed to phase separate according to bulk. **d)** The stepwise self-assembly protocol proceeds through transient Janus particles that aggregate into the final multicompartment morphology exemplified for spherical multicompartment micelles. **e)** Spherical MCMs of SBT with $x_T=0.31$ in 60:40 v/v acetone/isopropanol. The Scale bar denotes 100 nm and the sample is stained with OsO_4 rendering the B block dark grey, S light grey and T is not visible due to e -beam degradation.

Applying the above-mentioned concept, decreasing the corona block length leads to spherical and cylindrical micellar superstructures as well as sheets and vesicles all decorated with spherical B patches if the B volume fraction f_B is small compared to f_S . Up to now, compartmentalized cylinders and especially two-dimensional sheets and vesicles are rarely reported for linear triblock terpolymers. The evolution from cylinders with thick B patches to sheets and finally vesicles can be monitored with so far unprecedented detail. The patchy cylinders start to fuse to sheets while the B patches start to interdigitate and fuse to form B cylinders on the surface (“striped” sheets). This transformation can be clearly seen in Figure 2.8a for a striped sheet from which several cylindrical “arms” protrude carrying B patches.

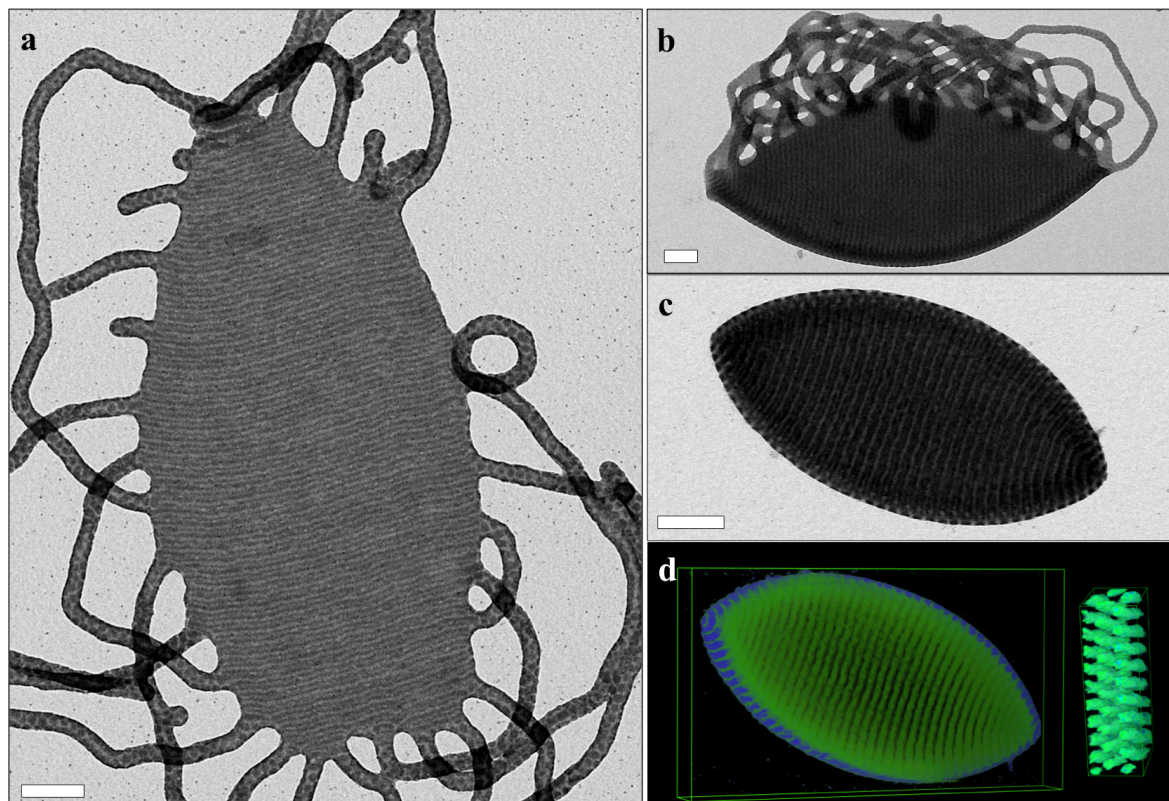


Figure 2.8. Evolution from Striped Sheet to Striped Vesicle. **a)** TEM image of a striped sheet with protruding patchy cylinders. **b)** Folded, not yet closed sheet. **c)** Final lemon-shaped, striped vesicles. **d)** A 3D reconstruction of the vesicle reveals the arrangement of cylinders on the in and on the outside of the membrane. Scale bars denote 200 nm.

When sheets grow large enough, the line energy of the edges becomes unfavourable and the sheets start to roll up to form vesicles (Figure 2.8b,c). Transmission electron tomography (ET) of one of the deflated lemon-shaped vesicles reveal the distribution of B cylinders on the in and outside of the bilayer-membrane (Figure 2.8d). The shape of the final vesicle is thereby governed by the anisotropy of B cylinders on the surface, which induces an ellipsoidal deformation with pronounced curvature on both ends.

Analogous to the previously reported transition from patchy cylinders to stripes on sheets, cylinders carrying B helices fuse into two-dimensional sheets with a gyroidal arrangement of S and B blocks (Figure 2.9a). This interpenetrating arrangement of S and B can be visualized more clearly with a 3D tomographic reconstruction as shown in Figure 2.9b. Here, only the B phase is displayed showing a porous structure that usually is filled by the S phase. However, phase separation takes place in the confined space of the bilayer sheet and hence, the gyroidal motif is cut down to a thin section making the interpretation challenging.

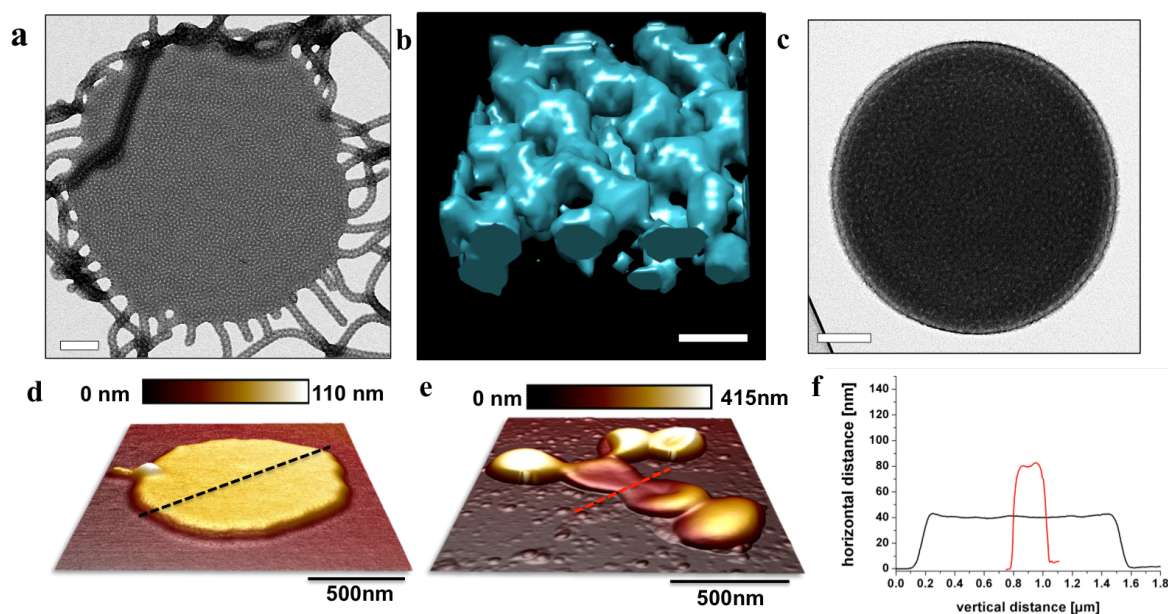


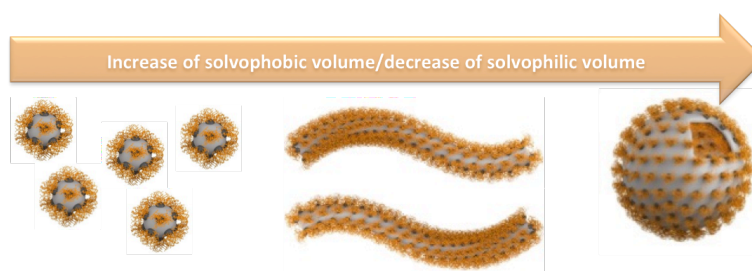
Figure 2.9. Bicontinuous Sheets and Vesicles. **a)** TEM image of helix-on-cylinder micelles that fuse together to form a perforated sheet. **b)** Isosurface model of a section of a bicontinuous sheet displaying only the B phase while S is omitted for clarity (scale bar is 25 nm). **c)** Deflated bicontinuous vesicles. All samples are stained with OsO_4 rendering B black and S light grey. The scale bar is 200 nm in the TEM images and 25 in the isosurface model. **d)** AFM height image of a bicontinuous sheet and **(e)** bicontinuous vesicles. **f)** The height analysis shows that even the deflated vesicles are at least double the height of a bilayer sheet.

This gyroid motif of the membrane is transported into the vesicle (Figure 2.9c) and we frequently observe that the final vesicles can flatten upon TEM sample preparation even without buckling, due to plasticization of the S block with acetone and the soft nature of the B phase. However, AFM height analysis proves the thickness of a vesicle is at least twice as thick as the corresponding sheet (Figure 2.9d-f).

2.4. Tuning Multicompartment Nanostructures

The morphological transition from spherical MCMs to vesicles through synthetic variation has been investigated in previous chapters. This chapter focuses on parameters that can induce a morphological change apart from synthetic pathways. A shift in morphology can be achieved through changing the solvophobic/solvophilic ratio (Scheme 2.1).

Scheme 2.1. An increase of the solvophobic volume and/or a decrease of solvophilic volume lead to a morphological transition from spherical multicompartment micelles towards polymersomes.



Variances in the resulting morphology were induced through solvent conditions, homopolymer blending and post-modification of one of the solvophobic blocks. Polystyrene-*block*-polybutadiene-*block*-poly(methyl methacrylate) (SBM) in acetone/isopropanol mixtures was used as a model system. As explained earlier in chapter 2.3, acetone plasticises and swells the S block and here, the M corona contracts at the same time upon addition of isopropanol. Proper tuning of the solvent conditions allows tuning the morphology of a single triblock terpolymer from spherical multicompartment micelles towards vesicles as demonstrated for $S_{73}B_{11}M_{16}^{74}$ (subscripts denote block weight fractions and superscript overall molecular weight in kg/mol) in Figure 2.10. Blending PS and PB homopolymers with SBM induces a shift of morphology depending on the amount of added homopolymer as the solvophobic/solvophilic ratio increases and guides the transition towards particles with decreased total interfacial area, *i.e.* from cylinders to vesicles.

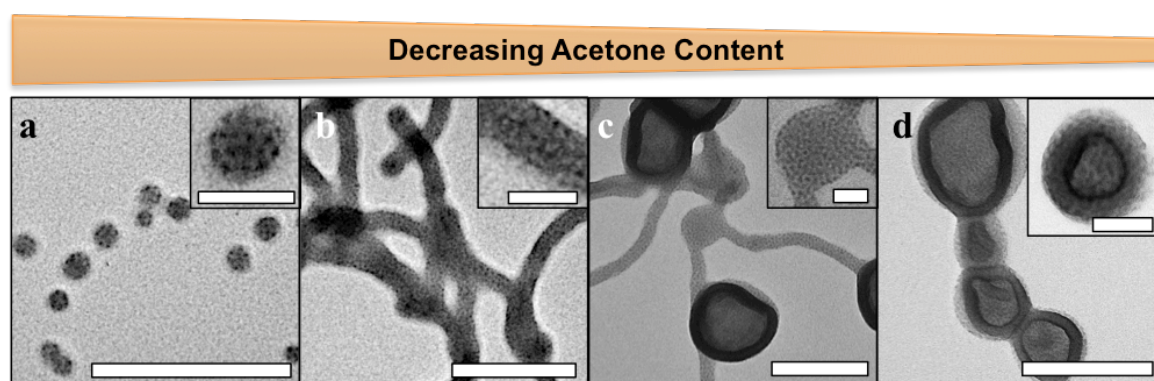


Figure 2.10. Influence of Solvent Composition on the Resulting $S_{73}B_{11}M_{16}^{74}$ Morphology. **a)** TEM image of spherical MCMs at 80:20 v/v acetone/isopropanol. **b)** Cylindrical micelles at 70:30 v/v. **c)** Compartmentalized cylinders, sheets and onset of vesicle formation at 60:40 v/v. **d)** Exclusively vesicles at 50:50 v/v. All samples are stained with OsO_4 rendering B as the black phase and S light grey. Scale bars denote 500 nm in the overview images and 100 nm in the insets.

The B units within SBM are accessible for post-modification. Thiol-ene click reaction of hexyl mercaptan was performed to increase the volume of the B phase and induce a morphological transition from a mixture of compartmentalized cylinders and vesicles to exclusively vesicles carrying hexyl-modified B cylinders on the surface. We demonstrated that besides synthetically controlled block length, non-synthetic methods such as solvent conditions or blending with homopolymer are suitable to precisely targeted multicompartment micelles of triblock terpolymers.

2.5. Bulk Phase Behavior of Polystyrene-*block*-Polybutadiene-*block*-Poly(*tert*-butyl methacrylate) Triblock Terpolymers

To complete the structure-morphology relationship of SBT, this chapter deals with the bulk morphologies of the SBT triblock terpolymers synthesized for Chapter 2.3. In total 16 SBT triblock terpolymers with different block volume fractions, ϕ_S , ϕ_B and ϕ_T , were synthesized *via* sequential living anionic polymerization and their bulk morphologies were investigated by means of TEM and SAXS. The resulting phase diagram in Figure 2.11 shows the phase

behaviour of SBT with four distinct morphologies. The morphologies range from lamella-lamella (Figure 2.11 green area), core-shell cylinder (Figure 2.11 blue area), core-shell gyroid morphology (Figure 2.11 yellow area) to a cylinder-in-lamella phase (Figure 2.11 orange area).

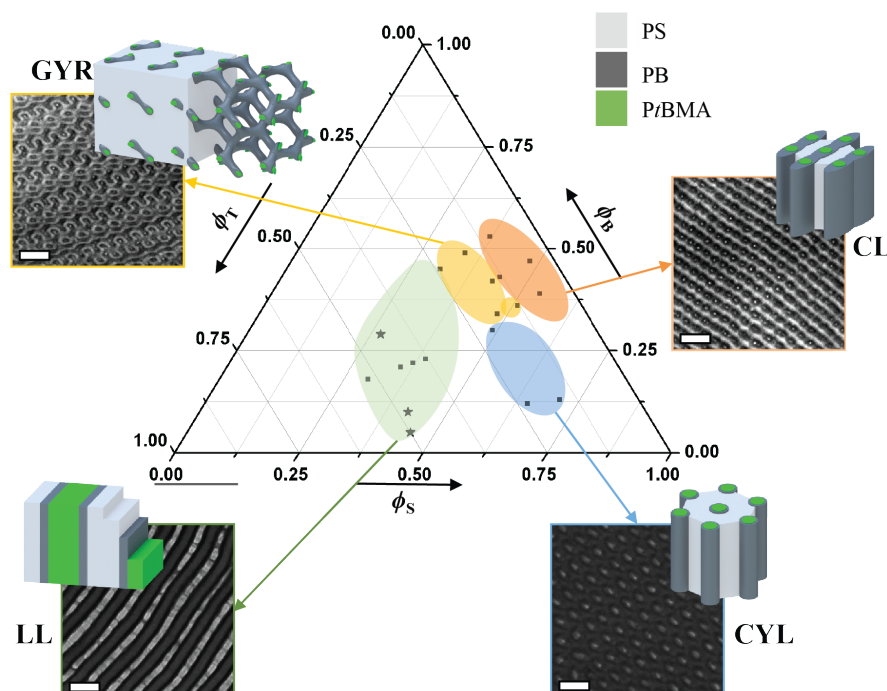


Figure 2.11: SBT phase diagram. The colored areas mark regions of the same morphology: **blue:** core-shell cylinder; **green:** lamella-lamella (stars denote literature values); **orange:** cylinder-in-lamella; **yellow:** core-shell gyroid. All phases are exemplified in TEM images with frames in corresponding colors. The scale bars are 100 nm.

The observed straightforward phase behaviour of SBT is a direct result from the large differences in the segment-segment incompatibilities described by the Flory-Huggins interaction parameter, χ , of S/T ($\chi_{ST} = 0.025$) and B/T ($\chi_{BT} = 0.007$). The higher enthalpic penalties at the S/B and S/T interface cause B to preferably spread on T adopting the T geometry. As a result, the morphology is mostly determined by the two end blocks S and T whereas the B block can adopt a wide range of volume fractions without changing the morphology. This phase behaviour, achieved by thoroughly encoding polymer-polymer interaction parameters into the triblock terpolymer, is interesting because morphologies that are usually only in a small stability region like the core-shell gyroid adopt a broader region. Consequently, these morphologies are synthetically easier to target.

2.6. Janus Nanoparticles Compatibilize Immiscible Polymer Blends under Technologically Relevant Conditions

This chapter comprises the large-scale synthesis and application of Janus nanoparticles as compatibilizer in immiscible polymer blends. The focus was put on the compatibilization of poly(2,6-dimethyl-1,4-phenylene ether) (PPE) with poly(styrene-*co*-acrylonitrile) (SAN) as a technologically relevant polymer blend in a large-scale industry extruder with a

throughput of 1 kg/h. In general, the aim for all polymer blends is the facile and economic combination of the properties of the single components into one material. For PPE/SAN this is the heat resistance and dimensional stability in PPE in combination with the stiffness and easy processability of SAN. The immiscibility of the PPE/SAN blend, however, requires the use of a compatibilizer to prevent coagulation of polymer droplets and the formation of irregular co-continuous structures in the final material. In the work presented here, Janus particles (JPs) made from polystyrene-*block*-polybutadiene-*block*-poly(methyl methacrylate) (SBM) triblock terpolymers were used as suitable compatibilizers, as the PS block is fully miscible with PPE and the PMMA block is compatible with SAN (Figure 2.12).

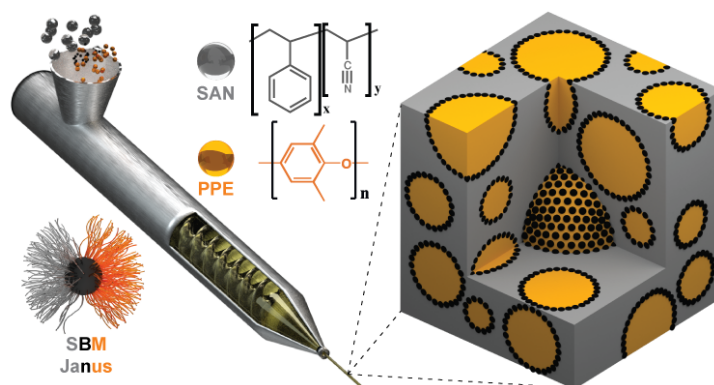


Figure 2.12: Schematic overview of polymer blend extrusion with Janus nanoparticles. Within the extrusion experiment, the PPE droplets (yellow) are stabilized by the Janus particles (black dots) in the SAN (grey) matrix.

For the first time, Janus particles were synthesized in large enough quantities (200 g) to enable blend experiments on a technologically relevant scale. A solution based protocol, developed in our group was upscaled to yield 100 g of Janus micelles per batch. Therefore, the SBM triblock terpolymer is first dissolved in THF and dialyzed against 60:40 v/v acetone/isopropanol mixture which induces the formation of multicompart ment micelles (MCMs) consisting of a PS core, patches of PB and a stabilizing corona of PMMA. In this state the PS/PMMA chains are fully phase-separated and can be locked by cross-linking of the PB double bonds with a photoinitiator. After precipitation, the Janus particles can be dried, cryo-milled and then used in the blend experiments.

After mixing PPE and SAN (60/40 w/w) with 10 wt.-% of JPs, an industry-scale Brabender twin-screw extruder was used for extrusion. To compare the effect of JPs on the resulting blend morphology, the neat blend as well as PPE/SAN mixed with 10 wt.-% of an SBM triblock terpolymer were extruded. Figure 2.13 shows TEM micrographs and schematics of the neat PPE/SAN blend (60/40 w/w) without compatibilization, with 10 wt.-% SBM triblock terpolymer and with 10 wt.-% JPs. A clear transition from irregular shaped PPE droplets (dark phase) in the neat blend towards a small drop morphology with addition of JPs was achieved, which is significantly smaller than the SBM triblock terpolymer compatibilized sample. The average droplet radii of the neat as well as SBM compatibilized blends are around 600 nm, whereas the JPs stabilize PPE droplets with only 150 nm.

We relate this improved behavior to an increased interfacial activity of JPs attributed to the Pickering effect. Also more regular droplets are achieved through addition of SBM triblock terpolymer, one can clearly see inclusions of the terpolymer in the SAN or PPE phase resulting from the formation of micelles within the one or the other phase.

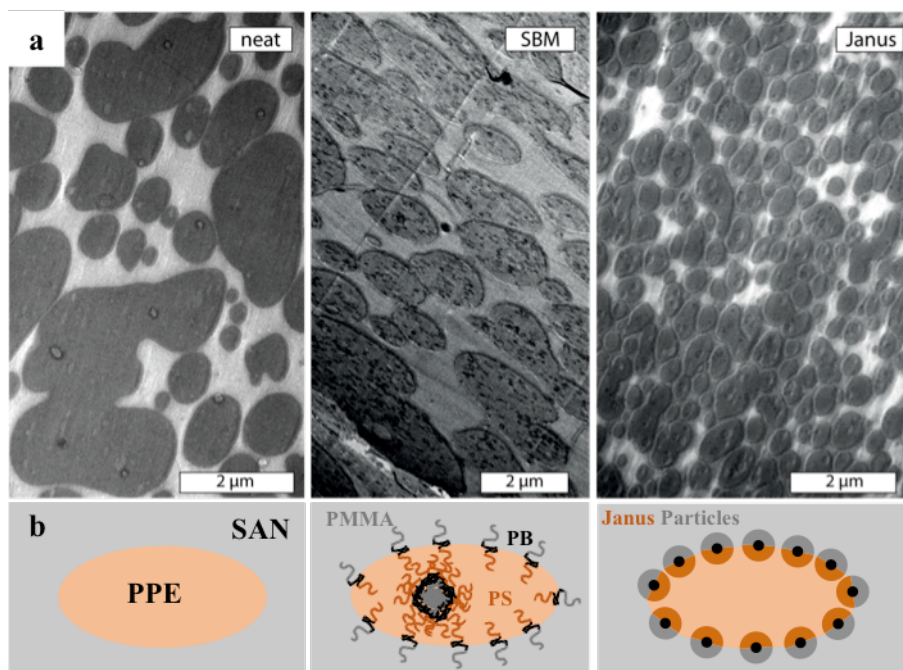


Figure 2.13: Impact of compatibilizer on blend morphology. **a)** TEM micrographs of the neat PPE/SAN blend (60/40 w/w), compatibilized with 10 wt.-% SBM and with 10 wt.-% JPs (slight contrast differences originate from varying film thicknesses). **b)** Schematics of a PPE droplet in SAN matrix without compatibilization, with SBM triblock terpolymer chains showing micelle formation and with JPs at the interface.

TEM images of the blend with 10 wt.-% JP show a morphology that is reminiscent of a double emulsion, with SAN inclusions in PPE droplets which we assume to originate from an excess of JPs so that an additional interface is built to satisfy the stabilization capability of the JPs in the system. To find an optimal, economic amount of compatibilizer for sufficiently small drop morphology, a series of experiments were performed with varying JP content between 0.5-10 wt.-%. The optimum JP fraction is in the range of 2-5 wt.-% where small droplets form but no double emulsion is present. Blend experiments on a lab-scale mini-compounder with low shear forces result in entirely different co-continuous morphology. The low shear force is not able to break up the PPE phase into droplets, which demonstrates the importance of large-scale studies for future work.

2.7. Individual Contributions to Joint Publications

The publications were achieved in collaboration with other researchers and listed below. In the following, the individual contributions of all co-authors are specified. † denotes that authors contributed equally to the work and asterisk(s) mark the corresponding author(s).

Chapter 3:

This work has been published in *Macromolecules* 46, pp. 6466-6474 (2013) under the title:

“Micellar Interpolelectrolyte Complexes with a Compartmentalized Shell”

by Christopher V. Synatschke[†], Tina I. Löbling[†], Melanie Förtsch, Andreas Hanisch, Felix H. Schacher* and Axel H. E. Müller*

I performed all experiments, was involved in planning of the experiments and corrected the manuscript. Exceptions are as followings:

C.V. Synatschke synthesized the BVT triblock terpolymer, co-designed experiments and wrote the manuscript.

M. Förtsch performed cryo-TEM measurements.

A. Hanisch assisted with BVT synthesis and corrected the manuscript.

F.H. Schacher and A.H.E. Müller were involved in scientific discussions and corrected the manuscript.

Chapter 4:

This work has been published in *ACS Nano* 8, pp. 11330-11340 (2014) under the title:

“Hidden Structural Features of Multicompartment Micelles Revealed by Cryogenic Transmission Electron Tomography”

by Tina I. Löbling[†], Johannes Haataja[†], Christopher V. Synatschke, Felix H. Schacher, Melanie Müller, Andreas Hanisch, André H. Gröschel* and Axel H. E. Müller*

I performed all experiments, was involved in planning of the experiments and wrote the manuscript. Exceptions are as followings:

J. Haataja performed cryogenic Transmission Electron Tomography and corrected on the manuscript.

C.V. Synatschke synthesized the BVT triblock terpolymer and corrected the manuscript.

F.H. Schacher corrected the manuscript.

M. Müller performed some cryo-TEM measurements.

A. Hanisch assisted with BVT synthesis and corrected the manuscript.

A.H. Gröschel co-designed experiments, discussed results and wrote the manuscript.

A.H.E. Müller was involved in scientific discussions and corrected the manuscript.

Chapter 5:

This work was accepted in *Nature Communications* under the title:

“Rational Design of ABC Triblock Terpolymer Solution Nanostructures with Controlled Patch Morphology”

by Tina I. Löbbling, Oleg Borisov, Johannes S. Haataja, Olli Ikkala*, André H. Gröschel* and Axel H. E. Müller*

I synthesized all polymers, planned and performed all experiments, Transmission Electron Tomography and wrote the manuscript. Exceptions are as followings:

O. Borisov developed the theory, was involved in scientific discussions and wrote parts of the manuscript

J. Haataja assisted with Transmission Electron Tomography, performed cryo-TEM measurements and corrected on the manuscript.

A.H. Gröschel performed SEM measurements, some of the TEM measurements, was involved in planning the experiments, discussed results and wrote the manuscript.

O. Ikkala and A.H.E. Müller were involved in scientific discussions and corrected the manuscript.

Chapter 6:

This work is submitted to *ACS Macro Letters* under the title:

“Control of Multicompartment Nanostructures of Linear Triblock Terpolymers by Post-Polymerization Processes”

by Tina I. Löbbling, Olli Ikkala, André H. Gröschel* and Axel H. E. Müller*

I conceived the project, performed all experiments and wrote the manuscript. Exceptions are as followings:

A.H. Gröschel, A.H.E. Müller and O. Ikkala were involved in scientific discussions and corrected the manuscript.

Chapter 7:

This work was published in *Polymer* 72, pp. 479-489 (2015) under the title:

“Bulk Morphologies of Polystyrene-*block*-Polybutadiene-*block*-Poly(*tert*-butyl methacrylate) Triblock Terpolymers”

by Tina I. Löbbling, Panu Hiekkataipale, Andreas Hanisch, Francesca Bennet, Holger Schmalz, Olli Ikkala, André H. Gröschel* and Axel H. E. Müller*

I synthesized most of the polymers, performed all experiments and wrote the manuscript. Exceptions are as followings:

P. Hiekkataipale performed SAXS measurements.

A. Hanisch and F. Bennet synthesized four polymers and corrected the manuscript.

H. Schmalz synthesized one polymer and corrected the manuscript.

O. Ikkala corrected the manuscript.

A.H. Gröschel and A.H.E. Müller were involved in scientific discussions and corrected the manuscript.

Chapter 8:

This work was published in *ACS Nano* 8, pp. 10048-10056 (2014) under the title:

“The Impact of Janus Nanoparticles on the Compatibilization of Immiscible Polymer Blends under Technologically Relevant Conditions”

by Ronak Bahrami¹, Tina I. Löbbling¹, André H. Gröschel, Holger Schmalz, Axel H. E. Müller* and Volker Altstädt*

I synthesized Janus particles, co-designed experiments and wrote part of the manuscript. Exceptions are as followings:

R. Bahrami performed blend experiments and wrote part of the manuscript.

A.H. Gröschel discussed the results, planned experiments and wrote the manuscript.

H. Schmalz was involved in scientific discussions and corrected the manuscript.

A.H.E. Müller and V. Altstädt were involved in scientific discussions and corrected the manuscript.

Chapter 3

Micellar Interpolyelectrolyte Complexes With a Compartmentalized Shell

Christopher V. Synatschke,^{a,†} Tina I. Löbling,^{a,†} Melanie Förtsch,^a Andreas Hanisch,^a

Felix H. Schacher,^{*,b} and Axel H. E. Müller^{*,a,c}

^a Makromolekulare Chemie II und Bayreuther Zentrum für Kolloide und Grenzflächen, Universität Bayreuth, D-95440 Bayreuth, Germany.

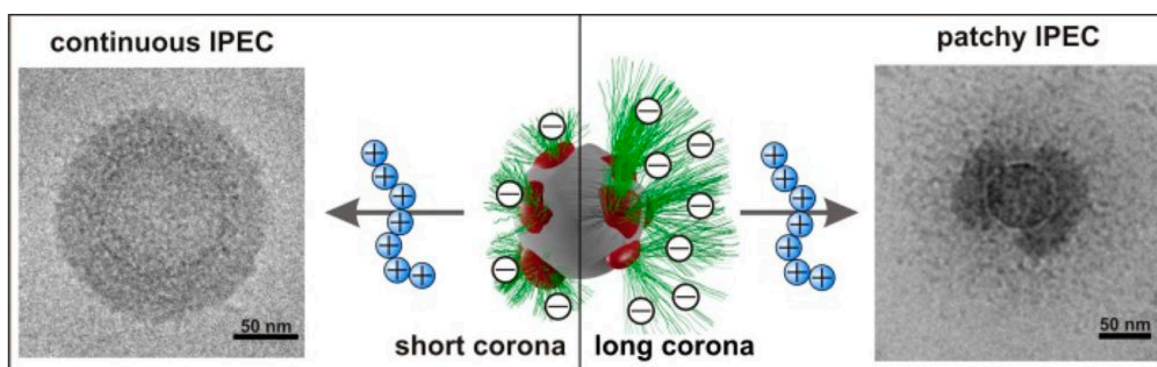
^b Institut für Organische Chemie und Makromolekulare Chemie and Jena Center for Soft Matter (JCSM), Friedrich-Schiller-Universität Jena, Humboldtstraße 10, D-07743 Jena, Germany.

E-mail: felix.schacher@uni-jena.de

^c Present address: Institut für Organische Chemie, Johannes Gutenberg-Universität Mainz, D-55099 Mainz, Germany.

E-Mail: axel.mueller@uni-mainz.de

[†] Both authors contributed equally to this work



Published in: *Macromolecules*, **2013**, 46, 6466-6474

Abstract

We investigate the formation of micellar interpolyelectrolyte complexes (IPECs) from multicompartment micelles of polybutadiene-*block*-poly(1-methyl-2-vinylpyridinium methylsulfate)-*block*-poly(methacrylic acid) (BVqMAA) triblock terpolymers and polycations of opposite charge. As cationic material, predominantly a polymer with a high charge density is used: quaternized poly(2-((2-(dimethylamino)ethyl)methyl-amino)ethyl methacrylate) (PDAMAq), which carries two positive net charges per monomer unit. Upon IPEC formation at different charge stoichiometries, particles with a compartmentalized IPEC shell are formed. These rather unusual structures even form when both BVqMAA micelles and PDAMAq are mixed at rather high salinity, followed by dialysis, indicating that the structures formed are not kinetically trapped. Whereas the nature of the polycation seems to play a minor role, our studies suggest that the length of the PMAA corona is the key factor for the formation of a compartmentalized IPEC shell.

Introduction

Block copolymers have the ability to form a great variety of nanostructures both in the bulk and in solution through microphase separation originating from the intrinsic immiscibility between different polymer chains.¹ Understanding and controlling such self-assembly processes allows for the preparation of functional materials for various kinds of applications.² Some of these materials have been known for several decades, for example the use of ABA-type block copolymers as thermoplastic elastomers (Kraton) or as polymeric emulsifiers (Pluronic). In recent years, other fields have also demonstrated the potential of block copolymer nanostructures for different purposes. As such, semiconducting polymers with precisely tuned bandgaps can act as organic solar cells, transforming light into electricity or in the reverse process as organic light emitting diodes.³ Also, thin films of block copolymers have been used as templates for the deposition of inorganic materials⁴ and in lithographic applications,⁵ where well-defined domain sizes and periodic structures are desirable.^{6,7} In solution, block copolymers form well-defined micelles or vesicles, depending on the volume fraction of solvophobic and solvophilic segments. Apart from studying the underlying principles of structure formation,⁸ such particular systems have already been extensively used for the transportation of therapeutic cargos in biomedical applications. Often, hydrophobic drug molecules are enclosed in the core of such micelles, thereby enhancing solubility, circulation time, and bio-availability at the same time.⁹ Further, ionic cargo such as plasmid DNA,¹⁰⁻¹² small interference RNA^{13,14} and photosensitizers¹⁵ have been encapsulated as well, when ionic diblock copolymers were used for micellization.

The level of structural variety and complexity of the resulting structures increases dramatically as compared to diblock copolymers when ternary or even quaternary block copolymers are considered. Already for ABC triblock terpolymers, a vast library of bulk structures has been found.^{16,17} In solution-based structures, the additional segment can lead to further segregation of core or corona. Core-segregated micelles are often termed multi-compartment micelles (MCM), and are an interesting class of materials, since they can combine different chemical environments in close proximity. Common examples for a compartmentalization of the core were achieved with triblock terpolymers containing a hydrocarbon and a fluorocarbon block.^{18,19} Janus particles can be seen as an extreme case of nanostructures with a phase separated corona, since it is strictly segregated into two hemispheres.²⁰⁻²³ MCMs are potentially useful as nanoreactors or multifunctional drug carriers, as has been reviewed recently.²⁴ Individual MCMs from triblock terpolymers can further be used as building blocks for the formation of even larger superstructures, as has been shown in a controlled manner by controlling the kinetic pathway via suitable solvent sequences.²⁵

If more than three (core, shell, corona) individual compartments within micellar structures are targeted, one possibility would be the use of ABCD tetrablock quaterpolymers. However, their synthesis is challenging and often limited to certain block sequences. We have recently shown that interpolyelectrolyte complex (IPEC) formation between charged

MCMs from amphiphilic and ampholytic triblock terpolymers and oppositely charged homopolymers or diblock copolymers can be used to generate well-defined and multi-layered soft nanoparticles. The IPEC formation is driven by both electrostatic interactions and a gain in entropy for the whole system via the release of low molecular weight counterions.^{26,27} Our initial system was based on polybutadiene-*block*-poly(1-methyl-2-vinylpyridinium)-*block*-poly(methacrylic acid) (BVqMAA) triblock terpolymers, which formed MCMs with a negatively charged poly(methacrylic acid) (PMAA) corona in aqueous media.²⁸⁻³⁰ The structures featured a soft and dynamic polybutadiene (PB) core and a patchy shell, consisting of intramicellar interpolyelectrolyte complexes (*im*-IPECs) between positively charged poly(1-methyl-2-vinylpyridinium) (P2VPq) and PMAA. We demonstrated that additional shells can be formed by adding either quaternized poly(2-(dimethylamino)ethyl methacrylate) (PDMAEMAq) or double hydrophilic block copolymers of P2VPq or PDMAEMAq with poly(ethylene oxide) (VqEO or DqEO).^{28,30} This facile approach can also be used to introduce new functionalities, *e.g.* a thermo-responsiveness, by using poly(sodium acrylate)-*block*-poly(*N*-isopropylacrylamide) as a complexing polymer to form a PNiPAAm corona to an MCM with inverse sequence of charges, polybutadiene-*block*-poly(sodium methacrylate)-*block*-poly(2-((methacryloyloxy)ethyl)trimethylammonium methylsulfate) (BMAADq).³¹

In the work presented here, we extend our concept to polycations with higher charge density, poly(2-((2-(dimethylamino)ethyl)methylamino)ethyl methacrylate) (PDAMAq), quaternized with methyl iodide, carrying two positive charges per monomer unit. Complex formation was carried out with two different BVqMAA systems, where PB and P2VPq are of the same length but with a shorter (DP = 400) and longer (DP = 1350) PMAA corona. In case of the long PMAA corona, we found rather unexpected structures with a compartmentalized IPEC shell for charge ratios, $Z_{+/-}$, below 0.7. The micellar IPECs were in all cases characterized in detail by cryogenic transmission electron microscopy (cryo-TEM) and dynamic light scattering (DLS).

Experimental Part

Materials

trans-2-[3-(4-*tert*-Butylphenyl)-2-methyl-2-propenylidene]malononitrile (DCTB, 99.0%, Aldrich), silver trifluoroacetate (AgTFA, 99.99%, Aldrich), basic aluminum oxide (Sigma-Aldrich), ammonia solution (32%, VWR International), HCl (37%, VWR International) and pH 10 buffer solution (Titrim, VWR International) with an ionic strength of approximately 0.05 M were used as received. Dioxane, methanol, isopropanol, anisole and chloroform were of analytical grade and used as received. Deuterated chloroform and deuterated water were provided by Deutero (Kastellaun, Germany). For anionic polymerization THF (Sigma-Aldrich, p.a. quality) was first distilled over CaH₂ followed by a distillation over potassium and stored under N₂ before use. Butadiene (Rießner-Gase, 2.5) was purified by passing through columns filled with molecular sieves (4 Å) and basic aluminum oxide, before condensation into a glass reactor and storage over dibutylmagne-

sium. 2-Vinylpyridine (97%, Aldrich) was de-inhibited by passing through a basic aluminium oxide column, subsequently stirred for 30 min with 2 mL of trioctylaluminium per 10 mL of 2-vinylpyridine and finally condensed to a sealable glass ampule under reduced pressure. *tert*-Butyl methacrylate (*t*BMA, 98%, Aldrich) was stirred with 0.5 mL of trioctylaluminium per 10 mL of *t*BMA for 30 min and then condensed to a sealable ampule under reduced pressure. 1,1-Diphenylethylene (DPE, Aldrich, 97%) was stirred with *sec*-Butyllithium (*sec*-BuLi) under N₂ and then distilled. *sec*-BuLi (Aldrich, 1.4 M in cyclohexane), dibutylmagnesium (Aldrich, 1M in heptane) and trioctylaluminum (Aldrich, 25 wt.% in hexane) were used as received. For the synthesis of the 2-((2-(dimethylamino)ethyl)methylamino)ethyl methacrylate (DAMA) monomer, 2-((2-(dimethylamino)ethyl)methylamino)ethanol (98%, Aldrich), methacryloyl chloride (97 %, Fluka), triethyl amine (99 %, Merck) and dry pyridine were used without further purification. RAFT polymerization was achieved with 2-(2-cyanopropyl)dithio benzoate (CPDB, 97 %, Aldrich) as chain transfer agent and azobisisobutyronitrile (AIBN, 98 %, Aldrich) as initiator, which were used without further purification. Quaternization reactions were performed with either methyl iodide (99 %, Merck) in case of PDAMA or dimethyl sulfate (Me₂SO₄, >99%, Aldrich) for 2-vinylpyridine and were used without further purification. Milli-Q water purified with a Millipore filtering system was used in all cases. For dialysis, membranes made from regenerated cellulose (Spectrum Laboratories, Spectra/Por MWCO 3.5 kDa and 12-14 kDa) were used.

Synthesis of Polybutadiene-*block*-poly(2-vinylpyridine)-*block*-poly(*tert*-butyl methacrylate) (BVT) Block Terpolymers. Sequential living anionic polymerization with *sec*-BuLi as initiator and THF as solvent in a laboratory autoclave (2.5 L) at low temperatures was used for the synthesis of BVT triblock terpolymers. The procedure was carried out analogue to our previously published procedures (see Scheme S3.1).^{16,32} During the polymerization of the *tert*-butyl methacrylate (*t*BMA) block, samples were withdrawn at different conversions, thereby creating polymers varying only in the block length of their final block, while both previous blocks are of the same length. In detail, 1.6 L of dry THF were placed in a 2.5 L laboratory autoclave (Büchi) and titrated at -20 °C with 1.6 mL of *sec*-BuLi solution (1.4 M in hexane) to remove any protic species that might terminate the polymerization and left to warm to room temperature overnight. The so-formed alkoxides exhibit stabilizing effects on the living chain end and in the case of *t*BMA well-defined polymers are accessible without addition of LiCl.³³ After cooling the reaction solution to -70 °C, 0.69 mL of *sec*-BuLi (1 eq., 9.66×10^{-4} mol) were added, followed by the addition of 63.5 mL of butadiene (41.91 g, 800 eq., 0.7748 mol) and polymerization for 8 h at -25 °C and further 2 h at -10 °C. 2-Vinylpyridine (21.68 g, 210 eq., 0.2062 mol) was added at -70 °C and stirred for 2 h, before 0.85 mL of DPE (5 eq., 4.815×10^{-3} mol) was injected and the solution stirred for 2.5 h at -50 °C. Then, at -70 °C, 167.9 g of *t*BMA (1200 eq., 1.181 mol) were added to the solution, which led to an immediate rise in the temperature to -60 °C. The reaction temperature was increased to -50 °C and approximately 1/3 of the reaction solution was withdrawn and quenched in degassed isopropanol (200 mL) after 40 min, 2 h and 8 h of reaction time, respectively. The final polymer was obtained after pre-

precipitation from THF containing butylated hydroxytoluene (BHT) as stabilizer into a 1/1 mixture of methanol and H₂O. The degrees of polymerization (DP) of each block were calculated from a combination of MALDI-ToF-MS of the polybutadiene block and ¹H NMR of the final triblock terpolymer and determined to be B₈₃₀V₁₈₀T₄₀₀ (40 min) and B₈₃₀V₁₈₀T₁₃₅₀ (8 h) for the two polymers used in this work, respectively. Size exclusion chromatography (SEC) of the two polymers showed bimodal distributions in the elution curves of both polymers (Figure S3.1), which come from a small amount of terminated BV diblock copolymer during the injection of *t*BMA monomer. The polydispersity indices (PDI) were determined to be 1.04 and 1.08 for B₈₃₀V₁₈₀T₄₀₀ and B₈₃₀V₁₈₀T₁₃₅₀, respectively.

Preparation of Polybutadiene-*block*-poly(1-methyl-2-vinylpyridinium methylsulfate)-*block*-poly(methacrylic acid) (BVqMAA) Precursor Micelles. In a typical reaction, 100 mg of the desired BVT triblock terpolymer were dissolved in 100 mL of dioxane and 200 equiv of Me₂SO₄ compared to the moles of 2-vinylpyridine units were added to the solution (Scheme S3.1). After stirring at 40 °C for 5 d, 200 equiv of HCl (concentrated HCl, 37%) per mol of *t*BMA units was added, and the mixture was refluxed at 110 °C for 24 and 48 h in case of the B₈₃₀V₁₈₀T₄₀₀ and B₈₃₀V₁₈₀T₁₃₅₀, respectively. Self-assembly of the resulting BVqMAA polymers was achieved through dialysis (MWCO = 12-14 kDa) to pH 10 buffer with an ionic strength of approximately 0.05 M over a period of at least three days.

Synthesis of 2-((2-(dimethylamino)ethyl)methylamino)ethyl methacrylate (DAMA). In a 1 L two-neck-flask equipped with a magnetic stir bar, 300 mL of dry pyridine, 67 mL of 2-((2-(dimethylamino)ethyl)methylamino)ethanol (0.414 mol, 1 equiv) and 115 mL of triethylamine (0.828 mol, 2 equiv) were mixed, sealed with a septum, and purged with argon for 30 min. Then, the reaction mixture was cooled to 0 °C and 81 mL of methacryloyl chloride (0.828 mol, 2 equiv) was added slowly *via* a dropping funnel. The reaction mixture was allowed to warm to room temperature and stirred for 24 h before excess of methacryloyl chloride was converted to isopropyl methacrylate through addition of 15 mL isopropanol. After evaporation of the volatile components, the crude product was separated *via* column-chromatography using an eluent of chloroform/methanol/concentrated ammonia in a ratio of 100/10/1. The DAMA monomer was obtained after vacuum distillation as a clear colorless liquid in rather low yields (~ 20 %) and purity was proven with ¹H NMR spectroscopy (Figure S3.2).

RAFT polymerization of DAMA. In a typical reaction 1.00 g DAMA (4.67 mmol, 200 equiv), 5.20 mg 2-(2-cyanopropyl)dithio benzoate (CPDB, 2.35 × 10⁻² mmol, 1 equiv), 1.00 mg AIBN (6.09 × 10⁻³ mmol, 0.25 equiv) and 4.00 mL anisole were placed in a round bottom flask sealed with a rubber septum and equipped with a stir bar. After purging the reaction mixture with argon for 30 min, the polymerization was started by placing the flask in an oil bath at 70 °C. Periodically, aliquots of 0.1 mL were removed with a gastight, argon-flushed syringe for ¹H NMR analysis to monitor the conversion. The reaction was stopped after 5 h and 45 min at a conversion of 42% by rapid cooling of the reaction mix-

ture to room temperature and opening to air. Purification was achieved through dialysis to THF and subsequent freeze-drying from dioxane.

Quaternization of PDAMA. For the quaternization 0.0562 g of PDAMA (0.52 mmol of nitrogen atoms) was dissolved in 10 mL of deionized water and 0.25 mL methyl iodide (4.02 mmol, 7.7 fold excess compared to nitrogen atoms) was added. The solution was stirred for at least 48 h at room temperature. Excess quaternization agent was removed by dialysis against 20:80 and 50:50 water:dioxane mixtures for two days, respectively. Afterward, the quaternized PDAMAq was freeze-dried, and from ^1H NMR measurements a degree of quaternization of 100 % was determined, as indicated by the complete shift of the corresponding signals (Figure 3.2).

Characterization

Size Exclusion Chromatography (SEC). For the PB and BV precursor polymers and BVT triblock terpolymers, an instrument equipped with four PSS-SDVgel columns (5 μm , 8×300 mm) with a porosity range from 10^2 to 10^5 Å (PSS Mainz, Germany) was used together with a differential refractometer and a UV detector at 260 nm. Measurements were performed in THF with a flow rate of 1 mL/min using toluene as internal standard at 40 °C. The system was calibrated with narrowly distributed 1,4-PB standards. SEC measurements of PDAMA were performed on a system equipped with a set of two columns (8 μm , 8×300 mm), PL-aquagel-OH and PL-aquagel-OH-30 and a differential refractometer. A mixture of 60 % H_2O with 0.01 mol/L NaH_2PO_4 and 0.1 mol/L NaN_3 at pH = 2.5 and 40 % methanol was used as eluent at an elution rate of 1 mL/min at 35 °C. PDMAEMA samples were used for calibration.

MALDI-ToF-MS. Measurements were performed on a Bruker Daltonics Reflex III instrument equipped with an N_2 Laser (337 nm) and an acceleration voltage of 20 kV in positive ion mode. Sample preparation was done according to the “dried-droplet” method. In detail, matrix (DCTB, concentration 20 mg / mL), analyte (concentration 10 mg / mL) and salt (AgTFA, concentration 10 mg / mL) were separately dissolved in THF, subsequently mixed in a ratio of 20/5/1 μL . Approximately 1 μL of the final mixture was applied to the target spot and left to dry under air.

^1H NMR. Spectra were recorded on a Bruker Ultrashield 300 machine with a 300 MHz operating frequency using either deuterated chloroform or deuterated water as solvents.

Dynamic Light Scattering (DLS). Measurements were performed on an ALV DLS/SLS-SP 5022F compact goniometer system with an ALV 5000/E cross correlator and a He-Ne laser ($\lambda = 632.8$ nm). The measurements were carried out in cylindrical scattering cells ($d = 10$ mm) at an angle of 90° . Angular-dependent light scattering experiments were performed at angles ranging from 30° to 120° with an interval of 10° . Prior to the measurements samples were passed through nylon filters (Magna, Roth) with a pore size of 5 μm to remove impurities/dust particles. The CONTIN algorithm was applied to analyze the obtained correlation functions. Apparent hydrodynamic radii (harmonic z-average ra-

dus, $\langle R_h \rangle_{z,app}$) were calculated according to the Stokes–Einstein equation and polydispersities were obtained *via* the cumulant analysis where applicable.

ζ -Potential. The zeta potential of micellar solutions was determined on a Malvern Zetasizer Nano ZS. The electrophoretic mobilities (u) were converted into zeta potentials *via* the Smoluchowski equation $\zeta = u\eta/\epsilon_0\epsilon$, where η denotes the viscosity and $\epsilon_0\epsilon$ the permittivity of the solvent (water). Values were determined in triplicate from the same sample.

Cryogenic Transmission Electron Microscopy (cryo-TEM). For cryo-TEM studies, a drop ($\sim 2 \mu\text{L}$) of the aqueous micellar solution ($c \sim 0.5 \text{ g}\times\text{L}^{-1}$) was placed on a lacey carbon-coated copper TEM grid (200 mesh, Science Services), where most of the liquid was removed with filter paper, leaving a thin film spread between the carbon coating. The specimens were shock vitrified by rapid immersion into liquid ethane in a temperature-controlled freezing unit (Zeiss Cryobox, Zeiss NTS GmbH) and cooled to approximately 90 K. The temperature was monitored and kept constant in the chamber during all of the preparation steps. After freezing the specimens they were inserted into a cryo-transfer holder (CT3500, Gatan) and transferred to a Zeiss EM922 OMEGA EFTEM instrument. Measurements were carried out at temperatures around 90 K. The microscope was operated at an acceleration voltage of 200 kV. Zero-loss filtered images ($\Delta E = 0 \text{ eV}$) were taken under reduced dose conditions. All images were recorded digitally by a bottom mounted CCD camera system (Ultrascan 1000, Gatan), and processed with a digital imaging processing system (Gatan Digital Micrograph 3.9 for GMS 1.4).

Results and Discussion

We have previously shown that polybutadiene-*block*-poly(1-methyl-2-vinylpyridinium)-*block*-poly(methacrylic acid) (BVqMAA) triblock terpolymers form multicompart ment micelles in aqueous media with a polybutadiene core, an *im*-IPEC shell consisting of P2VPq and PMAA and a negatively charged corona of PMAA (when the degree of polymerization was higher for PMAA than for P2VPq). BVqMAA with different lengths of the PMAA segment were used and further complexation with VqEO or DqEO diblock copolymers or with quaternized PDMAEMAq led to multi-layered micellar IPECs, in case of DqEO even with a clearly distinguishable second IPEC shell.^{28,30} Herein, we investigate the complexation between BVqMAA with two different lengths of the corona segment (400 and 1350 repeating units) and poly(2-((2-(dimethylamino)ethyl)methylamino)ethyl methacrylate) (PDAMAq, Scheme 3.1), a polycation carrying two positive net charges per monomer unit and with a high structural similarity to PDMAEMAq. First, we shortly describe the structure of the BVqMAA before we focus on the preparation of PDAMAq using reversible addition fragmentation transfer (RAFT) polymerization, followed by subsequent quaternization. Afterward, PDAMAq and BVqMAA are mixed at different ratios of positive to negative charges, $Z_{+/-}$, and the resulting structures are analyzed in detail with microscopic and light scattering techniques.

Characterization of the precursor micelles (BVqMAA₄₀₀ and BVqMAA₁₃₅₀)

The synthesis of the polybutadiene-*block*-poly(2-vinylpyridine)-*block*-poly(*tert*-butyl methacrylate) (BVT) triblock terpolymers has been described previously and was achieved through sequential living anionic polymerization in THF at low temperatures (see Scheme S3.1).^{16,32} However, slight termination occurred upon addition of *t*BMA, shown in the SEC traces in Figure S3.1. We expect traces of the BV diblock copolymer to be incorporated in the final micellar structures. The degrees of polymerization, DP, for each block and the characterization data of the two triblock terpolymers used for this study are given in Table 3.1. We describe materials with identical lengths of the first (PB) and second (P2VP) block, only differing in the length of the third segment, *Pt*BMA.

Table 3.1. Molecular Characterization of BVT and BVqMAA Triblock Terpolymers.

polymer ^{a)}	M _n [kg/mol]	PDI ^{d)}	block weight fractions (PB; P2VP/P2VPq; <i>Pt</i> BMA/PMAA)
B ₈₃₀ V ₁₈₀ T ₄₀₀	121 ^{b)}	1.04	0.37; 0.16; 0.47
B ₈₃₀ V ₁₈₀ T ₁₃₅₀	256 ^{b)}	1.08	0.18; 0.07; 0.75
B ₈₃₀ Vq ₁₈₀ MAA ₄₀₀	101 ^{c)}	-	0.45; 0.21; 0.34
B ₈₃₀ Vq ₁₈₀ MAA ₁₃₅₀	183 ^{c)}	-	0.24; 0.12; 0.64

^{a)}Subscripts denote the degrees of polymerization of the respective blocks. ^{b)} Calculated from a combination of MALDI-ToF-MS and ¹H NMR data. ^{c)} Calculated from degrees of polymerization without taking the counterions of P2VPq into account. ^{d)} Determined from SEC measurements with THF as eluent and linear polystyrene as calibration standard.

The transformation of BVT to BVqMAA was carried out according to procedures reported earlier.^{29,30} Briefly, the P2VP segment was quaternized using dimethyl sulfate, followed by hydrolysis of the *Pt*BMA block to yield PMAA. The respective weight fractions of the constituting blocks before and after this modification route are also shown in Table 3.1. For BVqMAA₄₀₀, the PB has the largest weight fraction (45%), followed by PMAA (34%). On the other hand, for BVqMAA₁₃₅₀, the PMAA segment with 64% has the largest weight fraction. Micelle formation was achieved through dialysis to aqueous buffer solution at pH 10, and the resulting MCMs were characterized with cryogenic transmission electron microscopy (cryo-TEM) and dynamic light scattering (DLS) (Figure 3.1).

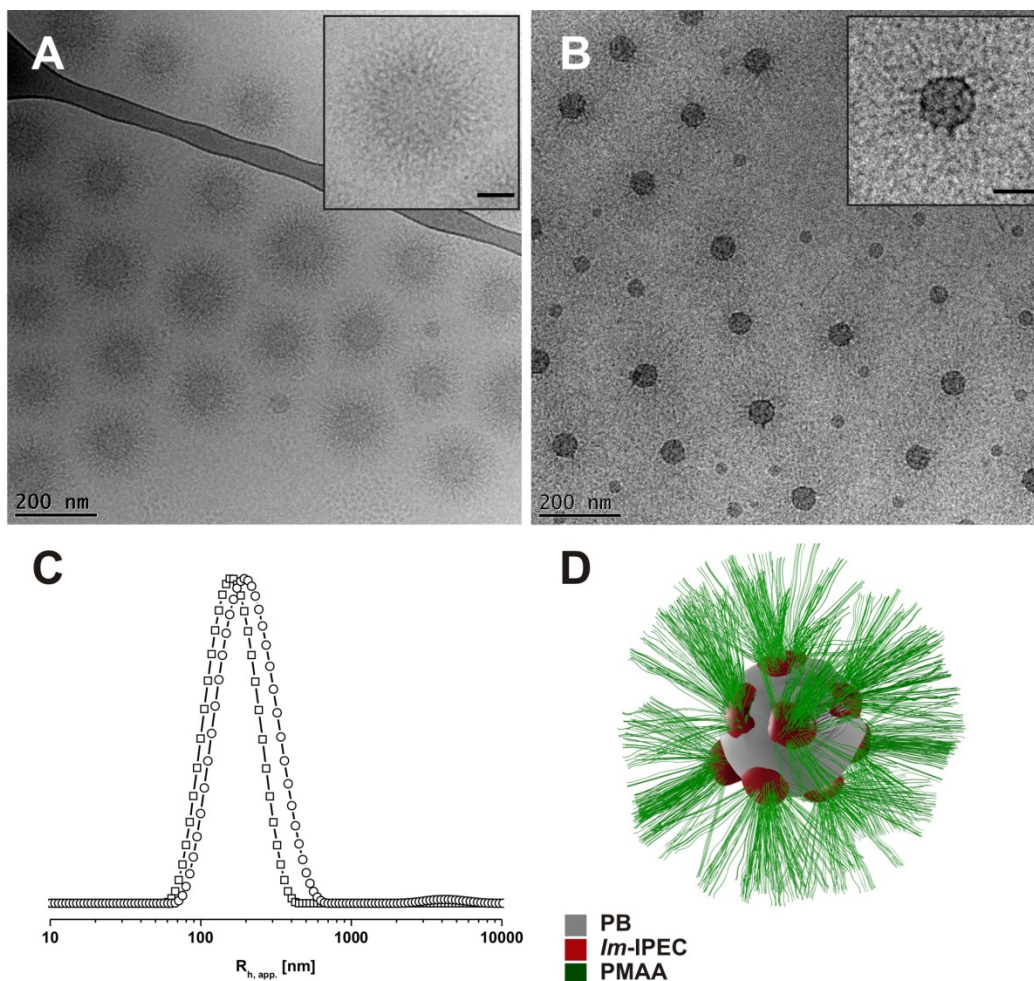


Figure 3.1. Cryo-TEM micrographs of BVqMAA₄₀₀ (**A**, concentration = 1.2 g/L) and BVqMAA₁₃₅₀ (**B**, concentration = 0.29 g/L) MCMs in pH 10 buffer with an ionic strength of ca. 0.05 M. Insets show enlargements of single micelles with the scalebar representing 50 nm. **C**) Intensity weighted CONTIN plots of the same micellar solutions from DLS measurements, BVqMAA₄₀₀, \square , $\langle R_h \rangle_{z,app.} = 164$ nm, DI = 0.14; BVqMAA₁₃₅₀, \circ , $\langle R_h \rangle_{z,app.} = 187$ nm, DI = 0.15. **D**) Schematic illustration of the proposed general MCM structure. The dimensions of individual compartments are not drawn according to scale.

Both BVqMAA₄₀₀ and BVqMAA₁₃₅₀ feature a PB core, a P2VPq/PMAA *im*-IPEC shell, and a PMAA corona, the latter being distinctly longer in case of BVqMAA₁₃₅₀. From DLS measurements, BVqMAA₄₀₀ micelles are slightly smaller with $\langle R_h \rangle_{z,app.} = 164$ nm (dispersity index, DI = 0.14) as compared to BVqMAA₁₃₅₀ with $\langle R_h \rangle_{z,app.} = 187$ nm (DI = 0.15). In case of BVqMAA₁₃₅₀, a minute fraction of aggregates at higher hydrodynamic radii can be seen. The size of the micellar core and corona was separately determined from the cryo-TEM micrographs by counting of at least 30 micelles (Table 3.2).

Table 3.2. Number-Average Compartment Sizes with Standard Deviation of the BVqMAA Micelles as Determined from cryo-TEM Micrographs

compartment	BVqMAA ₄₀₀ [nm]	BVqMAA ₁₃₅₀ [nm]
R_{micelle}	114 ± 9	128 ± 16
R_{core}	46 ± 6	31 ± 3
D_{corona}	55 ± 7	-
$R_{\text{micelle}} - R_{\text{core}}$	68	97
$N_{\text{agg.}}$	5500	1700

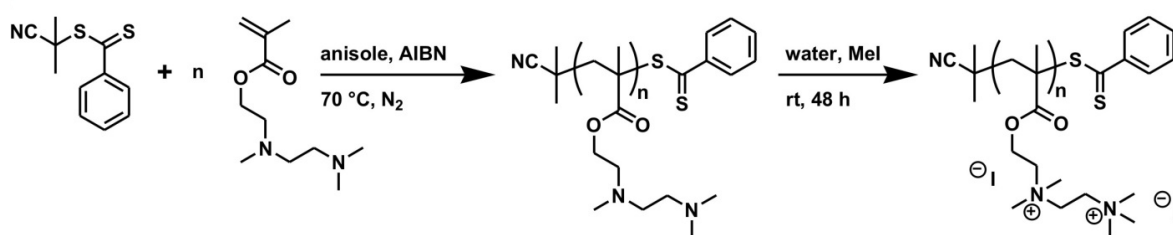
We have used the half-distance between two micellar cores in Figure 3.1 as an estimate of the micellar radius, R_{micelle} , confirming the trends from DLS measurements, although the overall sizes are smaller in cryo-TEM as compared to DLS data. This can be explained as the value from DLS represents a harmonic z-average radius, while cryo-TEM provides a number average. Furthermore, confinement of the micelles in the thin film during cryo-TEM measurements could lead to underestimation of the true micelle size in case of closely packed micelles. The core radii of BVqMAA₄₀₀ and BVqMAA₁₃₅₀ micelles differ significantly, even though the core-forming block is of the same length. BVqMAA₁₃₅₀ micelles have a core radius of 31 ± 3 nm, which is smaller than in case of BVqMAA₄₀₀ (46 ± 6 nm). From the core radius we roughly estimated the aggregation number, $N_{\text{agg.}}$, according to eq 3.1, where we assumed the core to consist of pure PB. This assumption probably leads to an overestimation of the true $N_{\text{agg.}}$ since we did not take solvent molecules (*e.g.*, dioxane) into account, which might be still trapped inside the core. Since we are mainly interested in the relative values of the two micelles the possible errors will cancel.

$$N_{\text{agg.}} = \frac{m_{\text{core}}}{m_{\text{PB}}^{\text{chain}}} = \frac{4 \cdot \pi \cdot N_A \cdot \rho_{\text{PB}} \cdot R_{\text{core}}^3}{3 \cdot M_{\text{PB}}^{\text{chain}}} \quad (3.1)$$

The calculated $N_{\text{agg.}}$ of BVqMAA₄₀₀ is approximately more than three times larger than that of BVqMAA₁₃₅₀. This is in accordance with theoretical prediction and our previous studies, where $N_{\text{agg.}}$ also decreased with increasing corona length.^{30,34} Because of the rather weak contrast, it was only possible to roughly determine the corona size of BVqMAA₄₀₀, but not that of BVqMAA₁₃₅₀. However, when subtracting R_{core} from the overall micelle radius, R_{micelle} , one can obtain an estimate of the corona size. Not surprisingly, this is considerably larger for BVqMAA₁₃₅₀ than for BVqMAA₄₀₀, by about 30 nm, highlighting the difference in hydrophilicity between the two triblock terpolymers presented here.

Synthesis of PDAMA

In comparison to our previous work using PDMAEMAq for further IPEC formation, here we were interested in polycations of similar structure, but with higher charge density. Poly(2-((2-(dimethylamino)ethyl)methylamino)-ethyl methacrylate) (PDAMA, Scheme 3.1) carries two amino groups per monomer unit. We were particularly interested in structural characteristics of micellar IPEC layers formed between PDAMAq and PMAA where we would expect a change in the IPEC compartment to a more dense structure due to the higher charge density in PDAMAq. The synthesis of PDAMA was first described by Sherrington *et. al.* by free radical polymerization and used as a chelating agent and polymeric support for copper complexes in the catalytic decomposition of the nerve agent Sarin.³⁵ Homo- and copolymers of PDAMA have already been used as non-viral gene transfection agents.³⁶⁻³⁸



Scheme 3.1. RAFT polymerization of DAMA and quaternization of PDAMA.

We used RAFT polymerization to synthesize PDAMA of desired molecular weight. 2-(2-Cyanopropyl) dithiobenzoate (CPDB) was used as chain transfer agent (CTA) with AIBN as initiator in anisole as solvent, shown in Scheme 3.1. The DAMA/CTA/AIBN ratio was 200/1/0.25; the polymerization was conducted at 70 °C. After an induction period of about 50 min the polymerization started and the linearity of the first-order time-conversion plot (Figure S3.3) indicates a controlled polymerization. The reaction was quenched after 5.5 h, and a conversion of 42% was determined from NMR measurements corresponding to a theoretical DP of 83 for PDAMA ($M_{n,theor.} = 17\,900$ g/mol). SEC measurements of the resulting material proved to be rather difficult, presumably due to strong interaction of PDAMA with the column material in THF, DMF, and DMAc as solvents. Even with a water/methanol mixture as eluent the interaction between column material and analyte was probably not fully suppressed and when using a PDMAEMA calibration a large deviation between theoretical and apparent molecular weight ($M_{n,app.} = 65\,500$ g/mol; $M_{w,app.} = 97\,400$ g/mol; PDI = 1.48) was observed. We therefore used the molecular weight of 17 900 g/mol calculated from conversion for the further description of PDAMA. Quaternization to PDAMAq was carried out by methylation of both tertiary nitrogens with methyl iodide. The ¹H NMR spectra before and after quaternization are given in Figure 3.2. Full quaternization was achieved, as can be seen from the complete shift of the -CH₃ signals e and h (9 protons at 2.0-2.3 ppm to 15 protons at 3.1-3.6 ppm) and -CH₂- signals g, f and d (6 protons at 2.3-2.8 ppm to 6 protons at 3.8-4.3 ppm).

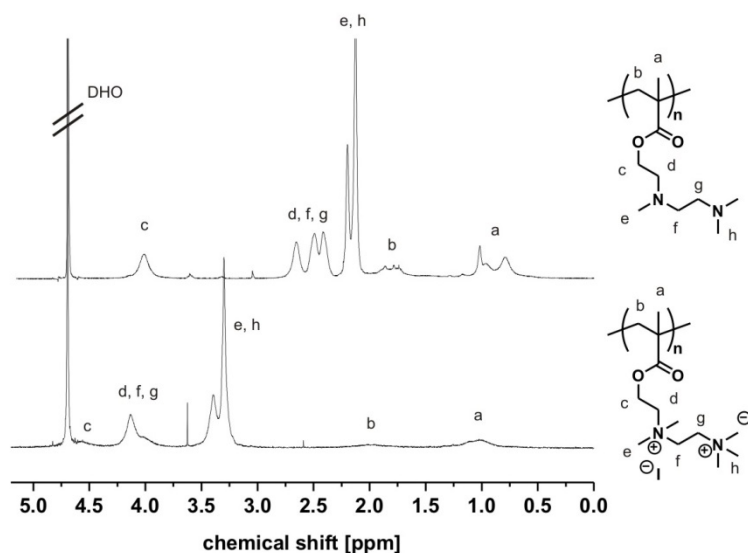


Figure 3.2. ^1H NMR spectra of PDAMA before (top) and after quaternization (bottom) in DHO.

Micellar IPECs of BVqMAA₁₃₅₀ with PDAMAq

We first mixed PDAMAq with BVqMAA₁₃₅₀ micelles in pH 10 buffer solution, where PMAA is completely dissociated. The mixing ratio $Z_{+/-}$ is defined as the number of positive charges from the added polycation divided by the number of residual negative charges in the BVqMAA micelles (eq 3.2). The total amount of MAA units in the corona of the BVqMAA₁₃₅₀ micelles is reduced to 1170 by the *im*-IPEC formation with the 180 P2VPq units of the middle block. Therefore, $Z_{+/-} = 0$ refers to the pure BVqMAA₁₃₅₀ precursor micelles, while a ratio of 1 assumes that all MAA units are complexed.

$$Z_{+/-} = \frac{n_{\text{cationic}}}{n_{\text{anionic}}} = \frac{2 \cdot n_{\text{PDAMAq}}}{n_{\text{MAA}} - N_{\text{Vq}}} \quad (3.2)$$

In the past, we observed remarkably slow kinetics for the IPEC formation when poly(1-methyl-2-vinylpyridinium methylsulfate)-*block*-poly(ethylene oxide) (VqEO) was used for complexation.²⁸ To ensure that complex formation was complete, here, the micellar IPECs were stirred for at least one week after the addition of PDAMAq. Subsequently, the structures were analyzed using a combination of cryo-TEM and DLS (Figure 3.3). Stable micellar solutions were obtained for $Z_{+/-} \leq 0.75$, while macroscopic precipitation occurred at $Z_{+/-} = 0.9$, probably due to insufficient stabilization of the particles by PMAA. Zeta potential measurements of the micellar solutions in pH 10 buffer solution gave strongly negative values below -30 mV for all $Z_{+/-}$ values, ranging from 0 to 0.75 (see Table S3.1), indicating that sufficient uncomplexed PMAA remains in the corona to stabilize the micelles. According to the cryo-TEM micrographs, low charge ratios ($Z_{+/-} = 0.1$) lead to a slight increase in the overall contrast within the corona, and the occurrence of small protrusions, attributed to IPEC compartments (Figure 3.3A, the inset shows a single object). More drastic structural changes can be seen at $Z_{+/-} = 0.25$, where newly formed IPEC

patches can be clearly distinguished (Figure 3.3B). We expect these patches to consist of IPECs of PMAA and PDAMAq, collapsed due to charge neutralization, in analogy to earlier observations using PDMAEMAq.³⁰ However, instead of observing a rather homogeneous IPEC shell as before, distinct patches of a certain size are found. The proposed structure of such micellar IPECs with a patchy second IPEC shell is schematically illustrated in Figure 3E. With increasing $Z_{+/-}$, the patch size increases, as is expected for a further incorporation of PDAMAq chains. However, growth of the patches seems to proceed anisotropically along the *im*-IPEC/corona interface rather than radially outwards from the original patch. This is most prominent at $Z_{+/-} = 0.5$ (Figure 3.3C), where up to 3 patches per particle can be observed.

To better illustrate the growth of the patchy compartments with increasing $Z_{+/-}$ values, we counted the micelles from the available cryo-TEM images and sorted them into four categories (Table S3.2) according to their compartment size. The four categories used are no visible compartment, small compartment(s) enclosing less than half of the core, large compartment(s) enclosing more than half of the core and a complete shell. At low $Z_{+/-}$ values, only small compartments are formed, which grow in size with increasing amounts of added PDAMAq. When even more PDAMAq was added ($Z_{+/-} = 0.75$, Figure 3.3D), the majority of the structures features a complete second IPEC shell. In DLS experiments, Γ versus q^2 plots gave a linear relationship for all tested $Z_{+/-}$ values (Figure S3.4) and the autocorrelation functions decreased monotonously (Figure S3.5). The $\langle R_h \rangle_{z,app.}$ at a scattering angle of 90° first decreases from 187 nm for $Z_{+/-} = 0$ (Figure 3.1) to 116 nm at $Z_{+/-} = 0.5$, while it again increases to 182 nm at $Z_{+/-} = 0.75$ (Figure 3.3F). The initial decrease is probably a result of corona contraction, while the increase of $\langle R_h \rangle_{z,app.}$ and the dispersity index, DI, at higher $Z_{+/-}$ -ratios hints towards some aggregation.

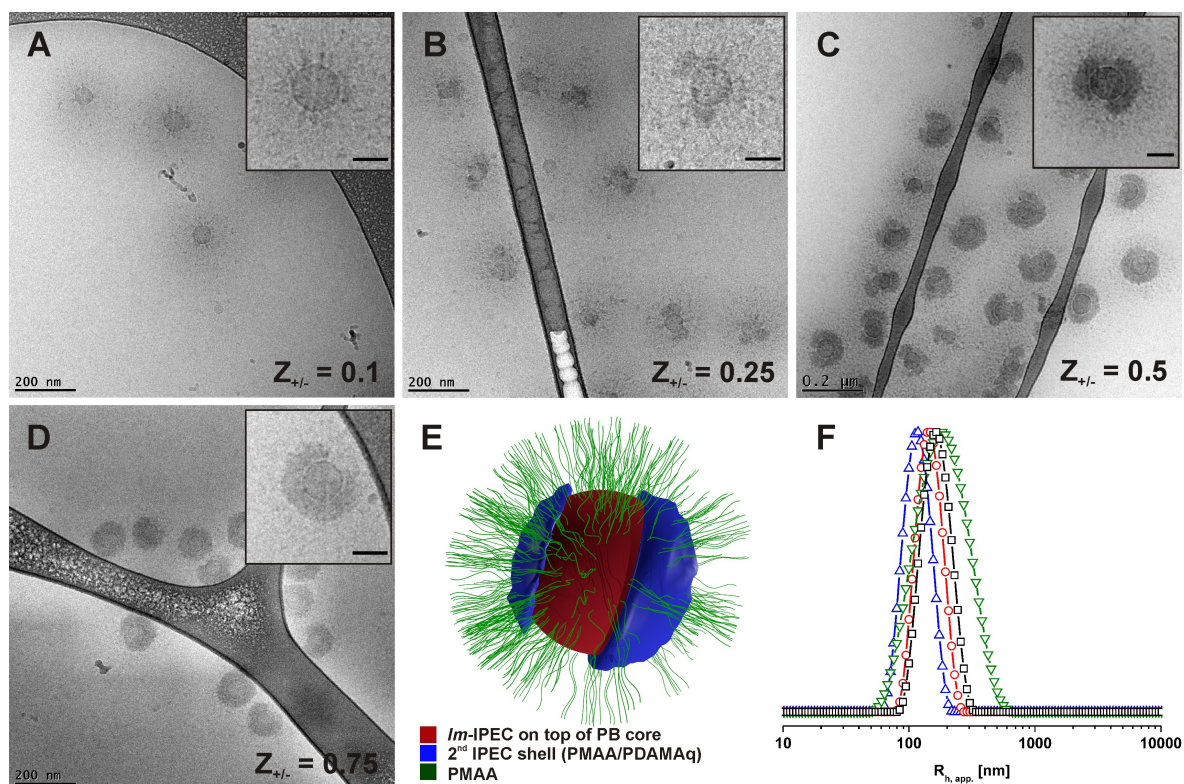


Figure 3.3. A-D) Cryo-TEM micrographs of micellar IPECs of BVqMAA₁₃₅₀/PDAMAq with increasing charge ratios, $Z_{+/-} = 0.1, 0.25, 0.5$ and 0.75 in pH 10 buffer and an ionic strength of ca. 0.05 M; the scale bars represent 200 nm. The insets show single objects at higher magnification, the scale bars representing 50 nm. E) Schematic representation of the proposed general structure of the micellar IPECs with two patches. F) DLS CONTIN plots of micellar IPECs at different $Z_{+/-}$ (black \square : $Z_{+/-} = 0.1$, $\langle R_h \rangle_{z,app.} = 166$ nm, DI = 0.07; red \circ : $Z_{+/-} = 0.25$, $\langle R_h \rangle_{z,app.} = 145$ nm, DI = 0.05; blue \triangle : $Z_{+/-} = 0.5$, $\langle R_h \rangle_{z,app.} = 116$ nm, DI = 0.06; green ∇ : $Z_{+/-} = 0.75$, $\langle R_h \rangle_{z,app.} = 182$ nm, DI = 0.18).

The spontaneous formation of anisotropic structures from a centrosymmetric precursor MCM through ionic interactions is rather unexpected. One possible explanation could be that the structures are kinetically trapped due to rapid initial IPEC formation as has been observed for BVqMAA micelles after the complexation with VqEO diblock copolymers.²⁸ As a result, insufficient chain mobility would prevent the relaxation to more energetically favorable structures, *i.e.*, a homogeneous distribution of the IPEC around the core. To increase chain mobility, we increased the ionic strength of micellar IPECs from BVqMAA₁₃₅₀/PDAMAq with $Z_{+/-} = 0.5$ to approximately 0.55 M through the addition of NaCl (pH 10 buffer with additional 500 mM NaCl). Under these conditions, the charges of the polyelectrolytes are screened and the IPEC shell is dissolved, resulting in a coexistence of BVqMAA₁₃₅₀ micelles and free PDAMAq chains. This is shown in Figure 3.4A, where the former patchy IPEC (PMAA/PDAMAq) has vanished and BVqMAA₁₃₅₀ micelles can be found. From these micrographs it is impossible to determine whether all PDAMAq chains are free in solution or if some PDAMAq still remains within the micellar corona. Even bare BVqMAA₁₃₅₀ micelles ($Z_{+/-} = 0$) show a certain corona contraction due to charge screening under these conditions (data not shown), resulting in similar structures in cryo-TEM. Subsequently, the same sample was dialyzed against pH 10 buffer without ad-

ditional salt, allowing the IPEC shell to be slowly formed again. After dialysis we again observed micellar IPECs with a patchy IPEC shell (Figure 3.4B) similar to the structures observed before. Consequently, the patchy IPEC structure seems to be energetically favored and is not a result of kinetic trapping effects.

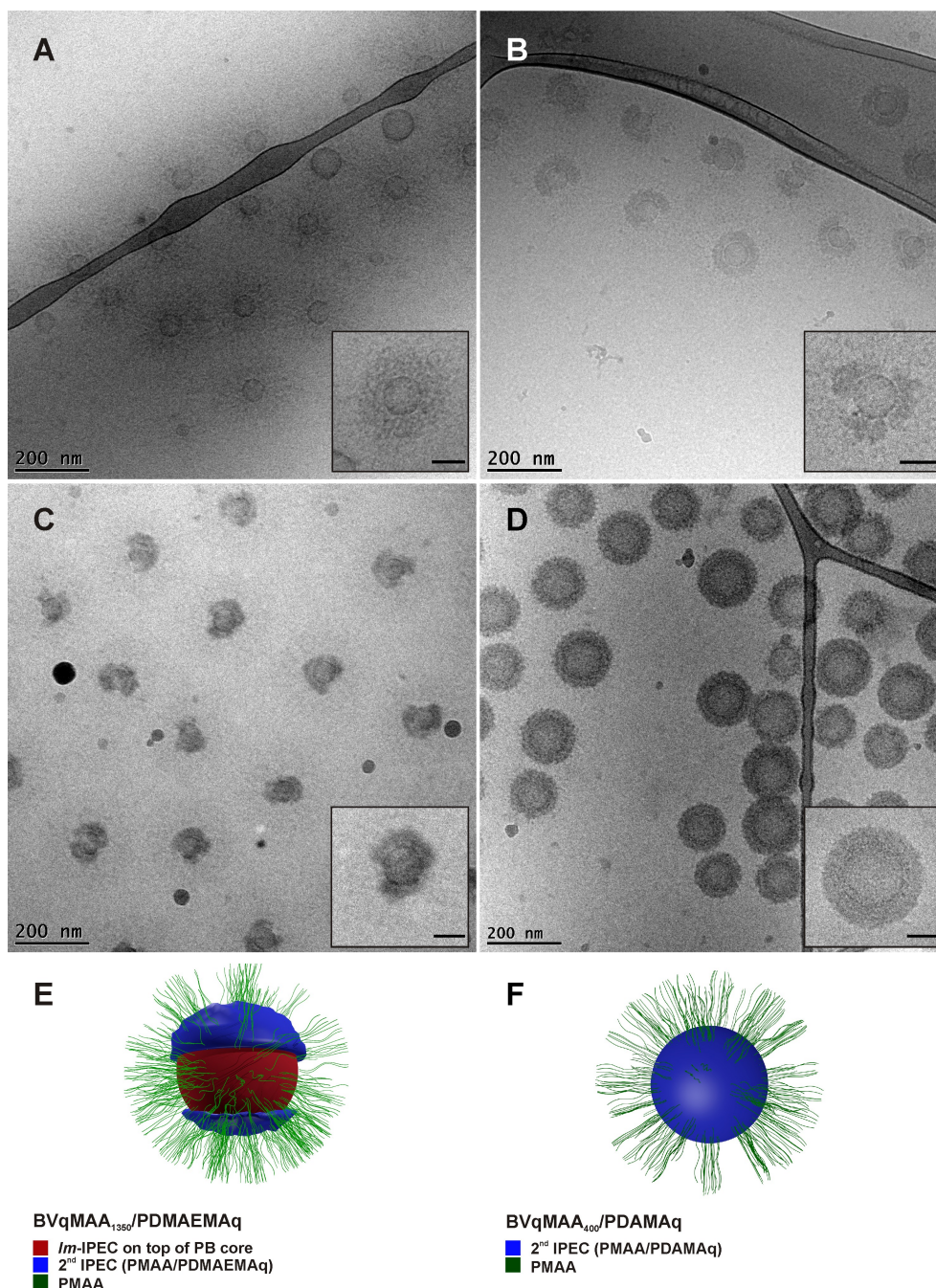


Figure 3.4. **A)** Cryo-TEM micrographs of micellar IPECs of BVqMAA₁₃₅₀/PDAMAq in pH 10 buffer at $Z_{+/-} = 0.5$ with 500 mM NaCl and an ionic strength of ca. 0.55 M; **B)** the same sample after dialysis to pH 10 buffer solution without additional salt (ionic strength = 0.05 M); **C)** micrographs of BVqMAA₁₃₅₀/PDMAEMAq micelles in pH 10 buffer solution (ionic strength = 0.05 M) at $Z_{+/-} = 0.5$; **D)** micrographs of BVqMAA₄₀₀/PDAMAq micelles in pH 10 buffer solution (ionic strength = 0.05 M) at $Z_{+/-} = 0.25$. The insets show single objects at higher magnification, the scale bars representing 50 nm. Schematic representation of the micellar IPECs of BVqMAA₁₃₅₀/PDMAEMAq (**E**) and BVqMAA₄₀₀/PDAMAq (**F**).

To check whether the patches originate from the increased charge density offered by PDAMAq, we also used PDMAEMAq₁₆₂³⁰ as a polycation. As can be seen in Figure 3.4C, comparable micellar IPECs were obtained, exhibiting several localized IPEC patches instead of a homogeneous IPEC shell.

Since neither kinetic trapping of the IPEC, nor the increased charge density of PDAMAq are responsible for the peculiar morphology of the micellar IPECs, we also investigated the influence of the PMAA corona length. The BVqMAA₁₃₅₀ used here has an exceptionally long corona compared to any of the previously used BVqMAA polymers. As compared to BVqMAA₁₃₅₀ with 1170 net negative charges BVqMAA₄₀₀ has only 400 - 180 = 220 net negative charges per PMAA chain. When mixed with PDAMAq at $Z_{+/-} = 0.25$, stable micellar solutions were obtained and subsequently analyzed by cryo-TEM (Figure 3.4D). In this case, well-defined structures adopting a core-shell-shell-corona morphology with a continuous IPEC shell of PMAA/PDAMAq and a corona of excess PMAA were observed. These structures are indeed very similar to those observed previously, where continuous IPEC layers were found for B₈₀₀Vq₁₉₀MAA₃₄₅, B₈₀₀Vq₁₉₀MAA₄₆₅ and B₈₀₀Vq₁₉₀MAA₅₅₀ MCMs upon complexation with PDMAEMAq.³⁰ Thus, the corona length seems to be the critical factor for the formation of the observed patchy IPEC shell. For an estimation of the hydrophilic-to-hydrophobic balance of the terpolymer micelles the weight fractions of the corona- and core-forming blocks are compared. Consequently, the *im*-IPEC of P2VPq/PMAA is included within the hydrophobic part while counterions are not taken into account for the calculation. According to this rough estimation, the materials used in our previous study (BVqMAA₃₄₅, BVqMAA₄₆₅, and BVqMAA₅₅₀) exhibit rather large hydrophobic weight fractions, w_h , between 0.73 and 0.86. In the case reported here, BVqMAA₄₀₀ is in the same range with $w_h = 0.81$, whereas BVqMAA₁₃₅₀ has a predominant hydrophilic weight fraction with $w_h = 0.45$. This seems to affect further IPEC formation, *i.e.*, the formation of a patchy second IPEC shell. Since we already excluded that the structures are kinetically trapped or influenced by the nature of the polycation, it seems to be energetically favorable for the system to form isolated IPEC patches rather than a thin continuous layer. This effect is also supposed to play a role during the formation of localized IPEC patches within the *im*-IPEC shell of different BVqMAA MCMs.²⁹ A more detailed explanation can be given considering the respective interfaces: the newly formed IPEC shell has an interface with the micellar core consisting of PB and the *im*-IPEC (IF-1, Figure 3.5, dashed yellow line), another one with the PMAA corona (IF-2, dashed red line), and at high $Z_{+/-}$ -ratios an additional interface with the surrounding medium (water) would be formed (IF-3, Figure 3.5B, dashed purple line).

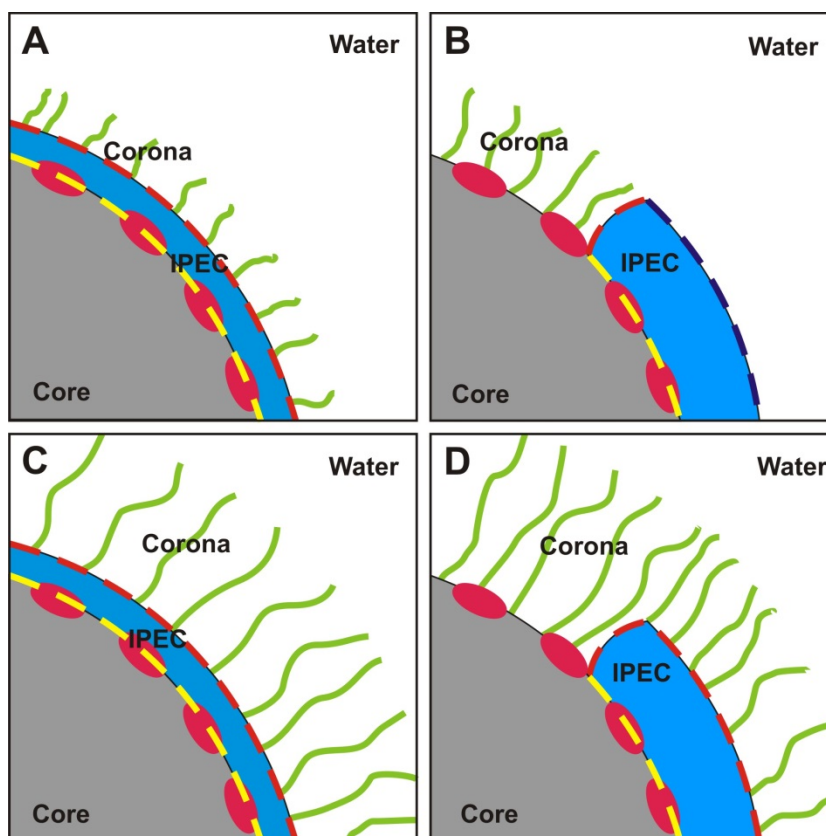


Figure 3.5. Schematic illustration of the potentially relevant interfaces in the formation of an additional IPEC shell in BVqMAA micelles with a short (**A, B**) or long (**C, D**) corona, leading to either continuous (**A, C**) or patchy (**B, D**) IPECs. The relevant interfaces of the newly formed IPEC are highlighted as dashed lines and are between the IPEC and the core (yellow), the corona (red), or water as the selective solvent (purple).

Four different cases of IPEC formation involving BVqMAA₄₀₀ (Figure 3.5A and 3.5B) and BVqMAA₁₃₅₀ (Figure 3.5C and 3.5D) micelles can now be considered. When micellar IPECs with a continuous shell are formed, the interfaces IF-1 and IF-2 are maximized, while IF-3 is absent (Figure 3.5A, C). On the other hand, when patches are formed, IF-1 is minimized. However, in case of a short PMAA segment this leads to the generation of a significant interface IF-3 (Figure 3.5B) and, potentially, a loss of colloidal stability, whereas long-corona micelles can minimize IF-1 without creating an additional IF-3 (Figure 3.5D). It therefore seems that micelles with a very long ionic corona, as demonstrated for BVqMAA₁₃₅₀, preferentially form patchy IPEC compartments when complexed with oppositely charged polycations at low to intermediate $Z_{+/-}$ -ratios. We are aware that this explanation is solely based on simple considerations of the respective interfaces and does not include other effects like chain entropy or partial dissociation of the IPEC domains. However, our tentative model is supported by the results obtained for the systems BVqMAA₁₃₅₀/PDAMAq and BVqMAA₁₃₅₀/PDMAEMAq.

Conclusions

The formation of micellar IPECs between negatively charged BVqMAA precursor micelles and either PDAMAq or PDMAEMAq polycations leads to well-defined core-shell-shell-corona structures. We demonstrate that the formation of a compartmentalized additional IPEC shell in micellar IPECs can be favorable at low to intermediate $Z_{+/-}$ ratios when MCMs with a long corona-forming PMAA block are used. We propose an explanation for the structure formation based on the generated interfaces for different corona lengths of the underlying BVqMAA precursor micelles. In more general terms, this work represents a facile route for the formation of well-defined particles where the size can be adjusted by the underlying MCM system (*e.g.*, molecular weight of BVqMAA) and compartmentalization of the shell is controlled by charge stoichiometry and corona length. Such structures represent very interesting models for pH-responsive soft and patchy colloids or multifunctional delivery vehicles. We are currently investigating the drug delivery properties of BVqMAA micelles. Furthermore, the presence of surface patches of unlike charge stoichiometry and hydrophilicity might turn out to be advantageous for the pH-dependent interaction with living matter, *e.g.*, cell cultures when performing transfection or uptake studies.

ASSOCIATED CONTENT

Conflict of Interest

The authors declare no conflict of interest.

Supporting Information

Molecular characterization data on BVT polymers and DAMA monomer, the kinetic plot of the DAMA polymerization, zeta potential and dynamic light scattering measurements of BVqMAA/PDAMAq micelles. These data are available free of charge *via* the Internet at <http://pubs.acs.org>.

Notes

CVS and TIL contributed equally to this work.

Acknowledgements

C.V.S. acknowledges a scholarship from the State of Bavaria through the BayEFG program as well as ongoing support from the Elite Network of Bavaria (ENB). We thank Marietta Böhm for performing the SEC measurements. O. Borisov (Pau, France) and D.V. Pergushov (Moscow, Russia) are acknowledged for helpful discussions. F. H. S. is grateful for a starting independent researcher fellowship (Verband der Chemischen Industrie, VCI). Matthias Karg is acknowledged for help during manuscript preparation.

References

1. Bates, F. S.; Hillmyer, M. A.; Lodge, T. P.; Bates, C. M.; Delaney, K. T.; Fredrickson, G. H. *Science* **2012**, 336, 434.
2. Schacher, F. H.; Rupa, P. A.; Manners, I. *Angew. Chem., Int. Ed.* **2012**, 51, 7898.
3. Botiz, I.; Darling, S. B. *Mater. Today* **2010**, 13, 42.
4. Li, J.-G.; Lin, R.-B.; Kuo, S.-W. *Macromol. Rapid Commun.* **2012**, 33, 678.
5. Son, J. G.; Gwyther, J.; Chang, J.-B.; Berggren, K. K.; Manners, I.; Ross, C. A. *Nano Lett.* **2011**, 11, 2849.
6. Hamley, I. W. *Prog. Polym. Sci.* **2009**, 34, 1161.
7. Hawker, C. J.; Russell, T. P. *Mrs Bull.* **2005**, 30, 952.
8. Moffitt, M.; Khougaz, K.; Eisenberg, A. *Acc. Chem. Res.* **1996**, 29, 95.
9. Savic, R.; Eisenberg, A.; Maysinger, D. *J. Drug Targeting* **2006**, 14, 343.
10. Funhoff, A. M.; Monge, S.; Teeuwen, R.; Koning, G. A.; Schuurmans-Nieuwenbroek, N. M. E.; Crommelin, D. J. A.; Haddleton, D. M.; Hennink, W. E.; van Nostrum, C. F. *J. Control. Release* **2005**, 102, 711.
11. Harada-Shiba, M.; Yamauchi, K.; Harada, A.; Takamisawa, I.; Shimokado, K.; Kataoka, K. *Gene Ther.* **2002**, 9, 407.
12. Itaka, K.; Yamauchi, K.; Harada, A.; Nakamura, K.; Kawaguchi, H.; Kataoka, K. *Biomaterials* **2003**, 24, 4495.
13. Hinton, T. M.; Guerrero-Sanchez, C.; Graham, J. E.; Le, T.; Muir, B. W.; Shi, S.; Tizard, M. L. V.; Gunatillake, P. A.; McLean, K. M.; Thang, S. H. *Biomaterials* **2012**, 33, 7631..
14. Matsumoto, S.; Christie, R. J.; Nishiyama, N.; Miyata, K.; Ishii, A.; Oba, M.; Koyama, H.; Yamasaki, Y.; Kataoka, K. *Biomacromolecules* **2009**, 10, 119.
15. Nishiyama, N.; Jang, W.-D.; Kataoka, K. *New J. Chem.* **2007**, 31, 1074.
16. Schacher, F.; Yuan, J.; Schoberth, H. G.; Müller, A. H. E. *Polymer* **2010**, 51, 2021.
17. Stadler, R.; Auschra, C.; Beckmann, J.; Krappe, U.; Voight-Martin, I.; Leibler, L. *Macromolecules* **1995**, 28, 3080.
18. Li, Z. B.; Kesselman, E.; Talmon, Y.; Hillmyer, M. A.; Lodge, T. P. *Science* **2004**, 306, 98.
19. Marsat, J.-N. 1.; Heydenreich, M.; Kleinpeter, E.; Berlepsch, H. v.; Böttcher, C.; Laschewsky, A. *Macromolecules* **2011**, 44, 2092.
20. Gröschel, A. H.; Walther, A.; Löbbling, T. I.; Schmelz, J.; Hanisch, A.; Schmalz, H.; Müller, A. H. E. *J. Am. Chem. Soc.* **2012**, 134, 13850.
21. Voets, I. K.; de Keizer, A.; de Waard, P.; Frederik, P. M.; Bomans, P. H. H.; Schmalz, H.; Walther, A.; King, S. M.; Leermakers, F. A. M.; Stuart, M. A. C. *Angew. Chem., Int. Ed.* **2006**, 45, 6673.
22. Walther, A.; Müller, A. H. E. *Soft Matter* **2008**, 4, 663.
23. Walther, A.; Müller, A. H. E. *Chem. Rev.* **2013**, ASAP, DOI: 10.1021/cr300089t.

24. Moughton, A. O.; Hillmyer, M. A.; Lodge, T. P. *Macromolecules* **2012**, 45, 2.
25. Gröschel, A. H.; Schacher, F. H.; Schmalz, H.; Borisov, O. V.; Zhulina, E. B.; Walther, A.; Müller, A. H. E. *Nat. Commun.* **2012**, 3.
26. Kabanov, V. A. *Russ. Chem. Rev.* **2005**, 74, 3.
27. Pergushov, D. V.; Müller, A. H. E.; Schacher, F. H. *Chem. Soc. Rev.* **2012**, 41, 6888.
28. Schacher, F.; Betthausen, E.; Walther, A.; Schmalz, H.; Pergushov, D. V.; Müller, A. H. E. *ACS Nano* **2009**, 3, 2095.
29. Schacher, F.; Walther, A.; Müller, A. H. E. *Langmuir* **2009**, 25, 10962.
30. Synatschke, C. V.; Schacher, F. H.; Förtsch, M.; Drechsler, M.; Müller, A. H. E. *Soft Matter* **2011**, 7, 1714.
31. Betthausen, E.; Drechsler, M.; Förtsch, M.; Pergushov, D. V.; Schacher, F. H.; Müller, A. H. E. *Soft Matter* **2012**, 8, 10167.
32. Sperschneider, A.; Schacher, F.; Gawenda, M.; Tsarkova, L.; Müller, A. H. E.; Ulbricht, M.; Krausch, G.; Köhler, J. *Small* **2007**, 3, 1056.
33. Auschra, C.; Stadler, R. *Polym. Bull.* **1993**, 30, 257.
34. Borisov, O. V.; Zhulina, E. B. *Macromolecules* **2002**, 35, 4472.
35. Blacker, N. C.; Findlay, P. H.; Sherrington, D. C. *Polym. Adv. Technol.* **2001**, 12, 183.
36. Bos, G. W.; Kanellos, T.; Crommelin, D. J. A.; Hennink, W. E.; Howard, C. R. *Vaccine* **2004**, 23, 460.
37. Cherng, J. Y. *J. Pharm. Pharmaceut. Sci.* **2009**, 12, 346.
38. Funhoff, A. M.; Van Nostrum, C. F.; Lok, M. C.; Kruijtzter, J. A. W.; Crommelin, D. J. A.; Hennink, W. E. *J. Control. Release* **2005**, 101, 233.

Supporting Information

to

Micellar Interpolyelectrolyte Complexes with a

Compartmentalized Shell

Christopher V. Synatschke, Tina I. Löblich, Melanie Förtsch, Andreas Hanisch,
Felix H. Schacher,^{*} and Axel H. E. Müller^{*}

Scheme S3.1. Synthesis of BVT triblock terpolymers by sequential living anionic polymerization in THF at low temperatures and their conversion to BVqMAA triblock terpolymers through quaternization and subsequent acidic hydrolysis in dioxane.

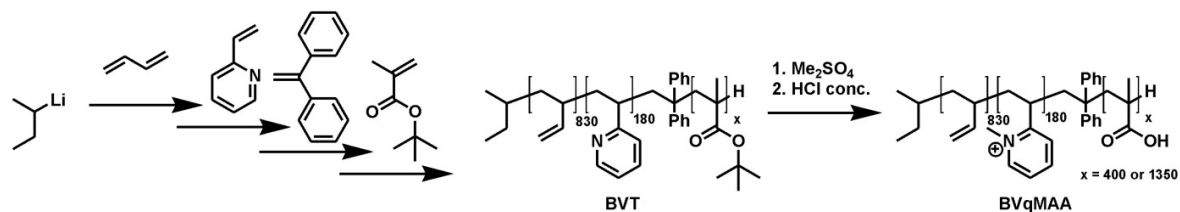
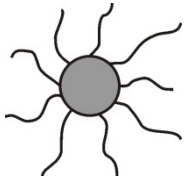
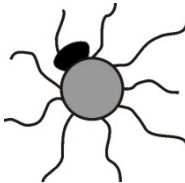
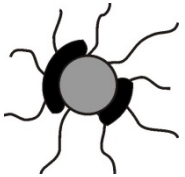
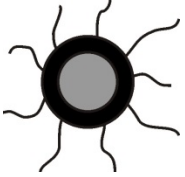


Table S3.1. Zeta potential of BVqMAA₁₃₅₀/PDAMAq micelle solutions. Values represent mean \pm s. d.

Z _{+/-} value	BVqMAA ₁₃₅₀ /PDAMAq				
	0	0.1	0.25	0.5	0.75
Zeta Potential [mV]	-34.0 ± 1.2	-33.2 ± 2.6	-33.9 ± 0.6	-31.8 ± 1.5	-31.8 ± 2.3

Table S3.2: Distribution of micelle types (no compartment, small compartment(s), large compartment(s) and complete shell) in BVqMAA₁₃₅₀/PDAMAq samples at different $Z_{+/-}$ values counted from cryo-TEM micrographs. At least 70 micelles were counted per sample.

BVqMAA ₁₃₅₀ / PDAMAq				
$Z_{+/-} = 0$	100%	0%	0%	0%
$Z_{+/-} = 0.1$	82%	18%	0%	0%
$Z_{+/-} = 0.25$	15%	76%	9%	0%
$Z_{+/-} = 0.5$	2%	6%	79%	13%
$Z_{+/-} = 0.75$	0%	0%	18%	82%

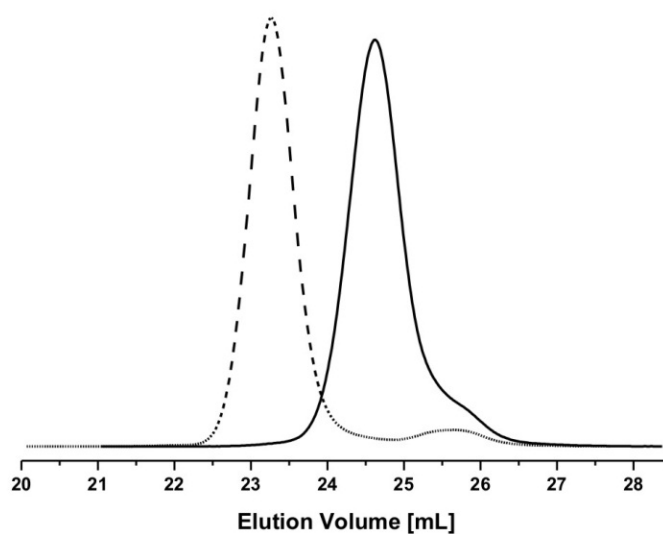


Figure S3.1. SEC elution curves of B₈₃₀V₁₈₀T₄₀₀ (solid line) and B₈₃₀V₁₈₀T₁₃₅₀ (dotted line) triblock terpolymers in SEC with THF as solvent (RI signal).

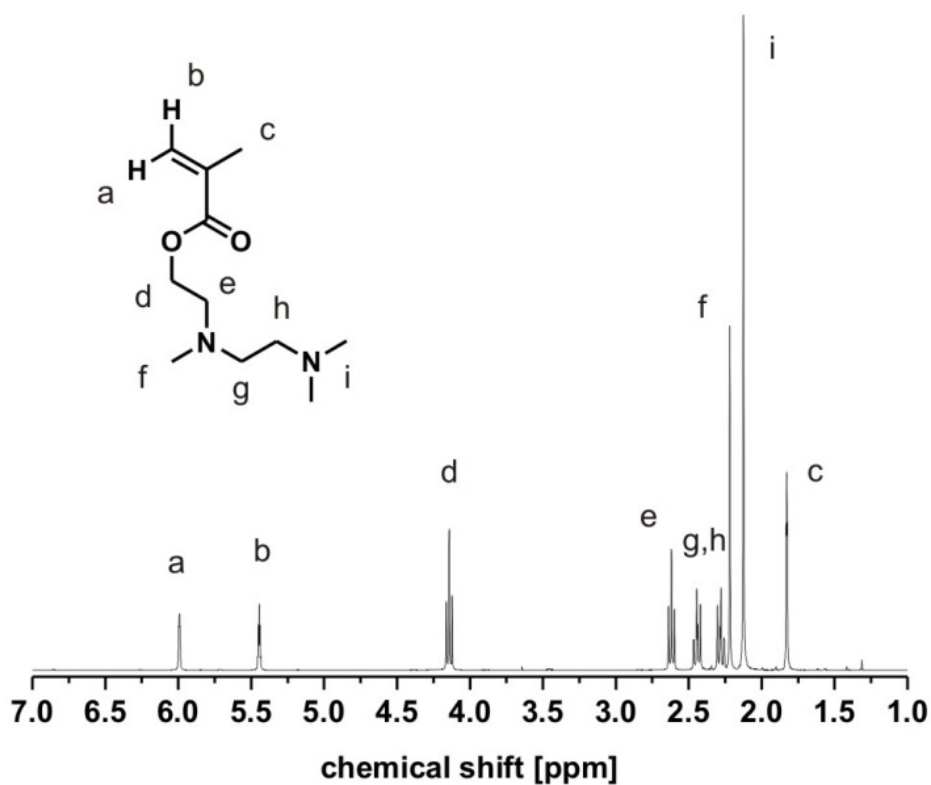


Figure S3.2. ¹H NMR spectrum of DAMA in CDCl₃ after purification by column chromatography.

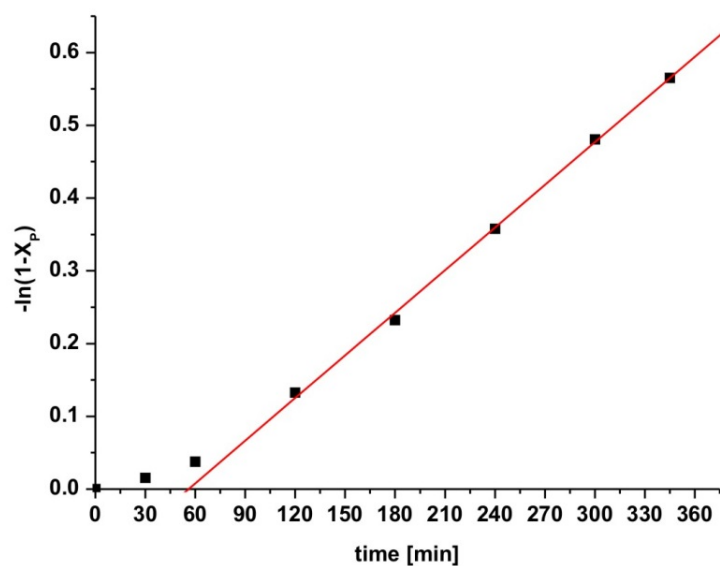


Figure S3.3: First order kinetic plot for the RAFT polymerization of DAMA.

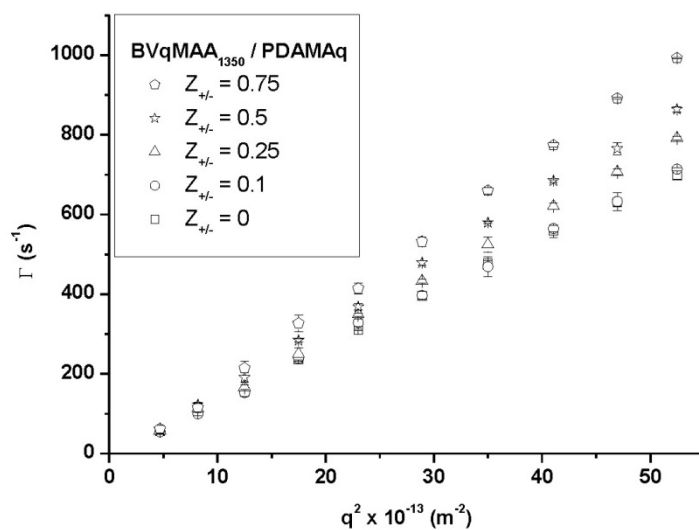


Figure S3.4: Γ versus q^2 plots for BVqMAA₁₃₅₀/PDAMAq micelles at various $Z_{+/-}$ values.

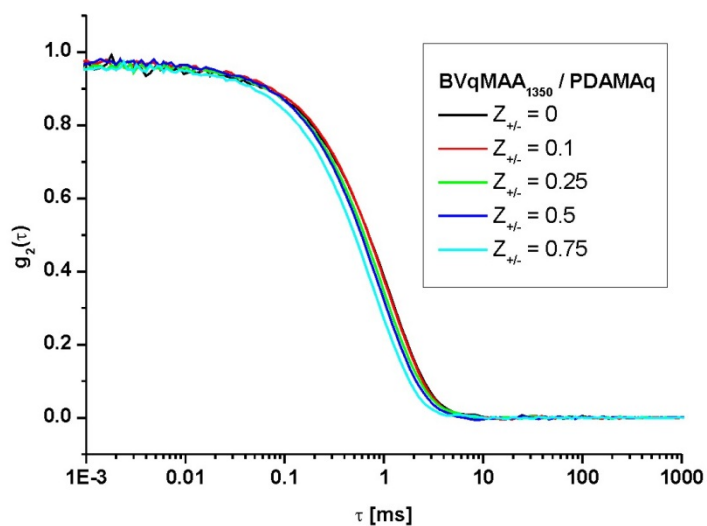


Figure S3.5: Autocorrelation functions of BVqMAA₁₃₅₀/PDAMAq micelles at various $Z_{+/-}$ values from DLS measurements at a scattering angle of 90°.

Chapter 4

Hidden Structural Features of Multicompartment Micelles Revealed by Cryogenic Transmission Electron Tomography

Tina I. Löbling,^{a, †} Johannes S. Haataja,^{b, †} Christopher V. Synatschke,^a Felix H. Schacher,^c
Melanie Müller,^a Andreas Hanisch,^a André H. Gröschel,^{*,b} and Axel H. E. Müller^{*,a,c}

^a Makromolekulare Chemie II und Bayreuther Zentrum für Kolloide und Grenzflächen, Universität Bayreuth, D-95440 Bayreuth, Germany.

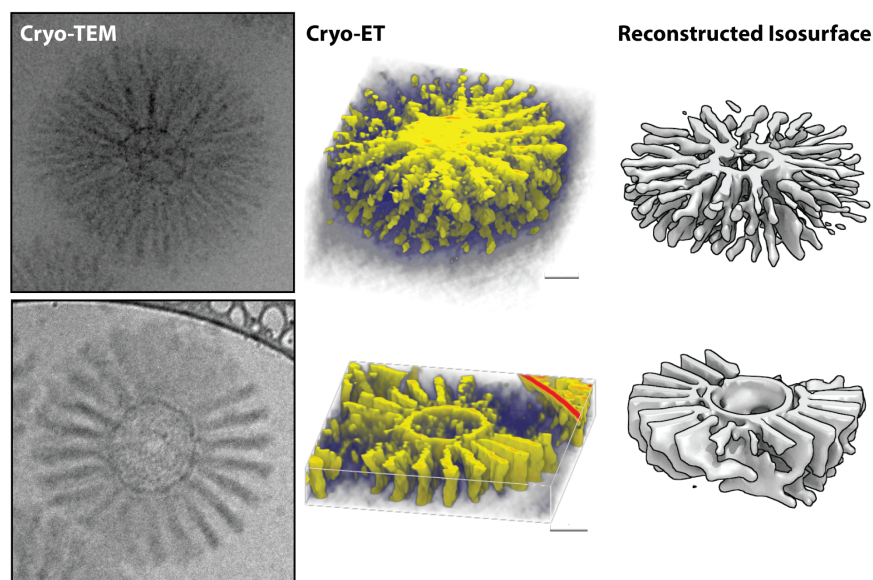
^b Department of Applied Physics, School of Science, Aalto University, FIN-02150 Espoo, Finland

^c Institut für Organische Chemie und Makromolekulare Chemie and Jena Center for Soft Matter (JCSM), Friedrich-Schiller-Universität Jena, Humboldtstraße 10, D-07743 Jena, Germany.

[†]Institut für Organische Chemie, Johannes Gutenberg-Universität Mainz, D-55099 Mainz, Germany

E-Mail: andre.groschel@aalto.fi; axel.mueller@uni-mainz.de

[†] Both authors contributed equally to this work



Published in: *ACS Nano*, **2014**, 8, 11330-11340

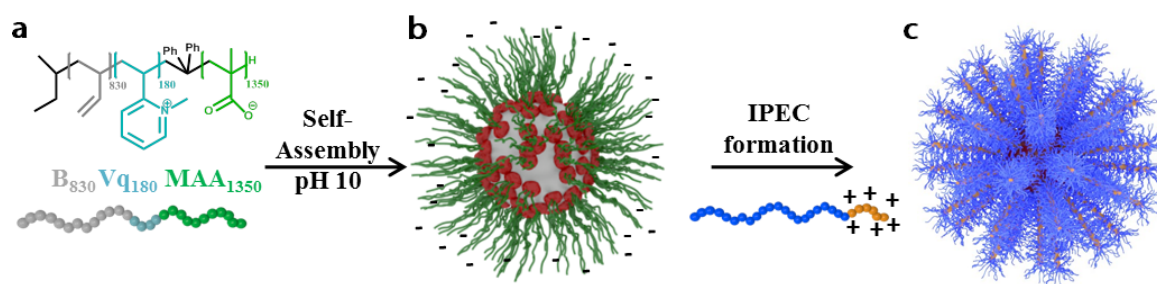
Abstract

The demand for ever more complex nanostructures in materials and soft matter nanoscience also requires sophisticated characterization tools for reliable visualization and interpretation of internal morphological features. Here, we address both aspects and present synthetic concepts for the compartmentalization of nanoparticle peripheries as well as their *in-situ* tomographic characterization. We first form negatively charged spherical multicompartment micelles from ampholytic triblock terpolymers in aqueous media, followed by interpolyelectrolyte complex (IPEC) formation of the anionic corona with bis-hydrophilic cationic/neutral diblock copolymers. At a 1:1 stoichiometry of anionic and cationic charges, the so-formed IPECs are charge neutral and thus phase separate from solution (water). The high chain density of the ionic grafts provides steric stabilization through the neutral PEO corona of the grafted diblock copolymer and suppresses collapse of the IPEC; instead, the dense grafting results in defined nanodomains oriented perpendicular to the micellar core. We analyze the 3D arrangements of the complex and purely organic compartments, *in-situ*, by means of cryogenic transmission electron microscopy (cryo-TEM) and tomography (cryo-ET). We study the effect of block lengths of the cationic and nonionic block on IPEC morphology, and while 2D cryo-TEM projections suggest similar morphologies, cryo-ET and computational 3D reconstruction reveal otherwise hidden structural features, *e.g.*, planar IPEC brushes emanating from the micellar core.

Introduction

The synthetic design of complex colloidal particles underwent great progress in the nanoengineering of particle shape (anisotropy), compartmentalization (core or surface patches), and functionality (directional forces).¹⁻³ While top-down procedures dominate particle structuring on the micron-scale, bottom-up concepts continue to evolve as potential preparative tools on the nanoscale.⁴⁻⁶ In this regard, the self-assembly of block copolymers offers straightforward strategies to unify multiple environments within one nanoobject.⁷ The number of compartments is proportional to the number of incompatible polymer blocks, where ABC triblock terpolymers already display a rich repertoire of bulk and solution morphologies.^{8,9} Amphiphilic block copolymers are a highly frequented source for water-stable polymeric particles, as they spontaneously self-assemble into a hydrophobic core stabilized by either a non-ionic (*e.g.*, poly(ethylene oxide), PEO) or a polyionic hydrophilic corona.¹⁰⁻¹² A charged corona opens up further coordination possibilities, *e.g.*, for templating, nanoparticle immobilization (inorganic or biological) or complementarily charged polyelectrolytes. Ballauff *et al.* immobilized anionic metal nanoparticles in cationic spherical polyelectrolyte brushes, creating hybrid heterogenic catalyst systems.¹³ Proteins or enzymes were also captured by either cationic or anionic brushes.¹⁴⁻¹⁷ To compartmentalize the polyionic corona brush, polymer blending⁴ and intra- or inter-polyelectrolyte complex (IPEC) formation have proven their efficiency.¹⁸⁻²³ Ionic polymers coassemble with complementarily charged blocks through noncovalent electrostatic interactions to form a new compartment with high incompatibility to the surrounding phases (polymer blocks, water or interfaces).²⁴⁻²⁶ Applying this concept, vesicles with IPEC walls were coassembled from two block ionomers in organic solvents²⁷ as well as in water,^{28,29} Janus particles with IPEC cores in water³⁰ and vesicles with nano-segregated walls *via* salt-induced chelation.³¹

In previous works we demonstrated that polybutadiene-*block*-poly(1-methyl-2-vinylpyridinium)-*block*-poly(methacrylic acid) (PB-*b*-PVq-*b*-PMAA, BVqMAA) triblock terpolymers self-assemble into multicompartment micelles with a soft PB core, intramicellar IPEC (*im*-IPEC) patches of PVq/PMAA and a short stabilizing PMAA corona (~360 residual units of MAA).²⁰ Complexation with polycations of comparable length to the residual anionic corona usually led to homogeneous second IPEC shells.^{21,22} In the case of a much longer anionic PMAA corona (~1170 residual units of MAA), IPECs with cationic homopolymers collapsed as irregularly shaped, discontinuous compartments onto the micellar core.²³ This segregation phenomenon led us to the hypothesis that the combination of a long PMAA corona and a bis-hydrophilic block copolymer with short polycationic blocks could generally phase-separate into a variety of anisotropic corona morphologies (Scheme 4.1).^{32,33} Concepts to structure nanoparticle peripheries are desirable, because corona compartments are directly accessible for loading and modification, they allow (inter)particle recognition, and they provide directional forces for hierarchical self-assembly.³⁴⁻⁴¹



Scheme 4.1. **a)** Chemical Structure of the $B_{830}Vq_{180}MAA_{1350}$ triblock terpolymer. **b)** Schematic of the BVqMAA multicompartment micelles with PB core (grey), PVq/PMAA *im*-IPEC patches (red), and excess PMAA corona (green) in aqueous solution. **c)** Complexation of PMAA with bis-hydrophilic cationic diblock copolymers to form particles with anisotropic IPEC domains.

Although research in many fields greatly benefits from higher structural complexity (*e.g.*, advanced gating materials, energy storage, nanoreactors and biomedical applications), this also demands sophisticated methods to reliably characterize and visualize internal morphological features. In case of entirely organic nanoparticles, transmission electron microscopy (TEM) usually is the first choice. This technique visualizes differences in electron contrast in the dried and often collapsed state. In the case of soft matter, particle flattening or buckling (*e.g.*, capsules) is a common drying artifact that has to be taken into account when discussing particle morphology. Cryogenic TEM (cryo-TEM) circumvents most of these issues through vitrification and *in-situ* imaging of a thin solvent film that contains the specimen.⁴² Although cryo-TEM is a valuable characterization tool in many scientific fields,⁴³ the obtained images are 2D projections of 3D objects. Overlapping internal features may complicate the analysis of complex nanostructures and may lead to false interpretations. Cryogenic transmission electron tomography (cryo-ET) on the other hand emerges as a powerful and versatile tool to obtain structural information in three dimensions.⁴⁴ Here, a series of 2D image projections is captured from the same vitrified particle (or area) at different viewing angles. After image alignment of the 2D images a 3D tomogram can be reconstructed using computational methods. Although this technique is well established for biological matter characterization with nanometer resolution,⁴⁵ cryo-ET only gradually progresses to other research fields.^{46–48} In particular, soft matter materials could benefit from *in-situ* characterization, where particles become increasingly complex. Tomographic particle visualization is still challenging, because the contrast difference of (mostly) hydrocarbon constituents is usually low as compared to, for example, electron-dense inorganic nanoparticles, and long exposure times increase the risk of electron beam damage of particles or solvent film. So far, cryo-ET unfolds its full potential in aqueous solution, where contrast differences between solvent and hydrocarbon specimens are acceptable and vitrified films allow for sufficiently long exposure. It was only recently when Sommerdijk *et al.* used cryo-ET to resolve the structure of spherical polymer aggregates with an internally curved bicontinuous morphology self-assembled from amphiphilic double-comb diblock copolymers.⁴⁹ These and other works in the field of (cryogenic) tomography impressively demonstrated the benefits of 3D reconstruction for the

interpretation of particle features towards a deeper understanding of the underlying formation mechanism.^{50–54}

Here, we pursue two objectives, the structuring of compartmentalized organic nanoparticles as well as their in-depth tomographic characterization. We utilize ionic grafting of complementarily charged polyions to create ordered IPEC nanodomains within the charged corona of multicompartment micelles. A predefined mismatch in polyion chain length facilitates dense grafting of defined numbers of diblock copolymer chains per corona chain up to the point of charge neutralization. The large quantity of polymer chains and dense chain packing of the non-ionic block causes massive overcrowding within the corona that suppresses a collapse of the IPEC to globules, but instead forces corona chains to stretch into anisotropic IPEC morphologies. We then resolve the periodic 3D arrangements of the purely organic nanophases with cryogenic transmission electron tomography as an emerging *in-situ* technique for soft matter characterization.

Results and Discussion

Components for IPEC Formation. The triblock terpolymer $B_{830}Vq_{180}MAA_{1350}$ (subscripts denote the degree of polymerization; see Chart 4.1 and Table S4.1 of the Supporting Information) self-assembles into spherical multicompartment micelles in aqueous solution with an aggregation number of $N_{agg} \approx 650$ $B_{830}Vq_{180}MAA_{1350}$ chains per micelle (see the Supporting Information for calculations). As was shown earlier for a polymer with shorter PMAA block,²¹ these $B_{830}Vq_{180}MAA_{1350}$ precursor micelles exhibit a hydrophobic PB core, intramolecular IPEC (*im*-IPEC) patches of PVq/PMAA on the surface, and an anionic corona of excessPMAA (Figure 4.1a). Dynamic light scattering (DLS) gives a hydrodynamic radius of $\langle R_h \rangle_{z,app} = 172$ nm after *im*-IPEC formation (Figure S4.1) originating from the 1170 units of charged and noncoordinated MAA per corona chain. At $pH \geq 7$ the MAA units are sufficiently deprotonated²⁰ (ζ -potential ≈ -32 mV) and are accessible for quantitative intermolecular complexation with cationic polymers (ζ -potential ≈ 0 mV).^{21–23} For that, we use two bis-hydrophilic cationic diblock copolymers (Chart 4.1 and Table 4.1), poly(L-lysine)-*block*-poly(ethylene oxide) ($LL_{40}EO_{270}$) and quaternized poly(2-(dimethylamino)ethyl methacrylate)-*block*-poly(ethylene oxide) ($Dq_{82}EO_{114}$).

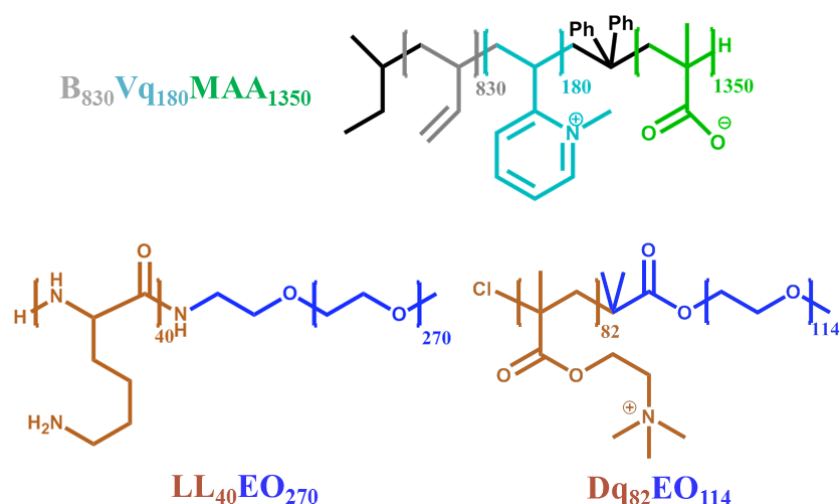


Chart 4.1. Chemical structures of the used triblock terpolymer and diblock copolymers.

Both diblock copolymers, LL₄₀EO₂₇₀ and Dq₈₂EO₁₁₄, have comparable molecular weights and contain one cationic (PLL or PDq) and one non-ionic water-soluble block (PEO). The block length of the polycation regulates the number of polymer chains that ionically graft per anionic PMAA corona chain, whereas the PEO block length determines the volume requirement of the grafted brush and acts as the new stabilizing corona. The differences in the length of both blocks should have distinct effects on chain packing and the resulting corona morphology.

Table 4.1: Specification of Cationic Bis-Hydrophilic Diblock Copolymers

Polymer	DP (polycation)	DP (PEO)	Mn [kg/mol] ^{a)}	PDI ^{b)}
LL ₄₀ EO ₂₇₀	40	270	17.7	1.05
Dq ₈₂ EO ₁₁₄	82	114	17.9	1.17

^{a)} Calculated from ¹H-NMR using the M_n of the PEO block provided by the supplier. ^{b)} Determined with SEC in DMF (protected LL₄₀EO₂₇₀) or THF (D₈₂EO₁₁₄) as eluent and PEO standards.

To calculate the mixing ratio of polyion chains, we define the charge ratio, $Z_{+/-}$, in eq 4.1. A value of $Z_{+/-} = 0$ corresponds to the PMAA corona without addition of polycations and $Z_{+/-} = 1$ to quantitative complexation with the polycationic block copolymers (charge neutralization).

$$Z_{+/-} = \frac{n_{\text{cationic}}}{n_{\text{anionic}}} = \frac{n_{\text{LL (or Dq)}}}{n_{\text{MAA}} - n_{\text{Vq}}} \quad (4.1)$$

In the following we will first give a detailed morphological characterization of IPECs formed by complexation of the B₈₃₀Vq₁₈₀MAA₁₃₅₀ precursor micelles with LL₄₀EO₂₇₀ and Dq₈₂EO₁₁₄ and then discuss particle composition and chain arrangements.

Self-Assembly of IPEC1. Figure 4.1b shows the self-assembly strategy as well as the resulting nanostructure after IPEC formation of the BVqMAA₁₁₇₀ precursor micelles with LL₄₀EO₂₇₀ (1170 units of MAA are left after *im*-IPEC formation). At quantitative complexation of the micellar corona (ζ -potential ≈ -2 mV), we observe an overall spherical shape with ray-like protrusions, the appearance of which is reminiscent of sea urchins. We reported about this IPEC morphology in a previous work, where we focused on the application of the highly PEGylated micelles as remarkably effective drug carrier systems in photodynamic cancer therapy.³² Here, we subject this intricate morphology to a detailed structural characterization to determine its origin.

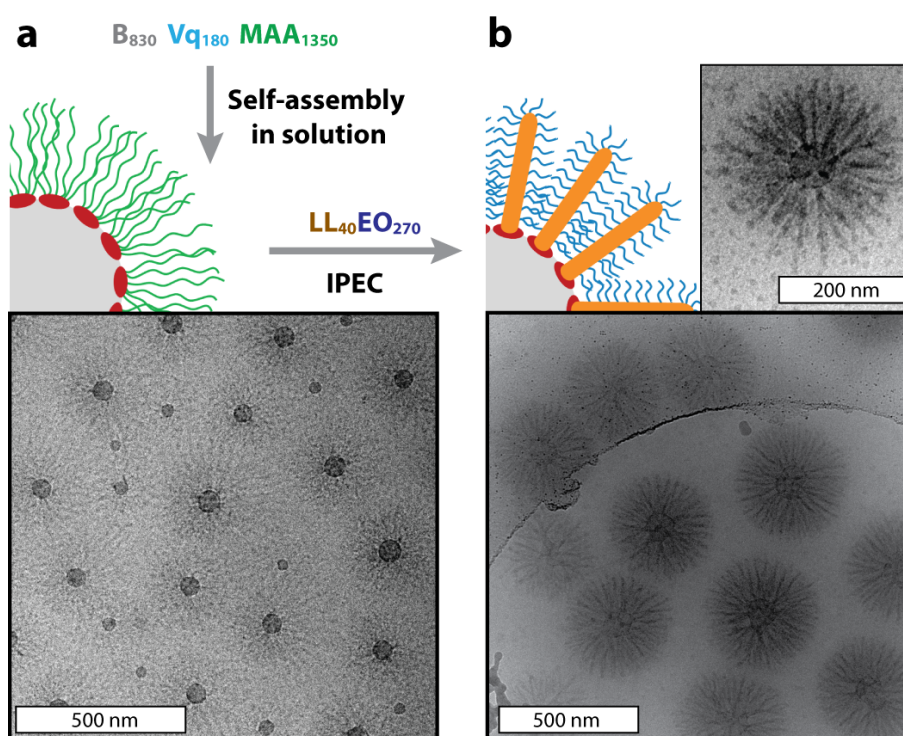


Figure 4.1. Formation of BVqMAA precursor micelles and IPEC1 (BVqMAA₁₁₇₀/LL₄₀EO₂₇₀). **a)** Solution self-assembly of BVqMAA₁₁₇₀, cryo-TEM image, and schematic of the micelles with PB core (gray), PVq/PMAA *im*-IPEC patches (red), and excess PMAA corona (green) in pH 10 buffer solution. **b)** Complexation of PLL (brown) with PMAA (green) results in bottlebrush formation of IPEC1 (orange) stabilized by PEO brush (blue). The inset shows one of the IPEC1 micelles at higher magnification.

According to eq 4.1, 29.3 equiv of LL₄₀EO₂₇₀ is required to reach charge neutral conditions, $Z_{+/-} = 1$. Considering the $N_{\text{agg}} \approx 650$ of the BVqMAA₁₁₇₀ micelle, 650 PMAA chains in the corona of one micelle accommodate approximately 19 000 diblock copolymer chains. As illustrated in Figure 4.1b, the PMAA chains (green) undergo IPEC formation with the PLL block (brown) and most likely form a cylindrical brush (orange) stabilized by the PEO corona (blue). Two main parameters dominate the formation of an anisotropic IPEC: (i) the mismatch of chain lengths of polyionic blocks, PMAA and PLL, and (ii) the resulting overcrowding and dense packing of diblock copolymer chains within the confined space of the particle corona. To validate these observations and gain a deeper insight into the morphology, we further characterized these micellar IPECs by means of cryo-ET.

Cryo-ET Characterization of IPEC1. To extract more information on the architecture and to confirm the proposed cylindrical brush morphology of IPEC1, we performed cryo-ET, *i.e.* a series of 2D cryo-TEM images of the same area at tilted angles from -69° to $+69^\circ$, allowing 3D reconstruction after image alignment (Figure 4.2, see Methods and Supporting Movies, SM4.1 and SM4.2). For cryo-ET, a high electron acceleration voltage (here 300 kV) is beneficial to minimize beam damage to the sample and matrix. Yet, this poses challenges for visualizing soft matter, because less interaction of the electron beam with the organic material also reduces contrast. The soft nanoparticles proved surprisingly resilient against electron beam damage, and we recorded a total of 46 images in 3° increments (while observing noticeable degradation of the supporting carbon film in some cases). Figure 4.2a shows one particle measured with cryo-ET, and Figure 4.2b the calculated 3D reconstruction using the maximum entropy iterative method (see Methods and the Supporting Information). The isosurface model shows a compartmentalized corona structure, where single rays support the assumption of “sea urchin-like” morphology (Figure 4.2c). At first sight, the arrangement of the cylindrical IPECs seems chaotic, but from side view we see an onset of a hexagonal order (Figure 4.2d). Also the top view of the middle slice supports single IPEC rays protruding from the spherical core (Figure 4.2e,f). The overall shape of the otherwise spherical micellar IPEC appears slightly flattened, reminiscent of a bulgy cylinder, which is an effect of sample preparation. The soft particles are deformed by the limited thickness of the solvent film that is close to the diameter of the particle ($\langle D_h \rangle_{z,app} \approx 280$ nm). Nevertheless, the reconstruction unambiguously proves the cylindrical brush morphology of IPEC1. The cylindrical IPEC brushes on a sphere occupy a considerable volume within the confined space of the corona. The hydrophilic PEO chains phase separate and intercalate between the charge-neutral, hydrophobic IPEC domains. The large quantity of polymer chains and the hydrolytic pressure within the water-soluble PEO phase force the corona chains into a stretched conformation.³³ At the same time, the PEO brush provides steric stabilization for the IPEC, which then adapts the cylindrical brush morphology instead of the usually observed collapsed homogeneous shell.²² The PEO chains not only occupy the space between individual IPEC domains but also form an additional corona surrounding and stabilizing the entire micellar IPECs.

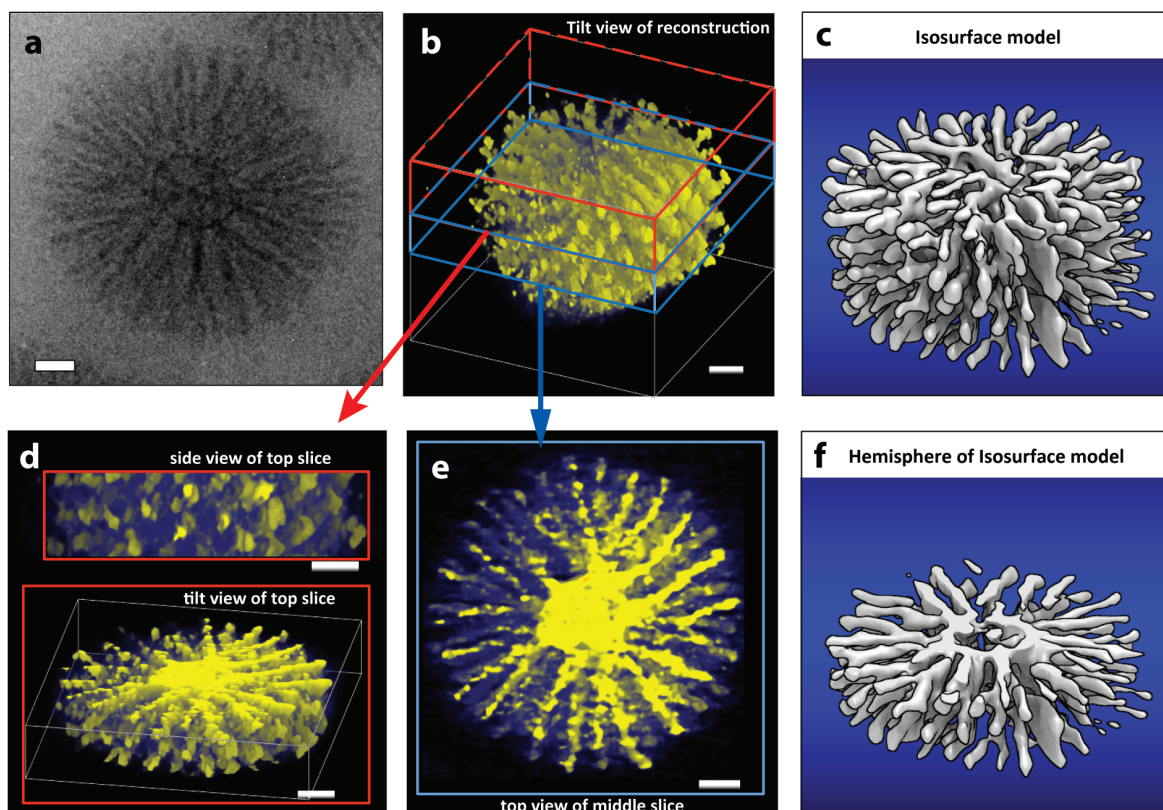


Figure 4.2. Cryo-ET reconstruction of IPEC1 (BVqMAA₁₁₇₀/LL₄₀EO₂₇₀). **a**) Cryo-TEM image of the reconstructed micelles. **b**) Overview of reconstruction. The colored frames indicate entire reconstruction (white), top slice (red) and middle slice (blue). **c**) Isosurface of entire reconstructed micelle. **d**) Side and tilt view of top slice (red). **e**) Top view of middle slice (blue). **f**) Isosurface of micelle cropped to hemisphere. Scale bars in reconstruction images correspond to 50 nm.

Self-Assembly of IPEC2. For the formation of IPEC2 we chose a diblock copolymer, Dq₈₂EO₁₁₄, where the cationic chain is twice as long as for LL₄₀EO₂₇₀, while the PEO block has less than half the length (Figure 4.3). According to eq 4.1, we reach charge neutralization by grafting 14.3 chains of Dq₈₂EO₁₁₄ to each BVqMAA₁₁₇₀ chain (ζ -potential \approx -5 mV). With $N_{\text{agg}} \approx 650$, about 9 300 chains of Dq₈₂EO₁₁₄ are required for quantitative complexation. From the alternating bright and dark regions found in cryo-TEM (Figure 4.3), one might assume a similar cylindrical brush morphology to that described above, however with slight differences in appearance. Most notably, the elongated rays of IPEC2 are thicker, more pronounced, and fewer in number as compared to IPEC1. We again assume that PEO chains are located between the IPEC domains as well as expand to the outside of the whole micellar IPEC. However, the zoom-in of Figure 4.3b,c depicts one IPEC2 particle where continuous stripes are present across the entire core. The pronounced stripes clearly differ from the rays of IPEC1. Blurring of only some corona segments points toward an anisotropic morphology and random orientation of particles toward the observation direction (Figure S4.2), further corroborating the assumption of anisotropy.

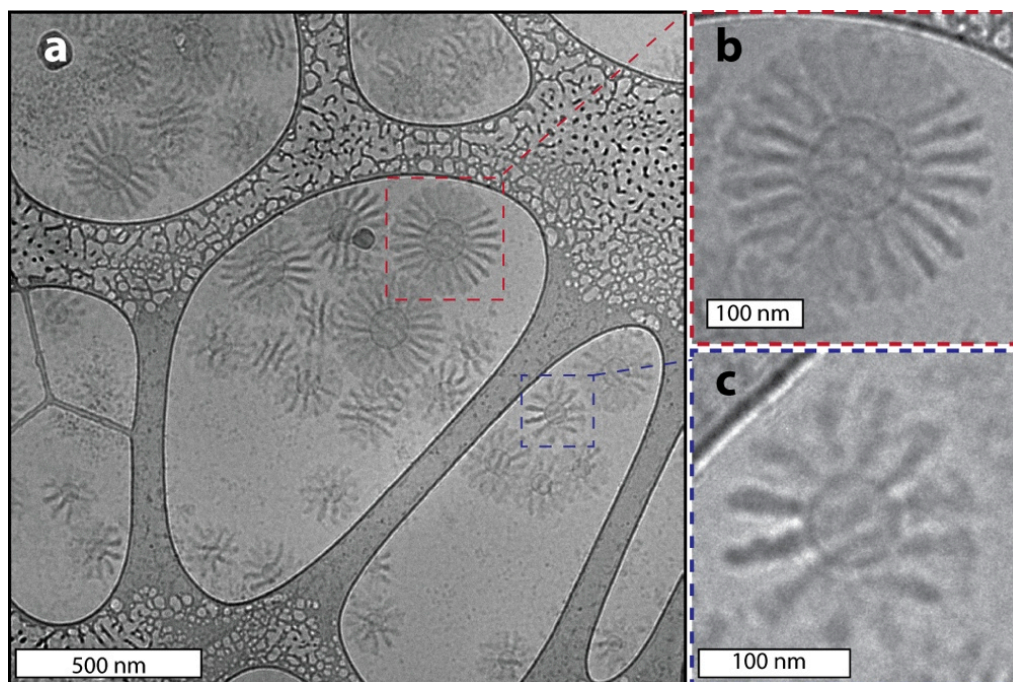


Figure 4.3. Cryo-TEM of IPEC2 (BVqMAA₁₁₇₀/Dq₈₂EO₁₁₄). **a)** Cryo-TEM overview of IPEC2 with striped structural features. **b,c)** Zoom-in of selected micelles with high (b) and low (c) IPEC brush density.

Cryo-ET Characterization of IPEC2. In the following, we will first elaborate on the larger particle (Figure 4.3b $d \approx 300$ nm) and classify its morphology, and then proceed to discuss peculiarities regarding the smaller (Figure 4.3c $d < 200$ nm) particles. Figure 4.4 summarizes the cryo-ET of IPEC2, featuring a high IPEC brush density (see also Supporting Movies SM4.3 and SM4.4). Surprisingly, we learn from the 3D reconstruction (Figure 4.4b-f) that the corona is a rather complex construct of lamellae. The reconstructed topographic isosurface of the entire particle suggests that the IPEC lamellae are oriented perpendicular to the curved particle core with an overall appearance of a “turbine” (Figure 4.4c). Moving along the stack of lamellae (from particle center to poles), the lamellae first run parallel and become progressively more bent when approaching the particle poles (Figure 4.4d). The cross-section in Figure 4.4e and the reconstructed isosurface in Figure 4.4f show regions of equal electron density (in Figure 4.4e displayed as yellow = medium and red = high). Both the IPEC lamellae and the bumpy *im*-IPEC shell on the particle core have similar contrast, which can be expected since both phases consist of similar polyelectrolytes. Since reconstruction visualizes differences in electron densities and the PB core has a contrast close to that of the background, the isosurface model of Figure 4.4f exclusively shows the IPECs with a seemingly hollow core. The flattening of the poles is again an effect of the finite thickness of the solvent film that compresses and deforms the particle. The existence of poles might also be an indication for defects that must occur when two immiscible phases (IPEC and PEO) arrange on a spherical substrate (particle core). The lamellae may thus curve to obey defect rules,⁵⁵ which could be the explanation why for some particles the lamellar features are well-visible, while they overlap and blur on the others (even within the same particle; see also Figure S4.2).

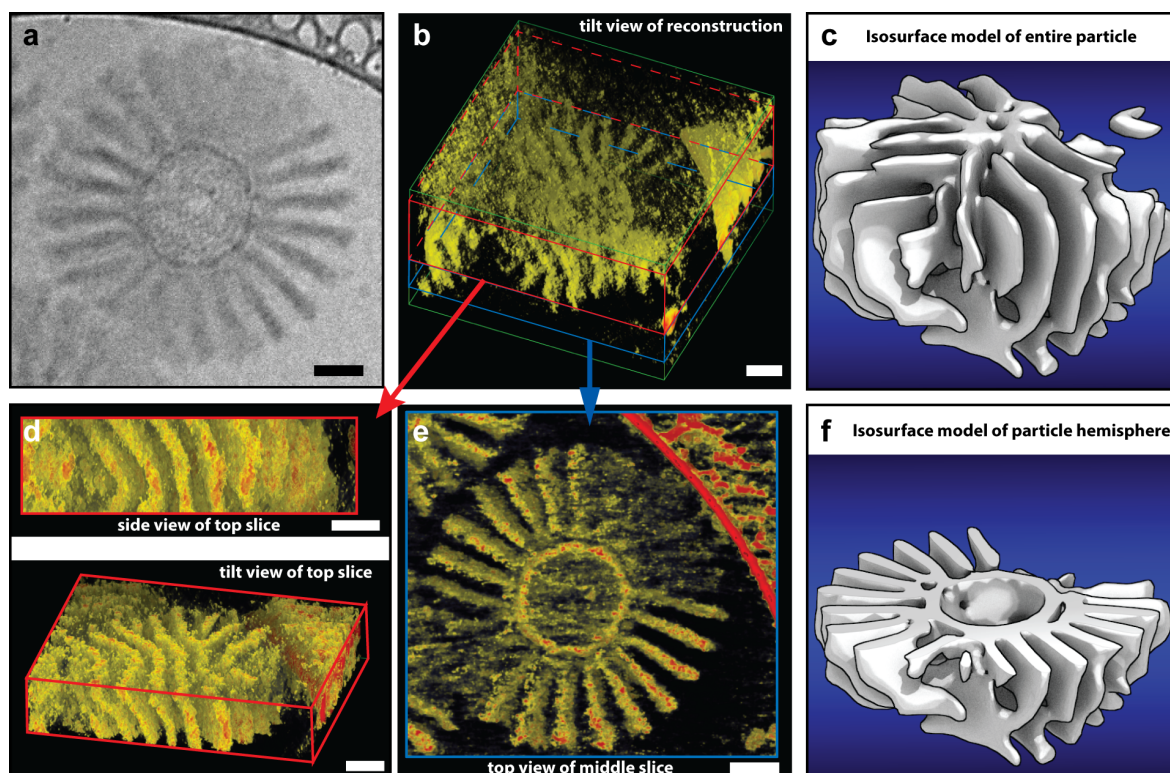


Figure 4.4. Cryo-ET reconstruction of IPEC2 (BVqMAA₁₁₇₀/Dq₈₂EO₁₁₄). **a)** Cryo-TEM image of the reconstructed micelles. **b)** Overview of reconstruction. The colored frames indicate entire reconstruction (green), top slice (red), and middle slice (blue). **c)** Isosurface of entire reconstructed micelle. **d)** Side and tilt view of top slice (red). **e)** Top view of middle slice (blue). **f)** Isosurface of micelle cropped to hemisphere. Scale bars correspond to 50 nm.

Figure 4.5a,b show the cryo-TEM image and the 3D reconstruction of the smaller IPEC2 particles that originate from lower aggregation number. Cryo-ET reveals that on the smaller particle core with high curvature and lower surface area (as compared to larger particles) the lamellae are bent so that they fuse into one continuous spiral from top to bottom of this particle (Figure 4.5c,d and Supporting Movie SM4.5). Figure 4.5c shows the reconstruction as solid isosurface with the core erased for clarity as to visualize the remaining IPEC2 spiral. The red ribbon is a guide to the eye, which is also displayed as separate item in Figure 4.5d. This morphology is surprising given the rigid properties ascribed to polyionic complexes³¹ and the seemingly stiff morphologies we discussed so far. We hypothesize that the helical arrangement of the IPEC is actually the favored structure, which we are not able to distinguish for the larger particles due to particle deformation within the solvent film. The smaller particles are located entirely in the vitrified film, allowing visualization of the undisturbed helical conformation of the IPEC2 particles (see also Figure S4.3 for image series at varying angles).

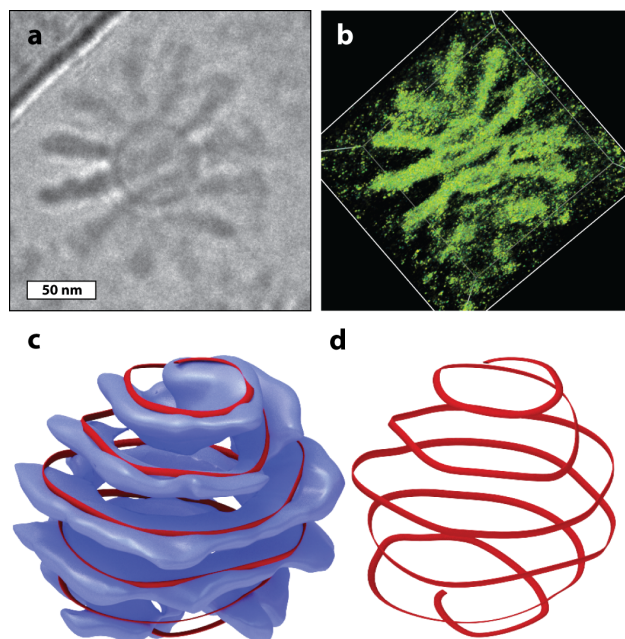


Figure 4.5. Characterization of the IPEC2 spiral morphology. **a)** Cryo-TEM showing a spherical core and IPEC lamellae bent toward the core. **b)** Reconstruction of the particle in (a). **c)** Core-subtracted isosurface of reconstruction (blue) with a red spiral as guide to the eye. **d)** The red spiral of (c) progressing from top to bottom.

Thermodynamic Stability of IPEC2. To establish whether IPEC2 is the thermodynamically favored morphology or is kinetically trapped by the fast complexation with $\text{Dq}_{82}\text{EO}_{114}$ (possibly relaxation of IPEC lamellae to cylinders), we followed the development of phase separation into lamellae by studying different $Z_{+/-}$ values and, thus, grafting density (Figure S4.4). At $Z_{+/-} = 0.25$ (low grafting density), the corona is barely visible as a shadow in cryo-TEM. With increasing $\text{Dq}_{82}\text{EO}_{114}$ content ($Z_{+/-} = 0.5$), the phase separation of the newly formed hydrophobic IPEC2 from the PEO/water phase becomes more evident in form of a dark (higher electron density) striped halo surrounding the micellar core. At $Z_{+/-} = 1$, the IPEC nanophase is fully developed and can be distinguished from the PEO/water phase. Following the complexation with DLS, the hydrodynamic radius decreases from $\langle R_h \rangle_{z,\text{app}} = 172$ nm for the ($Z_{+/-} = 0$) precursor micelles with a fully stretched PMAA corona to $\langle R_h \rangle_{z,\text{app}} = 99$ nm for the contracted, densely grafted IPEC after quantitative complexation with $\text{Dq}_{82}\text{EO}_{114}$ ($Z_{+/-} = 1$). In order to verify whether the proposed IPEC lamellae are the energetically favored structure, we increased the ionic strength from approximately 50 mM of the original buffer solution to 1000 mM by addition of NaCl (Figure S4.5). The screening of charges leads to the complete breakup of the IPEC morphology, and although the lamellar features completely vanish, the $\text{Dq}_{82}\text{EO}_{114}$ chains are assumed to remain entangled within the PMAA corona visible as a homogeneous, fuzzy shell. The added salt enhances chain mobility and causes the order-disorder transition from well-organized packed chains into a diffuse shell. Very similar structures were reported before by Schacher *et al.* complexing shorter corona chains with longer cationic homopolymer.²¹ After reducing the ionic strength by dialysis, the lamellar IPEC morphology is fully restored, indicating that the structure is energetically favored and not kinetically trapped.

Origin of the Structural Differences between IPEC1 and IPEC2. On the basis of the results of cryo-TEM and cryo-ET, we summarize the structural peculiarities of IPECs 1 and 2 in Figure 4.6 and give schematic suggestions for chain complexation and packing. Figures 4.6a-d compare both IPEC types with the help of isosurface models and schematic drawings. The isosurface models were calculated from the 3D reconstruction using an algorithmic approach (see Methods and the Supporting Information). From the isosurface models and the schematic drawings one can derive communalities between both particle types regarding the chain arrangement within the IPEC and the resulting nanophases (Figure 4.6e-f). Clearly, the dimensions of the IPECs are very different in both cases. The IPEC1 cylinders are longer and thinner compared to the IPEC2 lamellae. In general, the width of the cylinders or lamellae is too large for one single PMAA/polycation chain, but suggests that several ionically grafted chains bundle together (Figure 4.6e). To compensate the electrostatic repulsion among multiple PMAA chains, the polycations must protrude into the corona bundles and interdigitate with the polyanionic chains to reach charge neutrality. This observation is directly related to the block length of the polycations used for complexation reactions. For IPEC1 a shorter polycationic block is used, which is unable to penetrate as deep into the polyanion bundle as the longer polycationic block for the formation of the IPEC2 particles.

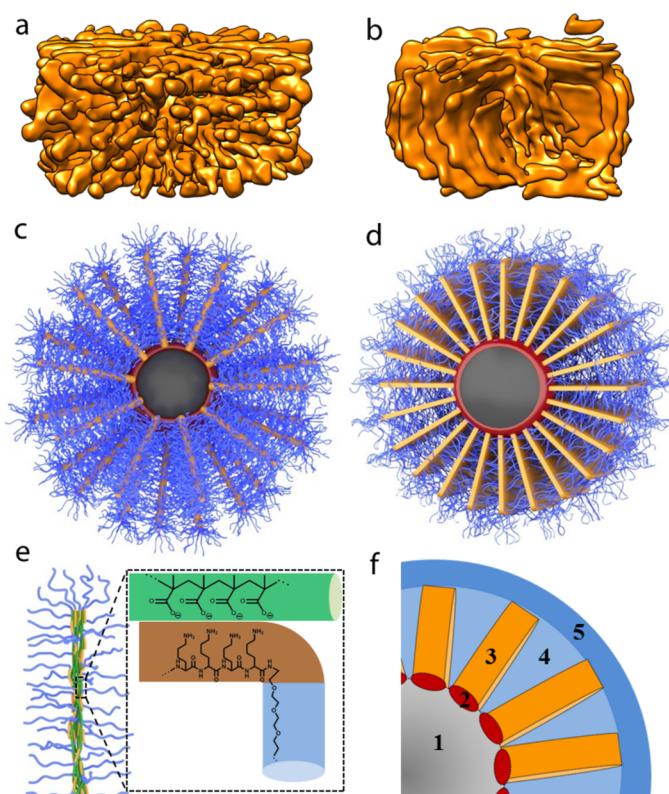


Figure 4.6. Summary of particle features. a,b) Isosurface model of the (a) “sea-urchin” micelles and (b) “turbine” micelles. **c,d)** Corresponding schematic cross-sectional cartoons. **e,f)** Both particle types have the block copolymer chain arrangements (e) in common as well as the distinct order of nanophases (f): (1) PB core, (2) *im*-IPEC, (3) secondary IPEC, (4) intercalated PEO brush, and (5) outer PEO corona.

To understand the formation of cylinders and lamellae, we determined the volume fractions of collapsed, hydrophobic IPEC domains, ϕ_{IPEC} , from the isosurface reconstructions (see the Supporting Information for calculations). We obtain a volume fraction of $\phi_{\text{IPEC1}} \approx 0.21$ for IPEC1 and $\phi_{\text{IPEC2}} \approx 0.43$ for IPEC2 (Figures S4.6 and S4.7), which are close to typical values for cylinder and lamellar bulk morphologies for highly incompatible blocks. This supports our hypothesis that the observed brush morphologies indeed originate from the occupied volumes of IPEC and PEO domains. Irrespective of the geometry of the IPEC, we classify five distinct nanodomains for all particles (Figure 4.6f): (1) The central hydrophobic PB core; (2) a patchy intramicellar IPEC shell surrounding the core; (3) the secondary IPEC brush (cylinder or lamellae) growing perpendicular from the core; (4) a PEO brush located between the hydrophobic IPEC domains; and (5) an outer PEO corona surrounding the entire particle.

Conclusions

We demonstrated the phase separation of organic nanoparticle coronas through interpolyelectrolyte complexation into anisotropic cylindrical and lamellar brush morphologies stabilized by a newly formed PEO corona. Mismatches in chain length of the participating polyions cause dense packing and overcrowding within the nanoparticle corona. This is accompanied by an immense volume requirement of the water-swollen nonionic block that provides steric stabilization for the IPEC and drives segregation into anisotropic geometries. Although the studied particles appear similar in cryo-TEM imaging, cryo-ET and computer-aided 3D particle reconstruction allowed to identify cylindrical and lamellar IPEC morphologies, depending on the length of the polycation block of bis-hydrophilic diblock copolymer used for the complexation. The volume fraction of the hydrophobic IPEC over solvent-swollen PEO corona thereby governs the resulting morphology. Strikingly, both IPEC structures are oriented perpendicular to the surface of the particle core. With the aid of cryo-ET we identify a spiral-on-sphere morphology where the IPEC lamellae fuse into a continuous spiral on the spherical core. The smaller particles are vitrified with an undisturbed corona morphology, indicating that the helical arrangement is the favored arrangement of the lamellar IPEC brush. The ability to dissect complex nanostructures into single structural components is necessary advancement for future characterization of complex soft matter.

Methods

Materials

N,N'-Dicyclohexylcarbodiimide (DCC, 99%, Fluka), 4-dimethylaminopyridine (DMAP, 99%, Acros), 1,1,4,7,10,10-hexamethyltriethylenetetramine (HMTETA, 97 % Aldrich), copper(I)chloride (CuCl, 99,9 % Acros) and pH 10 buffer solution (Titrimorm, VWR International) were used as received. Prior to use, 2-(dimethylamino)ethyl methacrylate (DMAEMA, 98%, Aldrich) was passed through a neutral silica column to remove stabilizer. Dioxane, dichloromethane and acetone were of analytical grade and used as received. α -Methoxy- ω -amino-PEG (PEG-NH₂, Mn = 12,000 g/mol, PDI = 1.03) was purchased from NOF Corporation (Tokyo, Japan), and monomethoxy-PEG (PEG-OH, Mn = 5,000 g/mol, PDI = 1.02) was purchased from Aldrich. Concentrated hydrochloric acid (37%) was used as received. Quaternization reactions were performed with either methyl iodide (99 %, Merck) in case of PEO-*b*-PDMAEMA or dimethyl sulfate (Me₂SO₄, >99%, Aldrich) for BVT and were used without further purification. Milli-Q water purified with a Millipore filtering system was used in all cases. For dialysis, membranes of regenerated cellulose (Spectrum Laboratories, Spectra/Por MWCO = 3.5 kDa and 12-14 kDa) were used.

Synthesis of B₈₃₀V₁₈₀T₁₃₅₀ Triblock Terpolymer and Conversion to B₈₃₀Vq₁₈₀MAA₁₃₅₀. The BVT triblock terpolymer was synthesized *via* sequential living anionic polymerization as reported elsewhere.⁵⁶ The polymer was characterized by a combination of MALDI-ToF-MS (molecular weight of PB), ¹H-NMR (for the composition of B₈₃₀V₁₈₀T₁₃₅₀) and size exclusion chromatography for the PDI (1.08). The conversion of BVT to BVqMAA micellar solutions was reported in a previous publication.²³

Synthesis of PEO₁₁₄ Macroinitiator. The PEO₁₁₄-Br macroinitiator was synthesized *via* Steglich esterification. To a 100 mL three-neck round-bottom flask equipped with a magnetic stirrer, 5.0 g (1.00 mmol) monomethoxy-poly(ethylene glycol) ($M_n = 5\ 000$, PDI = 1.02), a catalytic amount of DMAP (24.4 mg, 0.02 mmol) and 1.03 g (5 mmol) DCC were added, and all reactants were dissolved in 30 mL of dry DCM. The mixture was stirred at RT until complete dissolution of PEO. This solution was put in an ice bath and 0.47 g (3.00 mmol) 2-bromoisobutyric acid dissolved in 5 mL dichloromethane was added dropwise under a nitrogen atmosphere. The reaction solution was stirred at room temperature for 18 h, and produced salt was filtered. DCM was removed with a rotary evaporator. The white residue was dissolved in 40 mL ethanol by heating (50 °C). The clear yellowish solution then was rapidly cooled down with liquid nitrogen, and recrystallized PEO₁₁₄-Br centrifuged in order to remove the soluble compounds by decantation while the product remained precipitated. This procedure was repeated several times until the solution became clear and colorless. Finally the product was dissolved in dioxane and freeze dried overnight. In this manner 4.10 g of white macroinitiator could be obtained corresponding to a yield of 95 %.

Synthesis of PEO₁₁₄-*b*-PDMAEMA₈₂ Diblock Copolymer. The PEO-*b*-PDMAEMA diblock copolymer was synthesized by ATRP in acetone. The PEO macroinitiator with $M_n = 5000$ g/mol (3.00 g, 1.5 mmol), CuCl (149 mg, 1.5 mmol), DMAEMA (17.686 g, 113 mmol), and 40 ml of acetone were added to a 100 ml screw cap glass equipped with a magnetic stir bar. In another 10 ml screw cap glass the ligand (HMTETA, 0.81 g, 3 mmol) was dissolved in 2 ml of acetone (plus 5 mL acetone as excess for degassing). Both solutions were purged with nitrogen separately for about 20 min to remove traces of oxygen. The ligand then was transferred to the 100 ml screw cap glass with a nitrogen-flushed syringe, and the solution was immersed in a thermostated oil bath at 50 °C. The reaction was continued under stirring for two hours and quenched by cooling to room temperature and exposure to air. In order to remove the catalyst, the solution was diluted with THF and passed through a neutral silica column. The eluent was concentrated using a rotary evaporator. The highly viscous PEO-*b*-PDMAEMA was dissolved in a small amount of THF and precipitated in cold *n*-hexane (-30 °C) followed by freeze-drying from water. From SEC measurements a PDI of 1.17 was obtained, using PEO standards for calibration and from ¹H-NMR measurement a composition of PEO₁₁₄-*b*-PDMAEMA₈₂ was determined.

Quaternization of PDMAEMA. The quaternization of the PEO-*b*-PDMAEMA block copolymer was performed with methyl iodide in aqueous solution. In a typical experiment, 100 mg of the PEO-*b*-PDMAEMA diblock copolymer was dissolved in 10 mL of deionized water. Then, 10 equiv of methyl iodide (compared to DMAEMA units) was added to the solution while stirring. After 2 days, the polymer solution was dialyzed against dioxane/water (50:50 v/v) and then THF to remove excess methyl iodide and finally back to Milli-Q water. The resulting PEO-*b*-PDMAEMA_q (Dq₈₂EO₁₁₄) was recovered as a powder by freeze-drying.

Synthesis of PEO₂₇₀-*b*-PLL₄₀ Diblock Copolymer. The synthesis of the PEO-*b*-PLL diblock copolymer was described in detail in a previous publication.³² In short, the *N*-carboxy anhydride of the trifluoroacetyl protected _L-lysine was first dissolved in dry DMF under an argon atmosphere. Afterward, α -methoxy- ω -amino PEG dissolved in DMF was added to the protected _L-lysine, and the mixture was stirred at 25°C for 72 h until the polymerization was completed. After dialysis against methanol and freeze-drying from dioxane, the PLL block was deprotected under basic conditions (NaOH containing MeOH) by stirring for 10 h at 35 °C. Purification was performed by dialysis against pH 4 aqueous solution with subsequent freeze-drying. A PDI of 1.05 of the protected diblock copolymer was measured with SEC using DMF as eluent. From ¹H-NMR measurement a composition of PEO₂₇₀-*b*-PLL₄₀ was determined.

Preparation of IPEC1 Solutions. For complexation reactions of IPEC1, the precursor micelles were first transferred to a PBS buffer solution (pH 7.4 with additional 140 mM NaCl). After addition of a certain amount of a 10 g/L stock solution of LL₄₀EO₂₇₀ in PBS, the mixture was stirred for at least 7 days. Additionally cross-linking with *N*-(3-dimethylaminopropyl)-*N'*-ethylcarbodiimide hydrochloride was performed according to a recipe described elsewhere.³²

Preparation of IPEC2 Solutions. Dq₈₂EO₁₁₄ was first dissolved in buffer pH 10 to give a 5 g/L solution. Afterward, a defined amount of the Dq₈₂EO₁₁₄ solution was added to 2 mL of a 0.56 g/L solution of BVqMAA precursor micelles in pH 10 buffer solution while stirring to reach full complexation and a $Z_{+/-}$ -value of 1. The IPEC-solution was stirred for a week at room temperature before analysis.

Characterization

¹H-NMR. Spectra were recorded on a Bruker Ultrashield 300 spectrometer with a 300 MHz operating frequency using either deuterated chloroform or deuterated water as solvents.

Size Exclusion Chromatography (SEC). Size exclusion chromatography measurements were performed on a set of 30 cm SDV-gel columns of 5 mm particle size having a pore size of 10⁵, 10⁴, 10³, and 10² Å with refractive index and UV ($\lambda = 254$ nm) detection. SEC was measured at an elution rate of 1 mL/min with THF as eluent. For LL₄₀EO₂₇₀ a Tosoh instrument (Yamaguchi, Japan) calibrated with PEG standards and equipped with three TSK columns (TSK guard column HHR-L; TSKgel G4000HHR; TSKgel G3000HHR) and a refractive index detector (RI) at 40 °C was used. DMF with 10 mM LiCl was used as eluent at a flow rate of 0.8 mL/min.

Dynamic Light Scattering (DLS). Measurements were performed on an ALV DLS/SLS-SP 5022F compact goniometer system with an ALV 5000/E cross correlator and a He–Ne laser ($\lambda = 632.8$ nm). The measurements were carried out in cylindrical scattering cells ($d = 10$ mm) at an angle of 90°. Prior to the measurements samples were passed through nylon filters (Magna, Roth) with a pore size of 5 μm to remove impurities/dust particles. The CONTIN algorithm was applied to analyze the obtained correlation functions. Apparent hydrodynamic radii ($\langle R_h \rangle_{z, \text{app}}$) were calculated according to the Stokes–Einstein equation, and polydispersities were obtained *via* the cumulant analysis where applicable.

ζ -Potential Measurements. Measurements were performed with disposable capillary cells (DTS1061) on Malvern Zetasizer, using approximately 800 μL of the aqueous micellar solutions. The ζ -potential was calculated from electrophoretic mobility applying the Smoluchowski equation.

Cryogenic Transmission Electron Microscopy (cryo-TEM). Cryo-TEM measurements were performed at the University of Bayreuth as well as at the Aalto University. For cryo-TEM studies in Bayreuth, 3 μL of the aqueous micellar solution ($c \approx 0.5$ g/L) was placed on a lacey carbon-coated copper TEM grid (200 mesh, Science Services), where most of the liquid was blotted with filter paper, leaving a thin film spread between the fibers of the carbon network. The specimens were shock vitrified by rapid immersion into liquid ethane in a temperature-controlled freezing unit (Zeiss Cryobox, Zeiss NTS GmbH) and cooled to approximately 90 K. The temperature was monitored and kept constant in the chamber during all of the preparation steps. After freezing the specimens they were inserted into a cryo-

transfer holder (CT3500, Gatan) and transferred to a Zeiss EM922 Omega EFTEM instrument. Measurements were carried out at temperatures around -183°C . The microscope was operated at an acceleration voltage of 200 kV. Zero-loss filtered images ($\Delta E = 0$ eV) were taken under reduced dose conditions. All images were recorded digitally by a bottom mounted CCD camera system (Ultrascan 1000, Gatan), and processed with a digital imaging processing system (Gatan Digital Micrograph 3.9 for GMS 1.4). For cryo-TEM measurements at Aalto University, imaging was carried out using JEM 3200FSC field emission microscope (Jeol) operated at 300 kV in bright field mode with an Omega-type Zero-loss energy filter. The images were acquired with an Ultrascan 4000 CCD camera (Gatan) and with Gatan Digital Micrograph software (version 1.83.842), while the specimen temperature was maintained at -187°C . Vitri-fied samples were prepared using a FEI Vitrobot placing 3 μL sample solution on 200 mesh holey carbon copper grids under 100% humidity, then blotted with filter paper 0.5–1.5 s, and immediately plunged to -170°C ethane/propane mixture and cryotransferred to the microscope.

Cryogenic Transmission Electron Tomography (cryo-ET). Cryo-ET measurements were performed at the Aalto University with the same transmission electron microscope that was used for cryo-TEM imaging. Electron tomographic tilt series were acquired with the SerialEM software package (version 3.2.2). Samples were tilted between $\pm 69^{\circ}$ angles with $2\text{--}3^{\circ}$ increment steps. For a detailed description of the alignment and reconstruction procedure see the Supporting Information.

ASSOCIATED CONTENT

Conflict of Interest

The authors declare no competing financial interest.

Supporting Information

Figures S4.1–S4.7, Tables S4.1, supporting calculations and descriptions of cryo-ET method, and supporting movies SM4.1–SM4.5. This material is available free of charge *via* the Internet at <http://pubs.acs.org>.

Author Information

Corresponding Authors

andre.groschel@aalto.fi; axel.mueller@uni-mainz.de;

Notes

TIL and JH contributed equally to this work.

Acknowledgements

The authors acknowledge the Deutsche Forschungsgemeinschaft (DFG) for supporting this work within DFG Mu896/39-1. This work was carried out under the Academy of Finland's

Center of Excellence Programme (2014-2019) and supported by ERC-2011-AdG (291364-MIMEFUN). This work made use of the Aalto University Nanomicroscopy Center (Aalto-NMC) premises.

References

1. Glotzer, S. C.; Solomon, M. J. Anisotropy of Building Blocks and Their Assembly into Complex Structures. *Nat. Mater.* **2007**, *6*, 557–562.
2. Walther, A.; Müller, A. H. E. Janus Particles: Synthesis, Self-Assembly, Physical Properties, and Applications. *Chem. Rev.* **2013**, *113*, 5194–5261.
3. Du, J.; O'Reilly, R. K. Anisotropic Particles with Patchy, Multicompartment and Janus Architectures: Preparation and Application. *Chem. Soc. Rev.* **2011**, *40*, 2402–16.
4. Zhu, J.; Zhang, S.; Zhang, K.; Wang, X.; Mays, J. W.; Wooley, K. L.; Pochan, D. J. Disk-Cylinder and Disk-Sphere Nanoparticles via a Block Copolymer Blend Solution Construction. *Nat. Commun.* **2013**, *4*, 2297.
5. Rupar, P. A.; Chabanne, L.; Winnik, M. A.; Manners, I. Non-Centrosymmetric Cylindrical Micelles by Unidirectional Growth. *Science* **2012**, *337*, 559–562.
6. Gröschel, A. H.; Schacher, F. H.; Schmalz, H.; Borisov, O. V.; Zhulina, E. B.; Walther, A.; Müller, A. H. E. Precise Hierarchical Self-Assembly of Multicompartment Micelles. *Nat. Commun.* **2012**, *3*, 710.
7. Moughton, A. O.; Hillmyer, M. A.; Lodge, T. P. Multicompartment Block Polymer Micelles. *Macromolecules* **2012**, *45*, 2–19.
8. Bates, F. S.; Hillmyer, M. A.; Lodge, T. P.; Bates, C. M.; Delaney, K. T.; Fredrickson, G. H. Multiblock Polymers: Panacea or Pandora's Box? *Science* **2012**, *336*, 434–440.
9. Wyman, I. W.; Liu, G. Micellar Structures of Linear Triblock Terpolymers: Three Blocks but Many Possibilities. *Polymer* **2013**, *54*, 1950–1978.
10. Zhang, L.; Yu, K.; Eisenberg, A. Ion-Induced Morphological Changes in “Crew-Cut” Aggregates of Amphiphilic Block Copolymers. *Science* **1996**, *272*, 1777–1779.
11. Förster, S.; Hermsdorf, N.; Böttcher, C.; Lindner, P. Structure of Polyelectrolyte Block Copolymer Micelles. *Macromolecules* **2002**, *35*, 4096–4105.
12. Pergushov, D. V.; Müller, A. H. E.; Schacher, F. H. Micellar Interpolyelectrolyte Complexes. *Chem. Soc. Rev.* **2012**, *41*, 6888–6901.
13. Sharma, G.; Mei, Y.; Lu, Y.; Ballauff, M.; Irrgang, T.; Proch, S.; Kempe, R. Spherical Polyelectrolyte Brushes as Carriers for Platinum Nanoparticles in Heterogeneous Hydrogenation Reactions. *J. Catal.* **2007**, *246*, 10–14.
14. Wittemann, A.; Haupt, B.; Ballauff, M. Adsorption of Proteins on Spherical Polyelectrolyte Brushes in Aqueous Solution. *Phys. Chem. Chem. Phys.* **2003**, *5*, 1671–1677.
15. Wittemann, A.; Ballauff, M. Interaction of Proteins with Linear Polyelectrolytes and Spherical Polyelectrolyte Brushes in Aqueous Solution. *Phys. Chem. Chem. Phys.* **2006**, *8*, 5269–5275.

16. Wang, S.; Chen, K.; Li, L.; Guo, X. Binding between Proteins and Cationic Spherical Polyelectrolyte Brushes: Effect of pH, Ionic Strength, and Stoichiometry. *Biomacromolecules* **2013**, *14*, 818–827.
17. Haupt, B.; Neumann, T.; Wittemann, A.; Ballauff, M. Activity of Enzymes Immobilized in Colloidal Spherical Polyelectrolyte Brushes. *Biomacromolecules* **2005**, *6*, 948–955.
18. Harada, A.; Kataoka, K. Chain Length Recognition: Core-Shell Supramolecular Assembly from Oppositely Charged Block Copolymers. *Science* **1999**, *283*, 65–67.
19. Gohy, J.-F.; Varshney, S. K.; Jérôme, R. Water-Soluble Complexes Formed by Poly(2-Vinylpyridinium)- B Lock -Poly(ethylene Oxide) and Poly(sodium Methacrylate)- B Lock -Poly(ethylene Oxide) Copolymers. *Macromolecules* **2001**, *34*, 3361–3366.
20. Schacher, F.; Walther, A.; Müller, A. H. E. Dynamic Multicompartment-Core Micelles in Aqueous Media. *Langmuir* **2009**, *25*, 10962–10969.
21. Schacher, F.; Betthausen, E.; Walther, A.; Schmalz, H.; Pergushov, D. V; Müller, A. H. E. Interpolyelectrolyte Complexes of Dynamic Multicompartment Micelles. *ACS Nano* **2009**, *3*, 2095–2102.
22. Synatschke, C. V.; Schacher, F. H.; Förtsch, M.; Drechsler, M.; Müller, A. H. E. Double-Layered Micellar Interpolyelectrolyte Complexes— How Many Shells to a Core? *Soft Matter* **2011**, *7*, 1714–1725.
23. Synatschke, C. V; Löblich, T. I.; Förtsch, M.; Hanisch, A.; Schacher, F. H.; Müller, A. H. E. Micellar Interpolyelectrolyte Complexes with a Compartmentalized Shell. *Macromolecules* **2013**, *46*, 6466–6474.
24. Kabanov, V. A. Polyelectrolyte Complexes in Solution and in Bulk. *Russ. Chem. Rev.* **2005**, *74*, 3–20.
25. Lefèvre, N.; Fustin, C.-A.; Gohy, J.-F. Polymeric Micelles Induced by Interpolymer Complexation. *Macromol. Rapid Commun.* **2009**, *30*, 1871–1888.
26. Pergushov, D. V; Zezin, A. A.; Zezin, A. B.; Müller, A. H. E. Advanced Functional Structures Based on Interpolyelectrolyte Complexes. In *Adv Polym Sci*; 2012.
27. Schrage, S.; Sigel, R.; Schlaad, H. Formation of Amphiphilic Polyion Complex Vesicles from Mixtures of Oppositely Charged Block Ionomers. *Macromolecules* **2003**, *36*, 2–5.
28. Plamper, F. A.; Gelissen, A. P.; Timper, J.; Wolf, A.; Zezin, A. B.; Richtering, W.; Tenhu, H.; Simon, U.; Mayer, J.; Borisov, O. V; *et al.* Spontaneous Assembly of Miktoarm Stars into Vesicular Interpolyelectrolyte Complexes. *Macromol. Rapid Commun.* **2013**, *34*, 855–860.
29. Anraku, Y.; Kishimura, A.; Oba, M.; Yamasaki, Y.; Kataoka, K. Spontaneous Formation of Nanosized Unilamellar Polyion Complex Vesicles with Tunable Size and Properties. *J. Am. Chem. Soc.* **2010**, *132*, 1631–1636.
30. Voets, I. K.; Keizer, A. De; Waard, P. De; Frederik, P. M.; Bomans, P. H. H.; Schmalz, H.; Walther, A.; King, S. M.; Leermakers, F. A. M.; Stuart, M. A. C. Double-Faced Micelles from Water-Soluble Polymers. *Angew. Chem. Int. Ed.* **2006**, *45*, 6673–6676.

31. Christian, D. A.; Tian, A.; Ellenbroek, W. G.; Levental, I.; Rajagopal, K.; Janmey, P. A.; Liu, A. J.; Baumgart, T.; Discher, D. E. Spotted Vesicles, Striped Micelles and Janus Assemblies Induced by Ligand Binding. *Nat. Mater.* **2009**, *8*, 843–849.
32. Synatschke, C. V.; Nomoto, T.; Cabral, H.; Förtsch, M.; Toh, K.; Matsumoto, Y.; Miyazaki, K.; Hanisch, A.; Schacher, F. H.; Kishimura, A.; *et al.* Multicompartment Micelles with Adjustable Poly(ethylene Glycol) Shell for Efficient in Vivo Photodynamic Therapy. *ACS Nano* **2014**, *8*, 1161–1172.
33. Larin, S. V.; Pergushov, D. V.; Xu, Y.; Darinskii, A. A.; Zezin, A. B.; Müller, A. H. E.; Borisov, O. V. Nano-Patterned Structures in Cylindrical Polyelectrolyte Brushes Assembled with Oppositely Charged Polyions. *Soft Matter* **2009**, *5*, 4938–4943.
34. Pons-Siepermann, I. C.; Glotzer, S. C. Design of Patchy Particles Using Quaternary Self-Assembled Monolayers. *ACS Nano* **2012**, *6*, 3919–3924.
35. Kostiainen, M. A.; Hiekkataipale, P.; Laiho, A.; Lemieux, V.; Seitsonen, J.; Ruokolainen, J.; Ceci, P. Electrostatic Assembly of Binary Nanoparticle Superlattices Using Protein Cages. *Nat. Nanotechnol.* **2013**, *8*, 52–56.
36. Chen, Q.; Diesel, E.; Whitmer, J. K.; Bae, S. C.; Luijten, E.; Granick, S. Triblock Colloids for Directed Self-Assembly. *J. Am. Chem. Soc.* **2011**, *133*, 7725–7727.
37. Chen, Q.; Bae, S. C.; Granick, S. Staged Self-Assembly of Colloidal Metastructures. *J. Am. Chem. Soc.* **2012**, *134*, 11080–11083.
38. Gröschel, A. H.; Walther, A.; Löblich, T. I.; Schmelz, J.; Hanisch, A.; Schmalz, H.; Müller, A. H. E. Facile, Solution-Based Synthesis of Soft, Nanoscale Janus Particles with Tunable Janus Balance. *J. Am. Chem. Soc.* **2012**, *134*, 13850–13860.
39. Wang, X.; Guerin, G.; Wang, H.; Wang, Y.; Manners, I.; Winnik, M. A. Cylindrical Block Copolymer Micelles and Co-Micelles of Controlled Length and Architecture. *Science* **2007**, *317*, 644–647.
40. Hudson, Z. M.; Lunn, D. J.; Winnik, M. A.; Manners, I. Colour-Tunable Fluorescent Multiblock Micelles. *Nat. Commun.* **2014**, *5*, 3372.
41. Schmelz, J.; Karg, M.; Hellweg, T.; Schmalz, H. General Pathway toward Crystalline-Core Micelles with Tunable Morphology and Corona Segregation. *ACS Nano* **2011**, *5*, 9523–9534.
42. Zhong, S.; Pochan, D. J. Cryogenic Transmission Electron Microscopy for Direct Observation of Polymer and Small-Molecule Materials and Structures in Solution. *Polym. Rev.* **2010**, *50*, 287–320.
43. Newcomb, C. J.; Moyer, T. J.; Lee, S. S.; Stupp, S. I. Advances in Cryogenic Transmission Electron Microscopy for the Characterization of Dynamic Self-Assembling Nanostructures. *Curr. Opin. Colloid Interface Sci.* **2012**, *17*, 350–359.
44. Nudelman, F.; With, G. de; Sommerdijk, N. A. J. M. Cryo-Electron Tomography: 3-Dimensional Imaging of Soft Matter. *Soft Matter* **2011**, *7*, 17–24.
45. Song, F.; Chen, P.; Sun, D.; Wang, M.; Dong, L.; Liang, D.; Xu, R.-M.; Zhu, P.; Li, G. Cryo-EM Study of the Chromatin Fiber Reveals a Double Helix Twisted by Tetranucleosomal Units. *Science* **2014**, *344*, 376–380.
46. Majoinen, J.; Haataja, J. S.; Appelhans, D.; Lederer, A.; Olszewska, A.; Seitsonen, J.; Aseyev, V.; Kontturi, E.; Rosilo, H.; Österberg, M.; *et al.* Supracolloidal

- Multivalent Interactions and Wrapping of Dendronized Glycopolymers on Native Cellulose Nanocrystals. *J. Am. Chem. Soc.* **2014**, *136*, 866–869.
47. Nudelman, F.; Pieterse, K.; George, A.; Bomans, P. H. H.; Friedrich, H.; Brylka, L. J.; Hilbers, P. A. J.; With, G. de; Sommerdijk, N. A. J. M. The Role of Collagen in Bone Apatite Formation in the Presence of Hydroxyapatite Nucleation Inhibitors. *Nat. Mater.* **2010**, *9*, 1004–1009.
 48. McKenzie, B. E.; Nudelman, F.; Bomans, P. H. H.; Holder, S. J.; Sommerdijk, N. A. J. M. Temperature-Responsive Nanospheres with Bicontinuous Internal Structures from a Semicrystalline Amphiphilic Block Copolymer. *J. Am. Chem. Soc.* **2010**, *132*, 10256–10259.
 49. Parry, A. L.; Bomans, P. H. H.; Holder, S. J.; Sommerdijk, N. A. J. M.; Biagini, S. C. G. Cryo Electron Tomography Reveals Confined Complex Morphologies of Tripeptide-Containing Amphiphilic Double-Comb Diblock Copolymers. *Angew. Chemie Int. Ed.* **2008**, *47*, 8859–8862.
 50. Hanisch, A.; Förtsch, M.; Drechsler, M.; Jinnai, H.; Ruhland, T. M.; Schacher, F. H.; Müller, A. H. E. Counterion-Mediated Hierarchical Self-Assembly of an ABC Mikroarm Star Terpolymer. *ACS Nano* **2013**, *7*, 4030–4041.
 51. Dupont, J.; Liu, G.; Niihara, K.; Kimoto, R.; Jinnai, H. Self-Assembled ABC Triblock Copolymer Double and Triple Helices. *Angew. Chemie Int. Ed.* **2009**, *48*, 6144–6147.
 52. Hickey, R. J.; Koski, J.; Meng, X.; Riggelman, R. a; Zhang, P.; Park, S.-J. Size-Controlled Self-Assembly of Superparamagnetic Polymersomes. *ACS Nano* **2014**.
 53. Jinnai, H.; Spontak, R. J.; Nishi, T. Transmission Electron Microtomography and Polymer Nanostructures. *Macromolecules* **2010**, *43*, 1675–1688.
 54. Hermans, T. M.; Broeren, M. A. C.; Gomopoulos, N.; Schoot, P. van der; Genderen, M. H. P. van; Sommerdijk, N. A. J. M.; Fytas, G.; Meijer, E. W. Self-Assembly of Soft Nanoparticles with Tunable Patchiness. *Nat. Nanotechnol.* **2009**, *4*, 721–726.
 55. Zhang, L.; Wang, L.; Lin, J. Defect Structures and Ordering Behaviours of Diblock Copolymers Self-Assembling on Spherical Substrates. *Soft Matter* **2014**, *10*, 6713–6721.
 56. Schacher, F.; Yuan, J.; Schoberth, H. G.; Müller, A. H. E. Synthesis, Characterization, and Bulk Crosslinking of Polybutadiene-Block-poly(2-Vinyl Pyridine)-Block-Poly(tert-Butyl Methacrylate) Block Terpolymers. *Polymer* **2010**, *51*, 2021–2032.

Supporting Information

to

Hidden Structural Features of Compartmentalized Nanoparticles Revealed by Cryogenic Transmission Electron Tomography

by Tina I. Löbling, Johannes Haataja, Christopher V. Synatschke, Felix H. Schacher,

Melanie Müller, Andreas Hanisch, André H. Gröschel*, and Axel H. E. Müller*

Supporting Movies:

SM4.1: Cryo-ET tilt series of IPEC1. The movie shows a holey carbon grid with vitrified film containing several IPEC1 particles. The grid is rotating around an axis with 45° angle.

SM4.2: Isosurface model of IPEC1. This clip shows the reconstructed isosurface of one selected IPEC1 particle. The particle rotates around the z-axis while being cropped.

SM4.3: Cryo-ET tilt series of IPEC2. The movie shows a holey carbon grid with vitrified film containing several IPEC2 particles. The grid is rotating around an axis with 45° angle.

SM4.4: Isosurface model of IPEC2. This clip shows the reconstructed isosurface of one selected IPEC2 particle. The particle rotates around the z-axis while being cropped.

SM4.5: 3D reconstruction of IPEC2 showing spiral-on-sphere structure. SM5 shows the reconstructed volume of one selected IPEC2 particle with spiral morphology. The particle first rotates 180° around the z-axis and then 180° around the x-axis.

Cryo-Electron Tomography

Alignment and Reconstruction. For image alignment purposes, the TEM grids were dipped in gold nanoparticle solution before sample deposition ($\delta = 3\text{--}10$ nm, stabilized by *11-mercapto-1-undecanol* ligand).¹ Prealignment of tilt image series was done with IMOD² and the fine alignment and cropping with custom-made Silicon Graphics JPEGANIM-software package.³ The images were binned twice to reduce noise and computation time. Maximum entropy method (MEM) reconstruction scheme was carried out with custom-made script on Mac or Linux cluster with regularization parameter value of $\delta = 1.0E^3$.

Electron Tomography: Mathematical Considerations. Tomography is a method for reconstructing 3D objects from a set of its 2D projections. In transmission electron tomography (ET) and in cryo-ET the series of projection images is recorded with TEM at various angles between $\pm\phi_{\max}$. The typical value for ϕ_{\max} is 70° due to the obstruction of electron beam by the support mesh of the grid. Because of this boundary condition, ET is classified as limited-angle tomography and the reconstructed volume has an anisotropic resolution due to the limited data acquisition. The discretized forward model of ET can be described analogously to the forward model of light microscopy tomography by the linear operator $\mathbf{A}_{\phi_i}: \rightarrow \mathbb{R}^{KM}$

$$\mathbf{y} = \mathbf{A}_\phi \mathbf{f}$$

, where $\mathbf{f} \in \mathbb{R}^N$ is the piecewise continuous density volume of the structure of interest (N voxels, *i.e.* volumetric pixels) and $\mathbf{y} = [y_1, \dots, y_K] \in \mathbb{R}^{KM}$ is the set of piecewise continuous density images (each M pixels). The $\mathbf{A}_\phi = [\mathbf{A}_{\phi_1}^T, \dots, \mathbf{A}_{\phi_K}^T]$ is a set of products of three linear operators, which are the projection matrix, 3D convolution matrix, and rotation-translation matrix, along each respective projection angle $[\phi_1, \dots, \phi_K]$.⁴ The 3D convolution matrix describes the optical imperfections (spherical and chromatic aberration) of the electron microscope and the rotation-translation matrix accounts the movement of the sample during the image acquisition process. For this work maximum entropy method (MEM) was selected for reconstructing features in a low-amplitude background.⁵ In MEM entropy of the volume $E(\mathbf{f}) = -\sum_{i=1}^N f_i \log f_i/f_0$, where $f_0 > 0$ is a given constant, is used as regularizing term in the Tikhonov functional

$$\|\mathbf{y} - \mathbf{A}_\phi \mathbf{f}\|^2 + \delta E(\mathbf{f})$$

, *i.e.*, the regularization term is minimized by maximizing the entropy of the volume.

Visualization of 3D Reconstruction. Volumetric graphics and analyses were performed with the UCSF Chimera package.⁶ The isosurface models of the particles were prepared by using Trainable Weka Segmentation⁷ plug-in for the FIJI open-source software package⁸ and then consequently low-pass filtered with Chimera's Gaussian filter with 5.0 voxel radius.

Polymer Specifics

Table S4.1. Characteristics of the used polybutadiene-*block*-poly(2-vinylpyridine)-*block*-poly(*tert*-butyl methacrylate) (BVT) and polybutadiene-*block*-poly(1-methyl-2-vinylpyridinium)-*block*-poly(methacrylic acid) (BVqMAA) triblock terpolymer.

Polymer ^{a)}	M _n [kg/mol]	PDI ^{d)}	$\langle R_h \rangle_{z,app}$ [nm] ^{e)}	R _{core} [nm] ^{f)}	N _{agg} ^{g)}
B ₈₃₀ V ₁₈₀ T ₁₃₅₀	256 ^{b)}	1.08	-	-	-
B ₈₃₀ Vq ₁₈₀ MAA ₁₃₅₀	183 ^{c)}	-	172	22.9±5.1	650

^{a)} Degrees of polymerization are denoted as subscripts. ^{b)} Calculated from a combination of MALDI-ToF-MS (for the PB block) and ¹H NMR data. ^{c)} Calculated from degrees of polymerization without taking the counterions of PVq into account. ^{d)} Determined from SEC measurements with THF as eluent and linear polystyrene as calibration standard. ^{e)} Hydrodynamic radius determined from DLS. ^{f)} PB core diameters determined from cryo-TEM images. ^{g)} The number of chains, N_{agg}, was calculated from R_{core} according to equation S4.1.

Aggregation number, N_{agg}:

$$N_{agg} = \frac{m_{core}}{m_{PB}^{chain}} = \frac{4\pi N_A \rho_{PB} R_{core}^3}{3M_{PB}^{chain}} \quad (\text{S4.1})$$

m_{core} : mass of the micellar core; m_{PB}^{chain} : mass of an individual PB chain; N_A : Avogadro constant; ρ_{PB} : density of polybutadiene; R_{core} : radius of the core; M_{PB}^{chain} : molecular weight of an individual PB chain

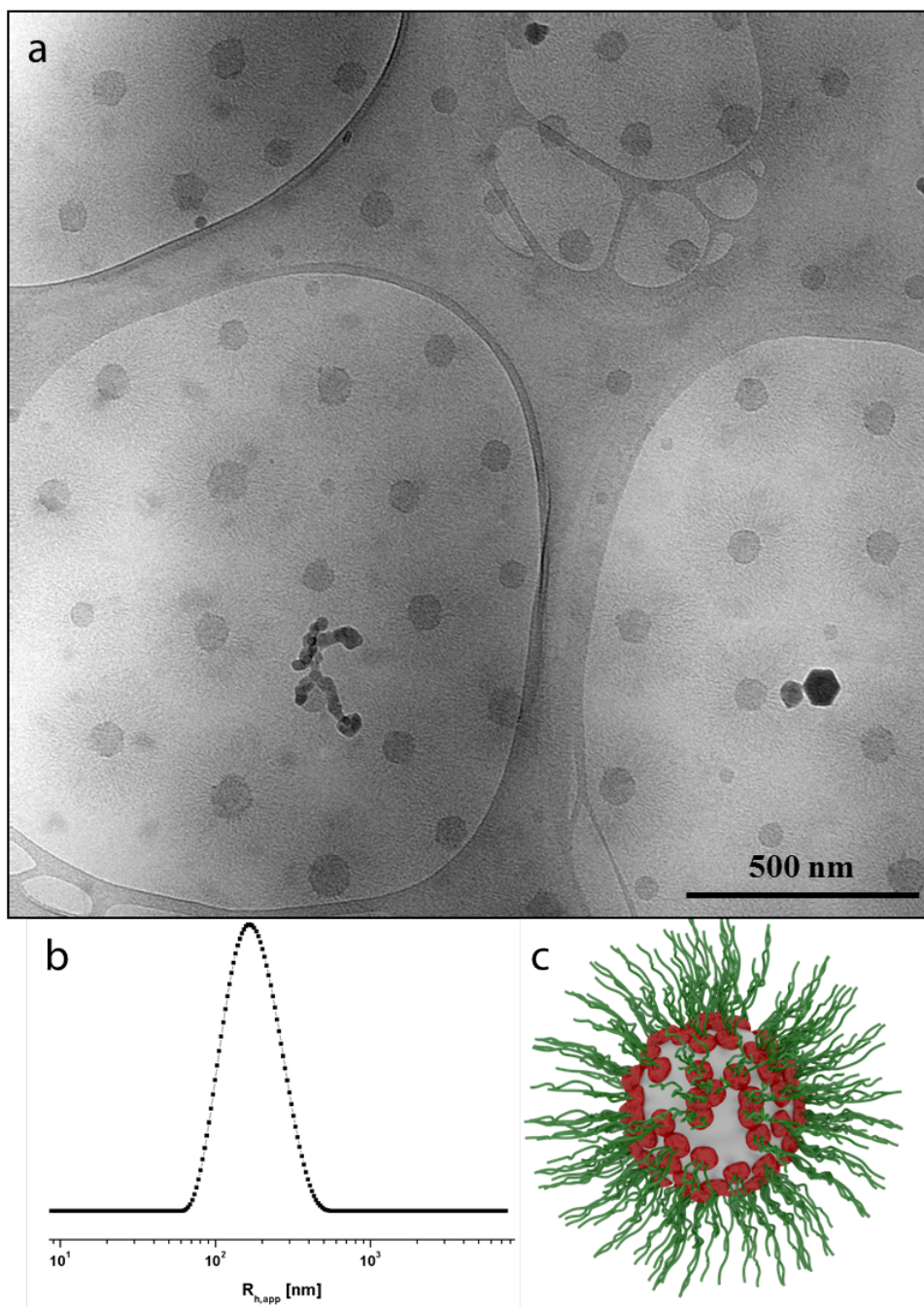


Figure S4.1. **a)** Cryo-TEM image of BVqMAA precursor micelles in pH10 buffer solution at a concentration of 0.56 g/L. **b)** Intensity weighted DLS CONTIN plot of the micelles ($\langle R_h \rangle_{z,app} = 172$ nm; DI=0.12) and **(c)** schematic illustration of the BVqMAA micelles.

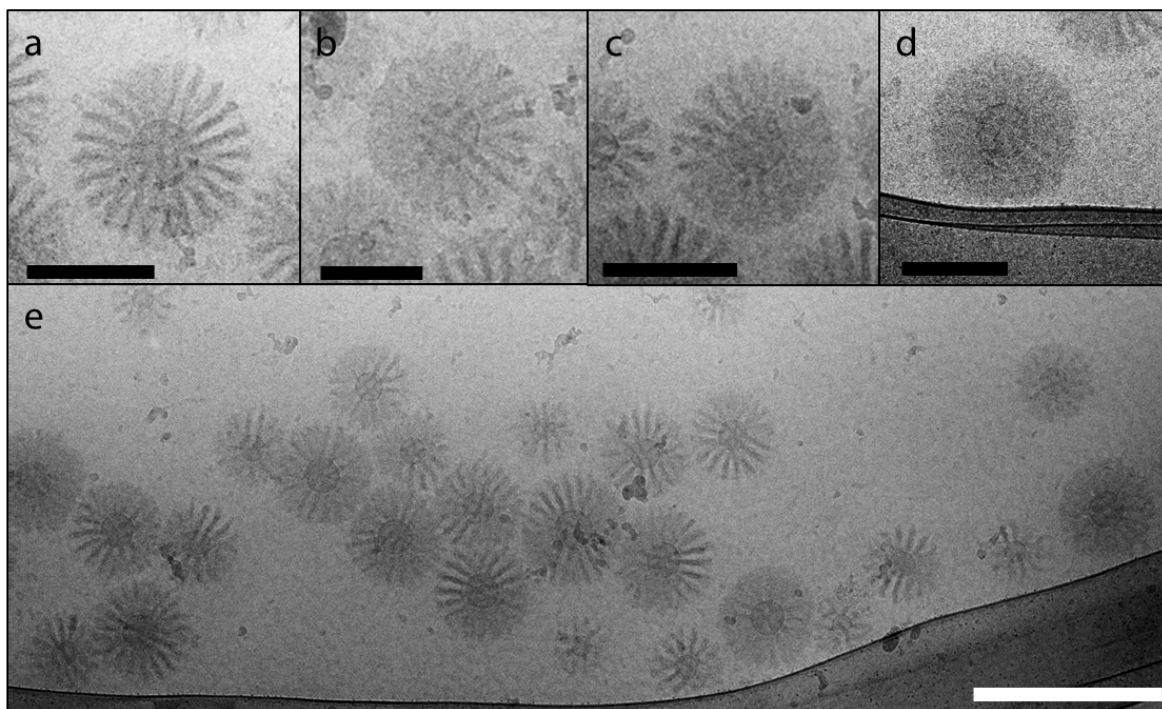


Figure S4.2: Cryo-TEM images of IPEC2 micelles in various directions at 0° tilt angle: **a)** The lamellae of the particle is perpendicular to the observation plane, so that the IPEC has a “ray-like” appearance. **b,c)** The lamellae of the particle is not perfect perpendicular leading to blurring. **d)** The lamellae of this particle are parallel to the observation plane and the IPEC appears as a homogeneous shell around the spherical PB core. The scale bars correspond to 200 nm. **e)** Overview image of IPEC2 micelles showing different orientations. The scale bar corresponds to 500 nm.

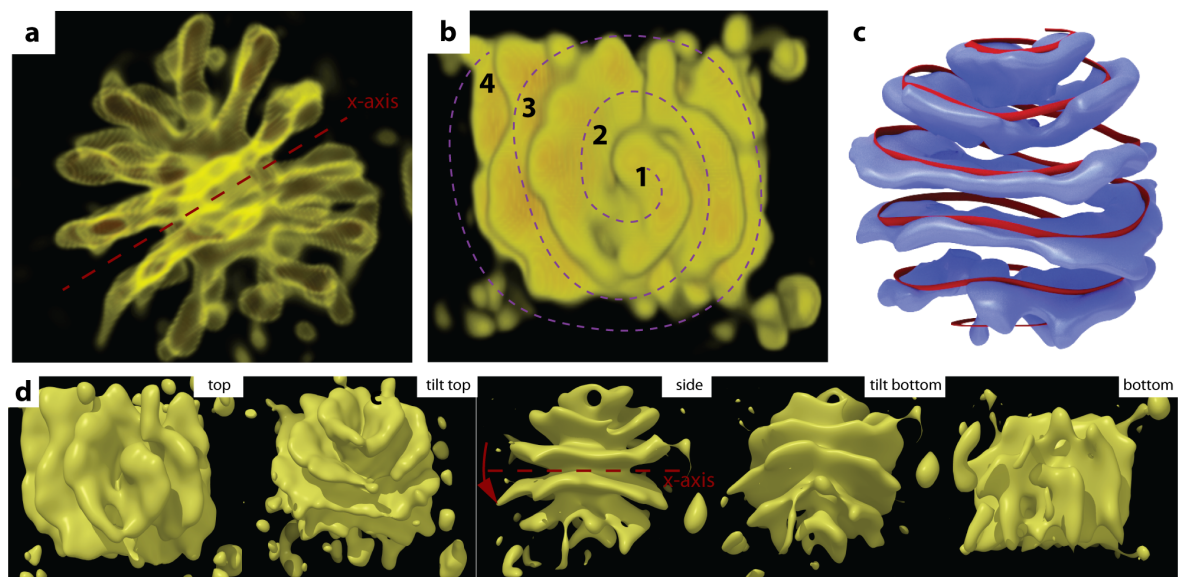


Figure S4.3. Supporting characterization of IPEC2 spiral. **a)** Semi-transparent reconstruction of the entire particle showing a spherical core and lamellae with varying angle towards the core center. **b)** Top view of reconstruction shows the lamella going around the spherical core, indicated by a purple line. **c)** Core-subtracted isosurface of the particle illustrating the spiral's origin and its path (the red spiral is a guide to the eye). **d)** Isosurface of the reconstruction viewed from on top views and rotated to side and bottom (rotation around x-axis in 45° steps from $\pm 180^\circ$).

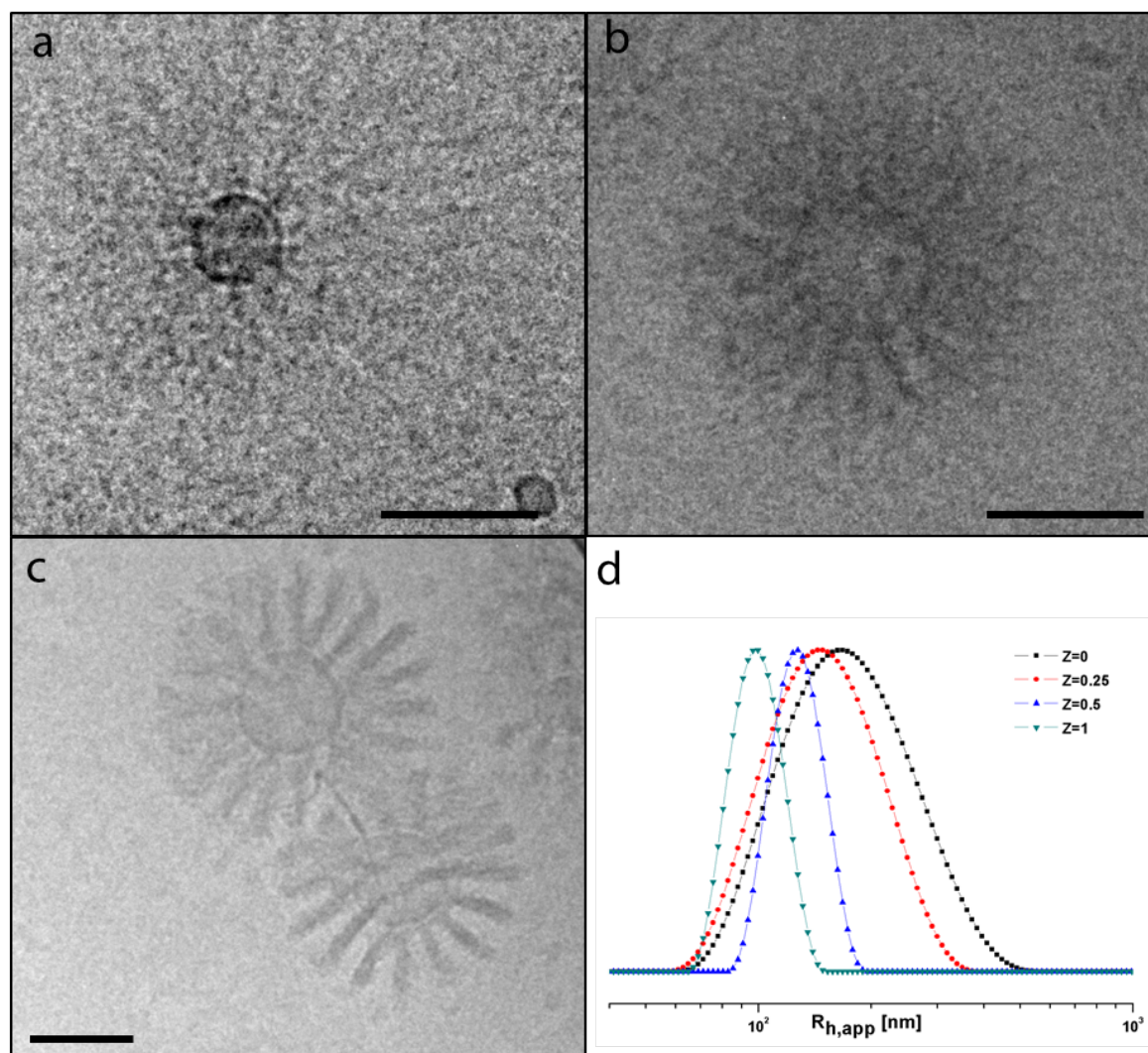


Figure S4.4. Morphological Evolution of IPEC2 with Increasing Z-Value. a-c) Cryo-TEM series of IPEC2 morphology evolution with increasing grafting density from $Z_{+/-} = 0.25$ (a), $Z_{+/-} = 0.5$ (b) to $Z_{+/-} = 1$ (c). The scale bars are 100 nm. d) DLS CONTIN plots of the BVqMAA precursor micelles in buffer pH 10 solution ($\langle R_h \rangle_{z,app} = 172.0$ nm; DI=0.12), IPEC2 at $Z_{+/-}=0.25$ ($\langle R_h \rangle_{z,app} = 147.2$ nm; DI=0.09), $Z_{+/-}=0.5$ ($\langle R_h \rangle_{z,app} = 126.6$ nm; DI=0.05) and $Z_{+/-}=1$ ($\langle R_h \rangle_{z,app} = 98.7$ nm; DI=0.07).

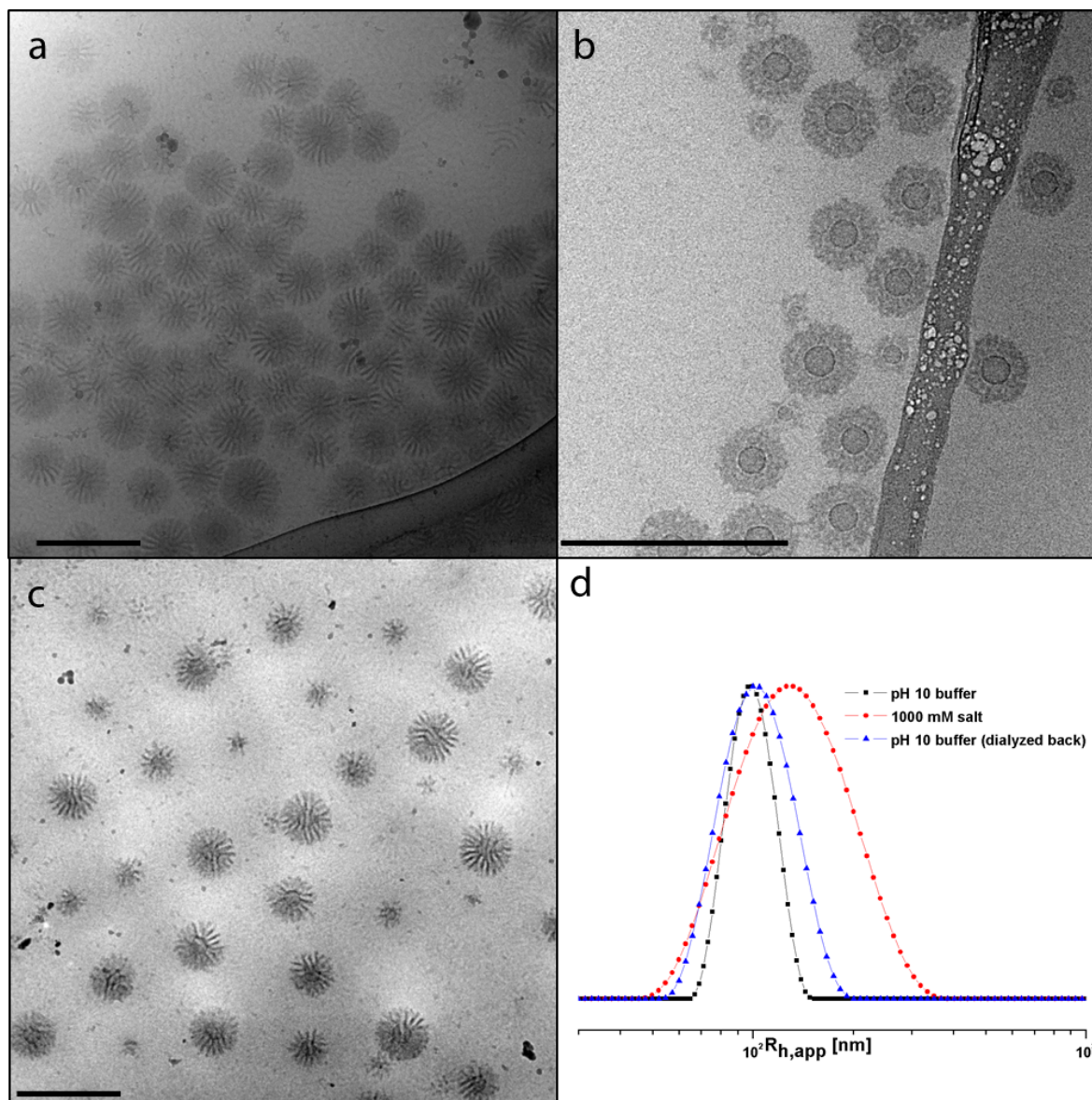


Figure S4.5. Thermodynamic Stability of Lamellar Brushes. a-c) Cryo-TEM images of IPEC2 with $Z_{+/-}=1$ in (a) pH10 buffer solution (b) at 1000 mM salt concentration (NaCl) and (c) after dialyzing back into buffer pH 10 solution; scale bars represents 500 nm. d) Corresponding DLS CONTIN plots of the IPECs in buffer pH 10 ($\langle R_h \rangle_{z,app} = 98.7$ nm; DI=0.07), 1000 mM salt ($\langle R_h \rangle_{z,app} = 130.1$ nm; DI=0.10) and after dialyzing back to buffer pH 10 solution ($\langle R_h \rangle_{z,app} = 102.6$ nm; DI=0.09).

Calculation of volume fractions of IPEC and PEO,aq (ϕ_{IPEC} and $\phi_{\text{PEO,aq}}$)

IPEC1:

Due to the missing wedge-effect, we estimated the volume fractions from a section of the micellar segment for a more accurate estimate (shown in Figure S4.6). First, the micellar core (r_{core}) was erased and the volume of the resulting IPEC isosurface V_{IPEC} was measured with UCSF Chimera volume tools. Then the volume of PEO V_{PEO} was approximated by subtracting the V_{IPEC} and $V_{\text{core}} = 0.25\pi R_{\text{core}}^2 h$ from the volume of bounding cylinder $V_{\text{bound.}} = 0.25\pi R_{\text{bound.}}^2 h$:

$$V_{\text{PEO}} = V_{\text{bound.}} - V_{\text{IPEC}} - V_{\text{core}}$$

, which resulted in a PEO volume fraction of

$$\phi_{\text{PEO}} = \frac{V_{\text{PEO}}}{V_{\text{PEO}} + V_{\text{IPEC}}} = 0.793 \approx 80\% .$$

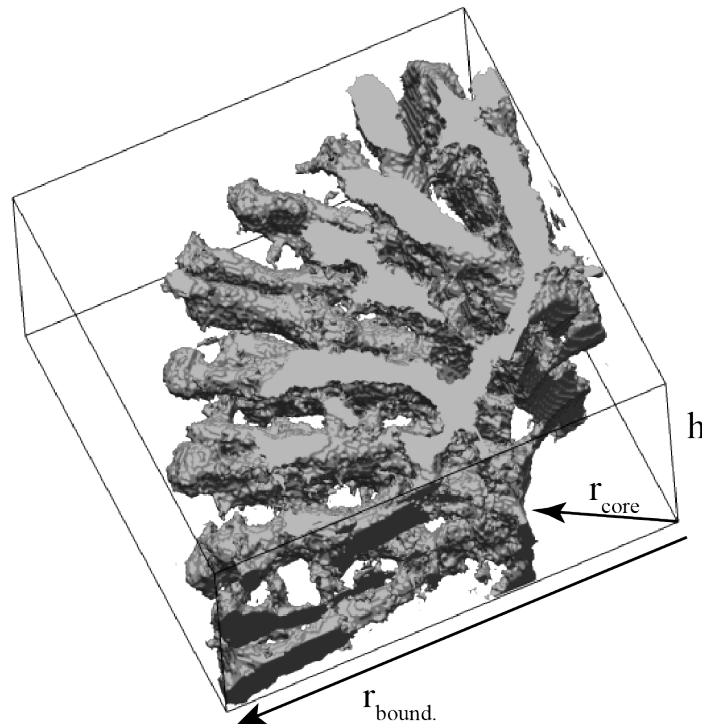


Figure S4.6. Volume segment. Isosurface of one fourth of the IPEC1 particle excluding the particle core (PB+*im*-IPEC) to calculate the volume fraction of the IPEC, ϕ_{IPEC1} , and the solubilized PEO corona.

IPEC2:

Using the same procedure as for IPEC1, we obtain a PEO volume fraction for IPEC2.

$$\phi_{\text{PEO}} = \frac{V_{\text{PEO}}}{V_{\text{PEO}} + V_{\text{IPEC}}} = 0.573 \approx 57\%.$$

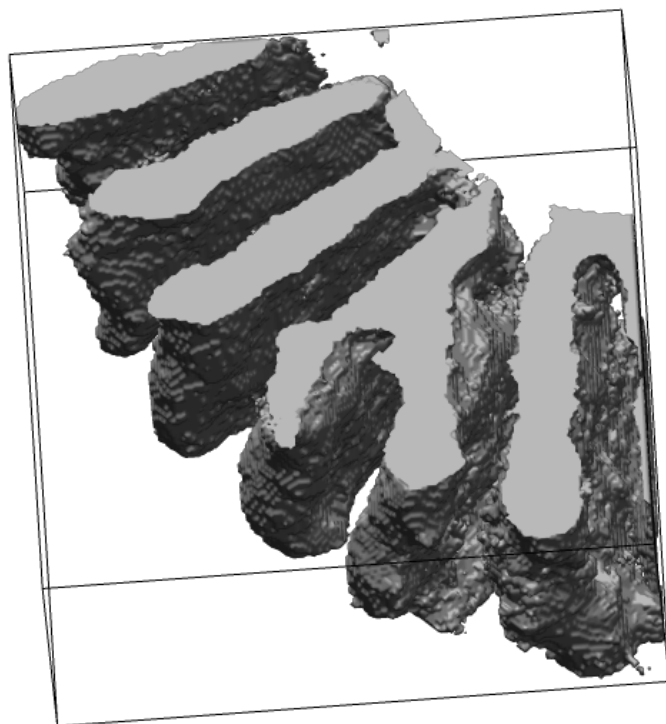


Figure S4.7. Volume segment. Isosurface of one fourth of the IPEC2 particle excluding the particle core (PB+*im*-IPEC) to calculate the volume fraction of the IPEC ϕ_{IPEC2} and the solubilized PEO corona.

Supporting References:

1. Raula, J.; Shan, J.; Nuopponen, M.; Niskanen, A.; Jiang, H.; Kauppinen, E. I.; Tenhu, H. Synthesis of Gold Nanoparticles Grafted with a Thermoresponsive Polymer by Surface-Induced Polymerization. *Langmuir*, **2003**, *19*, 3499–3504.
2. Kremer, J. R.; Mastronarde, D. N.; McIntosh, J. R. Computer Visualization of Three-Dimensional Image Data Using IMOD. *J. Struct. Biol.* **1996**, *116*, 71–76.
3. Engelhardt, P. Electron Tomography of Chromosome Structure. *Encycl. Anal. Chem.* **2000**, *6*, 4948–4984.
4. Laksameethanasan, D.; Brandt, S. S.; Engelhardt, P.- A Three-Dimensional Bayesian Reconstruction Method With The Point Spread Function For Micro-Rotation Sequences In Wide-Field Microscopy. *Proc. 3rd IEEE Int. Symp. Biomed. Imaging From Nano to Macro* **2006**, 1276–1279.
5. Kaipio, J.; Somersalo, E. Statistical and Computational Inverse Problems. In *Applied Mathematical Sciences*; 2005; Vol. 160, p. 68.
6. Pettersen, E. F.; Goddard, T. D.; Huang, C. C.; Couch, G. S.; Greenblatt, D. M.; Meng, E. C.; Ferrin, T. E. UCSF Chimera-A Visualization System for Exploratory Research and Analysis. *J. Comput. Chem.* **2004**, *25*, 1605–1612.
7. Hall, M.; Frank, E.; Holmes, G.; Pfahringer, B.; Reutemann, P.; Witten, I. H. The WEKA Data Mining Software : An Update. *SIGKDD Explor.* *11*, 10–18.
8. Schindelin, J.; Arganda-Carreras, I.; Frise, E.; Kaynig, V.; Longair, M.; Pietzsch, T.; Preibisch, S.; Rueden, C.; Saalfeld, S.; Schmid, B.; *et al.* Fiji: An Open-Source Platform for Biological-Image Analysis. *Nat. Methods* **2012**, *9*, 676–682.

Chapter 5

Rational Design of ABC Triblock Terpolymer Solution

Nanostructures with Controlled Patch Morphology

*Tina I. Löbling^{a,b}, Oleg Borisov^c, Johannes S. Haataja^b,
Olli Ikkala^{b,*}, André H. Gröschel^{b,d,*} and Axel H. E. Müller^{e,*}*

^aMacromolecular Chemistry II, University of Bayreuth, D-95440 Bayreuth, Germany.

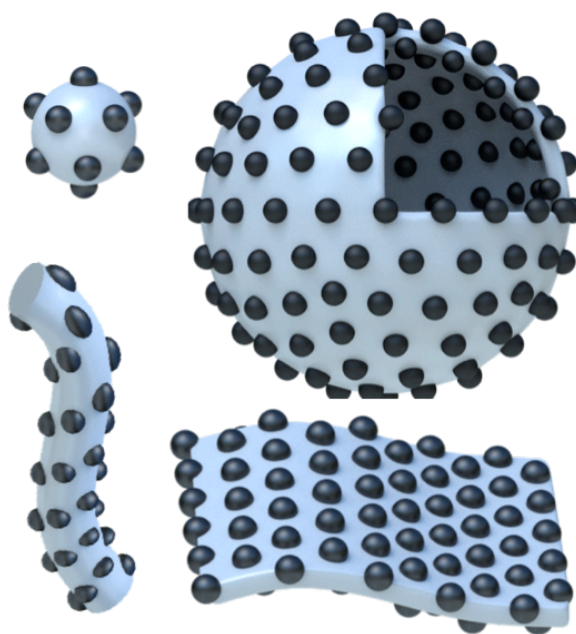
^bDepartment of Applied Physics, Aalto University School of Science, FIN-02150 Espoo, Finland.

^cInstitut Pluridisciplinaire de Recherche sur l'Environnement et les Matériaux UMR 5254 CNRS/UPPA, F-64053 Pau, France; Institute of Macromolecular Compounds, Russian Academy of Sciences, 199004, St. Petersburg, Russia, and St. Petersburg State Polytechnic University, 195251, St. Petersburg, Russia.

^dnew address: Department of Physical Chemistry, University of Duisburg-Essen, D-45127 Essen, Germany.

^eInstitute of Organic Chemistry, Johannes Gutenberg-University Mainz, D-55099 Mainz, Germany.

*Correspondence to: andre.groeschel@uni-due.de; olli.ikkala@aalto.fi;
axel.mueller@uni-mainz.de.



Nature Communications, accepted

Abstract

Block copolymers self-assemble into a variety of nanostructures that are relevant for science and technology. While the assembly of diblock copolymers is largely understood, predicting the solution assembly of triblock terpolymers remains challenging due to complex interplay of block/block and block/solvent interactions. Here, we provide guidelines for the self-assembly of linear ABC triblock terpolymers into a large variety of multicompartment nanostructures with C corona and A/B cores. The ratio of block lengths N_C/N_A thereby controls micelle geometry to spheres, cylinders, bilayer sheets and vesicles. The insoluble blocks then microphase separate to core A and surface patch B, where N_B controls the patch morphology to spherical, cylindrical, bicontinuous and lamellar. The independent control over both parameters allows constructing combinatorial libraries of unprecedented solution nanostructures, including spheres-on-cylinders/sheets/vesicles, cylinders-on-sheets/vesicles, and sheets/vesicles with bicontinuous or lamellar membrane morphology (patchy polymersomes). The derived parameters provide a logical toolbox towards complex self-assemblies for soft matter nanotechnologies.

Introduction

Upon pursuing increasingly functional materials, one approach aims at bridging the gap between simplistic self-assemblies and the sophisticated level of structural control that is characteristic for biological systems. Therein, multiphase synthetic building blocks that involve a rich interplay of interactions have demonstrated progressively complex self-assembly behaviour¹⁻⁵. In that regard, block copolymers find widespread application in materials science due to their ability to form nanostructures with progressively complex composition, shape and function⁶⁻⁹. The solution self-assembly of AB diblock copolymers is comparably straightforward, because solvent selectivity divides the blocks into micellar core and corona. Structural diversity is thereby controlled by block lengths and limited to the geometry that ranges from spheres to cylinders to bilayer sheets and vesicles (poly-mersomes)¹⁰⁻¹². For the next degree of complexity, i.e., multiphase particles^{13,14} or hierarchical assemblies, three or more polymer blocks are required so that at least two blocks phase separate inside the micellar core. Established synthetic techniques provide the necessary building blocks through sequential block extension to linear ABC triblock terpolymers (and beyond). And although some intricate multicompartment nanostructures have been experimentally verified in solution^{3,15-18}, the multitude of independent interaction parameters between polymer blocks and solvent still complicates rational structuring of terpolymers in solution. As a result, multiphase nanostructures are often perceived as exotic or surprising. So far, only few approaches offer precise control over block positioning in solution self-assembly of ABC triblock terpolymers, creating well-defined core-segmented cylinder micelles and spherical “patchy” micelles, therein¹⁹⁻²⁵. Nanostructured bilayer sheets and vesicles have been observed only in isolated cases.²⁶⁻²⁹ Controlling the polymorphism of both micelle geometry and patch morphology still remains a generic challenge.

Here, we provide guidelines for the self-assembly of linear ABC triblock terpolymers that allow the separate tuning of micelle geometry and patch morphology. The separate control enables us to construct a library of solution nanostructures, where classical micelle polymorphs such as spheres, cylinders, bilayer sheets and vesicles, are further subclassified by their patchy morphology. We identify 13 out of the 16 possible micelle/patch combinations, which are rationalized by a scaling theory that predicts structural transitions and stability regions for each respective combination.

Results

Self-assembly system. As model system we chose polystyrene-*block*-polybutadiene-*block*-poly(*tert*-butyl methacrylate) (PS-*b*-PB-*b*-PT or SBT) in acetone/isopropanol mixtures (Fig. 5.1a). Specifics for all polymers are summarized in Supplementary Table 5.1. Block solubilities and measurements to determine a swelling factor, q , to correct the PS volume in dependence of the acetone content are summarized in Supplementary Figs. 5.1-5.4 and Supplementary Tables 5.2-5.3. In an analogy to lipids and diblock copolymers^{30,31}, we ex-

pect the amphiphilic balance, i.e., the volume ratio of corona over core (related to the block PT), to direct self-assembly into spherical micelles, cylinders, and bilayer sheets and vesicles (Fig. 5.1b). Concurrent microphase separation of the insoluble and immiscible core blocks, PS and PB, then lead to an inner PS core and a PB surface pattern (Fig. 5.1c).^{32,33} The separate control over micelle geometry and patch morphology allows constructing combinatorial libraries of multicompartiment solution nanostructures, e.g. spheres-on-cylinders or cylinders-on-sheets, and so on. To target these and other combinations, we synthesized a series of SBT triblock terpolymers with systematically varied block lengths abbreviated as N_S , N_B and N_T (e.g. S₅₄₀B₁₇₃T₁₃₇).

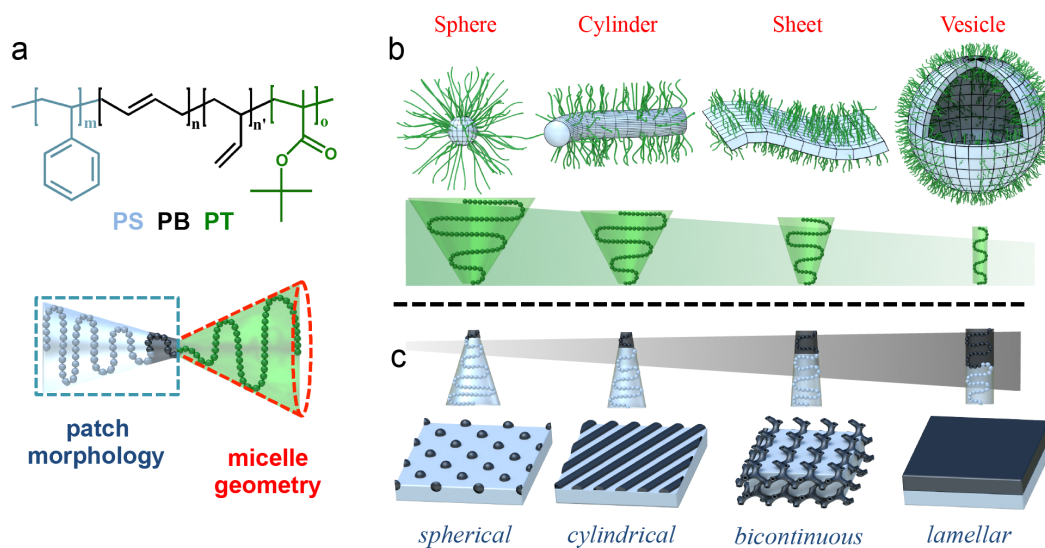


Figure 5.1. Parameters controlling micelle geometry and patch morphology. **a**, Chemical structure of the polystyrene-*block*-polybutadiene-*block*-poly(*tert*-butyl methacrylate) triblock terpolymer (SBT). **b**, Suggested structural control: the length of the soluble PT corona (green chain) controls the micelle geometry to spheres, cylinders, bilayer sheets and vesicles; the block lengths of the insoluble and immiscible blocks, PS (grey) and PB (black), determine the patch morphology to spherical, cylindrical, bicontinuous and lamellar.

Self-assembly procedure. In our particular system, i.e. PS-*b*-PB-*b*-PT in acetone/isopropanol mixtures, PT is always soluble, PB insoluble, and the collapse of PS is controlled by the solvent composition. We employ a two-step self-assembly process to direct each block into the desired location within the solution nanostructure.²¹ Starting in *N,N*-dimethylacetamide (DMAc), the PB middle block selectively collapses to form the core of precursor micelles with a corona composed of PT and PS blocks. Dialysis against acetone/isopropanol mixtures as non-solvent for both PB and PS induces aggregation of the precursor micelles to form spherical multicompartiment micelles with a PS core, spherical PB patches stabilized by a PT corona (see Supplementary Fig. 5.5 for assembly path). ¹H-NMR during dialysis (see Supplementary Fig. 5.6 for kinetic plot) proves that after 90 min the entire starting solvent, DMAc, had been replaced with the final solvent mixture. During solvent exchange and in the final solvent mixture, all polymer blocks remain in a soft and dynamic state, which reduces the probability of kinetic trapping and facilitates structural rearrangement ($T_{g, PB} < -20^{\circ}\text{C}$, acetone plasticises PS). As will be discussed be-

low, depending on the length of the stabilizing corona, the spherical multicompartment micelles undergo a morphological evolution towards higher order superstructures over time. This slow structural rearrangement occurs on the order of days and is attributed to slow rearrangement of the PS domains. All samples were allowed to equilibrate until no further structural evolution could be detected anymore in TEM (days to weeks depending on the sample). We will first discuss the control over micelle geometry and patch morphology and characterize the structural features of each identified nanostructure individually, before we go into more detail about the self-assembly kinetics later.

Controlling micelle geometry. We first address the effect of corona length, N_T , on micelle geometry (Fig. 5.2). Previously, we used scaling arguments to define stability criteria for the special case of spherical micelles with spherical patches²¹. Here, we extend this theory to rationalize the polymorphism of patchy micelles, i.e., to account for morphological transition from spheres-on-spheres to spheres-on-cylinders and further to spheres-on-bilayer sheets/vesicles (Supplementary Fig. 5.7). Polymorphism could be expected given the delicate balance between the gain in the conformational entropy of the core-forming PS blocks and the penalty in curvature-dependent part of repulsive interactions in the solvated coronal PT domains. These transitions would occur when the radius of the corona becomes smaller than the core radius ($H_{\text{corona}} \leq R_{\text{PS}}$), i.e., the micelles have the crew-cut shape. By acquainting the free energies per chain for different morphologies, we find the binodal (transition) lines as

$$(\tilde{N}_T / (qN_S^{2/3}))^{(sp.\leftrightarrow cyl.\leftrightarrow lam.)} \simeq (v_S / \ell^3)(\gamma_{\text{PS/solvent}} \ell^2)^{1/3} (v_T / \ell^3)^{-1/3}, \quad (5.1)$$

where numerical coefficients are omitted, $N_{S,B,T}$ are the degrees of polymerization, and $n_{S,B}$ the volumes of the monomer units of the respective blocks; $n_T \sim l^3$ is the excluded volume parameter under good solvent conditions, l the length of the monomer unit (the Kuhn segment), and $k_B T g_{\text{PS/sol.}}$ is the surface tension at the PS/solvent interface. The correction factor, q , accounts for selective swelling of the PS domain (Supplementary Figures 5.2-5.4 and Supplementary Note 5.1). A more detailed and generalized theory is given in Supplementary Note 5.2 and Supplementary Figures 5.7-5.8. Unlike in the bulk where the volume fractions of the blocks and incompatibility parameters control the morphology, in solution self-assembly the solvent is the dominating factor. Thus, the length ratio of the blocks, their selectivity towards the solvent and the degrees of swelling become more relevant.³¹ Hence, a decrease in the length of the soluble PT blocks (or increase of PS) should lead to successive transitions from spheres-on-spheres to cylinders and further to bilayers, all with PS core. For the micelle geometry, the PB block only enters through the correction term, $\tilde{N}_T = N_T - \Delta N_T$, equal to the number of monomer units in a segment of the PT block protruding from the PB domain up to the inter-patch distance, D . As we will see later, this correction term becomes relevant when $N_S n_S \approx N_B n_B$.

We experimentally approach this theory by successively decreasing the parameter $N_T/(qN_S^{2/3})$, here from 1.69 to 0.15, while maintaining constant block lengths of N_S and N_B , which should give spherical PB patches for $N_S n_S \gg N_B n_B$. For $N_T/(qN_S^{2/3}) = 1.69$, we observe spherical micelles in transmission electron microscopy (TEM) with spherical PB patches on top of the PS core (Fig. 5.2a). The PB phase (dark) was selectively stained with OsO_4 to enhance contrast. This sphere-on-sphere configuration or “patchy spherical micelle” has been observed before whenever a voluminous corona was present to stabilize the spherical shape of the solvophobic core.^{19–21,34} Applying our generalized parameter, $N_C/N_A^{2/3}$ (Supplementary Note 5.2), to these literature examples, both literature and our own values suggest a stability region for spheres-on-spheres of $N_C/N_A^{2/3} > 1$. For instance, a $N_C/N_A^{2/3}$ of 1.9 and 6.4 led to the formation of spherical multicompart ment micelles in case of polystyrene-*b*-polybutadiene-*b*-poly(2-vinyl pyridine)³⁴ and polybutadiene-*b*-poly(2-vinyl pyridine)-*b*-poly(*tert*-butyl methacrylate).²⁰ Also in a previous publication, we examined a large set of terpolymers without observing structural evolution to patchy cylinder micelles, which we now can explain given their $N_C/N_A^{2/3}$ of 4–10.²¹

Here, by reducing $N_T/(qN_S^{2/3}) < 1$ (e.g. 0.48), we indeed observe the transition to spheres-on-cylinders as suggested by our theory (Fig. 5.2b). The supramolecular nature of the assemblies and the plasticized core phases (acetone for PS, and $T_{g,\text{PB}} < -20$ °C) facilitate structural rearrangement into this structure. The employed two-step assembly procedure further aids in prearranging the polymer chains, reduces the conformational freedom of the participating blocks and promotes reaching equilibrium conditions.²¹ Interestingly, the self-assembly proceeds in a hierarchical manner, where first spherical multicompart ment micelles form that progressively merge into several micrometre-long patchy cylinder micelles at $N_T/(qN_S^{2/3}) = 0.48$ covered with a dense arrangement of small spherical PB patches.

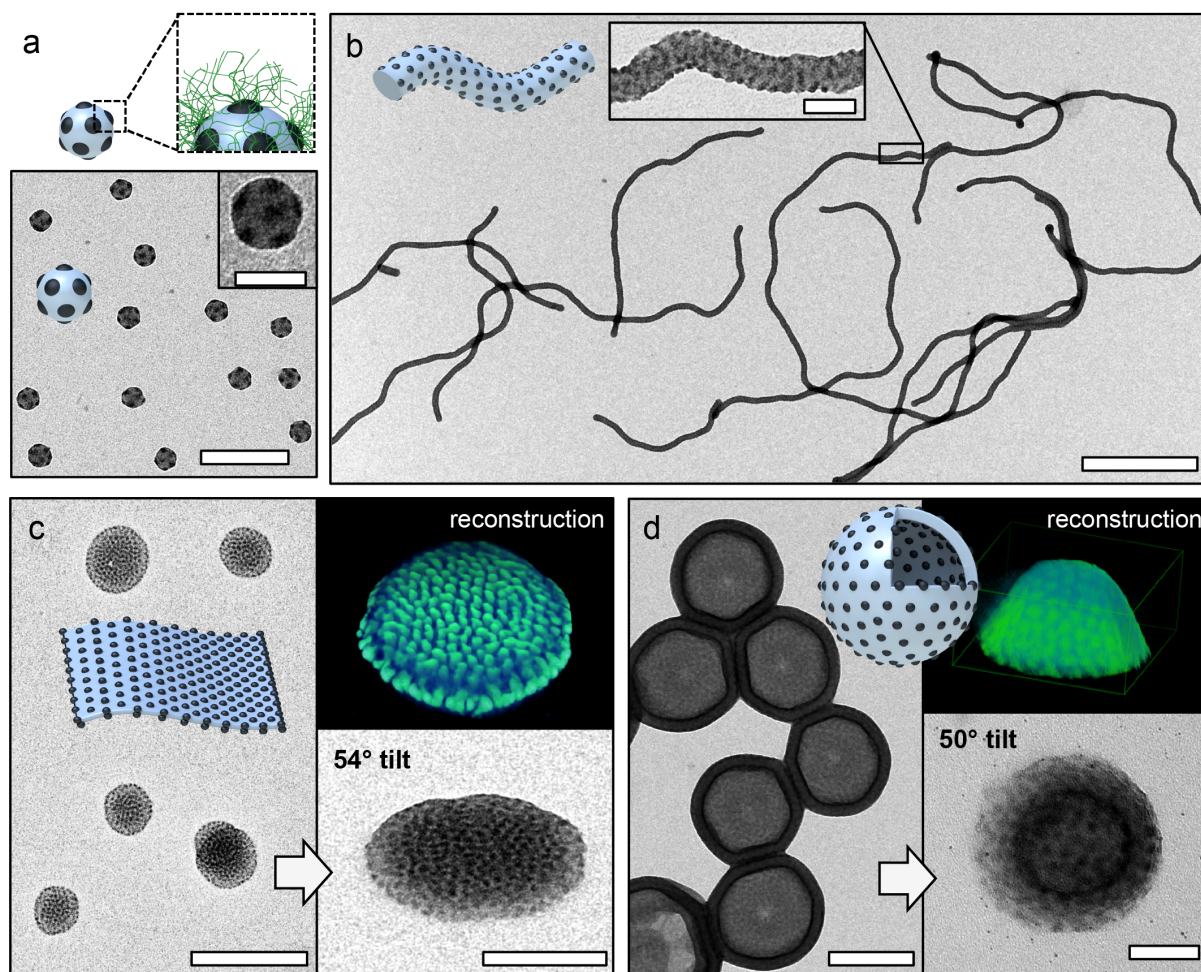


Figure 5.2. Micelle polymorphs with spherical patches. Samples were prepared from acetone/isopropanol 60:40 (v/v) unless otherwise noted. **a**, Spheres-on-spheres of $S_{1105}B_{237}T_{654}$. Schematic of block arrangement shows PS core (grey), PB patches (black) and PT corona (green); this domain sequence applies to all nanostructures and the PT corona always emanates from the dark PB domains. Scale bars are 200 nm and 50 nm in the inset. **b**, Spheres-on-cylinders of $S_{540}B_{173}T_{137}$; close-up shows the small PB patches. Scale bars are 1 μm and 100 nm in the inset. **c**, Spheres-on-sheets of $S_{540}B_{173}T_{137}$ in acetone/isopropanol (85:15 v/v), close-up recorded at 54° tilt angle and tomographic reconstruction showing PB patches in green. Scale bars are 500 nm and 200 nm in the inset. **d**, Spheres-on-vesicles of $S_{540}B_{173}T_{88}$; close-up recorded at 50° tilt angle and tomographic reconstruction showing PB patches in green. Scale bars are 200 nm and 50 nm in the inset.

Reducing $N_T/(qN_S^{2/3})$ further below 0.3, spheres-on-sheets become thermodynamically stable with a PS core of constant thickness and spherical PB patches decorating both sides of the sheets/discs (Fig. 5.2c). The characteristic arrangement of the patches indicates hexagonal packing, but the close proximity of the nano-sized patches and the overlapping features make visualization challenging in conventional TEM projection. We therefore use transmission electron tomography to resolve the patch morphology (Supplementary Fig. 5.9 and Supplementary Movie 5.1). The 3D reconstruction gives an electron density map of high-contrast PB domains (OsO₄ staining, green in inset of Fig. 5.2c) that indeed shows onset of hexagonal packing of the PB patches and confirms the bilayer structure. The template-free assembly of amorphous polymer into 2D sheets is rather unusual, because sheets (discs) are not the expected thermodynamic equilibrium morphology and mostly observed

for low-entropy motifs above the superstrong segregation limit (e.g. liquid-, semi-crystalline, and perfluorinated blocks).^{35–38} One other successful approach to form stable 2D polymer disks utilizes the co-assembly of cylinder- and vesicle-forming diblock copolymers (e.g. AB+AC). There the two immiscible blocks B/C form the phase-separated core, where the cylinder-forming diblock stabilizes the high energy edges of the planar phase.³⁹ In our case, the PB surface pattern seems to stabilize the sheet edges against roll-up. On closer inspection of the reconstruction, we can identify a ring of single layer PB patches at the sheet edge (Supplementary Fig. 5.9), whereas on the planar part is formed by a double layer of PB patches. The TEM images also support this assumption, because the contrast clearly is lower at the edges reminiscent of a ring surrounding the disc.

At smallest values of $N_T/(qN_S^{2/3}) = 0.15$, we find vesicles (polymersomes) with a compartmentalized shell, i.e. spherical PB patches are located on both sides of the vesicle membrane (Fig. 5.2d). These patchy vesicles adopt a homogeneous round shape with size distribution typical for block copolymer vesicles. The isotropic spherical PB patches do not influence the vesicle shape. As we will show later on vesicles with other patch morphologies, this is not always the case. Nanostructured vesicles are likewise very intriguing, because a generic concept to control the membrane morphology through self-assembly would impact their application as nanoreactors, drug delivery vehicles and artificial cell prototypes.^{40–42} As we will show in the following, our approach also allows tuning the microphase of the core or membrane forming blocks.

Controlling the patch morphology. We next explored the possibility to maintain constant micelle geometry, while tuning the patch morphology, i.e. from spherical to cylindrical, bicontinuous and lamellar PB patches, by increasing N_B relative to the corona length, N_T (Fig. 5.3). Equation (5.1) applies and spheres-on-cylinders are thermodynamically stable as long as $R_{PB} \leq D \leq H_{\text{corona}}$. For shorter soluble PT blocks and/or longer insoluble PB blocks, the size of patches becomes comparable to – or larger than – the extension of the corona (Supplementary Fig. 5.8). In this regime one can expect shape transformation of the PB domains. This transition is driven by the gain in the conformational entropy of the PB blocks, which is balanced by an increase in the overlap and repulsions between the PT blocks protruding from the surface of the PB domains. The exact numerical factors, which quantify the difference in the conformational entropy of the PB blocks confined in spherical or cylindrical segmental domains are, however, not available. If $N_S n_S \gg N_B n_B$, the transition from spherical PB patches to PB cylinders and further to a PB lamella (layered PS/PB) occurs on the surface of planar (or vesicular) PS domains. The length of the PS-block has virtually no influence on the position of the transition (tr),

$$(\tilde{N}_T / N_B^{2/3})^{(tr)} \approx (v_B / \ell^3)(\tilde{\gamma}_{BS} \ell^2)^{1/3} (v_T / \ell^3)^{-1/3}, \quad (5.2)$$

where $\tilde{\gamma}_{BS}$ accounts for surface tensions on both PB/solvent and PS/PB interfaces. However, at $N_S v_S \approx N_B v_B$ and for sufficiently short PT block, the PB patches may merge into a

cylindrical patch, whereas the PS core still retains a cylindrical shape and hence, a peculiar double-cylindrical patch on a cylindrical core can become thermodynamically stable. Moreover, for nearly symmetrical insoluble blocks one could expect interference of morphological transitions in the PS and PB domains (triggered, e.g. by variation in the solvent strength for the soluble PT block).

On cylindrical micelles the patch morphology indeed changes as a function of N_B (Fig. 5.3). While all cylindrical micelles exhibit comparable diameter ($D_{\text{cyl}} \approx 50\text{-}70$ nm) as suggested by $N_T/(qN_S^{2/3})$, varying $N_T/N_B^{2/3}$ from 4.41 to 1.15, systematically alters the PB patch morphology (overview images in Supplementary Fig. 5.10). For $N_T/N_B^{2/3} = 4.41$, we first find small spherical PB patches with diameter $d_{\text{PB}} = 12.6$ nm (Fig. 5.3a) that evolve into larger spherical PB patches with $d_{\text{PB}} = 24.2$ nm for $N_T/N_B^{2/3} = 2.33$ (Fig. 5.3b). Those pack in a dense hexagonal pattern and begin to arrange on a helical trajectory induced by the surface confinement of the cylindrical PS core⁴³. Under proper solvent conditions (acetone/isopropanol 80:20 v/v) the large spheres fuse into a continuous PB double helix and both patch morphologies coexist on the same cylinder micelle (Supplementary Fig. 5.11). As the increasing PB patches (relative to PS) require exceedingly large interfacial area, the spherical domains move closer together, overlap and fuse into the double helix winding around the PS cylinder core (Fig. 5.3c). Due to the relatively slow self-assembly kinetics of the micellar building blocks, structural rearrangement (fusion and fission) proceeds over a period of several days until the double helix is well developed. Supplementary Fig. 5.12 shows the time-dependent formation of cylindrical micelles decorated with the PB double helical patch. While after one and three days still precursor or multicompartment micelles are observed, the structure is fully developed after one week of aging. Such long time-scales for self-assembly are not entirely surprising as demonstrated before by Liu *et al.* on visually remarkable similar double helix micelles (assembly of 90 days). There, core-shell-corona cylinder micelles intertwine to form the final double helix. These double helices are thus merely visually similar, but with entirely different arrangement of the polymer blocks.. Likewise, Wooley, Pochan *et al.* found polymeric helices in aqueous solution where an organic molecular linker electrostatically drives cylindrical core-shell-corona micelles to curl either into a single-stranded helix or a double helix of two core-shell cylinders (solvent in the centre). At $N_T/N_B^{2/3} = 1.53$, cylindrical core-shell-corona micelles were expected, but instead the PB double helix persists with increased diameter of $d_{\text{PB}} = 22.8$ nm (Fig. 5.3d). Even at $N_T/N_B^{2/3} = 1.15$ the PB double helix rather continues to grow ($d_{\text{PB}} = 26.7$ nm) than transforming into the core-shell morphology (Fig. 5.3e). The delicate interactions of unfavourable interfaces, PS/PB, PS/solvent and PB/solvent most likely suppressed the transition. The slightly repulsive PS/solvent interface (PS swollen) would be replaced on the expense of creating unfavourable PS/PB interface ($\chi_{\text{PS/PB}} = 0.06$) and energetically much less favoured PB/solvent interface ($\chi_{\text{PB/solvent}} = 1.6\text{-}2.9$). The transition can thus be realized by decreasing the incompatibility between PB and the solvent, as demonstrated here by exchanging acetone with *n*-hexane (good solvent for PB). In *n*-hexane/isopropanol 50:50 (v/v), PS still remains collapsed in form of cylindrical micelles,

but PB now swells with *n*-hexane inducing the transition to cylindrical core-shell-corona micelles (Fig. 5.3f). These multicompartments nanostructures are merely bound by supramolecular forces and changes in solvent polarity allow transitions between morphologies, e.g. reversible switching from double helical to core-shell cylinders (Supplementary Fig. 5.13).

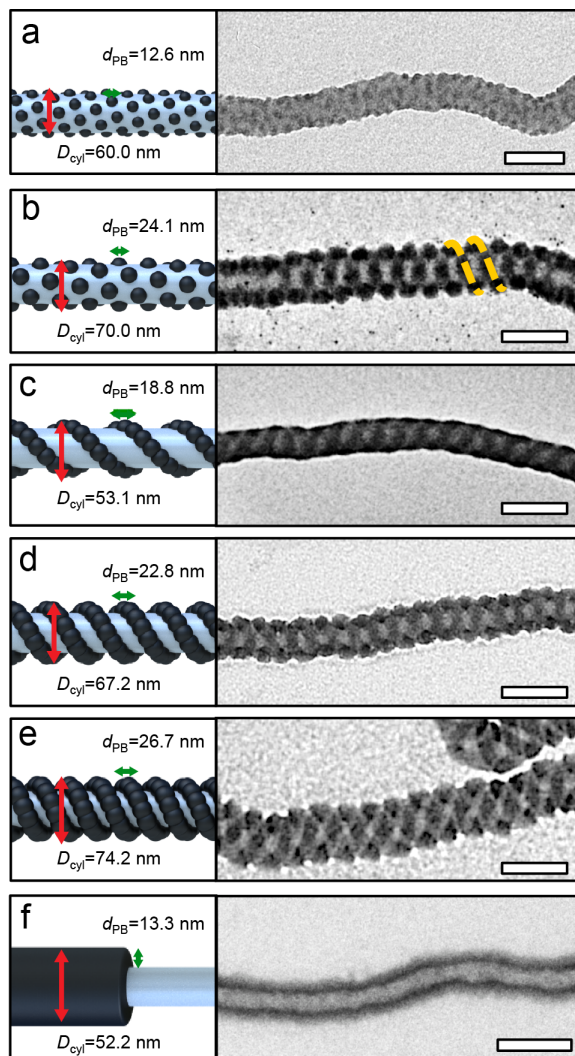


Figure 5.3. Cylinder micelles with controlled patch morphology. **a**, Small PB spheres of $S_{540}B_{173}T_{137}$ in acetone/isopropanol (60:40 v/v) and **b**, large PB spheres of $S_{510}B_{539}T_{154}$ in acetone/isopropanol (85:15 v/v). **c-e**, $S_{510}B_{539}T_{154}$ form thin, $S_{307}B_{385}T_{81}$ medium and $S_{307}B_{530}T_{75}$ thick PB double helices all in acetone/isopropanol (60:40 v/v). **f**, Core-shell-corona for $S_{307}B_{530}T_{75}$ in *n*-hexane/isopropanol (50:50 v/v). Scale bars are 100 nm.

Sheets and vesicles with membrane morphology. We also investigated the phase behaviour of patch morphologies on bilayer sheets and vesicle membrane (Fig. 5.4). As discussed in Fig. 5.2, by shortening N_T cylindrical micelles become unstable and sheets with a PS core are more favourable. By simultaneously increasing N_B , the patch morphology likewise transforms from spherical to cylindrical and further to bicontinuous and core-shell (lamellar) morphology.

Figs. 5.4a-c illustrate the morphological transition from spheres-on-cylinders to cylinders-on-sheets and vesicles when we reduce the corona length $N_T/(qN_S^{2/3})$ from $0.38 \rightarrow 0.28 \rightarrow 0.18$ and $N_T/N_B^{2/3}$ $4.41 \rightarrow 2.33$. On PS cores with reduced curvature (sheets), the spherical PB patches adapt to the decreasing overall surface area and merge together into cylindrical PB patches (Fig. 5.4b, Supplementary Movie 5.2). Tomographic reconstruction clarifies the strictly parallel and equidistant spacing of cylindrical PB patches (displayed in cyan) that locate on top and bottom of the PS sheet (also Supplementary Fig. 5.14). These cylinders-on-sheets grow larger as compare to the sphere-on-sheets in Figure 1, most likely facilitated by the surface pattern that works against the roll-up. These particles have numerous spheres-on-cylinder arms attached to their edges reminiscent of “jelly-fish” intermediates. A larger selection of these particles is summarized in Supplementary Fig. 5.15. In a mechanism that is remarkably similar to what is observed for the solution self-assembly of diblock copolymers^{35,46}, cylinder-on-sheets also grow to a critical size until the edge energy becomes unfavourable and sheets roll up to vesicles. Here, the tethered cylinder micelle arms continue to merge into the sheet fuelling membrane growth (Supplementary Fig. 5.16). Fusion and fission of the soft phases accompanied by equilibration and chain rearrangements facilitate vesicle closure. The cylindrical PB patches on top and bottom of the sheet is thereby transferred to the in- and outside of the vesicle membrane.

So far, only two works utilized the versatility of block terpolymers to implement morphologies into the vesicle membrane through phase separation of solvophobic blocks. Vesicles with a membrane morphology have been shown earlier by Russell *et al.* through rehydration of bulk films.²⁶ Also the special architecture of miktoarm star terpolymers allows to form compartmentalized vesicles, where the packing frustration of the two solvophobic blocks created laterally structured membranes²⁷. However, the decoration of a vesicle membrane with spherical and cylindrical patches is reserved for linearly sequenced polymers. The resulting cylinders-on-vesicles are noticeably elongated and adopt a prolate ellipsoidal “lemon” shape with low-curvature in longitudinal direction but pronounced increase in curvature at the tips (Fig. 5.4c). We interpret the elliptic shape as balance between curvature of the PS membrane and minimization of interfacial energies of the anisotropic PB patches. In AFM, the collapsed vesicles display twice the height of the precursor sheet (Supplementary Fig. 5.17), while not entirely deflated parts of the vesicle are considerable higher, confirming the hollow interior. In vesicular samples, we identify unassembled patchy precursor micelles (spheres and cylinders), all with the same height ($h \approx 50\text{nm}$) as the sheets and the vesicle membrane. This similarity in height further corroborates structural evolution from spherical micelles to cylinder micelles, sheet and finally vesicles. Cryo-TEM imaging of the cylinders-on-vesicles also proves that the “lemon” shape as well as the striped patch morphology are both present in solution and are not an effect of deposition (Supplementary Fig. 5.18 and Movie 5.3).

We chose this peculiar solution nanostructure as model to follow the formation of the final lemon-shaped vesicles, as morphological evolution progresses through all other ge-

ometries. The slow self-assembly kinetics not only allows us to distinguish single stages of the self-assembly process, but also to identify various intermediate structures before reaching a long-term stable nanostructure (assumed from TEM measurements after two years of ageing). As already mentioned, the solvent exchange during dialysis is completed after 90 min, while the structural evolution proceeds over the course of weeks in case of striped lemon-shaped vesicles (Supplementary Fig. 5.19). During the dialysis, first precursor micelles with a PB core and a PS/PT corona are dominant that successively assemble to form patchy spherical micelles (Supplementary Fig. 5.19a,b). After solvent exchange is completed, the patchy spherical micelles fuse into patchy cylinders, and progressively transform into striped sheets with patchy cylindrical arms after 24 h of ageing (Supplementary Fig. 5.19c-e). After three weeks, a majority of the sheets has rolled up to lemon-shaped vesicles (Supplementary Fig. 5.19f). The self-assembly from patchy spherical micelles towards striped lemon-shaped vesicles intriguingly demonstrates that fusion and fission processes of soft micellar particles are an integral part of structural evolution. The observed massive structural rearrangements obviously require chain mobility provided by the plasticizing solvent conditions.

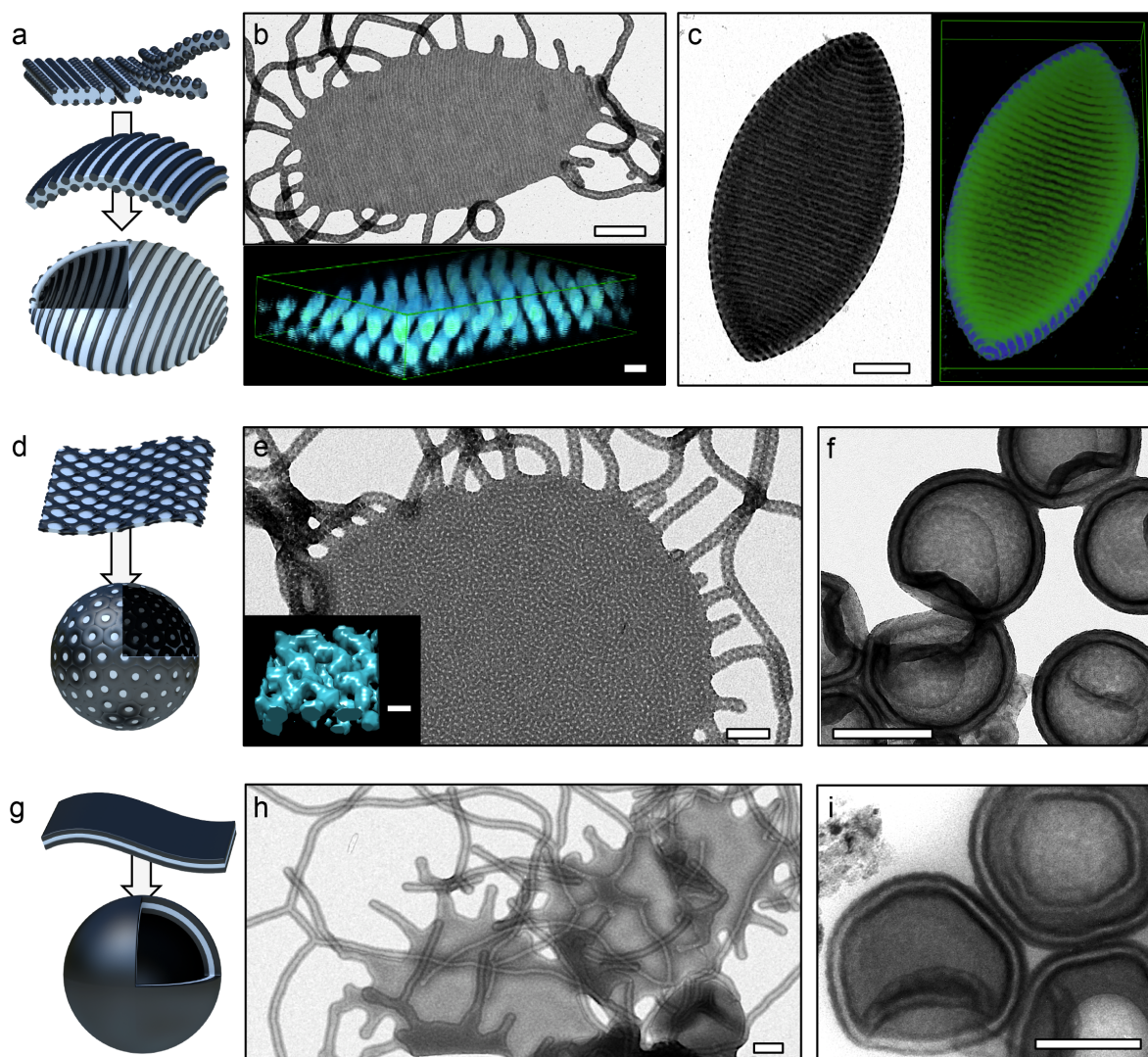


Figure 5.4. Polymer sheets and vesicles with defined patch morphology. Samples were prepared from acetone/isopropanol mixtures unless otherwise noted. **a**, Schematic of spheres-on-cylinders that transform to cylinders-on-bilayer sheets/vesicles. **b**, TEM image of cylinder-on-sheet of $S_{510}B_{539}T_{154}$ (75:25 v/v), and tomographic reconstruction of PB patches on top and bottom of the PS sheet (PB cyan, PS omitted). **c**, TEM and tomographic reconstruction of a “lemon”-shaped vesicle of $S_{510}B_{539}T_{154}$ with PB cylinders on in- and outside of the PS membrane after aging (85:15 v/v). **d**, Schematic of sheet and vesicles with bicontinuous membrane. **e**, TEM and tomographic reconstruction of PB network within the PS sheet of $S_{307}B_{530}T_{75}$ (60:40 v/v) (PB cyan, PS omitted). **f**, Fully evolved vesicle with bicontinuous membrane of $S_{307}B_{530}T_{63}$ upon ageing (60:40 v/v). **g**, Schematic of the core-shell sheets and (lamellar) vesicle. **h**, TEM image of a core-shell sheet of $S_{300}B_{756}T_{56}$ (*n*-hexane/isopropanol 50:50 v/v) and **i**, core-shell (lamellar) vesicle of $S_{300}B_{756}T_{56}$ in (*n*-hexane/isopropanol 35:65 v/v). Scale bars are 200 nm in TEM images and 25 nm in the reconstructions.

We also studied the transition of cylinder micelles with double-helix patches into sheets ($N_T/(qN_S^{2/3})$ from 0.41 to 0.38 and $N_T/N_B^{2/3}$ from 1.53 to 1.15). Here, the PB double helices change into a bicontinuous network of PB, which progresses through the PS domain from top to bottom as visualized in cyan in the reconstruction (Fig. 5.4d-e, PS omitted for clarity, Supplementary Movie 5.4). This PS/PB domain arrangement is unexpected given the large unfavourable interface. Then again, interfacial energies are not trivial for the entire system and morphologies under 2D quasi-confinement of the membrane may deviate from the expected case⁴⁷. The bicontinuous sheets are nevertheless long-term stable with double-helical arms protruding from the sheet (Supplementary Fig. 5.20). The tethered double helices are constrained in motion and we observe self-wrapping to minimize interface with the solvent (intermediate stage between cylinder and sheet). The slowed self-assembly kinetics further allow visualization of the transition from sheets to vesicles with bicontinuous membrane progressing through “jelly-fish” intermediates with double helical tentacles (Fig. 5.4f, Supplementary Fig. 5.20, and Supplementary Movie 5.5).

Core-shell-corona sheets and vesicles complete the morphological spectrum (Fig. 5.4g-i). As discussed for core-shell cylinders, the chosen block sequence and thus sequence of solubilities of PS-PB-PT only allows stable core-shell-corona morphologies under solvent conditions that promote spreading of PB on the PS core ($\chi_{ASolvent} < \chi_{BSolvent} < \chi_{CSolvent}$). For our system, exchange of acetone with *n*-hexane swells the PB domain and induces the change to a continuous PB shell completely engulfing the PS sheet or vesicle membrane. Core-shell micelles, cylinders and vesicles have been observed before in water^{48,49} and organic solvents⁵⁰. Interestingly in both cases the sequence of polymer blocks also followed $\chi_{A,Solvent} < \chi_{B,Solvent} < \chi_{C,Solvent}$, thus promoting the block arrangement into the core-shell-corona structure.

Experimental phase diagram. To rationalize the observed solution behaviour, we compiled an experimental phase diagram where each data point corresponds to one SBT triblock terpolymer in a specific acetone/isopropanol mixture (Fig. 5.5). The experimental values are in good agreement with the superimposed phase boundaries as predicted by our theory. Vertical lines represent predicted stability regions for each geometry, i.e., transitions from spherical to cylinder micelles and further to bilayer sheets and vesicles. These

are governed by the parameter $N_T/(qN_S^{2/3})$, whereas phase boundaries are separated by a factor $(N_T/(qN_S^{2/3}))^{(\text{sph.} \leftrightarrow \text{cyl.})} / (N_T/(qN_S^{2/3}))^{(\text{cyl.} \leftrightarrow \text{lam.})} = 1.28$ (Supplementary Note 5.2 and Supplementary Figures 5.7-5.8). Superposition of SBT terpolymers from different solvent mixtures requires a correction factor that accounts for selective solvent swelling of the polymer domains. Arrows connect identical polymers in different solvents. As stated in the beginning, we chose our system because only PS is affected by the solvent composition. The hydrodynamic radius of PT is unaffected in the employed range of compositions (as verified in DLS measurements on PT multiarm star polymers in acetone/isopropanol mixtures) and the unusually high $\chi_{\text{PB/solvent}} = 1.6\text{-}2.9$ (Supplementary Table 5.2) suggests completely collapsed PB blocks in all mixtures, though interfacial tensions for the PB-domains are affected by the solvent composition. The solvent dependence thus enters as correction factor, q , only for PS (Supplementary Fig. 5.2-5.4). The parameter $N_T/N_B^{2/3}$ on the other hand controls the resulting patch morphology to spherical, cylindrical and bicontinuous, as represented by the vertical dashed lines. Core-shell morphologies are omitted from this diagram, as they are only stable under special solvent conditions. Supplementary Table 5.4 contains all characteristics of the polymers found in the phase diagram and gives an overview over $N_T/(qN_S^{2/3})$ as well as $N_T/N_B^{2/3}$ values and the resulting micellar geometry and patch morphology.

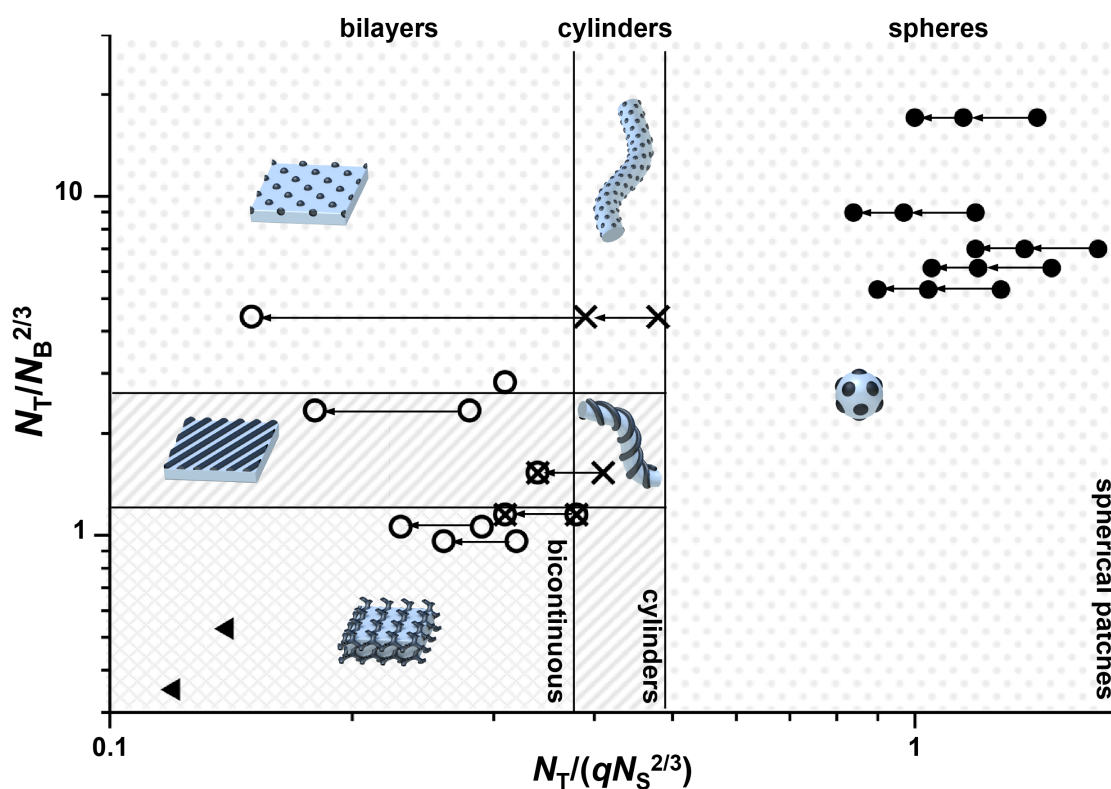


Figure 5.5. Experimental phase diagram in dependence of relative block lengths. (●) Spherical micelles with spherical patches. (X) Cylinder micelles with spherical and double-helical patch morphology. (⊗) Mixtures of cylinder micelles and bilayers (structural transition). (○) Bilayer sheets and vesicles with patchy, striped and bicontinuous membrane morphology. (▲) Large terpolymer particles with inverse core morphology. All data points were corrected by swelling factor

q (Supplementary Fig. 5.1-5.4), where arrows (\leftarrow) indicate same terpolymers, yet in solvents with increasing acetone content.

Fig. 5.6 finally summarizes the entire experimental library of multicompartment nanostructures, where classical micellar geometries are divided into subclasses according to the patch morphology (Supplementary Fig. 5.21 shows a complete schematic library). Characteristics of the polymers in Fig. 5.6 can be found in Supplementary Table 5.4 and are highlighted in green. Our combinatorial library allows deducing several trends towards a better understanding of the nanostructure formation of linear ABC triblock terpolymers. While curved spherical cores only support the spherical patch morphology, less curved cylinder micelles stabilize spherical as well as cylindrical patches, the latter in form of double helices with a synthetically controllable pitch size. For (quasi-)planar bilayer sheets and vesicles we find close resemblance of the patch morphology to the bulk case, i.e. the spherical, cylindrical and bicontinuous. Core-shell-corona morphologies are stable on all micellar geometries, but only under specific solvent conditions.

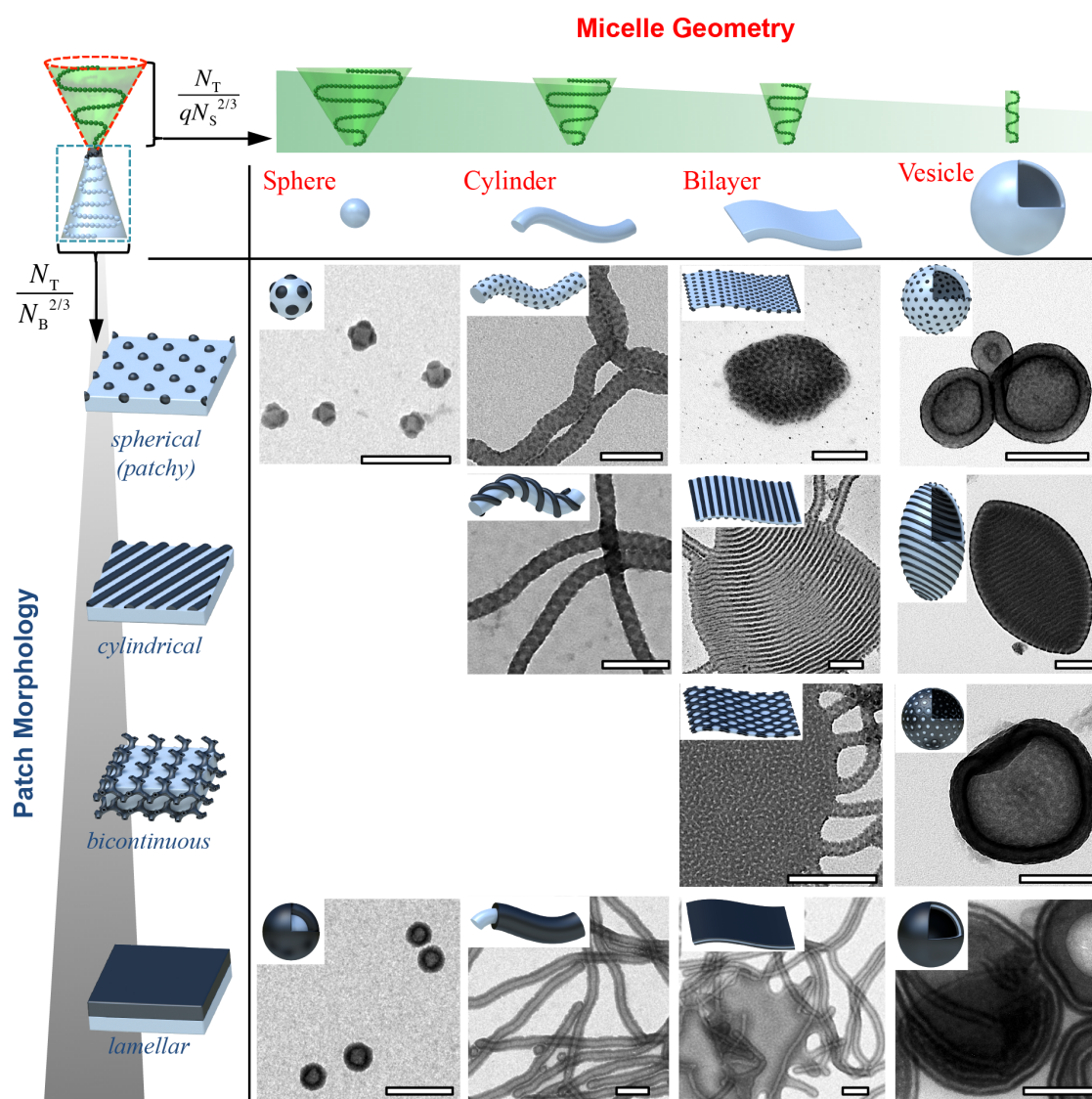


Figure 5.6. Experimental combinatorial table sub-classifying micelle geometry by patch morphologies. Sphere-on-spheres, spheres-on-cylinders, spheres-on-bilayer sheets and vesicles; cylinders-on-cylinders (double-helix patch), cylinders-on-bilayer sheets and vesicles; sheets and vesicles with bicontinuous membrane morphology; core-shell micelles, core-shell cylinders, lamellar sheets and vesicles. Solvent composition for each sample are given in Supplementary Table 5.4. Scale bars are 200 nm.

In summary, we have demonstrated how to construct a library of solution nanostructures from a single type of ABC triblock terpolymer, where classical micellar geometries are divided into subclasses according to their patch morphology. It is an interesting and surprising observation that the patch morphologies follow exactly the same trend as the bulk morphologies of AB diblock copolymers: from spheres to cylinders to bicontinuous (gyroid) to lamellar microphases, even though the AB-blocks are confined to the nanoscale core of the micelle. Given proper block design, these solution nanostructures may find application ranging from templates for nano-optics and -electronics (e.g. double helices) to advanced gating and intelligent delivery systems with controlled pharmacokinetic release profiles (e.g. vesicles with bicontinuous/porous membrane). In a broader context, mastering the self-assembly of linear ABC triblock terpolymers will provide understanding towards multiblock copolymers (ABCD, ABCDE, ...) with prospect to harvest the potential of their exponentially increasing number of conceivable self-assemblies⁵¹.

Methods

Polymer synthesis. A detailed description for the purification of chemicals and monomers involved in synthesis of PS-PB-PT triblock terpolymers is described elsewhere⁵². All SBT triblock terpolymers were synthesized *via* living anionic polymerization in THF at low temperatures in presence of alkoxides. In brief, *sec*-butyllithium (*sec*-BuLi) followed by styrene was added to THF at -70 °C and allowed to react for 10 min. After 1,3-butadiene was added, the reaction mixture was heated to -10 °C and stirred for 6.5 h. At -50 °C a 6-fold molar excess (compared to *sec*-BuLi) of diphenylethylene (DPE) was added and stirred for 1h. Then, *tert*-butyl methacrylate monomer was added at -70 °C and the reaction was heated to -50 °C for 2 h. After complete monomer consumption, 2 mL of degassed methanol was added to the polymer solution to terminate the living chain ends. Characteristics of all synthesized polymers can be found in Supplementary Table 5.1.

Dialysis procedure. For dialysis, membranes of regenerated cellulose (Spectrum Laboratories, Spectra/Por MWCO = 12-14 kDa) were used. After washing with Milliq water the membranes were washed with excess dioxane (Aldrich, analytical grade). *N,N*-dimethylacetamide (DMAc, Aldrich) was p.a. grade and used as received. All other solvents for dialysis experiments were of technical grade and used as received. PS-PB-PT was dispersed in DMAc to give a concentration of 0.1 g/L. After annealing at 70 °C over night, dialysis against a certain solvent-mixture was performed for 24 h although complete solvent exchange is reached after 90 min. Prior to analysis, the nanostructures were aged several days to allow full development of nanostructures.

Polymer characterization. $^1\text{H-NMR}$ Spectra were recorded on a Bruker Ultrashield 300 machine with a 300 MHz operating frequency using deuterated chloroform as solvent. Size exclusion chromatography (SEC) measurements were performed on a set of 30 cm SDV-gel columns of 5 mm particle size having a pore size of 10^5 , 10^4 , 10^3 , and 10^2 Å with refractive index and UV ($\lambda = 254$ nm) detection. SEC was measured at an elution rate of 1 mL/min with THF as eluent and polystyrene as calibration.

Transmission electron microscopy (TEM) was performed either on a Zeiss CEM 902 or a Fei Tecnai 12 electron microscope operated at 80 kV and 120kV respectively. The samples were prepared by placing one drop of the polymer solution onto carbon coated copper grids. Excess solvent was instantly absorbed by a filter paper. For selective staining of PB, the TEM specimens were exposed to OsO_4 vapour for 3 h.

Cryogenic transmission electron microscopy (cryo-TEM) imaging was carried out using a JEM 3200FSC field emission microscope (Jeol) operated at 300 kV in bright field mode with an Omega-type zero-loss energy filter. The images were acquired with an Ultrascan 4000 CCD camera (Gatan) and with Gatan Digital Micrograph software (version 1.83.842), while the specimen temperature was maintained at -187 °C. Vitrified samples were prepared using a FEI Vitribot placing 3 μL of sample solution on 200-mesh holey carbon copper grids under 100% humidity, then blotted with filter paper for 0.5-1.5 s, and immediately plunged into a -170 °C ethane/propane mixture and cryotransferred to the microscope.

Electron tomography (ET) was performed using the Fei Tecnai 12 electron microscope recording a series of projection images at various tilt angles between $\pm f_{\text{max}}$ with typical values of $\pm 60^\circ$ in 2° increments.

Cryogenic electron tomography (Cryo-ET) was performed with the same transmission electron microscope that was used for cryo-TEM imaging. Electron tomographic tilt series were acquired with the SerialEM software package (version 3.2.2). Samples were tilted between (69° angles with 3° increment steps).

Alignment and reconstruction. The TEM grids were dipped in gold nanoparticle solution before sample deposition ($d = 3\text{--}10$ nm, stabilized by 11-mercapto-1-undecanol ligand) to ensure proper alignment of captured images with IMOD^{53,54}. The fine alignment and cropping was conducted with custom-made Silicon Graphics JPEGANIM-software package⁵⁵. The images were binned twice to reduce noise and computation time and maximum entropy method (MEM) reconstruction scheme was carried out with custom-made program on Mac or Linux cluster with regularization parameter value of $l = 1.0\text{E}^{-3}$ ⁵⁵.

Visualization of 3D reconstruction. Volumetric graphics and analyses were performed with the UCSF Chimera package⁵⁶ and volume segmentation was carried out using trainable weka segmentation⁵⁷.

Data Availability

The authors declare that the data supporting the findings of this study are available within the article and its Supplementary Information Files.

References and Notes:

1. Yan, J., Bloom, M., Bae, S. C., Luijten, E. & Granick, S. Linking synchronization to self-assembly using magnetic Janus colloids. *Nature* **491**, 578–581 (2012).
2. Glotzer, S. C. & Solomon, M. J. Anisotropy of building blocks and their assembly into complex structures. *Nat. Mater.* **6**, 557–562 (2007).
3. Gröschel, A. H. *et al.* Guided hierarchical co-assembly of soft patchy nanoparticles. *Nature* **503**, 247–251 (2013).
4. Cademartiri, L. & Bishop, K. J. M. Programmable self-assembly. *Nat. Mater.* **14**, 2–9 (2015).
5. Qiu, H., Hudson, Z. M., Winnik, M. A. & Manners, I. Multidimensional hierarchical self-assembly of amphiphilic cylindrical block comicelles. *Science* **347**, 1329–1332 (2015).
6. Bates, F. S. & Fredrickson, G. H. Block Copolymers—Designer Soft Materials. *Phys. Today* **52**, 32–38 (1999).
7. Discher, D. E. & Eisenberg, A. Polymer vesicles. *Science* **297**, 967–973 (2002).
8. Schacher, F. H., Rupar, P. A. & Manners, I. Functional block copolymers: nanostructured materials with emerging applications. *Angew. Chemie Int. Ed.* **51**, 7898–7921 (2012).
9. Hudson, Z. M., Lunn, D. J., Winnik, M. A. & Manners, I. Colour-tunable fluorescent multiblock micelles. *Nat. Commun.* **5**, 3372 (2014).
10. Zhang, L. & Eisenberg, A. Multiple Morphologies of ‘Crew-Cut’ Aggregates of Polystyrene-*b*-poly(acrylic acid) Block Copolymers. *Science* **268**, 1728–1731 (1995).
11. Jain, S. & Bates, F. S. On the origins of morphological complexity in block copolymer surfactants. *Science* **300**, 460–464 (2003).
12. Discher, B. M. *et al.* Polymersomes: Tough Vesicles Made from Diblock Copolymers. *Science* **284**, 1143–1146 (1999).
13. Gröschel, A. H. & Müller, A. H. E. Self-assembly concepts for multicompartiment nanostructures. *Nanoscale* **7**, 11841–76 (2015).
14. Moughton, A. O., Hillmyer, M. A. & Lodge, T. P. Multicompartiment Block Polymer Micelles. *Macromolecules* **45**, 2-19 (2011).
15. Pochan, D. J. *et al.* Toroidal triblock copolymer assemblies. *Science* **306**, 94–97 (2004).

16. Zhu, J. *et al.* Disk-cylinder and disk-sphere nanoparticles via a block copolymer blend solution construction. *Nat. Commun.* **4**, 2297 (2013).
17. Schacher, F. *et al.* Interpolyelectrolyte complexes of dynamic multicompartment micelles. *ACS Nano* **3**, 2095–2102 (2009).
18. Löbbling, T. I. *et al.* Hidden Structural Features of Multicompartment Micelles Revealed by Cryogenic Transmission Electron Tomography. *ACS Nano* **8**, 11330–11340 (2014).
19. Kubowicz, S. *et al.* Multicompartment micelles formed by self-assembly of linear ABC triblock copolymers in aqueous medium. *Angew. Chemie Int. Ed.* **44**, 5262–5265 (2005).
20. Schacher, F., Walther, A., Ruppel, M., Drechsler, M. & Müller, A. H. E. Multicompartment Core Micelles of Triblock Terpolymers in Organic Media. *Macromolecules* **42**, 3540–3548 (2009).
21. Gröschel, A. H. *et al.* Precise hierarchical self-assembly of multicompartment micelles. *Nat. Commun.* **3**, 710 (2012).
22. Cui, H., Chen, Z., Zhong, S., Wooley, K. L. & Pochan, D. J. Block copolymer assembly via kinetic control. *Science* **317**, 647–650 (2007).
23. Fang, B. *et al.* Undulated multicompartment cylinders by the controlled and directed stacking of polymer micelles with a compartmentalized corona. *Angew. Chemie Int. Ed.* **48**, 2877–2880 (2009).
24. Dupont, J. & Liu, G. ABC triblock copolymer hamburger-like micelles, segmented cylinders, and Janus particles. *Soft Matter* **6**, 3654–3661 (2010).
25. Rugar, P. A., Chabanne, L., Winnik, M. A. & Manners, I. Non-centrosymmetric cylindrical micelles by unidirectional growth. *Science* **337**, 559–562 (2012).
26. Zhao, W., Chen, D., Hu, Y., Grason, G. M. & Russell, T. P. ABC Triblock Copolymer Vesicles with Mesh-Like Morphology. *ACS Nano* **5**, 486–492 (2011).
27. Li, Z., Hillmyer, M. A. & Lodge, T. P. Laterally nanostructured vesicles, polygonal bilayer sheets, and segmented wormlike micelles. *Nano Lett.* **6**, 1245–1249 (2006).
28. Brannan, A. K. & Bates, F. S. ABCA Tetrablock Copolymer Vesicles. *Macromolecules* **37**, 8816–8819 (2004).
29. Hu, H. & Liu, G. Miktoarm Star Copolymer Capsules Bearing pH-Responsive Nanochannels. *Macromolecules* **47**, 5096–5103 (2014).
30. Israelachvili, J. N., Mitchell, D. J. & Ninham, W. Theory of Self-Assembly of Hydrocarbon Amphiphiles into Micelles and Bilayers. *J. Chem. Soc. Faraday Trans. 2* **72**, 1525–1568 (1976).
31. Zhulina, E. B., Adam, M., Larue, I., Sheiko, S. S. & Rubinstein, M. Diblock copolymer micelles in a dilute solution. *Macromolecules* **38**, 5330–5351 (2005).

32. Khandpurj, A. K. *et al.* Diblock Copolymer Phase Diagram near the Order-Disorder Transition. *Macromolecules* **28**, 8796–8806 (1995).
33. Leibler, L. Theory of Microphase Separation in Block Copolymers. *Macromolecules* **1617**, 1602–1617 (1980).
34. Ma, Z., Yu, H. & Jiang, W. Bump-surface multicompartment micelles from a linear ABC triblock copolymer: a combination study by experiment and computer simulation. *J. Phys. Chem. B* **113**, 3333–3338 (2009).
35. Antonietti, M. & Förster, S. Vesicles and Liposomes: A Self-Assembly Principle Beyond Lipids. *Adv. Mater.* **15**, 1323–1333 (2003).
36. Rizis, G., van de Ven, T. G. M. & Eisenberg, A. ‘Raft’ formation by two-dimensional self-assembly of block copolymer rod micelles in aqueous solution. *Angew. Chemie Int. Ed.* **53**, 9000–9003 (2014).
37. Hudson, Z. M. *et al.* Tailored hierarchical micelle architectures using living crystallization-driven self-assembly in two dimensions. *Nat. Chem.* **6**, 893–898 (2014).
38. Kim, J.-K., Lee, E., Lim, Y. & Lee, M. Supramolecular capsules with gated pores from an amphiphilic rod assembly. *Angew. Chemie Int. Ed.* **47**, 4662–4666 (2008).
39. Zhu, J. *et al.* Disk-cylinder and disk-sphere nanoparticles via a block copolymer blend solution construction. *Nat. Commun.* **4**, 2297 (2013).
40. Torchilin, V. P. Recent advances with liposomes as pharmaceutical carriers. *Nat. Rev. Drug Discov.* **4**, 145–160 (2005).
41. Vriezema, D. M. *et al.* Self-assembled nanoreactors. *Chem. Rev.* **105**, 1445–1489 (2005).
42. Christian, D. A. *et al.* Spotted vesicles, striped micelles and Janus assemblies induced by ligand binding. *Nat. Mater.* **8**, 843–849 (2009).
43. Wood, D. A., Santangelo, C. D. & Dinsmore, A. D. Self-assembly on a cylinder: a model system for understanding the constraint of commensurability. *Soft Matter* **9**, 10016–10024 (2013).
44. Dupont, J., Liu, G., Niihara, K., Kimoto, R. & Jinnai, H. Self-assembled ABC triblock copolymer double and triple helices. *Angew. Chemie Int. Ed.* **48**, 6144–6147 (2009).
45. Zhong, S., Cui, H., Chen, Z., Wooley, K. L. & Pochan, D. J. Helix self-assembly through the coiling of cylindrical micelles. *Soft Matter* **4**, 90–93 (2008).
46. Blanazs, A., Madsen, J., Battaglia, G., Ryan, A. J. & Armes, S. P. Mechanistic insights for block copolymer morphologies: how do worms form vesicles? *J. Am. Chem. Soc.* **133**, 16581–16587 (2011).
47. Yabu, H., Higuchi, T. & Jinnai, H. Frustrated phases: polymeric self-assemblies in a 3D confinement. *Soft Matter* **10**, 2919–2931 (2014).

48. Gohy, J., Willet, N., Varshney, S., Zhang, J. & Jerome, R. Core-Shell- Corona Micelles with a Responsive Shell. *Angew. Chemie Int. Ed.* **40**, 3214–3216 (2001).
49. Lei, L. *et al.* Dependence of the structure of core–shell–corona micelles on the composition of water/toluene mixtures. *Polymer* **47**, 2723–2727 (2006).
50. Stewart, S. & Liu, G. Block Copolymer Nanotubes. *Angew. Chemie Int. Ed.* **6**, 340–344 (2000).
51. Bates, F. S. *et al.* Multiblock polymers: panacea or Pandora’s box? *Science* **336**, 434–440 (2012).
52. Löblich, T. I. *et al.* Bulk morphologies of polystyrene-block-polybutadiene-block-poly(tert-butyl methacrylate) triblock terpolymers. *Polymer* **72**, 479–489 (2015).
53. Raula, J. *et al.* Synthesis of gold nanoparticles grafted with a thermoresponsive polymer by surface-induced reversible-addition-fragmentation chain-transfer polymerization. *Langmuir* **19**, 3499–3504 (2003).
54. Kremer, J. R., Mastrorarde, D. N. & McIntosh, J. R. Computer visualization of three-dimensional image data using IMOD. *J. Struct. Biol.* **116**, 71–76 (1996).
55. Engelhardt, P. *Electron Tomography of Chromosome Structure. Encycl. Anal. Chem.* (2000).
56. Pettersen, E. F. *et al.* UCSF Chimera - A visualization system for exploratory research and analysis. *J. Comput. Chem.* **25**, 1605–1612 (2004).
57. Hall, M. *et al.* The WEKA data mining software: An update. *ACM SIGKDD Explor.* **11**, 10–18 (2009).

Acknowledgments

The authors thank Dr. Holger Schmalz for helpful discussions about polymer synthesis and Dr. Andreas Hanisch for the synthesis of four SBT terpolymers. We thank Adjunct Professor in Molecular Genetics Peter Engelhardt for help with transmission electron tomography. The authors acknowledge the Deutsche Forschungsgemeinschaft (DFG) for supporting this work within DFG Mu896/40-1. This work was carried out under the Academy of Finland's Centre of Excellence Programme (2014-2019) and supported by ERC-2011-AdG (291364-MIMEFUN). This work was partially supported by Russian Science Foundation grant # 14-33-00003. The authors further made use of the Aalto University Nanomicroscopy Center (Aalto-NMC) premises.

Author Contributions

T.I.L. synthesized the polymers. T.I.L. and A.H.G. performed experiments and collected all data. J.H. helped with the tomograms and commented on the manuscript. O.I. co-designed experiments, discussed results and commented on the manuscript. O.B. developed the theory and commented on the manuscript. T.I.L., A.H.G. and A.H.E.M. designed the

experiments, discussed results and wrote the manuscript. O.I., A.H.G. and A.H.E.M. supervised the project.

Competing financial interests

The authors declare no competing financial interests.

Additional information

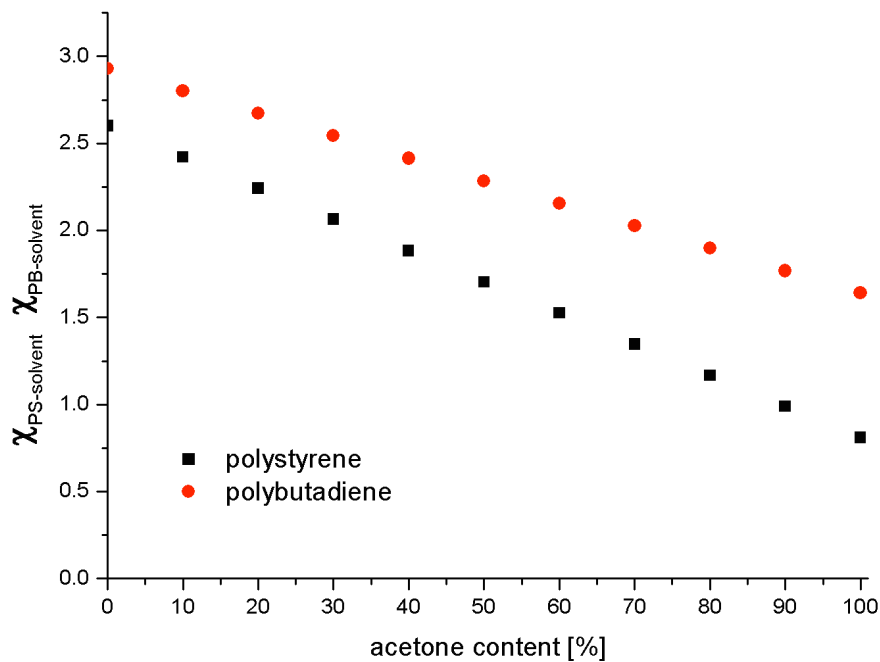
Correspondence and requests for materials should be addressed to A.H.G., O.I. or A.H.E.M.

Supplementary Information

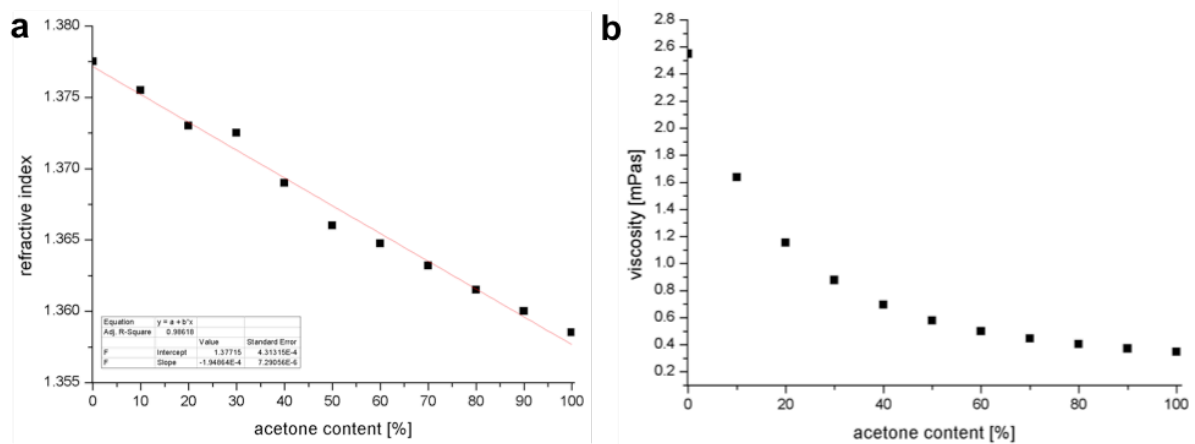
to

**Rational Design of ABC Triblock Terpolymer Solution
Nanostructures with Controlled Patch Morphology**

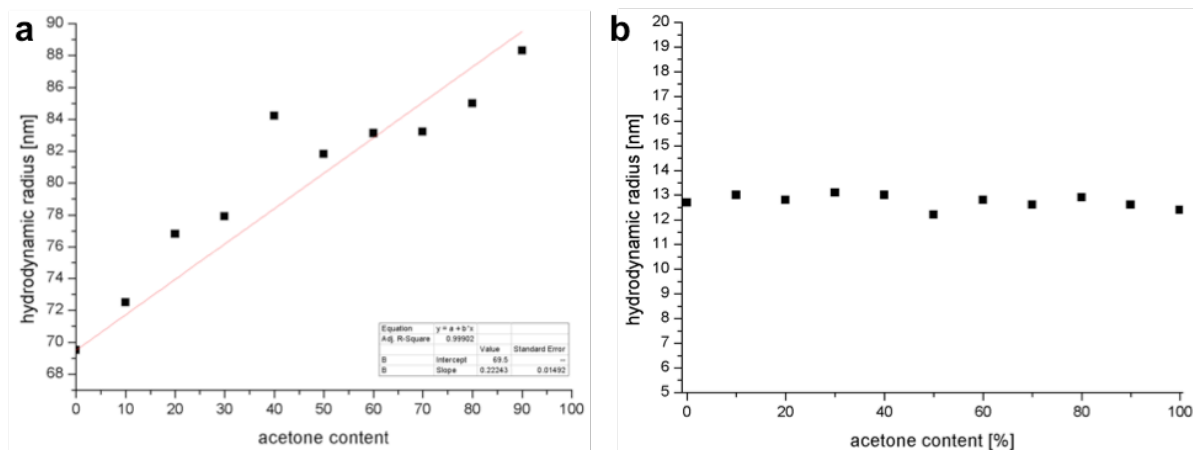
by Tina I. Löblich, Oleg Borisov, Johannes Haataja, Olli Ikkala*, André H. Gröschel* and
Axel H. E. Müller*



Supplementary Figure 5.1. Polymer-solvent interaction parameter, χ , in dependence of acetone/isopropanol content. As the polymer-solvent interaction parameter $\chi_{\text{PB-solvent}}$ is >1.5 we assume PB to be in a constant non-swollen state independent of the solvent composition. In case of PS, $\chi_{\text{PS-solvent}}$ decreases from 2.6 below 1 at high acetone contents, suggesting a plasticising effect of acetone on the PS block, although it remains above θ -conditions ($\chi > 0.5$). A summary of interaction parameters for our system can be found in Supplementary Table 5.1.

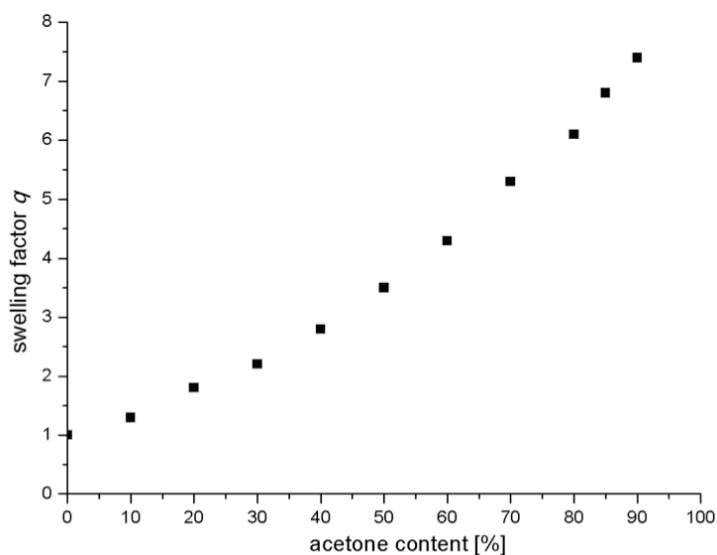


Supplementary Figure 5.2. a, Refractive index and **b**, dynamic viscosity of a series of acetone/isopropanol mixtures.

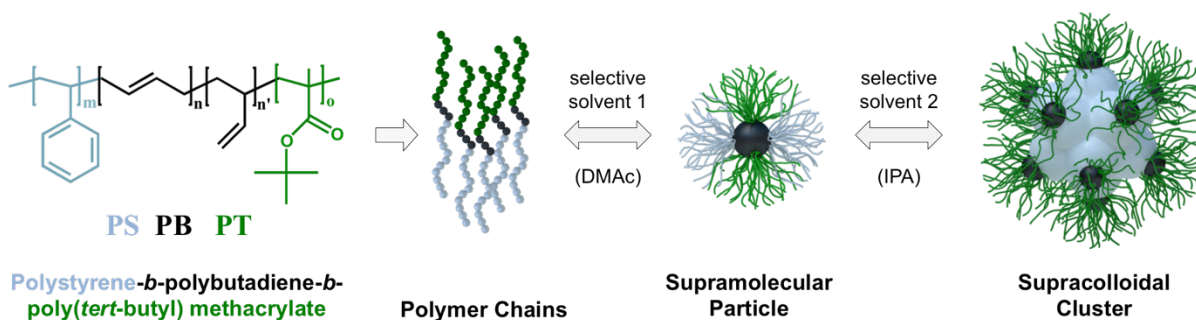


Supplementary Figure 5.3. Swelling of PS in dependence of the acetone-isopropanol content.

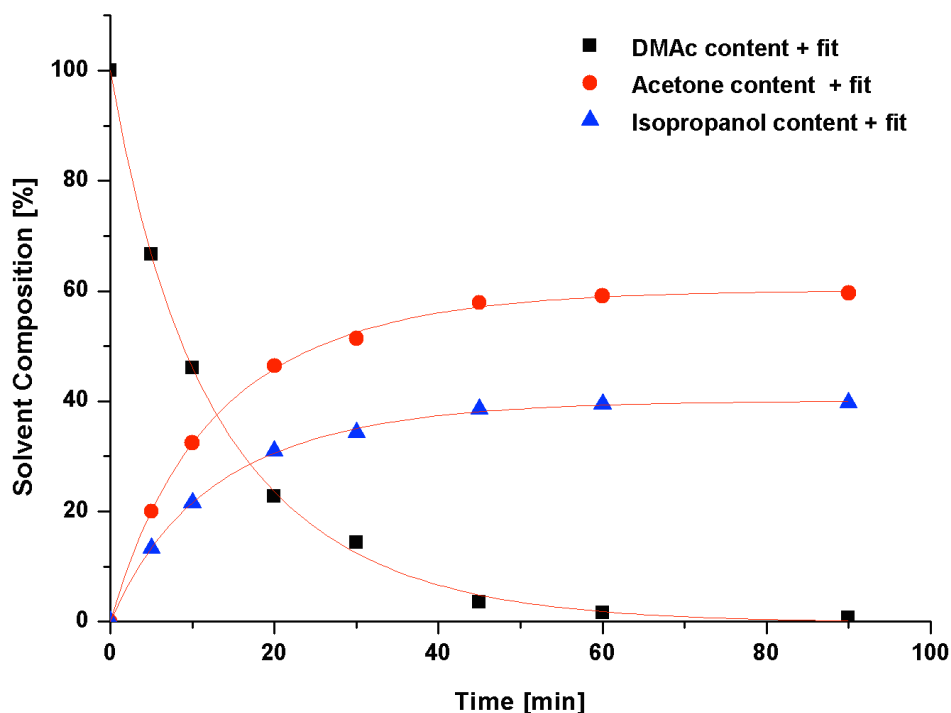
a, Hydrodynamic radius, R_h , of a $S_{366}T_{456}$ diblock copolymer as determined by DLS at 90° angle in varying acetone/isopropanol mixtures and **b**, of a poly(*tert*-butyl methacrylate) star homopolymer. While the R_h of PT is not affected by the acetone content, swelling of the PS core continuously increases the overall R_h of PS-PT block copolymer micelles.



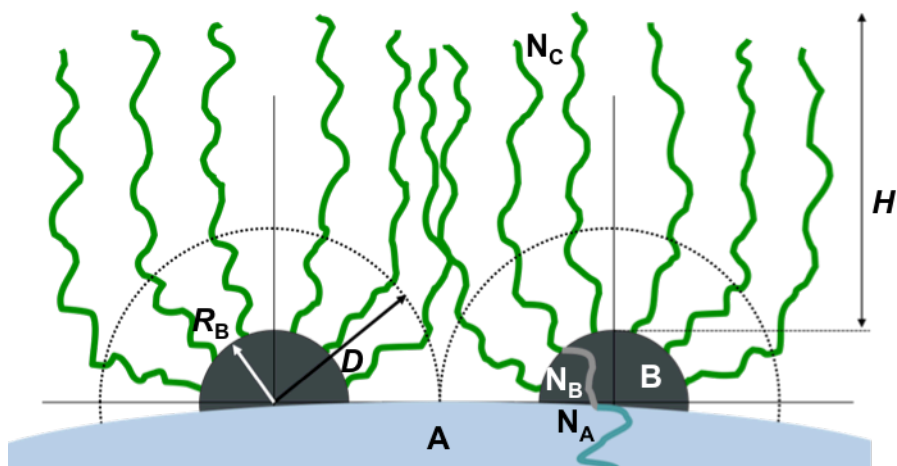
Supplementary Figure 5.4. Volume swelling factor, q , of PS in dependence of the acetone/isopropanol content. The volume swelling factor, q , was calculated from Supplementary Eq. (5.1) and (5.2) (see Supplementary Note 5.1 and Supplementary Table 5.3) and shows a significant swelling of the PS block with increasing acetone content leading to larger apparent PS volumes.



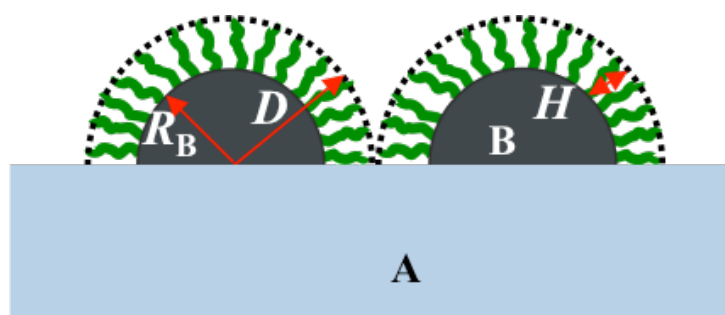
Supplementary Figure 5.5. Proposed self-assembly mechanism for PS-PB-PT triblock terpolymers to compartmentalized micelles. Polymer chains of PS-PB-PT are dispersed in a selective solvent for both outer blocks (*N,N*-dimethylacetamide; DMAc) to form micelles with a PB core and a PS/PT corona. The segmented PS and PT corona has valence-like directional interactions for controlled self-assembly into the final multicompartment nanostructure. This self-assembly step is triggered by solvent exchange to e.g. acetone/isopropanol which collapses the PS corona inducing aggregation of the preformed building blocks. Unlike for the self-assembly of the diblock copolymers that follows rules akin to lipids, variations in solubility of the terpolymer blocks will induce sequential collapse in selective solvents. The structural evolution of PS-PB-PT during dialysis from DMAc to the final solvent thus proceeds through soft amphiphilic Janus nanoparticles as the PS block starts to collapse and phase-separate from the soluble PT corona.



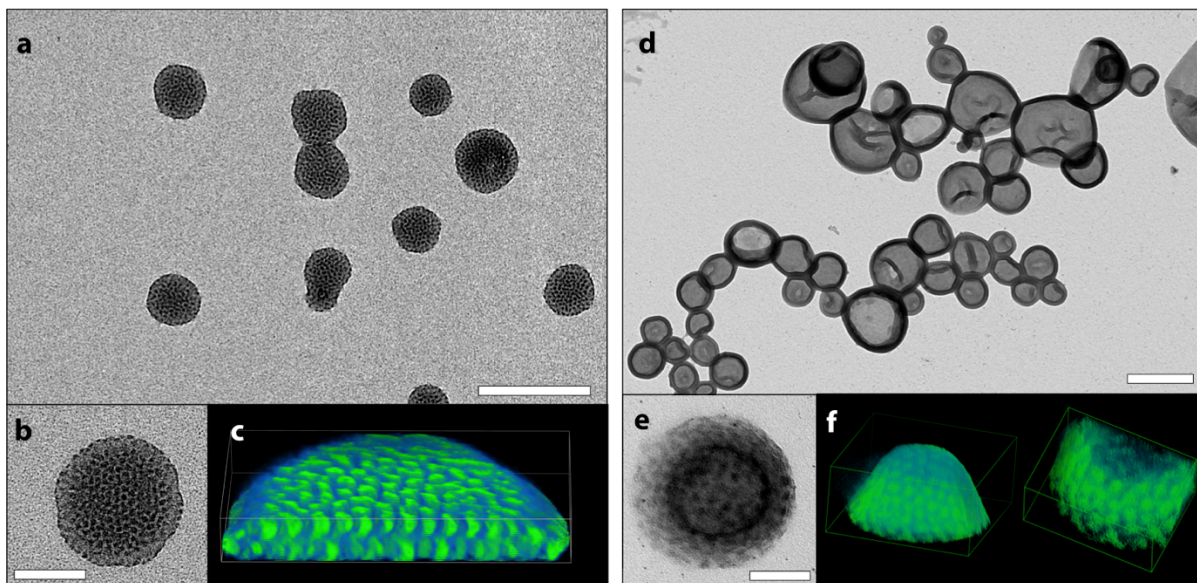
Supplementary Figure 5.6. $^1\text{H-NMR}$ study of the time dependent solvent composition. The solvent exchange is completed after 90 min of dialysis from *N,N*-dimethylacetamide to acetone/isopropanol 60:40 v/v.



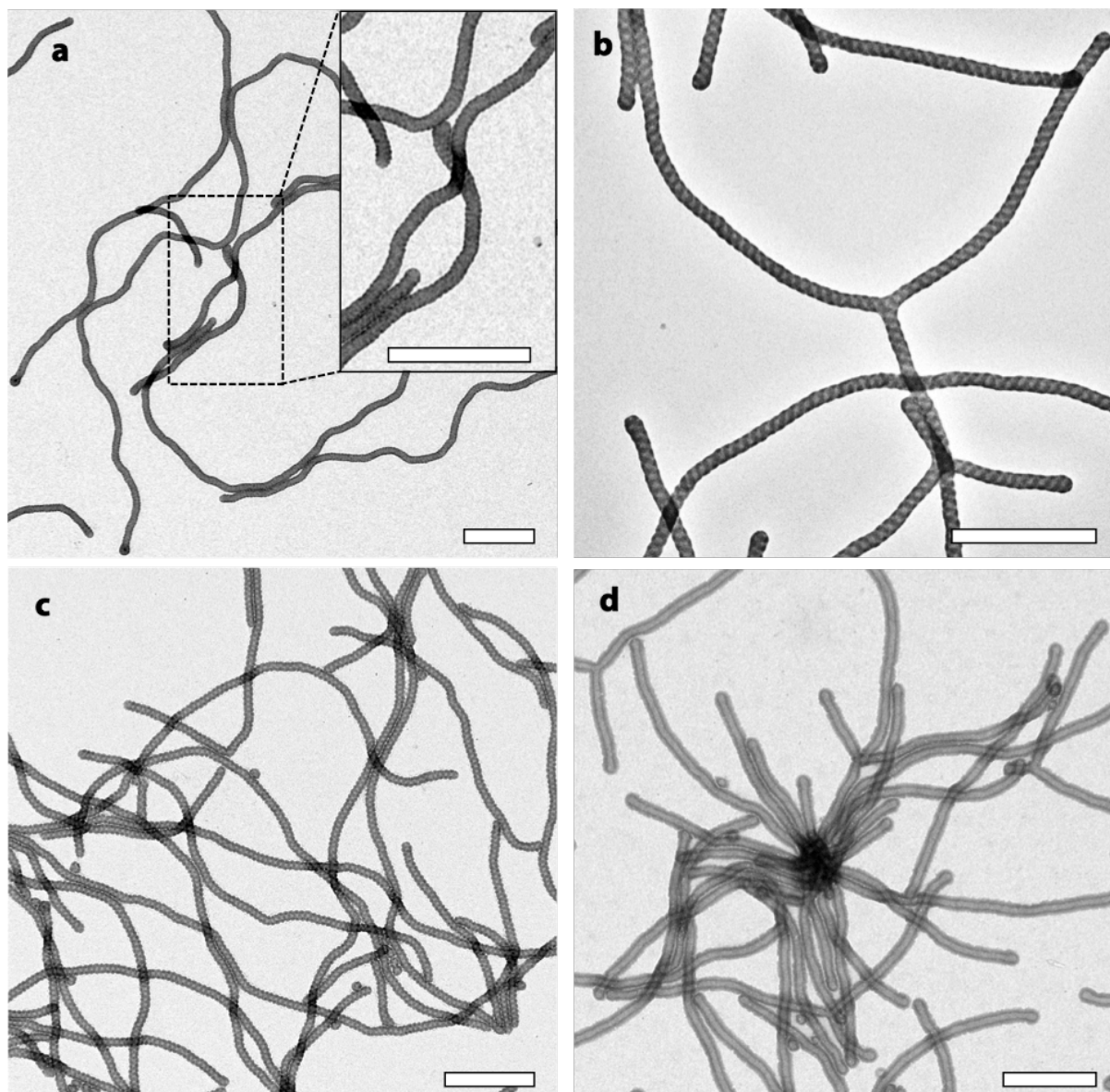
Supplementary Figure 5.7. Schematic presentation of crew-cut micelles with spherical B-patches and arbitrary geometry of the A-core, $R_B \ll H_{\text{corona}} \ll R_A$. With decreasing H_{corona}/R_A a transition from spherical to cylindrical micelle geometry occurs and further to lamellar or vesicular structures. For detailed description please see Supplementary Note 2.



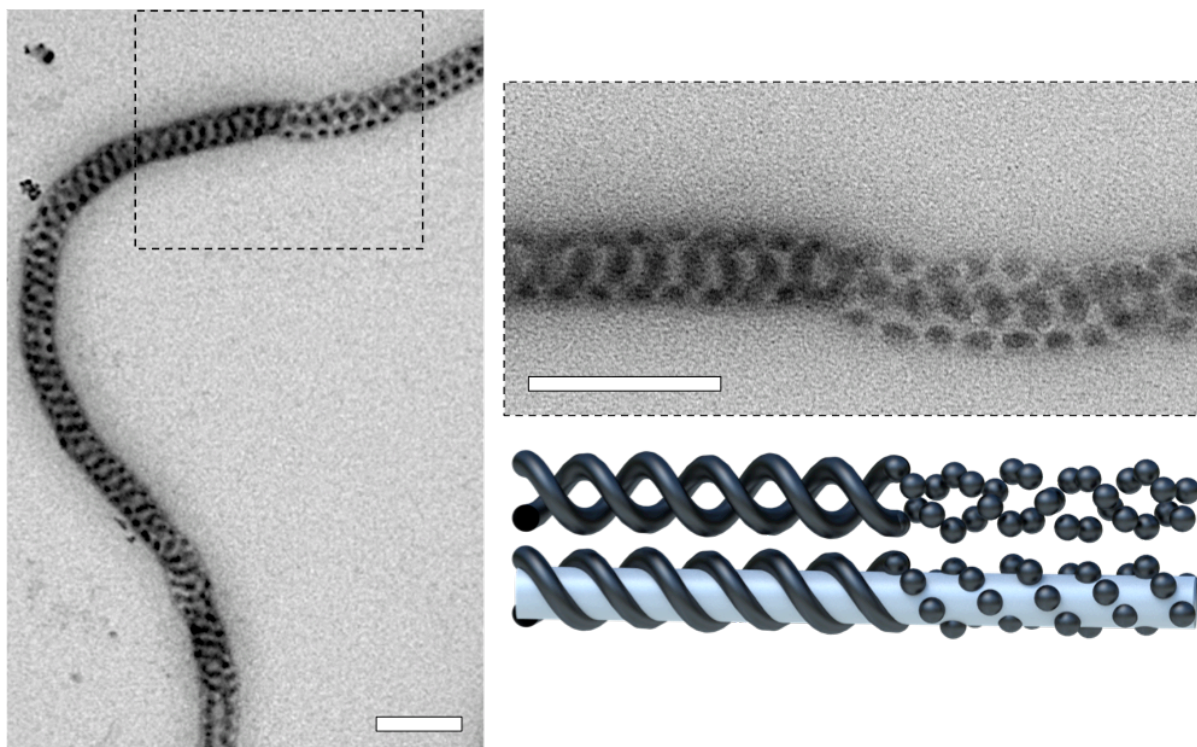
Supplementary Figure 5.8. Schematic presentation of crew-cut patchy micelles with spherical or cylindrical B-patches decorating the central A-core, $H_{\text{corona}} \ll R_B \ll R_A$. With increasing R_B/H_{corona} a transition from spherical to cylindrical B-patches occurs and further to the core-shell structure. For a detailed description please see Supplementary Note 2.



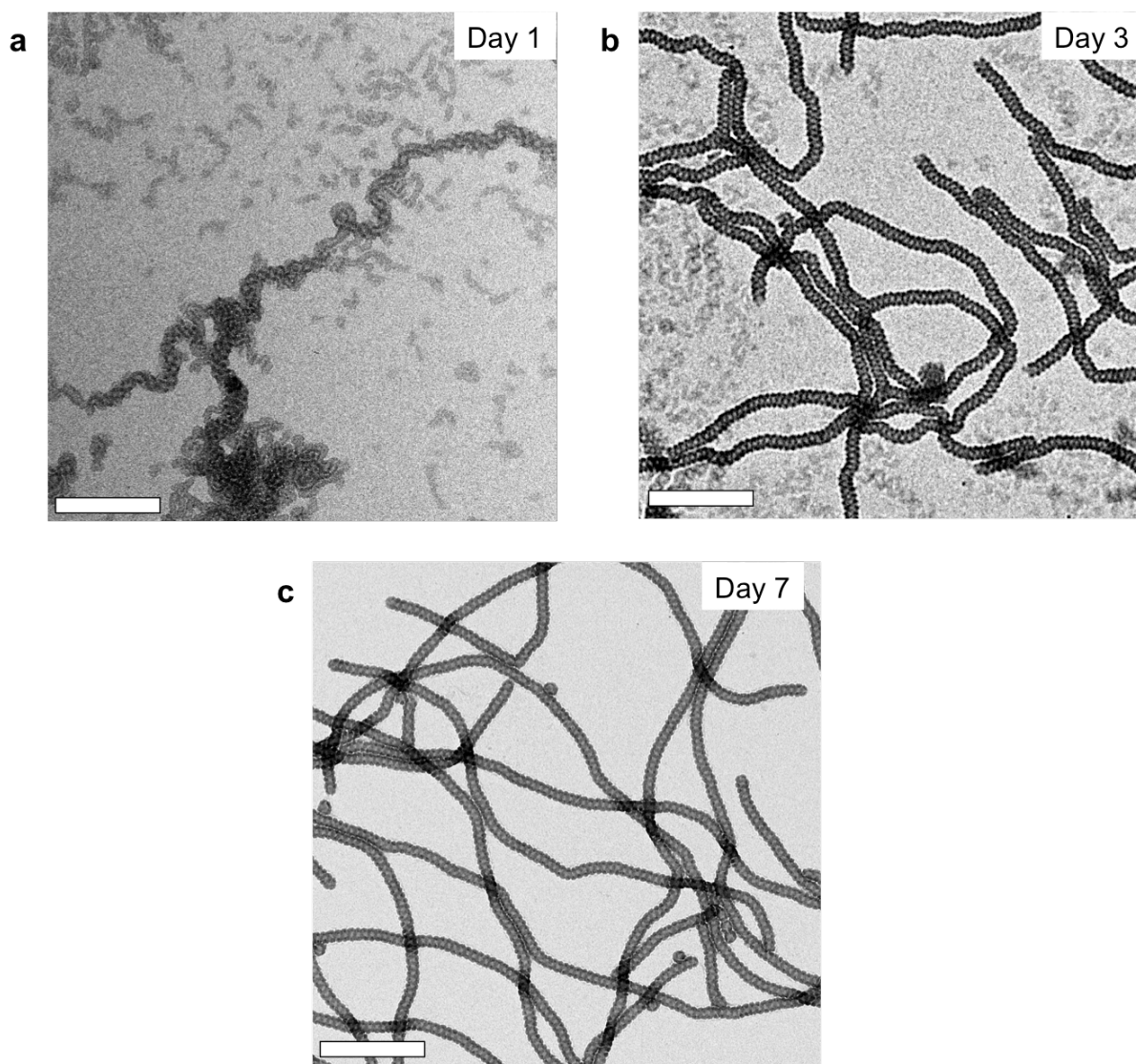
Supplementary Figure 5.9. Tomography and 3D reconstruction of patchy sheets and vesicles. **a**, and **d**, show TEM overview images of sheets with spherical patches of $S_{540}B_{173}T_{137}$ in 85:15 v/v and patchy vesicles of $S_{540}B_{173}T_{88}$ in 60:40 v/v acetone/isopropanol. **b**, and **e**, show a patchy sheet and vesicle subjected to electron tomography. Scale bars are 500 nm in the overview and 200 nm in the insets respectively. **c**, and **f**, Reconstruction confirming bilayer thickness for sheets and hollow interior for the vesicles. For TEM tomography, samples are prepared on carbon coated copper grids that have been pre-cast with gold particles with a diameter of $d = 10$ nm. The gold particles are fixed markers and later help to align the series of recorded TEM images of the same area taken between $\pm 60^\circ$ in 2° increments. 3D reconstruction yields a density map, where brighter colours correspond to higher electron contrast, i.e., the OsO_4 stained PB phase is displayed in bright green.



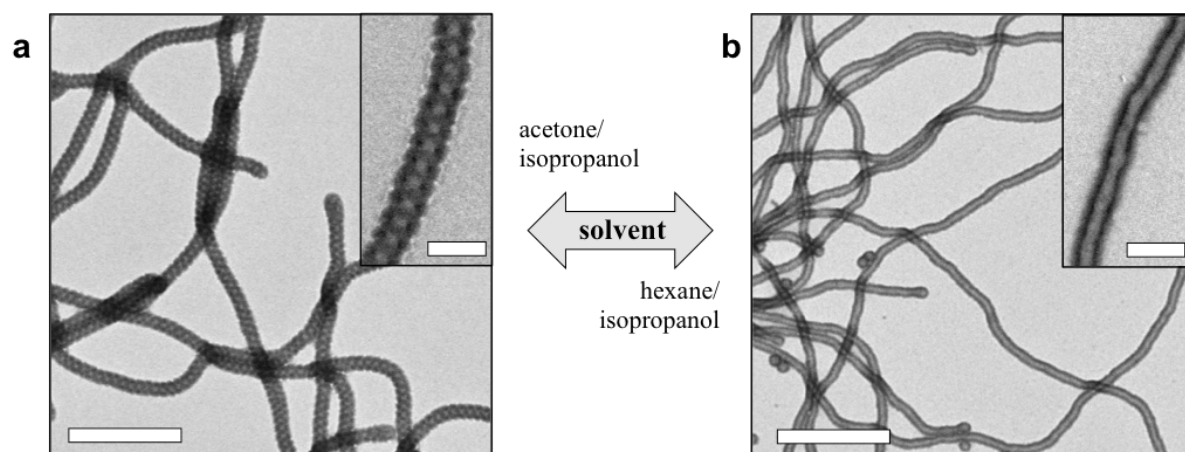
Supplementary Figure 5.10. TEM overviews of patch morphologies on cylinder micelles. a, Spherical patches of $S_{540}B_{173}T_{137}$ in acetone/isopropanol 60:40 v/v, **b,** thin double helical patches of $S_{510}B_{539}T_{154}$ in acetone/isopropanol 60:40 v/v, **c,** medium double helical patches of $S_{307}B_{385}T_{81}$ in acetone/isopropanol 60:40 v/v and **d,** core-shell cylinders of $S_{307}B_{530}T_{75}$ in *n*-hexane/isopropanol 50:50 v/v. Scale bars are 500 nm.



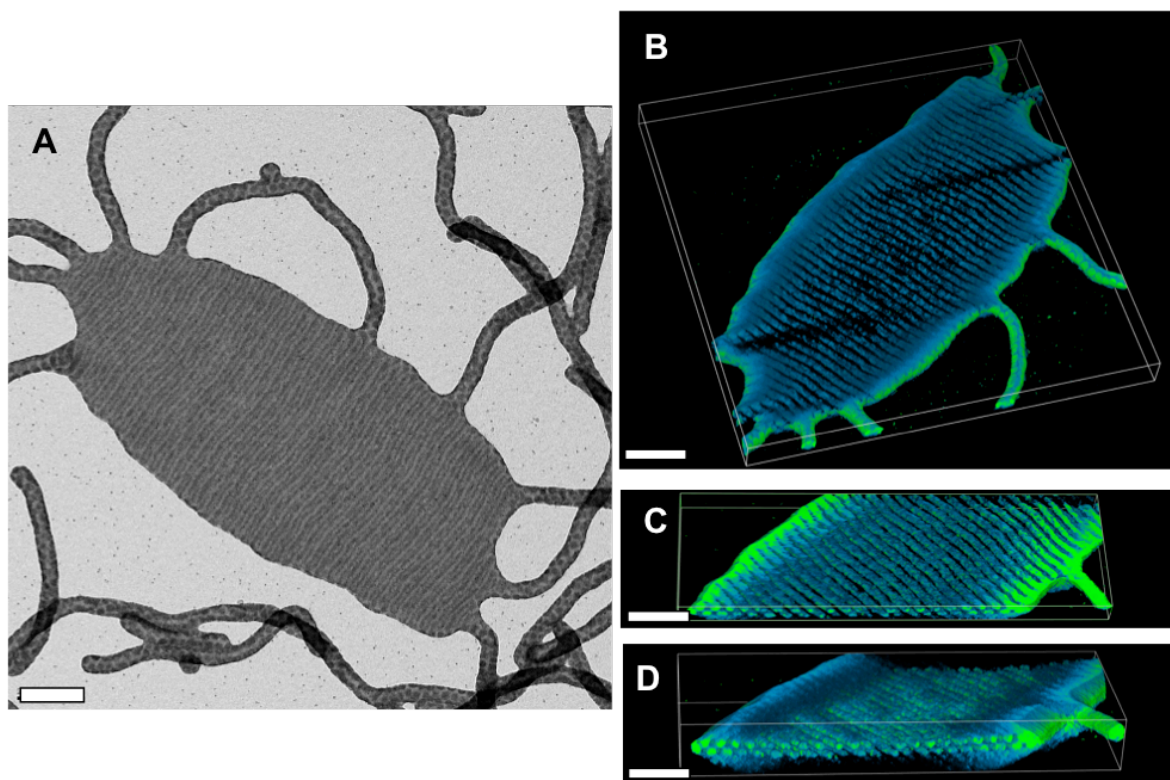
Supplementary Figure 5.11. Simultaneous appearance of PB spheres and helices on cylindrical micelles. $S_{510}B_{539}T_{154}$ in acetone/isopropanol 80:20 v/v forms PS cylinders with a mixture of PB spheres and helices. This solvent mixture demonstrates the crucial influence of solvent composition on the resulting nanostructure. The close up shows the transitions from large spheres to a double-helical arrangement of PB which is also shown in the schematics. Scale bars are 200 nm.



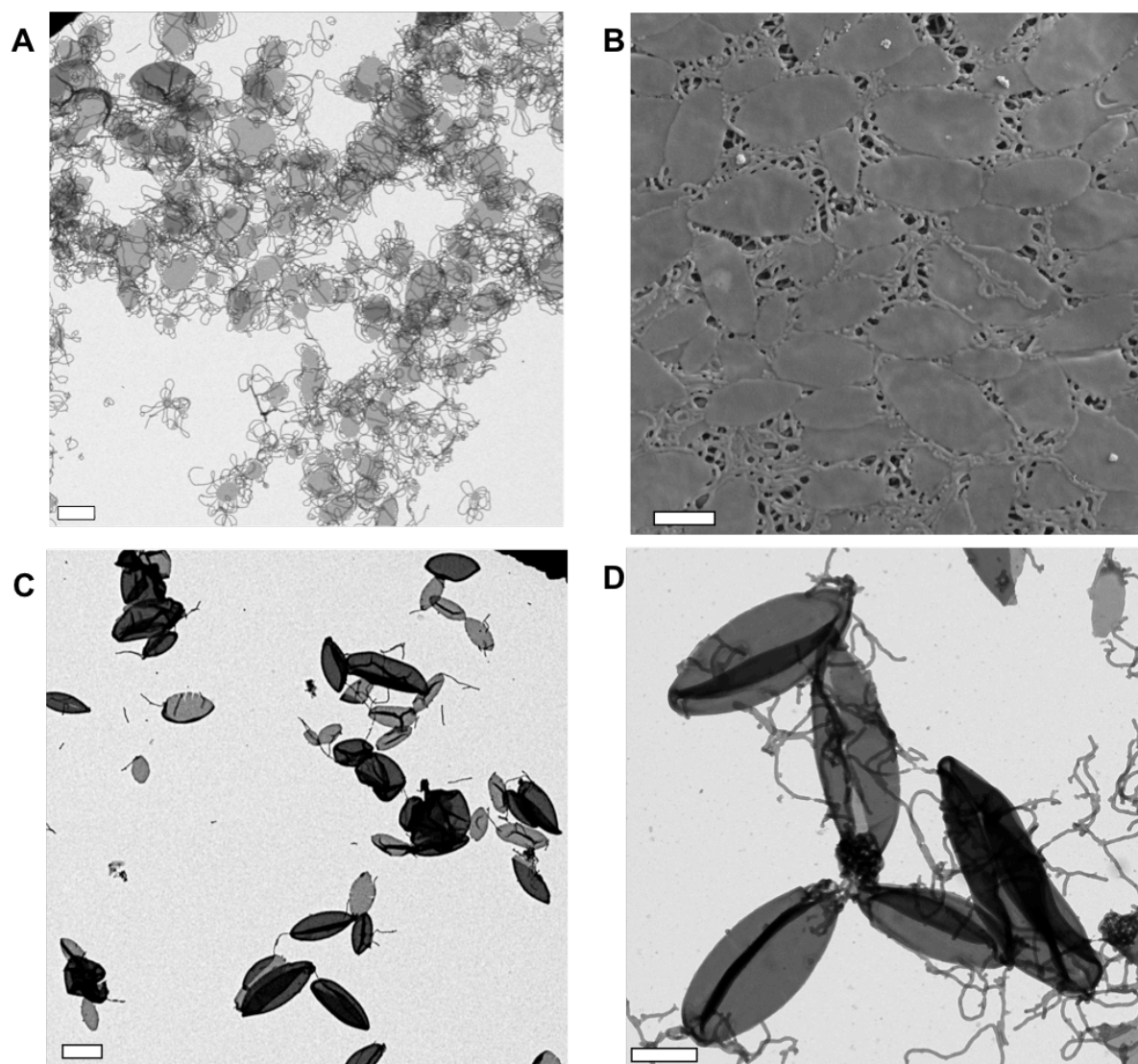
Supplementary Figure 5.12. Time-dependent morphological evolution of S₃₀₇B₃₈₅T₈₁ in acetone/isopropanol 60:40 v/v. The slowed self-assembly process of amphiphilic colloids compared to single polymer chains is demonstrated through time-dependent TEM measurements of one sample. **a**, Directly after dialysis few cylindrical micelles are visible mixed with smaller building blocks. **b**, The cylindrical micelles are more pronounced after 3 days of ageing although still smaller fragments are visible throughout the sample. **c**, After 5 days of ageing no small fragments are visible and the final structure does not noticeably change after 7 days. Scale bars are 500 nm.



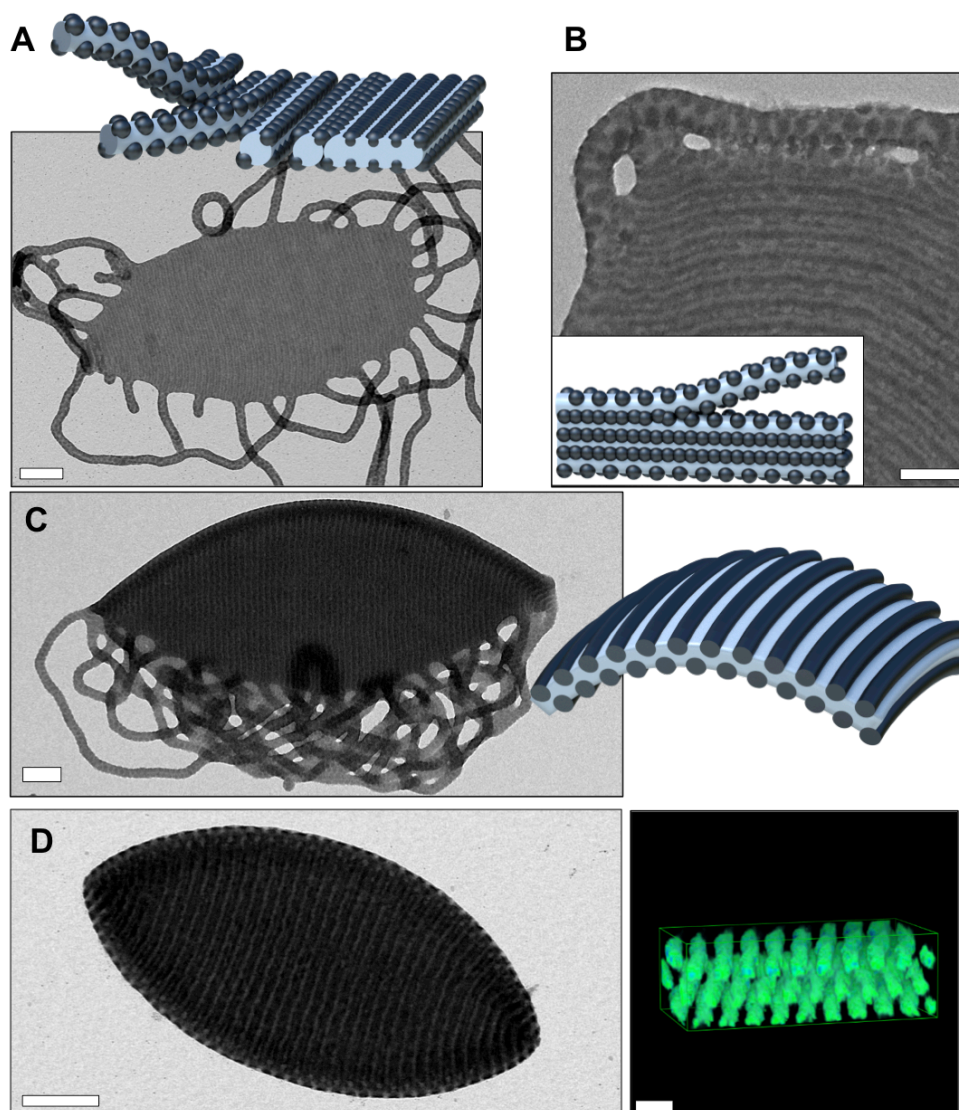
Supplementary Figure 5.13. Reversible dewetting/wetting of PB phase. **a**, The PB phase in $S_{307}B_{530}T_{75}$ can be reversibly switched from a double helical arrangement to **b**, a homogeneous shell by changing from acetone/isopropanol 60:40 v/v to isohexane-isopropanol 60:40 v/v. Scale bars are 500 nm in the overview and 100 nm in insets.



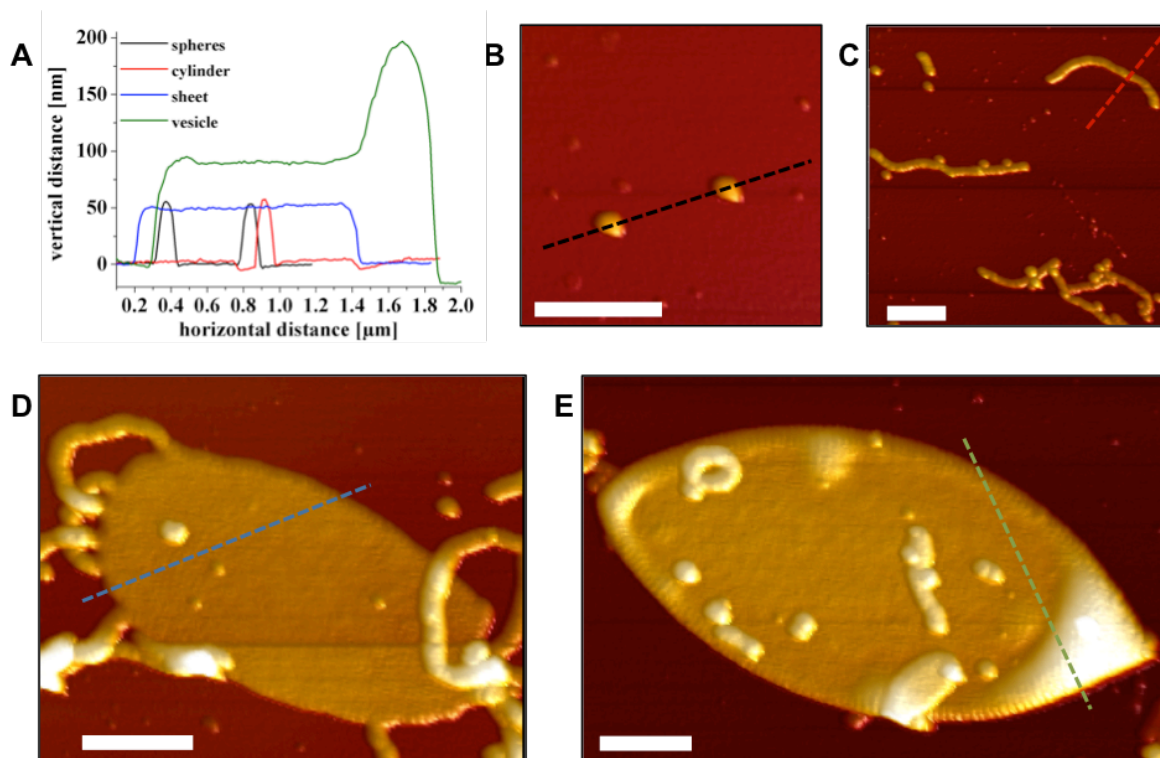
Supplementary Figure 5.14. Tomographic 3D reconstruction of striped sheet of $S_{510}B_{539}T_{154}$. **a**, TEM image of a striped sheet particle subjected to transmission electron tomography. **b**, Top-view of the entire sheet and **c**, slice from the middle section. **d**, Side view of 3D reconstruction of the striped sheet morphology. The hexagonal packing of the cylinders is visible through the offset of the cylinders on top and bottom side of the sheet in the side view. The scale bars are 200 nm.



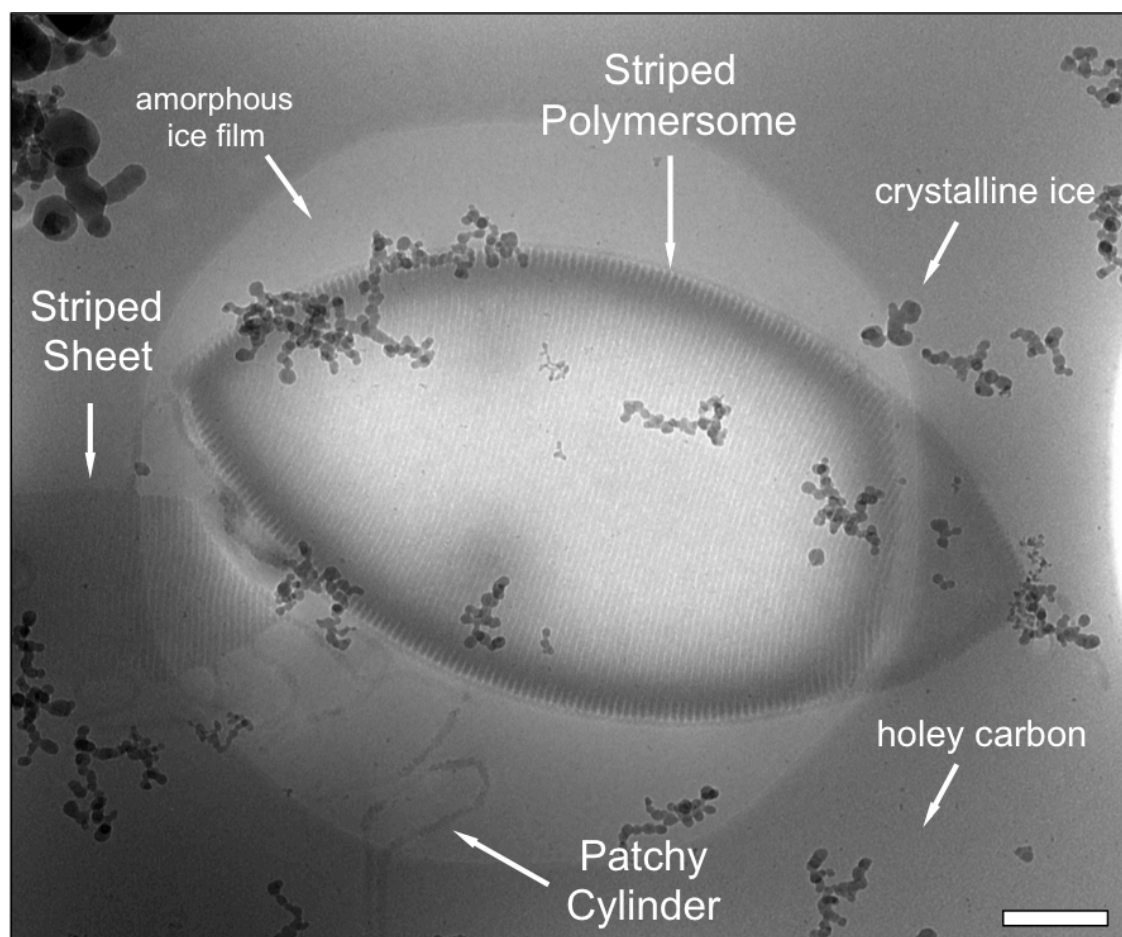
Supplementary Figure 5.15. Overview images of different striped sheets and vesicles. a, TEM overview of striped sheets of $S_{510}B_{539}T_{154}$ in acetone/isopropanol 75:25 v/v. **b,** SEM overview image of $S_{510}B_{539}T_{154}$ in acetone/isopropanol 75:25 v/v. **c,** $S_{510}B_{539}T_{154}$ in acetone/isopropanol 85:15 v/v gives predominately striped vesicles after aging for several months. **d,** The vesicles of sample in (c) show characteristic folding pattern upon deflation. Scale bars are 1000 nm.



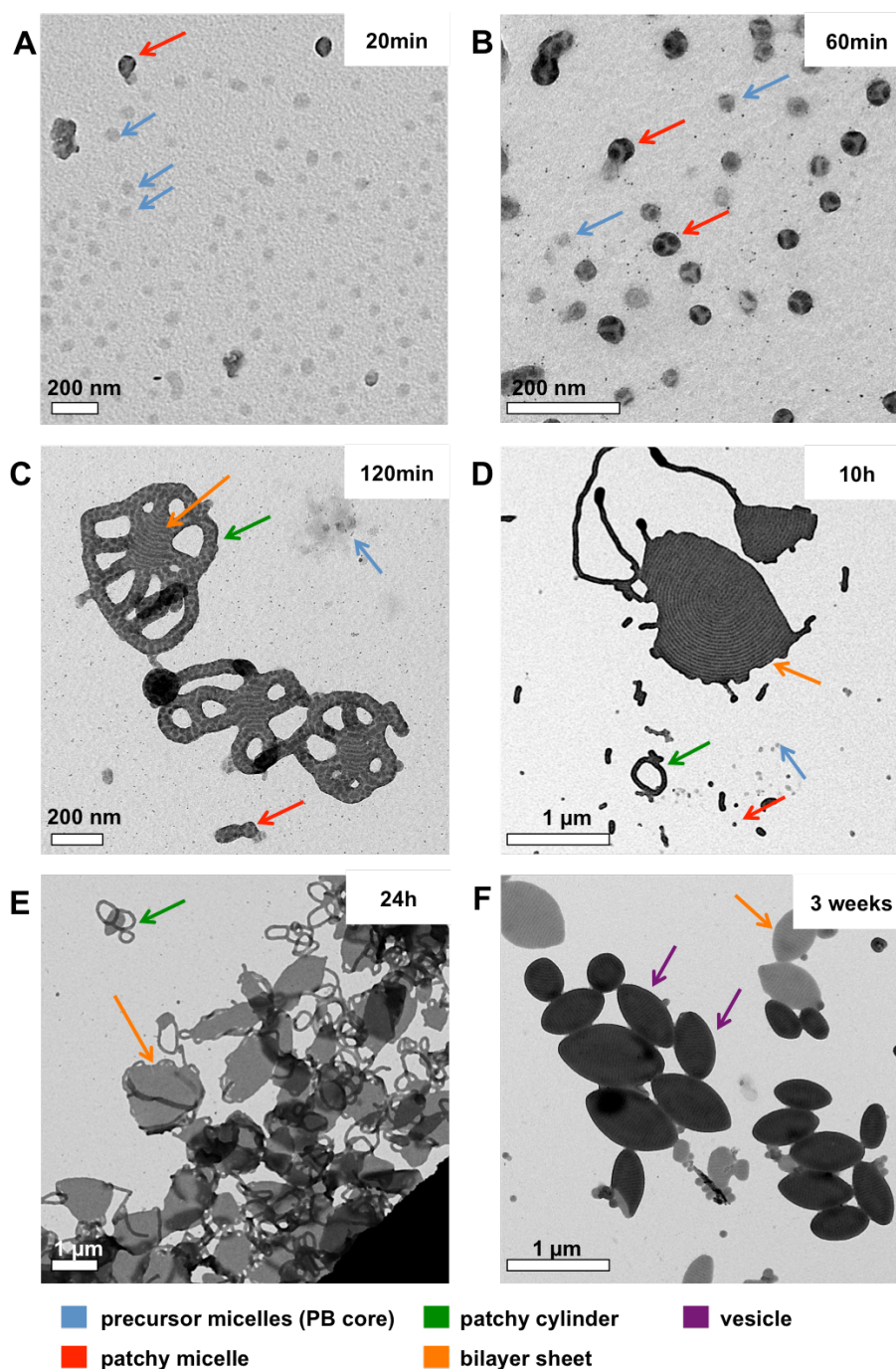
Supplementary Figure 5.16. Morphological transition from patchy cylinder to striped vesicles of $S_{510}B_{539}T_{154}$. **a**, TEM image of a cylinder-on-sheet particle with “tentacles” of cylinders carrying thick PB patches. The schematic shows the fusion of cylinders into a sheet through side to side addition of cylinders. **b**, A zoom-in shows a cylinder with PB patches attaching to a sheet already carrying PB cylinders. After attaching to the sheet, the PB patches fuse into PB cylinders as demonstrated by the schematics. **c**, When sheets grow large enough the unfavorable line energy of the edges force sheets to fold and roll up to vesicles. The TEM image shows the intermediate state also referred to as “jelly-fish” morphology. **d**, TEM image of a deflated vesicle. A slice from the middle section of the 3D reconstruction shows cylinders are on top, bottom and in the middle of the deflated vesicle. The scale bars are 200 nm (a, c, d) and 100 nm (b and e).



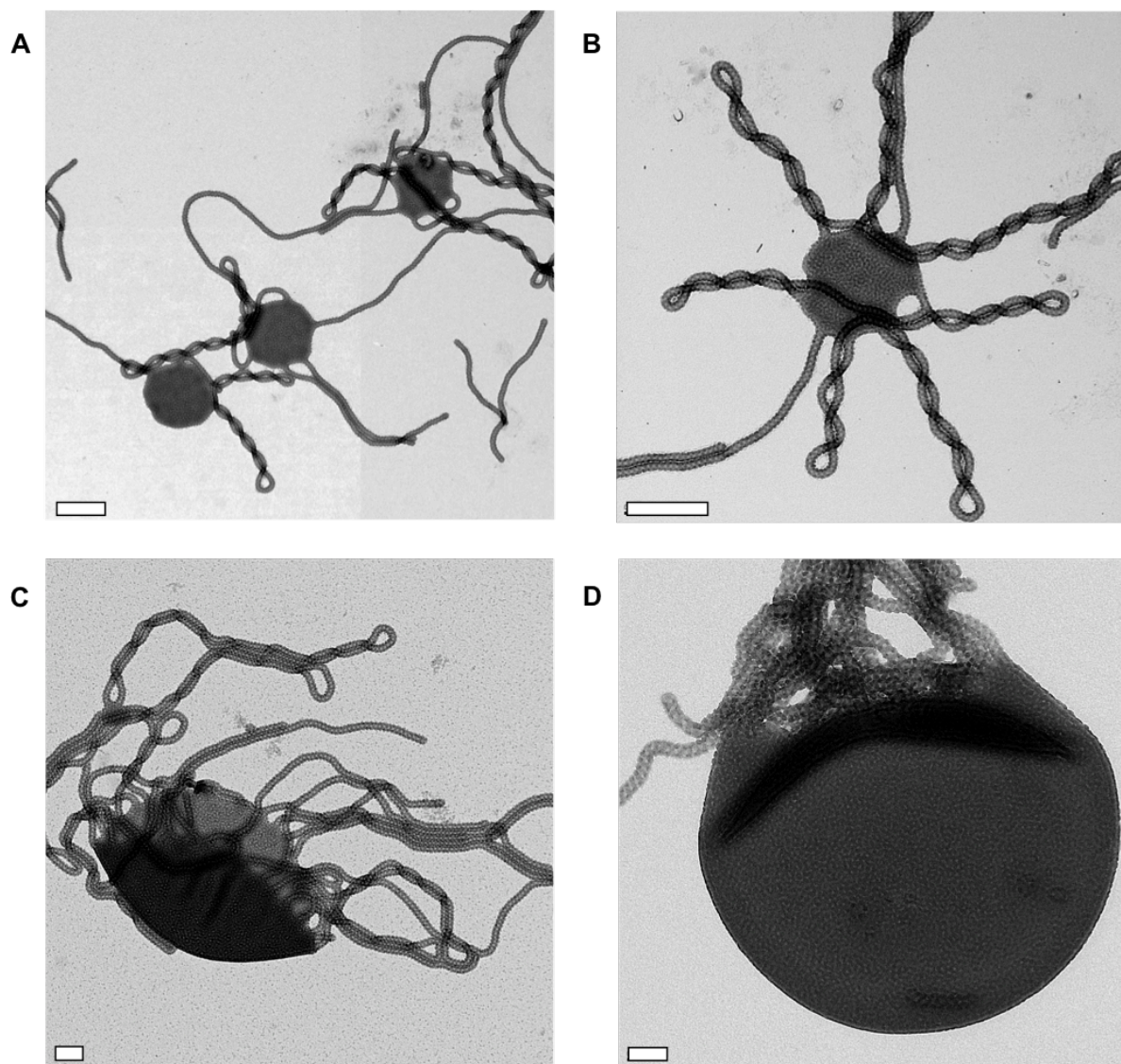
Supplementary Figure 5.17. AFM height profile measurements of $S_{510}B_{539}T_{154}$ in acetone/isopropanol 85:15 v/v. Although the decrease of the corona block length yields striped sheets and later vesicles at high fraction, we still find residues of the lower dimensional particles that have not evolved as of yet. Since we first assemble polymer chains to nanoparticles that in turn form the final structure, one should keep in mind that the drastically reduced diffusion rate slows down self-assembly kinetics. We thus often find a mixture of micelles at different stages of self-assembly at specific time frames that continuously develop into the final structure over time. **a**, The height profiles of sphere, cylinders, sheets and vesicles. **b**, Spherical micelles carrying PB spheres with height of $h_{\text{sph}}=53.4$ nm. **c**, Cylindrical micelles with spherical PB patches and height of $h_{\text{cyl}}=57.5$ nm and diameter comparable to spherical micelles of (a). **d**, The sheets have continuous height of $h_{\text{sh}}=48.4$ nm across the entire plane. The striped morphology of PB surface patches is faintly visible. **e**, The vesicle also carries PB cylinders noticeable at the rim. Vesicles deflate during drying and vesicle walls of bilayer thickness collapse on top of each other. In height measurements, we thus detect almost twice the height of the sheet. Also not entirely deflated areas show considerably increased height supporting the hollow interior. The scale bars denote 500 nm.



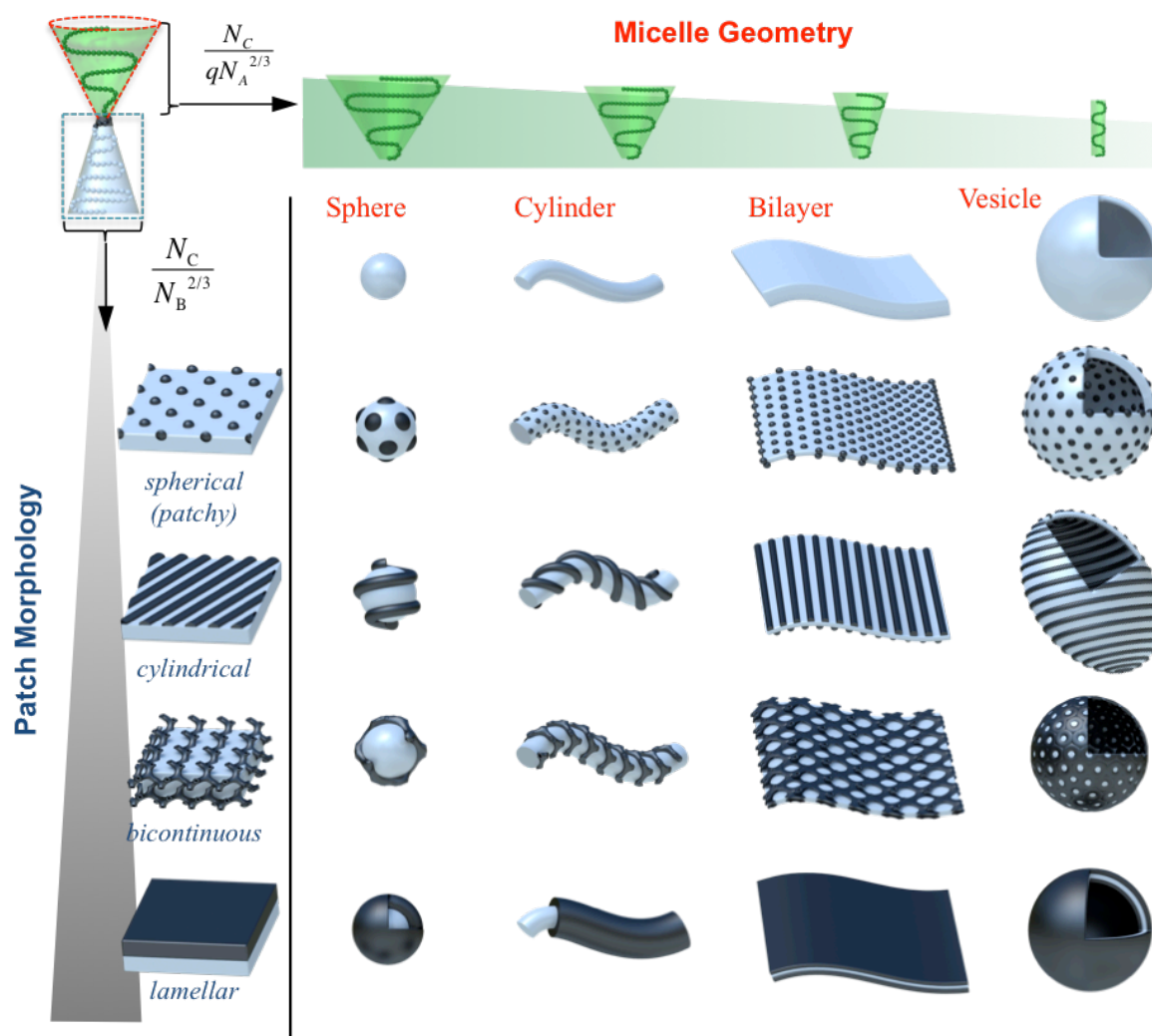
Supplementary Figure 5.18. Cryo-TEM image of a striped vesicle of $S_{510}B_{539}T_{154}$ in acetone/isopropanol 85:15 v/v. The cryo-TEM image shows a holey carbon film with a sheet and lemon-shaped vesicle with striped patch morphology embedded in vitrified (amorphous) acetone/isopropanol mixture. The scale bar is 500 nm.



Supplementary Figure 5.19. Time-dependent morphological evolution of $S_{510}B_{539}T_{154}$ in acetone/isopropanol 85:15 v/v. The slowed self-assembly process of amphiphilic colloids compared to single polymer chains is demonstrated through time dependent TEM measurements. During dialysis, first some ill-defined structures are formed **a**, before after 60min of dialysis spherical multicompartiment micelles are observed **b**. After 120 min, besides spherical micelles, also the onset of cylinder and sheet formation is visible **c**, that develop and grow in size as can be seen after 10 h **d**. After 24 h large fraction of sheets with cylindrical arms attached have formed **e**. Finally lemon-shaped vesicles developed after three weeks of ageing **f**. Scale bars are 200nm (a-d) and 500 nm (e, f).



Supplementary Figure 5.20. Bilayer sheets with bicontinuous morphology and jelly-fish intermediates. **a**, $S_{307}B_{530}T_{75}$ in acetone/isopropanol (60:40 v/v) forms sheets with bicontinuous patch morphology. **b**, Sheets often contain “tentacles” that are helically wrapped after ageing for two months. **c**, and **d**, “Jelly-fish” intermediates of $S_{307}B_{530}T_{63}$ in acetone/isopropanol 60:40 v/v before final closure to a vesicle. Scale bars are 500 nm (a, b) and 200 nm (c, d) respectively.



Supplementary Figure 5.21. Theoretical library of classical solution geometries sub-divided with internal morphologies. From left to right: Spheres, cylinders, sheets and vesicles with (from top to bottom) spherical, cylindrical/helical, bicontinuous and lamellar (core-shell) patch morphology.

Supplementary Table 5.1: Overview and characteristics of used SBT triblock terpolymers.

Code	Composition ^b	N_S^c	N_B^c	N_T^c	x_T^d	ϕ_{PB}^e	$N_T/N_S^{2/3}$	$N_T/N_B^{2/3}$	PDI
S ₃₀₀ B ₇₅₆ T ₅₆	S ₃₉ B ₅₁ T ₁₀ ⁸⁰	300	756	56	0.05	0.58	1.25	0.67	1.08
S ₃₀₇ B ₅₃₀ T ₆₃	S ₄₆ B ₄₁ T ₁₃ ⁶⁹	307	530	63	0.07	0.50	1.38	0.96	1.03
S ₃₀₇ B ₃₈₅ T ₅₆	S ₅₃ B ₃₄ T ₁₃ ⁶¹	307	385	56	0.07	0.42	1.23	1.06	1.03
S ₃₀₇ B ₅₃₀ T ₇₅	S ₄₅ B ₄₀ T ₁₅ ⁷¹	307	530	75	0.08	0.50	1.65	1.15	1.04
S ₃₀₀ B ₇₅₆ T ₁₀₄	S ₃₆ B ₄₇ T ₁₇ ⁸⁷	300	756	104	0.09	0.58	2.32	1.25	1.09
S ₃₀₇ B ₃₈₅ T ₈₁	S ₅₀ B ₃₂ T ₁₈ ⁶⁴	307	385	81	0.10	0.42	1.78	1.53	1.04
S ₅₄₀ B ₁₇₃ T ₈₈	S ₇₂ B ₁₂ T ₁₆ ⁷⁸	540	173	88	0.11	0.15	1.33	2.83	1.03
S ₅₁₀ B ₅₃₉ T ₁₅₄	S ₅₁ B ₂₈ T ₂₁ ¹⁰⁴	510	539	154	0.13	0.37	2.41	2.33	1.07
S ₅₄₀ B ₁₇₃ T ₁₃₇	S ₆₆ B ₁₁ T ₂₃ ⁸⁵	540	173	137	0.16	0.15	2.07	4.41	1.03
S ₅₁₀ B ₅₃₉ T ₃₅₁	S ₄₀ B ₂₂ T ₃₈ ¹³²	510	539	351	0.25	0.37	5.50	5.30	1.06
S ₅₁₀ B ₅₃₉ T ₄₀₇	S ₃₈ B ₂₁ T ₄₁ ¹⁴⁰	510	539	407	0.28	0.37	6.38	6.15	1.10
S ₅₁₀ B ₅₃₉ T ₄₆₃	S ₃₆ B ₂₀ T ₄₄ ¹⁴⁸	510	539	463	0.31	0.37	7.25	6.99	1.12
S ₆₃₁ B ₇₃ T ₃₇₇	S ₄₉ B ₁₁ T ₄₀ ¹³⁴	631	73	377	0.29	0.20	5.12	8.96	1.10
S ₃₀₀ B ₇₅₆ T ₁₅₉	S ₃₃ B ₄₃ T ₂₄ ⁹⁴	300	756	159	0.13	0.58	3.54	1.92	1.10
S ₁₁₀₅ B ₂₃₇ T ₆₅₄	S ₅₂ B ₆ T ₄₂ ²²¹	1105	237	654	0.33	0.06	6.12	17.08	1.10

^a Subscripts denote the degree of polymerization, N of the respective blocks. ^bSubscripts denote the weight fraction of each block, whereas the superscript is the molecular weight in kg/mol. ^c degree of polymerization, calculated from a combination of SEC and ¹H-NMR. ^d Molar fraction of the corona PT units. ^e Volume fraction of block PB as core segment ($\phi_{PS} + \phi_{PB} = 1$).

Supplementary Table 5.2: Polymer-solvent interaction parameters χ . [supplementary ref 1]. The χ -parameter for SBT are $\chi_{PS/PB} = 0.061$, $\chi_{PS/PT} = 0.025$ and $\chi_{PB/PT} = 0.007$ [supplementary ref 2].

solvent	$\chi_{PS} (T)$	$\chi_{PB} (T)$
acetone	0.81 (25°C)	1.64 (40°C)
isopropanol	2.60 (40°C)	2.93 (40°C)
ethanol	1.80 (162°C)	3.41 (40°C)
n-hexane	0.97 (40°C)	0.37 (40°C)
cyclohexane	0.51 (24°C)	0.22 (40°C)

Supplementary Table 5.3: Volume swelling of the PS phase. Based on results of DLS measurements a volume swelling factor, q , can be calculated (see Supplementary Fig. 4 and Supplementary Note 1).

Acetone [vol %]	Micelle radius, R_h [nm] ^a	Size increase, s	Volume swelling factor, q
0	72.1	1.00	1.0
10	73.8	1.10	1.3
20	75.7	1.21	1.8
30	77.5	1.31	2.2
40	79.3	1.41	2.8
50	81.2	1.52	3.5
60	83.0	1.63	4.3
70	84.9	1.74	5.3
80	86.6	1.83	6.1
85	87.5	1.89	6.8
90	88.6	1.95	7.4

^a Values adapted by interpolation of the the linear fit in Supplementary Fig. 3a.

Supplementary Table 5.4: Experimental Details for the Formation of Tailored Nanostructures. The green rows mark polymers shown in the experimental table in Fig. 5.6.

Polymer	Ace/IPA	$N_T/N_S^{2/3}$ ^c	Geometry	$N_T/N_B^{2/3}$	Patch Morphology
S ₅₁₀ B ₅₃₉ T ₃₅₁	60/40	1.28	sphere	5.30	spherical
S ₆₃₁ B ₇₃ T ₃₇₇	60/40	1.19	sphere	8.96	spherical
S ₅₁₀ B ₅₃₉ T ₄₀₇	60/40	1.48	sphere	6.15	spherical
S ₅₁₀ B ₅₃₉ T ₄₆₃	60/40	1.69	sphere	6.99	spherical
S ₁₁₀₅ B ₂₃₇ T ₆₅₄	60/40	1.42	sphere	17.08	spherical
S ₅₁₀ B ₅₃₉ T ₃₅₁	70/30	1.04	sphere	5.30	spherical
S ₆₃₁ B ₇₃ T ₃₇₇	70/30	0.97	sphere	8.96	spherical
S ₅₁₀ B ₅₃₉ T ₄₀₇	70/30	1.20	sphere	6.15	spherical
S ₅₁₀ B ₅₃₉ T ₄₆₃	70/30	1.37	sphere	6.99	spherical
S ₁₁₀₅ B ₂₃₇ T ₆₅₄	70/30	1.15	sphere	17.08	spherical
S ₅₁₀ B ₅₃₉ T ₃₅₁	80/20	0.90	sphere	5.30	spherical
S ₆₃₁ B ₇₃ T ₃₇₇	80/20	0.84	sphere	8.96	spherical
S ₅₁₀ B ₅₃₉ T ₄₀₇	80/20	1.05	sphere	6.15	spherical
S ₅₁₀ B ₅₃₉ T ₄₆₃	80/20	1.19	sphere	6.99	spherical
S ₁₁₀₅ B ₂₃₇ T ₆₅₄	80/20	1.00	sphere	17.08	spherical
S ₅₄₀ B ₁₇₃ T ₁₃₇	60/40	0.48	cylinder	4.41	spherical
S ₅₄₀ B ₁₇₃ T ₁₃₇	70/30	0.39	cylinder	4.41	spherical
S ₅₄₀ B ₁₇₃ T ₁₃₇	85/15	0.15	sheet	4.41	spherical
S ₅₄₀ B ₁₇₃ T ₈₈	60/40	0.31	vesicle	2.83	spherical
S ₃₀₇ B ₃₈₅ T ₈₁	60/40	0.41	cylinder	1.53	helical
S ₅₁₀ B ₅₃₉ T ₁₅₄	75/25	0.28	cylinder/sheet	2.33	spherical/cylindrical
S ₃₀₇ B ₃₈₅ T ₈₁	70/30	0.34	cylinder/sheet	1.53	helical/bicontinuous
S ₅₁₀ B ₅₃₉ T ₁₅₄	85/15	0.18	vesicle	2.33	cylindrical
S ₃₀₇ B ₅₃₀ T ₇₅	60/40	0.38	cylinder/sheet	1.15	helical/bicontinuous
S ₃₀₇ B ₅₃₀ T ₇₅	70/30	0.31	cylinder/sheet	1.15	helical/bicontinuous
S ₃₀₇ B ₅₃₀ T ₆₃	60/40	0.32	vesicle	0.96	bicontinuous
S ₃₀₇ B ₅₃₀ T ₆₃	70/30	0.26	vesicle	0.96	bicontinuous
S ₃₀₇ B ₃₈₅ T ₅₆	60/40	0.29	vesicle	1.06	bicontinuous
S ₃₀₇ B ₃₈₅ T ₅₆	70/30	0.23	vesicle	1.06	bicontinuous
S ₃₀₀ B ₇₅₆ T ₁₀₄	20/80 ^a	NA	sphere	1.25	continuous
S ₃₀₀ B ₇₅₆ T ₁₀₄	50/50 ^a	NA	cylinder	1.25	continuous
S ₃₀₀ B ₇₅₆ T ₅₆	50/50 ^a	NA	sheet	0.67	continuous
S ₃₀₀ B ₇₅₆ T ₅₆	35/65 ^b	NA	vesicle	0.67	continuous

^a *n*-hexane/isopropanol^b cyclohexane/isopropanol^c corrected values according to volume swelling factor, *q*.

Supplementary Note 1: Determination of solvent swelling factor, q , of polystyrene

To determine a swelling factor, q , of the PS block in acetone/isopropanol mixtures, dynamic light scattering (DLS) measurements of polystyrene-*block*-poly(*tert*-butyl methacrylate) ($S_{366}T_{456}$) diblock copolymer micelles were performed in different acetone/isopropanol ratios. For this purpose, the refractive index and the dynamic viscosity of the solvent mixtures were determined using a refractometer and an Ubbelohde viscosimeter (Supplementary Fig. 5.2) and used to evaluate the DLS data.

The hydrodynamic radius linearly increases with increasing acetone content and from the linear fit the swelling factor could be calculated for each solvent composition (Supplementary Fig. 5.3a). To exclude a volume change of the corona forming PT block, a PT homopolymer star (3 arm star prepared with ATRP, $M_{n,arm} = 50$ kg/mol) was investigated giving no change in the hydrodynamic radius (Supplementary Fig. 5.3b).

From TEM measurements of the diblock copolymer in isopropanol (assuming a non-swollen state of the PS block), a radius of the PS core is determined to be $R_{core,ipa} = 14.8 \pm 1.0$ nm. Subtracting this value from the micellar hydrodynamic radius, R_h , in isopropanol a thickness of the PT corona of $d_{corona} = 54.7$ nm was estimated. The size increase, s , and the volume swelling factor, q , of the PS core are calculated according to supplementary equations (5.1) and (5.2) with R_x being the hydrodynamic radius at certain acetone content. All calculations are based on a constant aggregation number of the micelles, N_{agg} .

$$S_x = \frac{R_x - d_{corona}}{R_{(x=0)} - d_{corona}} \quad (5.1)$$

$$q_x = s_x^3 \quad (5.2)$$

Supplementary Note 2: Generalized theoretical description of polymorphism of patchy micelles and morphology of patches

The following theoretical arguments aim at rationalizing the polymorphism of patchy micelles of ABC triblock terpolymers. Our theory is general and based on the scaling approach proposed in refs. [19, 28]. Let N_A , N_B , N_C be the degrees of polymerization of the respective blocks; v_A , v_B are the volumes of the monomer units of the insoluble A- and B-block. The second virial coefficient (excluded volume) of the C-monomer unit, $v_C \sim \ell^3$ is positive under good solvent conditions and ℓ is the monomer unit (or the Kuhn segment) length, which is assumed to be the same for all the blocks.

Polymorphism of patchy micelles. The morphological transitions from patchy spherical to patchy cylindrical micelles and further to patchy bilayers (lamellar) are governed by a delicate balance between the gain in the conformational entropy of the core-forming A-blocks and the penalty in curvature-dependent part of repulsive interactions in the solvated coronal C-domains. These transitions occur when the thickness of the corona, H , gets smaller than the radius R_A of the central A-core, $H_{corona} \leq R_A$, that is, the micelles have the crew-cut shape (Supplementary Fig. 5.7).

The free energy

$$F = F_{corona} + F_{core} + F_{interface} \quad (5.3)$$

(in $k_B T$ units) of patchy crew-cut micelle with arbitrary morphology i ($i = 3, 2, 1$ corresponds to spherical, cylindrical or lamellar structure of the A-core, respectively) comprises the following contributions:

$$F_{\text{corona}} \simeq F_{\text{corona}}^{(1)} + \delta F_{\text{corona}}^{(i)} \quad (5.4)$$

accounts for repulsions between coronal blocks where

$$F_{\text{corona}}^{(1)} \simeq m^{1/2} \ln(D / R_B) + \tilde{N}_C (S_A / \ell^2)^{-5/6} (v_C / \ell^3)^{1/3} \quad (5.5)$$

is the free energy per chain in the aggregate with large, $R_A \gg H_{\text{corona}} \gg R_B$, curvature radius of the central A-core, R_B and D are the radius of the B-patch and semi-distance between centers of the neighboring patches, respectively; $\tilde{N}_C = N_C - \Delta N_C$, where the correction term ΔN_C is specified below (Supplementary Fig. 5.7), and

$$\delta F_{\text{corona}}^{(i)} \simeq -(i-1) F_{\text{corona}}^{(1)} H_{\text{corona}}^{(1)} / R_A, i = 1, 2, 3 \quad (5.6)$$

is the morphology-dependent increment to the corona free energy. The term F_{core} accounts for the conformational entropy losses in the core-forming insoluble A-blocks

$$F_{\text{core}}^{(i)} = b_i R_A^2 / N_A l^2 \quad (5.7)$$

where the numerical coefficients are $b_1 = \pi^2 / 8$; $b_2 = \pi^2 / 16$; $b_3 = 3\pi^2 / 80$ [Supplementary Ref. 3].

$$F_{\text{interface}} = \gamma_{BS} S_{BS} + \gamma_{AS} S_{AS} + \gamma_{AB} S_{AB} \quad (5.8)$$

accounts for the excess free energy of the interfaces between A and B blocks and solvent as well as that of the interfaces between A and B domains. Here $\{S_{BS}, S_{CS}, S_{BC}\}$ are the interfacial areas and $\{\gamma_{BS}, \gamma_{CS}, \gamma_{BC}\}$ are the respective surface tensions in $k_B T$ units. For patchy micelles the interfacial free energy (Supplementary Eq. 5.8) can be represented as

$$F_{\text{interface}} \simeq \tilde{\gamma}_{BS} m^{-1/3} (v_B N_B / \ell^3)^{2/3} + \gamma_{CS} S_C \quad (5.9)$$

where following ref [19] we have introduced notation $\tilde{\gamma}_{BS} \simeq \gamma_{BS} (1 - \cos\theta)^{2/3} (1 + (\cos\theta / 2))^{1/3}$ and $\cos\theta = (\gamma_{AS} - \gamma_{AB}) / \gamma_{BS}$. By minimizing the free energy with respect to m and S_A we find equilibrium values of the number of chains per patch and the area of the A-core per chain. By acquainting the free energies (per chain) in the structures with different morphologies of the A-core, $F^{(i)} \simeq F^{(i+1)}$, $i = 1, 2$, we find the binodal (transition) lines between spherical and cylindrical ($i=2$) patchy micelles or between cylindrical patchy micelles and patchy lamellae ($i=1$).

$$\tilde{N}_C^{(sph. \leftrightarrow cyl., cyl. \leftrightarrow lam.)} \simeq \frac{N_A^{2/3} v_A}{\ell^3} \gamma_{AS}^{1/3} (v_C / \ell^3)^{-1/3} \quad (5.10)$$

and $\tilde{N}_C^{(sph.\leftrightarrow cyl.)} / \tilde{N}_C^{(cyl.\leftrightarrow lam.)} \approx 1.28$, that is a decrease in the length of the soluble C-blocks (or the solvent quality) leads to successive transitions from patchy spherical to patchy cylindrical micelles and further to patchy A-sheets. The parameters of the B-block enter the correction term, $\Delta N_C \approx (\tilde{\gamma}_{BS}^{3/5} / \gamma_{AS}^{3/11})(N_B v_B / \ell^3)^{2/5} N_C^{3/11} (v_C / \ell^3)^{1/11}$ equal to the number of monomer units in a segment of the C-block protruding from the B-domain up to the inter-patch distance $D \approx (S_A m)^{1/2}$.

Morphology of patches. The patchy micelles are thermodynamically stable and the above equations apply as long as $R_B \leq D \leq H_{corona}$. This is the case, if

$$N_C \geq (N_B v_B / \ell^3)^{11/15} (v_C / \ell^3)^{-1/3} \quad (5.11)$$

For shorter soluble C-blocks or/and longer insoluble B-blocks the size of patches R_B becomes comparable to or smaller than the extension of the corona H_{corona} . In this regime (Supplementary Fig. 5.8) one could expect transformation of quasi-semi-spherical B-domains to semi-cylindrical ones and further to core-shell structure. This transition is driven by the gain in the conformational entropy of the B-blocks, which is balanced by an increase in the overlap and repulsions between the C-blocks protruding from the surface of the B-domains.

The coronal contribution to the free energy can be presented as

$$F_{corona}^{(j)} \approx F_{corona}^{(1)} [1 - (j-1)H_{corona}^{(1)} / R_B], j = 1, 2, 3 \quad (5.12)$$

where

$$F_{corona}^{(1)} \approx N_C (S_{BS} / \ell^2)^{-5/6} (v_C / \ell^3)^{1/3} \quad (5.13)$$

and $j=3, 2, 1$ correspond to semi-spherical patches, cylindrical stripes or continuous layer formed by B-blocks at the A/S interface. Supplementary Eq. (5.8) for the interfacial free energy assumes the form $F_{interface} = S_{BS} \tilde{\gamma}_{BS}$ where $\tilde{\gamma}_{BS} = (\gamma_{BS} + \beta_j \gamma_{AB})$ with the B-domain geometry-dependent coefficient β_j and we have neglected contribution of the A/S interface assuming distance between neighboring B-domains $D - R_B \approx H^{(1)} \ll R_B$. The exact numerical factors, which quantify the difference in the conformational entropy of the B-blocks confined in spherical or cylindrical segments adjacent to the surface of the A-core (similar to Supplementary Eq. 5.7) are not available. However, one could expect that the transitions from B-patches to B-stripes and from B-stripes to layered structures occur at

$$N_C^{(tr)} \approx \frac{N_B^{2/3} v_B}{\ell^3} \tilde{\gamma}_{BS}^{1/3} (v_C / \ell^3)^{-1/3} \quad (5.14)$$

The latter equation does not include any dependence on the length of the A-block, since it pre-assumes that the curvature radius of the A-core exceeds by far that of the B-domains decorating its surface. This is the case if $N_A v_A \gg N_B v_B$. However, at $N_A v_A \approx N_B v_B$ this condition is violated and more refined analysis is required to unravel interference between morphological transitions in the A- and B-core domains.

Supplementary References

1. Mark JE. Physical properties of polymers handbook. Woodbury: American Institute of Physics Press; 2007.
2. T. I. Löblich *et al.*, Bulk morphologies of polystyrene-*block*-polybutadiene-*block*-poly(tert-butyl methacrylate) triblock terpolymers, *Polymer* **2015**, 72, 479-489.
3. Semenov, A.N., Contribution to the theory of microphase layering in block copolymer melts. *Sov. Phys. JETP* **1985**, 61, 733-742.

Chapter 6

Control of Multicompartment Nanostructures of Linear Triblock Terpolymers by Post-Polymerization Processes

Tina I. Löbling^{*,a,b}, Olli Ikkala^b, André H. Gröschel^{*,b,c} and Axel H. E. Müller^{*,d}

^a Macromolecular Chemistry II, University of Bayreuth, D-95440 Bayreuth, Germany.

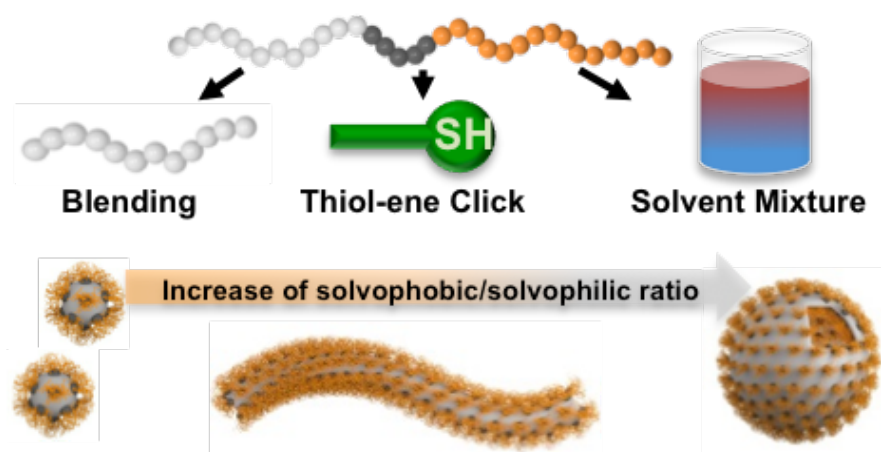
^b Department of Applied Physics, Aalto University School of Science, FIN-02150 Espoo, Finland.

^c Physical Chemistry and Centre for Nanointegration Duisburg-Essen (CENIDE), University of Duisburg-Essen, D-45127 Essen, Germany.

E-mail: andre.groeschel@uni-due.de

^d Institute of Organic Chemistry, Johannes Gutenberg-University Mainz, D-55099 Mainz, Germany.

E-Mail: axel.mueller@uni-mainz.de



submitted to: *ACS Macro Letters*

Abstract

The solution self-assembly of amphiphilic diblock copolymers into spheres, cylinders and vesicles (polymersomes) has been intensely studied over the past two decades and their morphological spectrum is well understood. Linear ABC triblock terpolymers with two insoluble blocks A/B, on the other hand, display a more complex morphological spectrum that has been recently explored by synthetic block length variations. Here we describe facile post-polymerization routes to tailor ABC triblock terpolymer solution morphologies by altering block solubility (solvent mixtures), blending homopolymers, and performing block-selective chemical reactions. The feasibility of such processes is demonstrated on polystyrene-*block*-polybutadiene-*block*-poly(methyl methacrylate) (SBM) that assembles to patchy spherical micelles, but can be modified to evolve into double and triple helices, or patchy and striped vesicles. These results demonstrate that post-polymerization reactions give access to a broad range of morphologies from single triblock terpolymers without the need for multiple polymer syntheses.

Introduction

Amphiphilic diblock copolymers feature two covalently linked blocks with different chemical structure that in selective solvents and in dependence of the length ratio of the solvophobic and solvophilic block form spherical micelles, cylinders or vesicles.¹ Two decades ago, Eisenberg *et al.* were among the first to study morphological transitions from micelles to vesicles for polystyrene-*block*-poly(acrylic acid) (PS-*b*-PAA).² Ever since, research efforts have been undertaken to control and manipulate block copolymer assemblies to achieve particular solution nanostructures.³ Solvophobic blocks with a low glass transition temperature, T_g , have a high chain mobility and thermodynamic equilibrium structures can be reached by direct re-hydration of bulk films.^{1,4} By contrast, solvophobic blocks with a high T_g require plasticizing solvent/non-solvent mixtures to enhance chain mobility within the micellar core to prevent kinetic trapping of ill-defined intermediates.⁵ In general, solvent mixtures are a great tool to tune the final morphology, because proper co-solvents influence the volumes of both the corona and the core-forming blocks, as well as the interfacial tension.⁶⁻⁸ Solution blending of homo- and block copolymers is another straightforward concept to control the morphology by expanding the volume of the micellar core.⁹⁻¹² To increase the structural complexity towards multicompartment micelles, several synthetic strategies have shown great versatility.^{13,14} For instance, ABC miktoarm star terpolymers consist of three incompatible blocks connected in one junction point leading to packing frustration of the core-forming blocks when brought into selective solvents. This frustration results in the formation of a myriad of multicompartment morphologies ranging from spherical and linear multicompartment micelles to nanostructured bilayers or “woodlouse” micelles. These morphologies can likewise be modified after assembly by blending with compatible diblock copolymers, variation of pH or counterions.¹⁵⁻¹⁹ In contrast, ABC triblock terpolymers with linear sequence and two solvophobic blocks mainly form spherical multicompartment micelles²⁰⁻²³, core-segmented cylinders²⁴⁻²⁷, and in rare cases core-shell toroids²⁸ or single- and double-stranded core-shell helices^{29,30}. All these structures have in common that the sequence of polymer phases follows the linear arrangement of the blocks, i.e., A-core, B-patch (or shell) and C-corona (different in miktoarm star terpolymers).

We recently showed that by synthesizing linear triblock terpolymers with properly designed length ratios of the blocks, a wide range of compartmentalized morphologies are obtained, i.e., cylinders, two-dimensional sheets and vesicles, all equipped with distinct patch morphologies.³¹ There, the two insoluble blocks A/B were nanoconfined to the core and stabilized by the corona-forming block, C. Through synthetic block length variation we screened all patch morphologies, which follow rules for the self-assembly of AB diblock copolymers in bulk. Still, a more facile way to induce morphological transformations without the need for multiple polymer syntheses is desirable to facilitate targeting certain particle shapes and/or patch morphologies.

Here, in order to allow a facile route for libraries of solution nanostructures, we describe concepts to tune self-assemblies of solvent-dispersed ABC triblock terpolymers in a wide range by controlling the post-polymerization conditions, while keeping the composition of the block copolymer fixed. We alter the solvophobic/solvophilic balance of polystyrene-*block*-polybutadiene-*block*-poly(methyl methacrylate) (PS-PB-PMMA, SBM) triblock terpolymers in order to modify the multicompartment morphology of patchy spheres, cylinders, sheets and vesicles. We therefore discuss the effects of solvent conditions, blending with homopolymer and chemical modification on the resulting nanostructure. Similar to diblock copolymers, controlling the solvophobic/solvophilic ratio guides the formation of certain micellar nanostructures, as schematically shown for SBM in Figure 6.1a. To illustrate the impact of corona length on morphology, we synthesized three SBM triblock terpolymers, $S_{306}B_{151}M_{340}$, $S_{510}B_{258}M_{260}$ and $S_{516}B_{140}M_{76}$ (subscripts denote degree of polymerization) with decreasing molar fractions of the PMMA corona, $x_{PMMA} = 0.43, 0.25$ and 0.10 (for detailed polymer characterization see Table S6.1). The self-assembly pathway includes a two-step procedure (see Experimental Section).²² First, SBM is dispersed in a non-solvent for PB, here *N,N*-dimethylacetamide (DMAc), to form micelles with a PB core and a mixed PS/PMMA corona. The final compartmentalized nanostructures are then obtained through solvent exchange with adequate acetone/isopropanol mixtures. Upon dialysis, the PS block starts to collapse and phase-separates from the PMMA coronal chains resulting in transient Janus micelles. These Janus particles are the colloidal subunits that aggregate *via* the PS patch into the final superstructures during the dialysis process due to insufficient stabilization by the PMMA corona.^{22,26} Decreasing the block length of the solvophilic PMMA corona from $x_{PMMA} = 0.43$ to $x_{PMMA} = 0.25$ and further to $x_{PMMA} = 0.10$ is accompanied by a morphological transition from patchy spherical (or multicompartment) micelles to patchy cylinders and finally, to patchy vesicles (Figure 6.1b-d). The PB fraction was kept small for all SBM terpolymers so that spherical PB patches would form on top of the PS core. The PMMA coronal chains emerge from the PB patches and direct the self-assembly into the observed geometry through chain-chain repulsion as well as the occupied chain volume. While a large corona of $x_{PMMA} = 0.43$ allows stabilization of spherical, high-curvature micelles, a decrease in corona size to $x_{PMMA} = 0.25$ (through shortening the block) drives the formation of less curved cylindrical micelles. This topology has a smaller core/corona interface and the corona provides sufficient protection of the solvophobic core. Further reduction of $x_M = 0.10$ leads to formation of vesicles, where the spherical PB patches aim at adopting a hexagonal pattern to homogeneously shield the solvophobic core from the solvent.

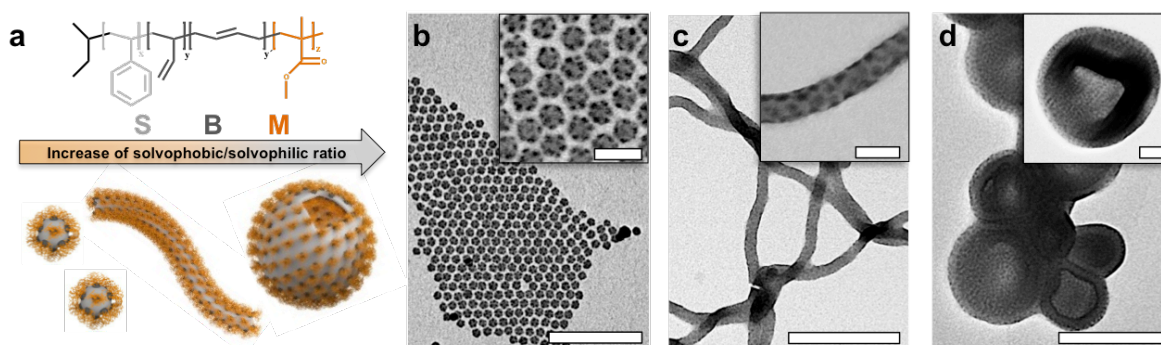


Figure 6.1: Polymorphism of patchy micelles. (a) SBM triblock terpolymer and schematics of particle shape changing from patchy spheres to cylinders to vesicles with increasing solvophobic/solvophilic ratio. (b-d) Compartmentalized nanostructures of SBM in acetone/isopropanol 60:40 (v/v). (b) Patchy spherical micelles of $S_{306}B_{151}M_{340}$, (c) patchy cylinders of $S_{510}B_{258}M_{260}$ and (d) patchy vesicles of $S_{516}B_{140}M_{76}$. All samples are stained with OsO_4 (PS: light grey; PB: dark-grey; PMMA: not visible due to e-beam degradation). Scale bars are 500 nm in overview images and 100 nm in insets.

The composition of the acetone/isopropanol mixture has a crucial impact on the morphology and can be utilized to fine-tune the nanostructure without the need of multiple polymer syntheses. Acetone is a good solvent for the PMMA corona, a near q -solvent for PS and a non-solvent for PB, whereas isopropanol is a near q -solvent for PMMA and a non-solvent for both PS and PB.²² Previously, we have shown that the PS volume increases with increasing acetone content due to swelling.³¹ DLS experiments with a PMMA homopolymer of high molecular weight show that also the PMMA volume is affected and increases with acetone content (Figure S6.1). Compared to PS and PMMA, the PB phase is assumed to be unaffected by the solvent composition ($\chi_{PB,acetone}$ and $\chi_{PB,isopropanol} \gg 0.5$).³² Figures 6.2a-d show morphological transitions of $S_{510}B_{258}M_{260}$ induced by decreasing the solvent quality (i.e. by increasing the isopropanol (IPA) content). Starting with acetone/IPA 80:20, $S_{510}B_{258}M_{260}$ forms patchy spherical micelles (Figure 6.2a), while patchy cylindrical micelles are stable at acetone/IPA 70:30 (Figure 6.2b). Although the contraction of the PS phase with increasing IPA content should promote the formation of spherical micelles, we assume that volume changes (contraction) of the largely expanded dissolved PMMA are much more pronounced. The contracted PMMA chains can only stabilize a lower total surface area favoring the evolution from spherical micelles to cylinders. The formation of spherical micelles at low IPA contents might be also explained in terms of the interfacial tension, γ , that scales with the polymer-solvent interaction parameter χ ($\gamma \sim \chi^{1/2}$) and decreases with decreasing IPA content (Figure S6.2). The PS-solvent interaction parameter, $\chi_{S,solvent}$, decreases from 1.17 in acetone/IPA 80:20 to 1.35 in acetone/IPA 70:30, which corresponds to a decrease in interfacial tension. This in turn promotes the formation of spherical micelles with higher total interfacial area as compared to cylindrical micelles. At acetone/IPA 60:40 the cylinder morphology is preserved, however, the spherical PB patches adapt a hexagonal dense packing motif until spherical patches overlap and morphological transition into a double helix occurs (Figure 6.2c). With increasing IPA content the PS core contracts accompanied by reduced surface area of

the cylindrical micelles. As a consequence the PB patches have to adapt to the decreased surface area, they come in close proximity and finally fuse into a double helix. This has been observed before for the transformation of cylindrical micelles to bilayer sheets in polystyrene-*block*-polybutadiene-*block*-poly(*tert*-butyl methacrylate) where the overall surface area and the surface curvature changes.³¹ Interestingly, at acetone/IPA 40:60 cylinders with PB triple helices emerge (Figure 2d). The formation of a triple helical patch morphology is rather unusual, but has been found for SBM in the bulk state.³³ Theoretical calculations for frustrated triblock terpolymer systems in bulk further confirm the stability of double and triple helices on cylinders.³⁴ The free energy of double and triple helices and the packing frustration is reduced as compared to e.g. the formation of straight cylinders, a mono helix or a ring-like arrangement. Although a morphological transformation to sheets or vesicles was expected at acetone/IPA 40:60, the cylindrical micelles instead start to bundle into larger agglomerates and sediment. The observed diameter of the cylinders increases from 45 ± 3 nm in acetone/IPA 60:40 to 55 ± 3 nm in acetone/IPA 40:60. We assign this to a slight flattening of the cylinders given the tendency to transform into bilayer sheets at this solvent composition (contraction of PMMA corona chains to the point of collapse; Figure S1). An onset of sheet formation is evident in this sample as shown in Figure S3. However, the rearrangement to sheets may be kinetically hindered at high IPA contents, because of the reduced plasticizing effect of acetone for the glassy PS core. The dense protective corona of the triple helix may also interfere with cylinder-cylinder fusion into sheets.

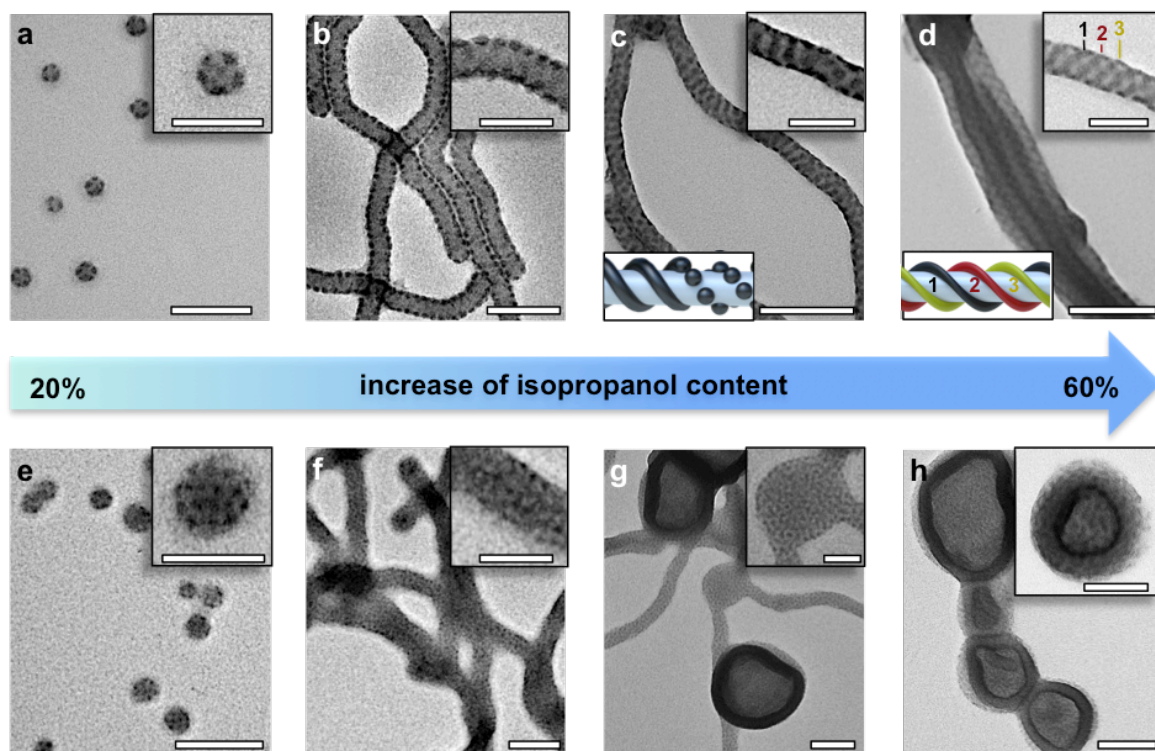


Figure 6.2: Solvent-induced morphological change of (a-d) $S_{510}B_{258}M_{260}$ and (e-h) $S_{516}B_{140}M_{118}$ in acetone/IPA mixtures. (a) Patchy spherical micelles at IPA = 20%, (b) patchy cylinders at IPA = 30% and (c) cylinders with a mixture of PB patches and PB double helices at IPA = 40%. (d) At IPA = 60% bundles of PS cylinders with PB triple-helices form. The schematics in (c, d)

show the PS cylinder in light grey and the PB helices in black, red and yellow. The PMMA corona is omitted for clarity. (e) Large patchy spherical micelles of $S_{73}B_{11}M_{16}^{74}$ at IPA = 20%, (f) patchy cylinders at IPA = 30% and (g) a mixture of patchy cylinders, patchy sheets/vesicles at IPA = 50%. (h) At IPA = 60% $S_{73}B_{11}M_{16}^{74}$ exclusively forms patchy vesicles. All samples are stained with OsO_4 . Scale bars are 200 nm in overview images and 100 nm in insets.

In order to screen the whole morphological spectrum from spherical patchy micelles to patchy vesicles, we chose $S_{516}B_{140}M_{118}$, where both the PMMA and the PB block lengths are shorter as compared to the previously discussed $S_{510}B_{258}M_{260}$. Morphological changes may be facilitated through the shorter PMMA corona while the again short PB block should lead to spherical PB patches in all micellar geometries that will not interfere with structural transformations. Starting with acetone/IPA 80:20, large patchy spherical micelles are observed (Figure 6.2e). The micelles are less homogeneous in shape and size as e.g. for $S_{510}B_{258}M_{260}$ (Figure 6.1a), because the large plasticized PS core (73 wt.-%) might noticeable flatten upon drying on the TEM grid. At acetone/IPA 70:30, the corona chains start to contract and the decrease in corona volume as well as an increased interfacial tension promote a morphological shift towards cylindrical micelles with PB patches. Further increase to acetone/IPA 60:40 first leads to a mixture of patchy cylinders, sheets and vesicles, until exclusively patchy vesicles are observed at acetone/IPA 40:60. These observations demonstrate that specific morphologies can be targeted by careful adjustment of solvent conditions that control swelling and contraction of participating blocks as well as interfacial tension.

Blending block copolymers morphologies with homo- and diblock copolymers is another tool to alter existing or create new bulk and solution morphologies.^{10,33,35–37} Here SBM is blended with a PS homopolymer to increase the volume of the core-forming PS phase (for details see Experimental Section). The PS homopolymer was added in proper ratios to SBM precursor micelles with PB core in the DMAc solution. During solvent exchange, both the PS homopolymer and the PS block of SBM collapse at similar IPA concentrations, which enriches the newly formed PS core with homopolymer chains. We investigated the morphological evolution of $S_{510}B_{258}M_{260}$ by blending PS_{192} homopolymer that exhibits lower molecular weight than the PS block of SBM. Shorter chains ensure chain mixing conditions in the “wet brush” regime and allow the homopolymer to uniformly swell the PS phase (see Figure S6.4).^{38,39} The total weight fraction of the PS block, f_{PS} , in SBM increases as a function of mixing ratio. An overview of the contribution of PS_{192} to the total f_{PS} and the resulting apparent changes in PS and PB weight fractions and molar fraction of the PMMA corona are summarized in Table S6.2.

$S_{510}B_{258}M_{260}$ ($f_{PS} = 0.57$, $x_{PMMA} = 0.25$) exclusively forms cylinders in acetone/isopropanol 50:50 (v/v), where both spherical PB patches and double helices are present (Figure 6.3a). Blending the PS core with PS_{192} to reach $f_{PS} = 0.61$ and $x_{PMMA} = 0.23$, predominantly results in patchy cylinders with onset of sheet formation (Figure 6.3b). Upon volume increase of the core, de-wetting of PB helices into PB patches occurs on both the sheet and cylinders. This order-order transition counteracts a loss in conformational entropy of the PB chains in case of stretching of the double helix to adapt

to the larger surface area of the cylinders driving the formation to spherical PB patches.³³ At $f_{PS} = 0.65$ and $x_{PMMA} = 0.21$ the number and size of sheets grow and onset of vesicle formation is observed (Figure 6.3c). At $f_{PS} = 0.70$ and $x_{PMMA} = 0.14$ (Figure 6.3d), we exclusively identify patchy vesicles with pronounced hexagonal arrangement of PB patches. Since the self-assembly process progresses *via* transient Janus particles, the effect of PS blending on the solvophobic/solvophilic balance of these amphiphilic colloidal building blocks can be explained considering apparent packing parameters for Janus building blocks (Figure 6.3e). Without added PS homopolymer, the large PMMA corona (as compared to PS) results in patchy cylindrical micelles. Israelachvillis theory for packing of low molecular weight surfactants showed that cylindrical micelles occur for a packing parameter of $1/3 < p < 1$.⁴⁰ When comparing the amphiphilic colloidal Janus building blocks to surfactants, these building blocks might inherit similar packing parameter to give cylindrical micelles. Addition of PS homopolymer now expands the apparent volume of the PS phase thereby shifting the solvophobic/solvophilic balance towards the solvophobic site, which corresponds to an increase of the packing parameter e.g. towards $p = 1$. The blending of PS₁₉₂ thus induces a gradual change from cylindrical to bilayer structures (i.e. sheets and vesicles).

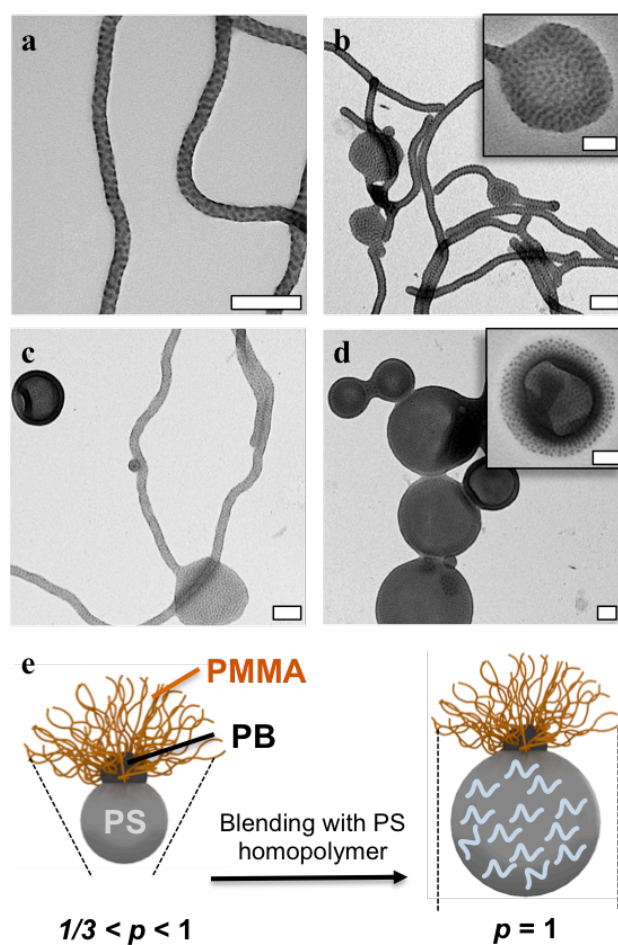


Figure 6.3: Morphological evolution through blending of PS homopolymer. (a-d) Successive increase of the PS phase $f_{PS} = 0.57$ of $S_{510}B_{258}M_{260}$ in acetone/isopropanol 50:50 (v/v) through swelling with PS_{192} leads to: (a) Patchy cylinders without PS homopolymer, (b) a mixture of patchy

cylinders and sheet at $f_{PS} = 0.61$, (c) larger sheets and onset of vesicle formation at $f_{PS} = 0.65$, and (d) exclusively patchy vesicles at $f_{PS} = 0.70$. Scale bars are 200 nm in overview images and 100 nm in insets. All samples are stained with OsO₄. (e) Illustration of increase of hydrophobic PS volume through PS homopolymer chains and its effect on packing parameter, p , of amphiphilic colloids.

Finally, we explore the possibility to selectively tune the PB patch morphology by chemical modification. Thiol-ene chemistry is a versatile tool to alter the chemical structure and block volume after polymerization in order to modify the nanostructures.⁴¹ S₅₁₆B₁₄₀M₁₁₈ with predominately 1,2-addition of the PB units is accessible to thiol-ene addition and was modified as schematically shown in Figure 6.4a (see Experimental Section). Exemplified on hexyl mercaptan, the chemical modification of S₅₁₆B₁₄₀M₁₁₈ results in S₅₁₆H₁₄₀M₁₁₈, where the modified PB block is now denominated as PH. The success of the modification was confirmed by a shift of the molecular weight in SEC traces as well as with ¹H-NMR spectroscopy (Figure S6.5 and S6.6). The combined weight fraction of both solvophobic blocks increases from $f_{PS+PB} = 0.84$ to $f_{PS+PH} = 0.87$ after click reaction, while PH maintains a comparably low solubility in acetone/isopropanol. Accordingly, the morphology changes from a mixture of compartmentalized cylinders and vesicles to exclusively vesicles (Figure 6.4b,c). The PS/PB volume ratio decreases from $V_{PS}/V_{PB} = 6.5$ to $V_{PS}/V_{PH} = 2.1$ after modification and induces a morphological change of the PB phase from spherical patches to PH cylinders on the vesicle surface (in- and outside). Thiol-ene chemistry thus is not only a versatile tool to change the geometry of solution nanostructures, but also the patch morphology due to influence on both the solvophobic/solvophilic ratio and the volume ratio of the two solvophobic blocks.

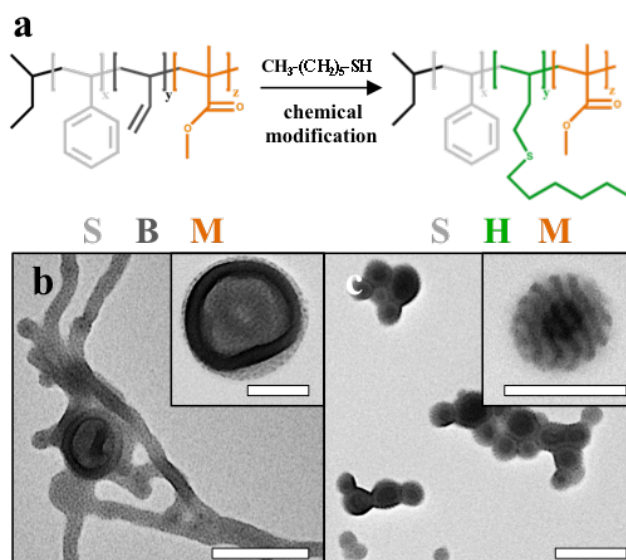


Figure 6.4: Influence of post-polymerization reaction on resulting morphology. (a) Schematic of thiol-ene click reaction of hexyl mercaptan to the 1,2-PB double bonds of S₅₁₆B₁₄₀M₁₁₈ to give S₅₁₆H₁₄₀M₁₁₈. The post-polymerization reaction alters the morphology from a mixture of patchy cylinders and vesicles to (b) exclusively striped vesicles with PB cylinders on the in- and outside of the vesicle membrane (c). The samples are in acetone/isopropanol 60:40 (v/v) and stained with OsO₄. Scale bars are 500 nm in overview images and 200 nm in insets.

In this study we demonstrated that morphological transformations for linear SBM triblock terpolymers could be achieved from patchy spherical micelles to cylinders and vesicles through changing solvent mixtures, homopolymer blending and block selective post-polymerization reaction, while keeping the block lengths fixed. The solvent composition plays a major role in structure formation due to swelling and interfacial tension effects that drive the self-assembly outcome. A good solubility of the corona and the presence of a plasticized core facilitate the formation of stable and reproducible structures and prevent kinetic trapping during self-assembly pathways. Changing the morphology using homopolymer blending or block-selective modification via thiol-ene chemistry represent model processes and provide a toolbox towards applications where tailor-made nanostructures are needed. Addition of homopolymers increases the volume of the solvophobic phase and induces a morphological change from patchy cylinders to vesicles but might likewise be used as selective staining agent to one of the phases e.g. by introducing fluorescent labeled polymers. The chemical modification of the PB block in SBM with hexyl mercaptan induced a shift of the overall geometry from cylindrical micelles to vesicles but also caused PB patches to change from spheres to cylinders due to the volume increase. Thiol-ene chemistry might be helpful to introduce new chemistries that change the polarity or even switch morphologies *in-situ*. We demonstrated that targeting specific nanostructures without synthetic effort and precise tailoring of the triblock terpolymer compositions could be achieved by influencing the solvophobic/solvophilic ratio. The corona length guides the overall geometry of the micelles from spheres to cylinders and vesicles, while a change of the volume ratio of the solvophobic blocks allow altering the patch morphology from spherical to cylindrical patches. The shown post-polymerization processes allow a facile approach towards libraries of complex multicompartment self-assemblies.

Experimental Section

Materials and characterization methods are given in the Supporting Information.

Preparation of micelle solutions. The SBM triblock terpolymer was first dissolved in DMAc at a concentration of 0.1 g/L and annealed over night at 70 °C to ensure formation and equilibration of micelles with PB core and PS/PMMA corona. The solution was then dialyzed against the final acetone/isopropanol mixture for one day to induce the formation of multicompartment nanostructures. For blend-experiments with PS homopolymer, a stock solution of PS was first prepared in DMAc (1 g/L), mixed with the SBM triblock terpolymer in desired ratios and stirred for one day prior to dialysis.

Chemical modification. For the thiol-ene reaction, 200 mg of $S_{516}B_{140}M_{118}$ were first dissolved in 6 mL THF. After complete dissolution, a 15-fold excess (compared to the PB double bonds) of hexyl mercaptan was added. The mixture was degassed for 20 min and then irradiated for 24 h using a UV-lamp with a cut-off filter of $\lambda = 300$ nm. Taking the weight of the clicked moiety into account, the composition of the modified polymer changes to $S_{516}H_{140}M_{118}$ and the volume ratio of $V_{PS}/V_{PB} = 3.5$ to $V_{PS}/V_{PH} = 2.1$. The block

volumes are calculated by multiplying the molar volume of the monomeric unit (PS = 99.0 cm³/mol; PB = 56.2 cm³/mol; PH = 174.5 cm³/mol) with the degree of polymerization of the respective blocks.

Associated Content

Supporting Information

Materials, Methods, DLS experiments, calculation of volume swelling, additional TEM images, SEC traces of chemical modification and calculations to blend-experiments. This material is available free of charge via the Internet at <http://pubs.acs.org>

Author Information

Corresponding Authors

*Email: andre.groeschel@uni-due.de; axel.mueller@uni-mainz.de

Notes

The authors declare no competing financial interest.

Acknowledgments

The authors acknowledge the Deutsche Forschungsgemeinschaft (DFG) for supporting this work within DFG Mu896/40-1. This work was carried out under the Academy of Finland's Centre of Excellence Programme (2014-2019) and supported by ERC-2011-AdG (291364-MIMEFUN).

References

1. Jain, S.; Bates, F. S. *Science* **2003**, *300*, 460–464.
2. Zhang, L.; Eisenberg, A. *Science* **1995**, *268*, 1728–1731.
3. Mai, Y.; Eisenberg, A. *Chem. Soc. Rev.* **2012**, *41*, 5969–5985.
4. Won, Y.; Davis, H. T.; Bates, F. S. *Science* **1999**, *283*, 960–963.
5. Choucair, A.; Eisenberg, A. *Eur. Phys. J. E. Soft Matter* **2003**, *10*, 37–44.
6. Yu, Y.; Eisenberg, A. *JACS* **1997**, *119*, 8383–8384.
7. Yu, Y.; Zhang, L.; Eisenberg, A. *Macromolecules* **1998**, *31*, 1144–1154.
8. Shen, H.; Eisenberg, A. *J. Phys. Chem. B* **1999**, *103*, 9473–9487.
9. Christian, D. A.; Tian, A.; Ellenbroek, W. G.; Levental, I.; Rajagopal, K.; Janmey, P. A.; Liu, A. J.; Baumgart, T.; Discher, D. E. *Nat. Mater.* **2009**, *8*, 843–849.
10. Zhu, J.; Zhang, S.; Zhang, K.; Wang, X.; Mays, J. W.; Wooley, K. L.; Pochan, D. J. *Nat. Commun.* **2013**, *4*, 2297.
11. Zhu, J.; Hayward, R. C. *Macromolecules* **2008**, *41*, 7794–7797.
12. LoPresti, C.; Massignani, M.; Fernyhough, C.; Blanazs, A.; Ryan, A. J.; Madsen, J.; Warren, N. J.; Armes, S. P.; Lewis, A. L.; Chirasatitsin, S.; Engler, A. J.; Battaglia, G. *ACS Nano* **2011**, *5*, 1775–1784.
13. Moughton, A. O.; Hillmyer, M. A.; Lodge, T. P. *Macromolecules* **2012**, *45*, 2–19.
14. Gröschel, A. H.; Müller, A. H. E. *Nanoscale* **2015**, *7*, 11841–11876.
15. Li, Z.; Hillmyer, M. A.; Lodge, T. P. *Langmuir* **2006**, *22*, 9409–9417.
16. Li, Z.; Hillmyer, M. A.; Lodge, T. P. *Macromolecules* **2006**, *39*, 765–771.
17. Hanisch, A.; Gröschel, A. H.; Förtsch, M.; Löbbling, T. I.; Schacher, F. H.; Müller, A. H. E. *Polymer* **2013**, *54*, 4528–4537.
18. Hanisch, A.; Gröschel, A. H.; Förtsch, M.; Drechsler, M.; Jinnai, H.; Ruhland, T. M.; Schacher, F. H.; Müller, A. H. E. *ACS Nano* **2013**, *7*, 4030–4041.
19. Hu, H.; Liu, G. *Macromolecules* **2014**, *47*, 5096–5103.
20. Kubowicz, S.; Baussard, J.-F.; Lutz, J.-F.; Thünemann, A. F.; von Berlepsch, H.; Laschewsky, A. *Angew. Chemie Int. Ed.* **2005**, *44*, 5262–5265.
21. Schacher, F.; Walther, A.; Ruppel, M.; Drechsler, M.; Müller, A. H. E. *Macromolecules* **2009**, *42*, 3540–3548.
22. Gröschel, A. H.; Schacher, F. H.; Schmalz, H.; Borisov, O. V.; Zhulina, E. B.; Walther, A.; Müller, A. H. E. *Nat. Commun.* **2012**, *3*, 710.
23. Gröschel, A. H.; Walther, A.; Löbbling, T. I.; Schmelz, J.; Hanisch, A.; Schmalz, H.; Müller, A. H. E. *J. Am. Chem. Soc.* **2012**, *134*, 13850–13860.
24. Cui, H.; Chen, Z.; Zhong, S.; Wooley, K. L.; Pochan, D. J. *Science* **2007**, *317*, 647–650.
25. Fang, B.; Walther, A.; Wolf, A.; Xu, Y.; Yuan, J.; Müller, A. H. E. *Angew. Chemie Int. Ed.* **2009**, *48*, 2877–2880.

26. Gröschel, A. H.; Walther, A.; Löbbling, T. I.; Schacher, F. H.; Schmalz, H.; Müller, A. H. E. *Nature* **2013**, *503*, 247–251.
27. Dupont, J.; Liu, G. *Soft Matter* **2010**, *6*, 3654–3661.
28. Pochan, D. J.; Chen, Z.; Cui, H.; Hales, K.; Qi, K.; Wooley, K. L. *Science* **2004**, *306*, 94–97.
29. Dupont, J.; Liu, G.; Niihara, K.; Kimoto, R.; Jinnai, H. *Angew. Chemie Int. Ed.* **2009**, *48*, 6144–6147.
30. Zhong, S.; Cui, H.; Chen, Z.; Wooley, K. L.; Pochan, D. J. *Soft Matter* **2008**, *4*, 90–93.
31. Löbbling, T. I.; Borisov, O.; Haataja, J. S.; Ikkala, O.; Gröschel, A. H.; Müller, A. H. E. *Nat. Commun.* **2016**, *accepted*.
32. Mark, J. E. *Physical Properties of Polymers Handbook*, Second Edi.; Springer Science+Business Media: New York, 2007.
33. Higuchi, T.; Sugimori, H.; Jiang, X.; Hong, S.; Matsunaga, K.; Kaneko, T.; Abetz, V.; Takahara, A.; Jinnai, H. *Macromolecules* **2013**, *46*, 6991–6997.
34. Li, W.; Qiu, F. *Macromolecules* **2012**, *45*, 503–509.
35. Abetz, V.; Goldacker, T. *Macromol. Rapid Commun.* **2000**, *21*, 16–34.
36. Goldacker, T.; Abetz, V.; Stadler, R.; Erukhimovich, I.; Leibler, L. *Nature* **1999**, *398*, 137–139.
37. Betthausen, E.; Dulle, M.; Hanske, C.; Müll, M.; Fery, A.; Förster, S.; Schacher, F. H.; Müller, A. H. E. *Macromolecules* **2014**, *47*, 6289–6301.
38. Hashimoto, T.; Tanaka, H.; Hasegawa, H. *Macromolecules* **1990**, *23*, 4378–4386.
39. Koizumi, S.; Hasegawa, H.; Hashimoto, T. *Macromolecules* **1994**, *27*, 6532–6540.
40. Israelachvili, J. N.; Mitchell, D. J.; Ninham, W. *J. Chem. Soc. Faraday Trans. 2* **1976**, *72*, 1525–1568.
41. Le Devedec, F.; Won, A.; Oake, J.; Houdaihed, L.; Bohne, C.; Yip, C. M.; Allen, C. *ACS Macro Lett.* **2016**, *5*, 128–133.

*Supporting Information**to***Control of Multicompartment Nanostructures of Linear Triblock Terpolymers by Post-Polymerization Processes**

by Tina I. Löbbling, Olli Ikkala, André H. Gröschel*, Axel H. E. Müller*

Materials and Methods

Materials. Hexyl mercaptan (Aldrich) and THF (Aldrich) were used without further purification. Dioxane and *N,N*-dimethylacetamide (DMAc) were of analytical grade and purchased from Roth. For dialysis, acetone and isopropanol of technical grade were used. Dialysis tubes of regenerated cellulose with a molecular weight cut-off of 12,000–14,000 g/mol were purchased from Roth, equilibrated in deionized water for 10 min and washed with excess dioxane before use.

Polymer Synthesis. All polymers were synthesized *via* living anionic polymerization in either toluene (PS192, S306B151M340) or THF (S510B258M260, S516B140M76, S516B140M118, PMMA5700) as reported elsewhere in detail.^{1,2} Subscripts denote the weight fractions of the blocks and superscripts the number-average molecular weight in kg/mol. The polymers were characterized by combination of SEC and ¹H-NMR as summarized in Table 1.

Table S6.1: Characteristics of the used polymers including degree of polymerization (DP), weight fractions of the blocks, overall molecular weight and polydispersity index.

Sample ^a	DP (S)	DP (B)	DP (M)	x_M	f_S	f_B	M_n [kg/mol] ^b	PDI ^c
PS ₁₉₂	192	-	-	-	1	-	20	1.02
PMMA ₅₇₀₀	-	-	5700	1	-	-	570	1.12
S ₃₀₆ B ₁₅₁ M ₃₄₀	306	151	340	0.43	0.43	0.11	74	1.06
S ₅₁₀ B ₂₅₈ M ₂₆₀	510	258	260	0.25	0.57	0.15	93	1.04
S ₅₁₆ B ₁₄₀ M ₇₆	516	140	76	0.10	0.78	0.11	69	1.05
S ₅₁₆ B ₁₄₀ M ₁₁₈	516	140	118	0.15	0.73	0.11	73.5	1.05

^a Subscripts denote degree of polymerization. ^b Calculated from a combination of SEC and ¹H-NMR. ^c Determined from SEC with THF as eluent and PS as calibration standard in case of PS₁₉₂ and SBM, while a PMMA calibration was used for PMMA₅₇₀₀.

¹H-NMR Measurements. Spectra were recorded on a Bruker Ultrashield 300 machine with a 300 MHz operating frequency using deuterated chloroform as solvent.

Size Exclusion Chromatography (SEC). SEC measurements were performed on a set of 30 cm SDV-gel columns of 5 mm particle size having a pore size of 10⁵, 10⁴, 10³, and 10² Å with refractive index and UV ($\lambda = 254$ nm) detection. SEC was measured at an elution rate of 1 mL/min with THF as eluent and with PS or PMMA as standards.

Transmission Electron Microscopy (TEM). Bright field transmission electron microscopy with an acceleration voltage of 80 kV was carried out using a Zeiss CEM 902 electron microscope. Samples were prepared by placing one drop of the polymer solution (0.1 g/L) onto carbon-coated copper grids. Excess solvent was instantly absorbed by a filter paper. To enhance the contrast of PB phase, the samples were stained with OsO₄ for 3h at ambient conditions.

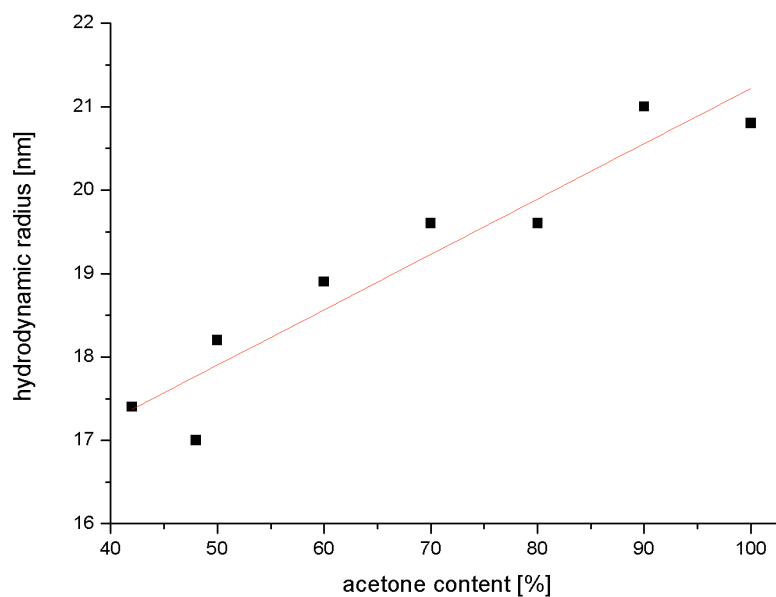


Figure S6.1: Dependence of hydrodynamic radius of PMMA₅₇₀₀ homopolymer (PDI = 1.20) on the acetone content in acetone/isopropanol mixtures. The polymer is insoluble at acetone contents below 42 vol.-%.

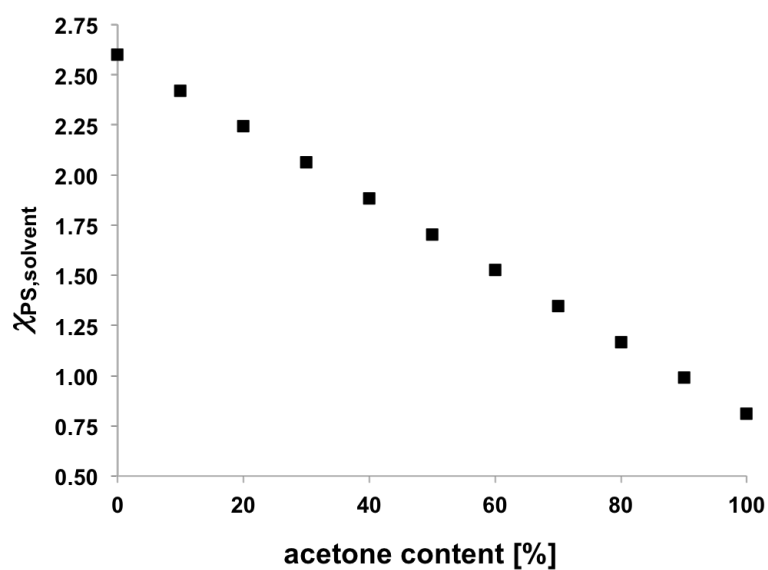


Figure S6.2: Change of $\chi_{PS,solvent}$ in acetone/isopropanol mixtures. Calculated based on values for $\chi_{PS,acetone} = 0.81$ and $\chi_{PS,IPA} = 2.6$.³

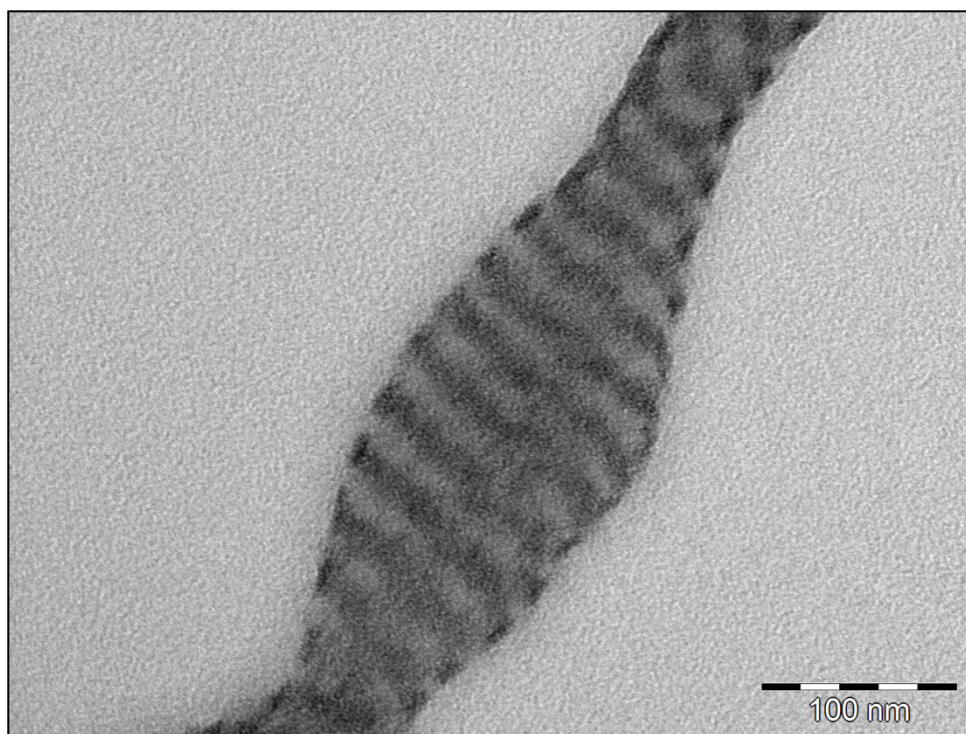
Onset of sheet formation

Figure S6.3: Onset of sheet-formation for $S_{510}B_{258}M_{260}$ with $x_{PMMMA} = 0.25$ in acetone/isopropanol 40:60 (v/v). The transformation of cylindrical micelles to sheets is only observed in some occasions, where the cylinders start to flatten to adopt a sheet-like structure.

Supporting Figures and calculations for blend experiments

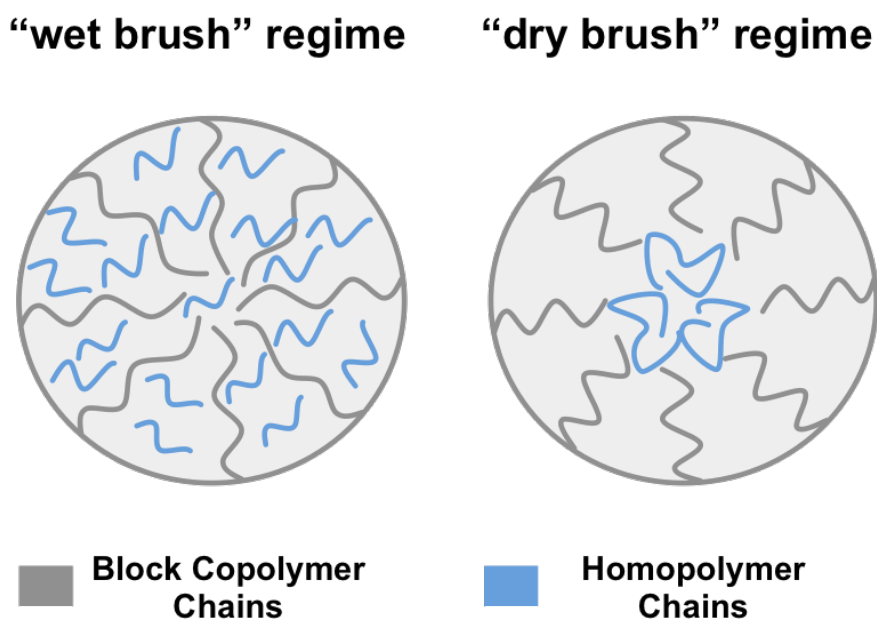


Figure S6.4: Schematic description of the “wet brush” and “dry brush” regime in the core of block copolymer micelles. Short homopolymer chains can interpenetrate the block copolymer chains and homogeneous distribute in the phase (“wet brush” regime). Long homopolymer chains accumulate in the middle of the micellar core since they cannot penetrate the block copolymer brush (“dry brush” regime).

Table S6.2: Calculation of the apparent change of the molar fraction, x_M , of PMMA, the weight fractions f_{PS} and f_{PB} of PS and PB in the SBM triblock terpolymer and the total molecular weight upon blending with PS_{192} homopolymer.

$S_{x+y}B_zM_z^{Mn^a}$	x_{PMMA}^b	f_{PS}^b	f_{PB}^b	M_n^b [kg/mol]
$S_{57+0}B_{15}M_{28}^{93}$	0.25	0.57	0.15	93
$S_{57+4}B_{14}M_{25}^{103}$	0.23	0.61	0.14	103
$S_{57+8}B_{12}M_{23}^{113}$	0.21	0.65	0.12	113
$S_{57+13}B_{10}M_{20}^{173}$	0.14	0.70	0.10	173

^a x,y,z denote the weight fraction of the blocks in %. The superscript shows the apparent molecular weight in kg/mol.

^b Apparent change of the molar fraction of the PMMA block, x_M the weight fractions, f_{PS} and f_{PB} of PS and PB and the overall molecular weight M_n .

Modification of PB with hexyl mercaptan

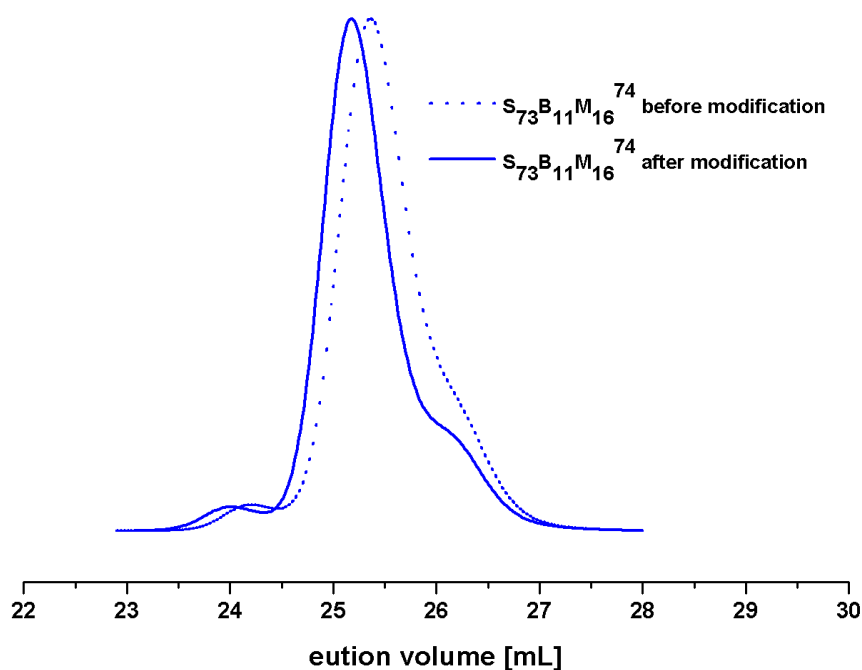


Figure S6.5: SEC traces of $S_{73}B_{11}M_{16}^{74}$ before (dotted) and after (solid line) thiol-ene click reaction.

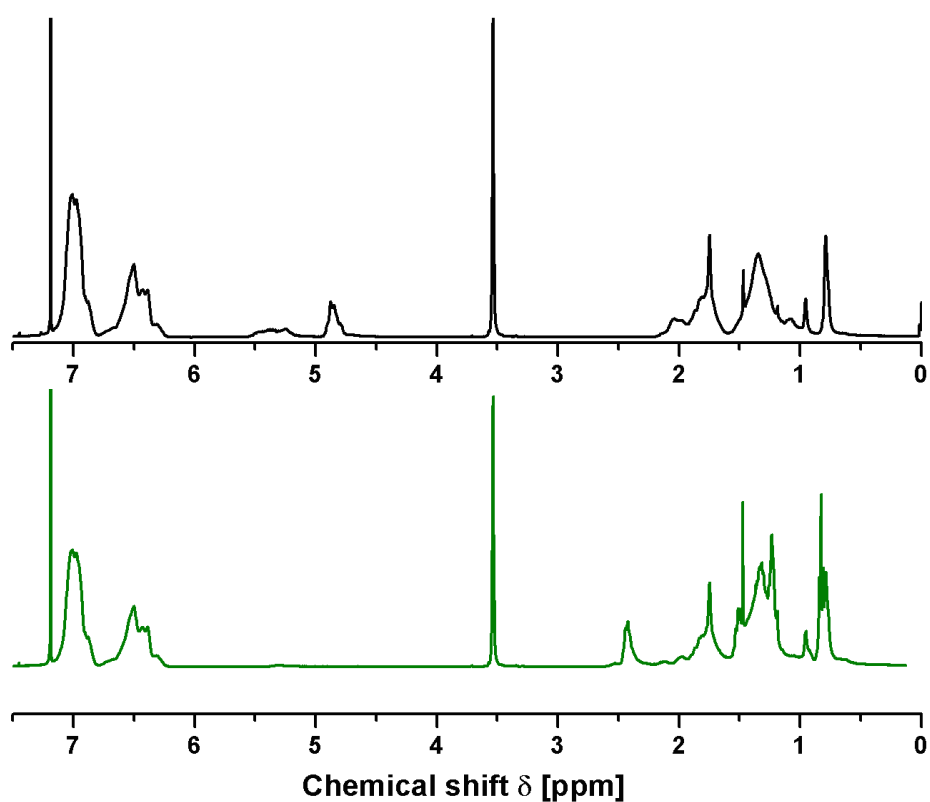


Figure S6.6: $^1\text{H-NMR}$ spectra of $S_{73}B_{11}M_{16}^{74}$ before (black) and after (green) thiol-ene click reaction. Vanishing of the 1,2-PB double bond peaks between 4.5-5.5 ppm shows that the click reaction was quantitative. There is a marginal peak between 5.0-5.5 originating from 1,4-PB moieties that are not accessible for click reaction (1.1 wt.-% 1,4-PB within the SBM triblock terpolymer).

Supporting References

1. Auschra, C.; Stadler, R. *Polym. Bull.* **1993**, *30*, 257-264.
2. Ruckdäschel, H.; Sandler, J.K.E.; Altstädt, V.; Rettig, C.; Schmalz, H.; Abetz, V.; Müller, A.H.E. *Polymer* **2006**, *47*, 2772-2790.
3. Orwall, R.A., Arnold, P.A. in *Physical Properties of Polymers Handbook*, 2nd ed.; Mark, J., Eds.; Wiley Science and Business Media: New York, **2007**; p 233-258

Chapter 7

Bulk Morphologies of Polystyrene-*block*-Polybutadiene-*block*-Poly(*tert*-Butyl Methacrylate) Triblock Terpolymers

Tina I. Löbbling,^a Panu Hiekkataipale^b, Andreas Hanisch,^a Francesca Bennet^a, Holger Schmalz^a, Olli Ikkala^b, André H. Gröschel^{*,b}, and Axel H. E. Müller^{*,a,c}

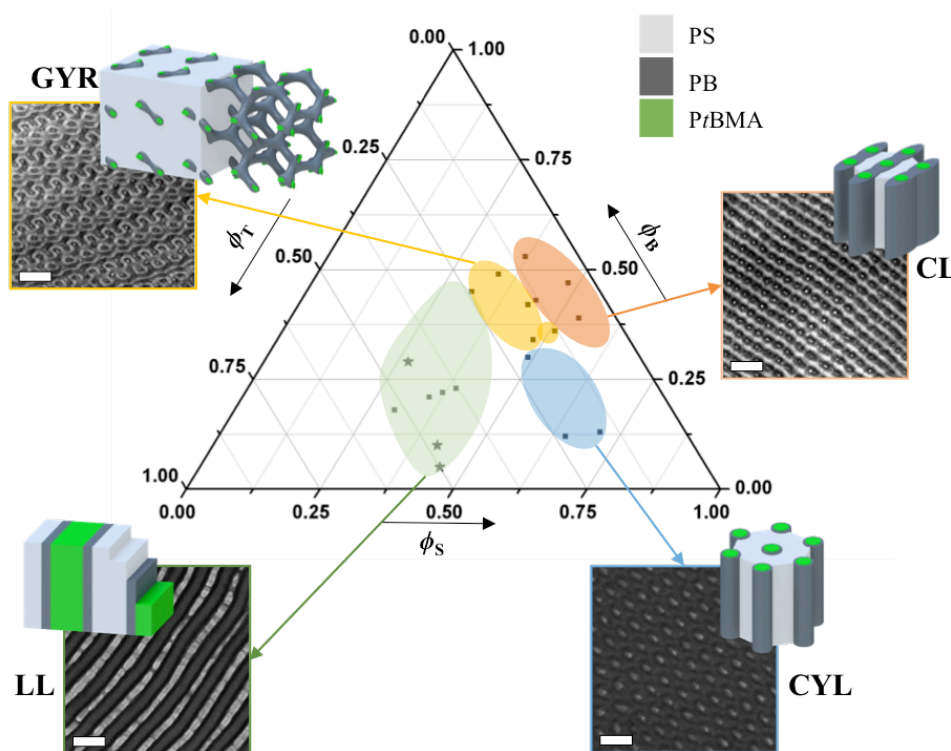
^a Makromolekulare Chemie II, Universität Bayreuth, D-95440 Bayreuth, Germany.

^b Department of Applied Physics, Aalto University School of Science, 02150 Espoo, Finland.

E-mail: andre.groschel@aalto.fi

^c Present address: Institut für Organische Chemie, Johannes Gutenberg-Universität Mainz, D-55099 Mainz, Germany.

E-Mail: axel.mueller@uni-mainz.de



Published in: *Polymer*, **2015**, doi:10.1016/j.polymer.2015.02.025

Abstract

The self-assembly of block copolymers in the bulk phase enables the formation of complex nanostructures with sub 100 nm periodicities and long-range order, both relevant for nanotechnology applications. Here, we map the bulk phase behavior of polystyrene-*block*-polybutadiene-*block*-poly(*tert*-butyl methacrylate) (SBT) triblock terpolymers on a series of narrowly distributed polymers with widely different block volume fractions, ϕ_S , ϕ_B and ϕ_T . In dependence of ϕ , we find the lamella-lamella, core-shell cylinder, cylinder-in-lamella and core-shell gyroid morphology, but also a rarely observed cylinder-in-lamella phase. The bulk morphologies are thoroughly characterized by transmission electron microscopy (TEM) and small angle X-ray scattering (SAXS) and display unusually broad stability regions, *i.e.* morphologies are observed over a broad range of compositions. We attribute this phase behavior to the asymmetric distribution of block-block incompatibilities, along the SBT block sequence, which are relatively large for S/B and S/T interfaces, but small for B/T. The higher enthalpic penalties at the S/B and S/T interface cause B to preferentially spread on the T microdomain thereby adopting its geometry. The morphological behavior of SBT is thus dominated by the volume ratio of the end blocks, ϕ_S and ϕ_T , which reduces the number of potential morphologies to only a few, mostly the core-shell analogue of diblock copolymer morphologies. In general, a simplified terpolymer bulk behavior with large stability regions for morphologies offers straightforward synthetic targeting of specific morphologies that usually only appear in a small parameter space as demonstrated here on the core-shell gyroid.

Introduction

Block copolymers consist of covalently linked polymer blocks with differences in physical or chemical properties. The resulting block-block incompatibility creates the conflict of short-range attraction and long-range repulsion that drives self-assembly of block copolymers into predictable bulk morphologies with nanometer periodicities. Important parameters that govern the geometric arrangement of the phases are the volume fractions, ϕ_A (with $\phi_B = 1 - \phi_A$) of the participating blocks, A and B, and their block-block incompatibility, $\chi_{AB}N$, which is the Flory-Huggins-interaction parameter χ_{AB} , multiplied by the number of monomer units (degree of polymerization), $N = N_A + N_B$.¹ The microphase separation is the result of enthalpic (interfacial energy of the two blocks) and entropic (chain stretching) contributions and is well understood given the dedicated efforts of theoretical²⁻⁴ and experimental characterization of bulk phase diagrams.⁵⁻⁸ AB diblock copolymers can adopt a limited number of stable bulk morphologies depending on these parameters such as the sphere, cylinder, gyroid and lamellar morphology, often found in the strong segregation regime above the order-disorder transition.¹ Except synthetic control of morphology (block length and choice of monomers), there are several post polymerization methods to manipulate the phase behavior of diblock copolymers, *e.g.*, by changing the volume fraction of one of the blocks *via* blending with homo- and copolymers,^{9,10} nanoparticles¹¹ or *via* hydrogen bonding.¹²⁻¹⁵ Also thermally induced order-order-transitions,^{16,17} shear alignment^{18,19} and alignment in electrical fields²⁰⁻²² have evolved to state-of-the-art techniques to induce, alter and optimize long-range order or to switch between morphologies.

Compared to the straightforward phase behavior of diblock copolymers, ABC triblock terpolymers feature higher morphological complexity due to the increased number of interaction parameters, χ_{AB} , χ_{BC} , χ_{AC} , and volume fractions, ϕ_A , ϕ_B (with $\phi_C = 1 - \phi_A - \phi_B$).^{23,24} Three blocks further give rise to variation in architecture (linear or miktoarm stars)²⁵⁻²⁷ and block sequence (ABC, BAC, CAB).^{28,29} Nowadays, the synthesis of tailor-made ABC triblock terpolymers (or multiblock copolymers) has become state-of-the-art through continuous progress and development of controlled/living radical and ionic polymerization techniques.³⁰ The increased number of participating blocks complicates the prediction of the bulk behavior, but also contributes to the tremendous variety and complexity of potential morphologies.^{31,32} Stadler *et al.* pioneered studies on ABC triblock terpolymer self-assembly of polystyrene-*block*-polybutadiene-*block*-poly(methyl methacrylate) (SBM) in bulk. Besides the core-shell analogues of cylindrical and gyroid diblock copolymer morphologies, they identified many more complex block arrangements, *e.g.*, the spheres-on-sphere, spheres-on-cylinder, helix-on-cylinder and a knitting pattern morphology, amongst others.³³⁻³⁵ Since then, ternary phase diagrams of several triblock terpolymers (*e.g.* SBM, SVT, BVT; S=styrene, B=butadiene, M=methyl methacrylate, V=2/4-vinylpyridine, T=*tert*-butyl methacrylate) have been thoroughly investigated and highlighted the vast morphological diversity.³⁶⁻³⁸ These and other works demonstrate the impressive complexity of ABC triblock terpolymer bulk morphologies.

Block copolymer bulk morphologies found widespread interest as precisely nanostructured templating materials for applications ranging from catalysis,^{39–41} photovoltaics⁴² and optics⁴³ to fuel cells and lithography.^{44–47} The gyroid morphology is a triply periodic minimal surface⁴⁸ and attracts special attention as precursor in hybrid materials design for applications requiring high surface area and symmetry (*e.g.* solar cells⁴⁹ or nanofoams⁵⁰). In this regard, ABC triblock terpolymers offer more sophisticated gyroid morphologies with either core-shell⁵¹ or double gyroid configuration, *i.e.* two interconnected gyroid networks separated by a matrix. Especially in the latter case, separate loading of individual gyroid phases with metal precursors gives access to bimetallic interpenetrating networks.⁵² ABC triblock terpolymers that form A/C lamellar morphologies were also used for the preparation of Janus particles of diverse geometry (sphere, cylinder, disc) through crosslinking of the B middle block of lamella-sphere, lamella-cylinder and lamella-lamella bulk morphologies with subsequent redispersion of the cross-linked particles.^{53–56} Polymer-based Janus particles show enhanced interfacial activity^{57,58} as demonstrated by their application as interfacial stabilizers in emulsion polymerization,⁵⁹ dispersants for carbon nanotubes⁶⁰ and compatibilizers for polymer blends.^{61,62} Given the diversity of terpolymer morphologies, their full potential has certainly not been harnessed as of yet, and several other morphologies could be attractive in view of applications. However to predict and reliably target specific morphologies also requires a comprehensive understanding of the parameters that control the bulk behavior for a given combination of blocks.

This work contributes to the understanding of the relationship between block volume fractions, block-block interactions, and the resulting bulk morphologies within the system polystyrene-*block*-polybutadiene-*block*-poly(*tert*-butyl methacrylate) (SBT). This block combination shows large differences in the segment-segment incompatibility of S/T ($\chi_{ST} = 0.025^{63}$) and B/T ($\chi_{BT} = 0.007^{64}$), causing the B phase to preferably spread on the T phase. Hence, the morphology that is formed is mostly guided by the two end blocks, leading to a decreased complexity of the phase behavior and to large stability regions of the single phases. The synthesized series of SBT triblock terpolymers with varying volume fractions, ϕ_S , ϕ_B and ϕ_T , cover a wide range of morphologies ranging from lamella-lamella to core-shell cylinder and core-shell gyroid morphology. Also a cylinder-in-lamella morphology was found, that was up to now only rarely reported. All bulk morphologies were characterized by transmission electron microscopy (TEM) and small angle X-ray scattering (SAXS). Stability regions for the various bulk morphologies are summarized in a ternary phase diagram. The functional SBT terpolymer offers post polymerization modifications, *e.g.*, the possibility to fixate the bulk structure *via* cross-linking of the B phase or form pH-responsive metal coordination sites, poly(methacrylic acid), by deprotection of the T phase. This may be interesting if combined *e.g.* with the gyroid morphology to create pH responsive channels.

Experimental Part

Materials

Sec-butyl lithium (*sec*-BuLi, 1.3 M solution in cyclohexane/hexane: 92:8, Acros) was used without further purification. THF (p.a., Aldrich) was distilled from CaH₂ and K under dry N₂ atmosphere. 1,1-Diphenyl-ethylene (Aldrich) was distilled from *sec*-BuLi under reduced pressure. Styrene was degassed with three freeze-pump-thaw cycles followed by the addition of 1 mL di-*n*-butylmagnesium (1.0 M solution in heptane, Aldrich) per 10 mL monomer. After evaporation of heptane and stirring for 1 h, the desired amount of monomer was condensed into a glass ampule and stored in liquid nitrogen under nitrogen atmosphere until use. Gaseous 1,3-butadiene (Messer-Griesheim) was passed through columns filled with molecular sieves (4 Å) and basic aluminum oxide. Afterwards, it was condensed into a glass reactor and stirred over di-*n*-butylmagnesium at least two days prior to use. *Tert*-butyl methacrylate (*t*BMA, Aldrich) was first degassed with three freeze-pump-thaw cycles. After addition of tri-*n*-octylaluminium (25 wt.-% in hexanes, Aldrich) until a slight yellow color occurred, hexane was evaporated under reduced pressure and the mixture was stirred for 1 h before the monomer was condensed into a glass ampule and stored in liquid nitrogen under nitrogen atmosphere until use.

Synthesis of SBT triblock terpolymers. All SBT triblock terpolymers were synthesized *via* living anionic polymerization in THF at low temperatures according to a previous publication (Scheme 7.1).⁶⁵ *Sec*-BuLi followed by styrene was added to THF at -70 °C. After the reaction was completed an aliquot of the precursor was taken for SEC analysis before 1,3-butadiene was added. The reaction mixture was heated to -10 °C and stirred for 6.5 h to ensure complete polymerization. The reaction mixture was cooled to -50 °C before a 6-fold molar excess (compared to *sec*-BuLi) of 1,1-diphenyl-ethylene was added. After stirring for 1 h an aliquot of the diblock precursor was taken for SEC analysis. Then, *t*BMA monomer was added at -70 °C and the reaction was heated to -50 °C for 2 h. During the polymerization of the *Pt*BMA block, larger amounts were taken at specific reaction times (monomer conversion was monitored with online FT-NIR spectroscopy, Figure 7.1) by direct precipitation into degassed methanol. After complete monomer consumption, 2 mL of degassed methanol were added to the polymer solution to terminate the still living chain ends. The characteristics of the synthesized polymers are summarized in Table 7.1.

Table 7.1: Characteristics of the used SBT triblock terpolymers.

Polymer ^{a)}	M _w [kg/mol] ^{b)}	PDI ^{c)}	ϕ _S : ϕ _B : ϕ _T ^{d)}	Bulk Morphology ^{e)}
S ₃₁ B ₁₇ T ₅₂	108	1.09	0.30 : 0.18 : 0.52	LL
S ₃₆ B ₂₀ T ₄₄	148	1.12	0.35 : 0.21 : 0.44	LL
S ₃₈ B ₂₁ T ₄₁	140	1.10	0.37 : 0.22 : 0.41	LL
S ₄₀ B ₂₂ T ₃₈	132	1.06	0.39 : 0.23 : 0.38	LL
S ₆₆ B ₁₁ T ₂₃	85	1.03	0.65 : 0.12 : 0.23	CYL
S ₅₁ B ₂₈ T ₂₁	104	1.07	0.49 : 0.30 : 0.21	CYL
S ₇₂ B ₁₂ T ₁₆	78	1.03	0.71 : 0.13 : 0.16	CYL
S ₄₆ B ₄₁ T ₁₃	69	1.03	0.44 : 0.43 : 0.13	CL
S ₃₉ B ₅₁ T ₁₀	80	1.08	0.37 : 0.53 : 0.10	CL
S ₅₆ B ₃₇ T ₇	57	1.07	0.54 : 0.39 : 0.07	CL
S ₅₀ B ₄₅ T ₅	64	1.04	0.48 : 0.47 : 0.05	CL
S ₃₃ B ₄₃ T ₂₄	94	1.10	0.31 : 0.45 : 0.24	L/GYR
S ₅₀ B ₃₂ T ₁₈	64	1.04	0.48 : 0.34 : 0.18	GYR
S ₃₆ B ₄₇ T ₁₇	87	1.09	0.34 : 0.49 : 0.17	GYR
S ₄₅ B ₄₀ T ₁₅	71	1.04	0.43 : 0.42 : 0.15	GYR
S ₅₃ B ₃₄ T ₁₃	61	1.03	0.51 : 0.36 : 0.13	GYR

^{a)} Subscripts denote the weight fractions of the corresponding blocks in % determined by ¹H-NMR

^{b)} Overall molecular weight determined by a combination of SEC and ¹H-NMR

^{c)} Determined *via* THF-SEC using PS standards

^{d)} Volume fractions of the corresponding blocks were calculated from the composition of the polymer using the density of the blocks according to equation (7.1).

^{e)} Determined with TEM and SAXS measurements: CYL = core-shell cylinder; GYR = core-shell gyroid; LL = lamella-lamella; CL = cylinder-in-lamella.

The volume fractions of the blocks in Table 7.1 were calculated from the degree of polymerization (N) and the molar volume of the respective monomer unit (V_m) as exemplified for the S block in equation (7.1):

$$\phi_S = \frac{N_S V_{m,S}}{(N_S V_{m,S} + N_B V_{m,B} + N_T V_{m,T})} \quad (7.1)$$

with V_{m,S} = 99.0 cm³/mol, V_{m,B} = 56.0 cm³/mol, and V_{m,T} = 139.4 cm³/mol calculated from the molecular weight of the monomers and their respective densities, ρ_S=1.04 g/cm³, ρ_B=0.96 g/cm³ and ρ_T=1.02 g/cm³.^{66,67}

Preparation of Bulk Films. All SBT triblock terpolymer bulk films were prepared the same way. For that purpose, 100 mg of the polymer was dissolved in 2 mL THF to give a concentration of $c = 50$ g/L. The polymer solution was cast into a 5 mL glass vial and the solvent was then allowed to evaporate slowly at room temperature over several days to yield the bulk film.

Transmission Electron Microscopy (TEM). For TEM analysis, ultra-thin sections were cut from the polymer film with a Reichert-Jung Ultracut E equipped with a diamond knife at temperatures below T_g of the PB block (90 K). TEM measurements were performed in bright-field mode on a Zeiss CEM 902 electron microscope operated at 80 kV. Prior to TEM imaging, the samples were stained with OsO_4 vapor for four hours at room temperature to increase the contrast of the PB phase.⁶⁸

Online FT-NIR Spectroscopy. A Nicolet Magna 560 FT-IR optical bench equipped with a white light source and a PbS detector was used to record the NIR spectra. Online monitoring was accomplished using a laboratory autoclave (Büchi) equipped with an all glass low-temperature immersion transmission probe (Hellma) with an optical path length of 10 mm and connected to the spectrometer *via* 2 m fiber-optical cables. The probe was fed through a port in the stainless steel top plate of the reactor and immersed into the reaction mixture.^{69,70}

Nuclear Magnetic Resonance Spectroscopy ($^1\text{H-NMR}$). $^1\text{H-NMR}$ Spectra were recorded on a Bruker Ultrashield 300 machine with a 300 MHz operating frequency using deuterated chloroform as solvent.

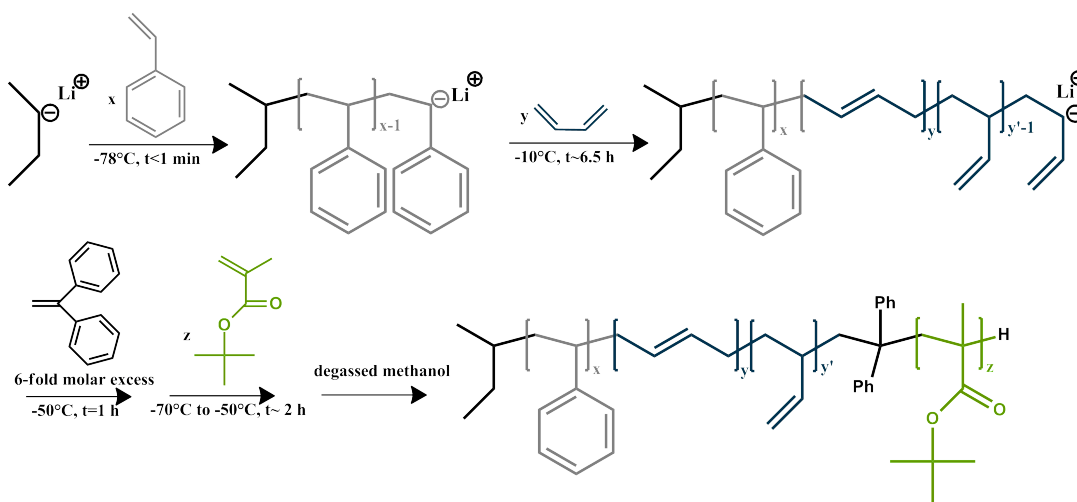
Size Exclusion Chromatography (SEC). Size exclusion chromatography measurements were performed on a set of 30 cm SDV-gel columns of 5 μm particle size having a pore size of $10^5, 10^4, 10^3$, and 10^2 Å with refractive index and UV ($\lambda = 254$ nm) detection. SEC was measured at an elution rate of 1 mL/min with THF as eluent and applying a calibration with linear PS standards.

Small Angle X-Ray Scattering (SAXS). Small angle X-ray scattering (SAXS) measurements of the films were performed in vacuum on a SAXS system, which includes a Bruker MICROSTAR rotating anode X-ray source with Montel collimating optics (CuK_α radiation $\lambda = 1.54$ Å). The X-ray beam was further collimated using four sets of 4-blade slits (JJ X-Ray) and the diffraction pattern of the sample was collected on a 2-D area detector (Bruker Hi-Star). The distance of the detector was 3.5 m from the sample. One-dimensional SAXS data were obtained by azimuthally averaging the 2D scattering data. The magnitude of the scattering vector is given by $q = (4\pi\lambda^{-1})\sin \theta$, where 2θ is the scattering angle and to calibrate the q -range, silver behenate (AgBe) was used as a standard. The Lorentz correction was applied to correct the intensities of the X-ray scattering, where the intensities are reduced to zero at zero diffraction angle. The electron densities of the participating blocks are: $\rho_S = 0.566$ mol/cm³, $\rho_B = 0.532$ mol/cm³ and $\rho_T = 0.561$ mol/cm³.^{37,38} Due to the low electron density difference between S and T only a weak scattering contrast is expected.

Results and discussion

The synthetic process for the sequential living anionic polymerization of polystyrene-*block*-polybutadiene-*block*-poly(*tert*-butyl methacrylate) (SBT) is summarized in Scheme 7.1. For this study, we synthesized a total of 16 SBT triblock terpolymers with varying weight (and thus volume) fractions as listed in Table 7.1. We abbreviate the polymers with $S_xB_yT_z^M$ throughout this manuscript, where the subscripts denote the weight fraction of each block in wt.-% (for easier comparison), and the superscript the weight-average molecular weight in kg/mol.

Scheme 7.1: Synthesis of SBT triblock terpolymers *via* sequential living anionic polymerization.



The monomer conversion was followed with FT-NIR spectroscopy. The solvent subtracted NIR-spectra for the polymerization of PB block in $S_{53}B_{34}T_{13}^{61k}$ at different reaction times are shown in Figure 7.1a. The signal at $\nu = 6116 \text{ cm}^{-1}$ corresponds to the first overtone of the vinyl C-H stretching and decreases with increasing conversion. The inset shows the first-order kinetic plot for this polymerization, where the conversion x_p was calculated according to eq (7.2) with A_0 as the initial absorbance, A_t the absorbance at a certain time and A_∞ the absorbance at 100% monomer conversion.

$$x_p = \frac{A_0 - A_t}{A_0 - A_\infty} \quad (7.2)$$

Figure 7.1b shows SEC elution traces of the PS precursor polymer (grey), the PS-*b*-PB diblock copolymer (black) and the final PS-*b*-PB-*b*-PtBMA triblock terpolymer ($S_{53}B_{34}T_{13}^{61k}$ green). The final SBT polymer shows a narrow distribution with only minor remains of PS homopolymers due to termination of few chains during addition of the butadiene block. The complete shift of the trace maintaining peak shape after addition of *t*BMA suggests quantitative initiation of the third block.

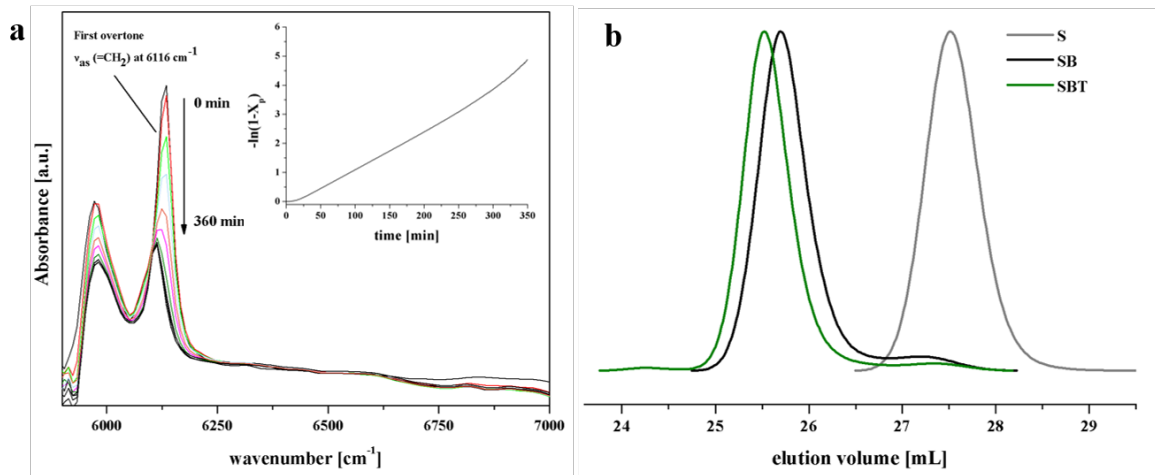


Figure 7.1: Polymerization kinetics exemplified on the $S_{53}B_{34}T_{13}^{61}$ triblock terpolymer. a) NIR-spectra of 1,3-butadiene polymerization in THF at $-10\text{ }^{\circ}\text{C}$ after subtraction of the solvent background between $t = 0\text{ min}$ and $t = 360\text{ min}$. The inset shows the corresponding linear first order kinetic plot. b) SEC elution traces the PS precursor (grey), the PS-*b*-PB diblock copolymer (black) and the final PS-*b*-PB-*b*-PtBMA triblock terpolymer (green).

The overall molecular weights were chosen to be larger than 50 kg/mol so that sufficiently high Flory-Huggins-interaction parameters drive microphase separation above the order-disorder transition. For the present SBT system, the χ -parameters for S/B and S/T are $\chi_{SB} = 0.061^{71}$ and $\chi_{ST} = 0.025^{63}$ respectively. For B/T a value of $\chi_{BT} = 0.007$ is estimated,⁶⁴ but this value inherits uncertainty as calculations are solely based on solubility parameters. The volume fractions, ϕ_S , ϕ_B and ϕ_T , are calculated in Table 7.1 and used throughout the manuscript as a measure to border each morphology as well as to discuss morphological transitions.

In the following, we discuss the phase behavior of SBT triblock terpolymers and their self-assembly into four distinct morphologies. The last section then summarizes the stability regions of the observed bulk phases in a ternary phase diagram.

Lamella-Lamella (LL) Morphology. SBT terpolymers with equal S and T volume fractions, $\phi_S \approx \phi_T$, result in the lamella-lamella bulk morphology as exemplified by the transmission electron microscopy (TEM) images of $S_{40}B_{22}T_{38}^{132}$ in Figure 7.2. The sample was stained with OsO_4 , which covalently binds to the polybutadiene double bonds and increases the contrast of the B phase. In TEM, S appears light grey, B dark grey, and T bright due to *e*-beam degradation.⁷² We determine a long period $L_0 = 68.3\text{ nm} \pm 4.2\text{ nm}$ as indicated by the red arrows in Figure 7.2b. The thicknesses of the B and S lamellae are $d_{l(B)} = 10.4\text{ nm} \pm 1.6\text{ nm}$ and $d_{l(S)} = 23.9\text{ nm} \pm 3.5\text{ nm}$, respectively, whereas the disintegrating T lamella cannot be measured reliably in TEM image analysis. The schematic in Figure 7.2c shows the lamellar bulk morphology with S lamellae in light grey, B dark grey and T in green. Although one can easily identify the lamellar sequence in TEM, *e*-beam degradation of the T block leads to shrinkage of the T phase as well as deformation and wrinkling of the entire morphology. Arising shear forces during ultra-thin sectioning of the film add further uncertainty to the characterization based on TEM image analysis. Small-

angle X-ray scattering (SAXS), on the other hand, is a non-invasive method and records distinct diffraction pattern from the sample. Figure 7.2c shows a representative SAXS curve of $S_{40}B_{22}T_{38}^{132}$ with peaks at the relative positions 1 : 2 : 4 : 6 corresponding to the [100], [200], [400] and [600] projections for a lamellar morphology. The [300] and [500] projections are missing or the intensity is within the range of the background noise of the spectra. This may be explained by the similar volume fractions, $\phi_S = 0.39$ and $\phi_T = 0.38$, and almost equal electron densities, $\rho_S = 0.566 \text{ mol/cm}^3$ and $\rho_T = 0.561 \text{ mol/cm}^3$. Thus, the relative maxima for lamellar spacing would appear at positions that are only half of the actual triblock terpolymer periodicity, *i.e.* comparable to the scattering curve of a “diblock copolymer”. Evaluation of the scattering curve maxima gives a long period of $L_0 = 76.6 \text{ nm} \pm 3.8 \text{ nm}$, which is slightly larger than the one obtained from TEM measurements ($L_0 = 68.3 \text{ nm} \pm 4.2 \text{ nm}$) due to the mentioned shrinkage of the T lamellae upon degradation. We obtain the LL morphology for various compositions covering a large range of B volume fractions from $\phi_B = 0.23$ -0.18 (Table 7.1, entries 1-4) to only $\phi_B = 0.05$ for polymers in previous reports.^{55,73} This behavior can be explained by comparing the χ -parameters. Since $\chi_{ST} > \chi_{BT}$, a B/T interface is more favored than S/T and considering also $\chi_{SB} > \chi_{BT}$, the B phase preferentially spreads on T. The asymmetry of χ -parameters between adjacent blocks has a crucial influence on the phase behavior was also shown earlier by Stadler *et al.* for triblock terpolymers with post modification of blocks to induce a change of the χ -parameter.⁷⁴ In principle, B always engulfs the T phase, which in the special case of a T lamella (infinite expansion in one direction) then results in the observed B lamella even for low B volume fractions $\phi_B = 0.18$ and $\phi_B = 0.05$, where usually B cylinders and spheres are expected. We will address this unusual behavior in more detail also on the other morphologies.

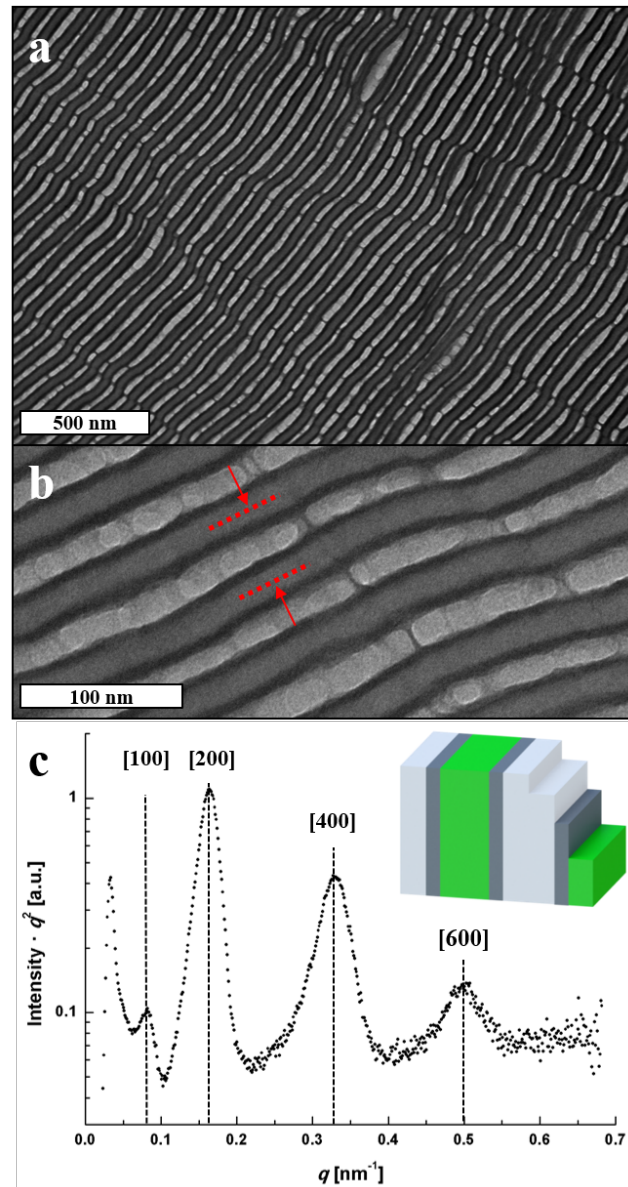


Figure 7.2: Lamella-lamella morphology. **a)** TEM overview image and **b)** zoom-in of the $S_{40}B_{22}T_{38}^{132}$ bulk film cast from THF. OsO_4 staining renders S light grey and B dark grey, while T is not visible due to e-beam degradation. The red arrows in (b) mark the long period of the lamella-lamella morphology. **c)** Lorentz corrected SAXS pattern with characteristic reflexes for lamellar morphology. The schematic drawing represents the lamellar phases: S = light grey, B = dark grey, T = green.

Core-Shell Cylinder (CYL) Morphology. For SBT triblock terpolymers with $\phi_S > \phi_T$, asymmetric endblocks drive phase separation to the core-shell cylinder morphology (Table 7.1, entries 5-7). Exemplified on $S_{66}B_{11}T_{23}^{85}$ the TEM overview image shows long-range order core-shell cylinder morphology (Figure 7.3a). The T cylinders arrange in a slightly distorted hexagonal lattice, wrapped by a B shell in an S matrix (Figure 7.3a,b). The long-range order is further corroborated by the *fast Fourier transform* (FFT) pattern (Figure 7.2a, inset). The angle of the unit cell is $\alpha = 81^\circ$ and $\beta = 99^\circ$ instead of $\alpha = 60^\circ$ and $\beta = 120^\circ$, and thus, the morphology displays a deformation that it is close to the orthorhombic core-shell cylinder morphology (see upper right corner of Figure 7.3a).

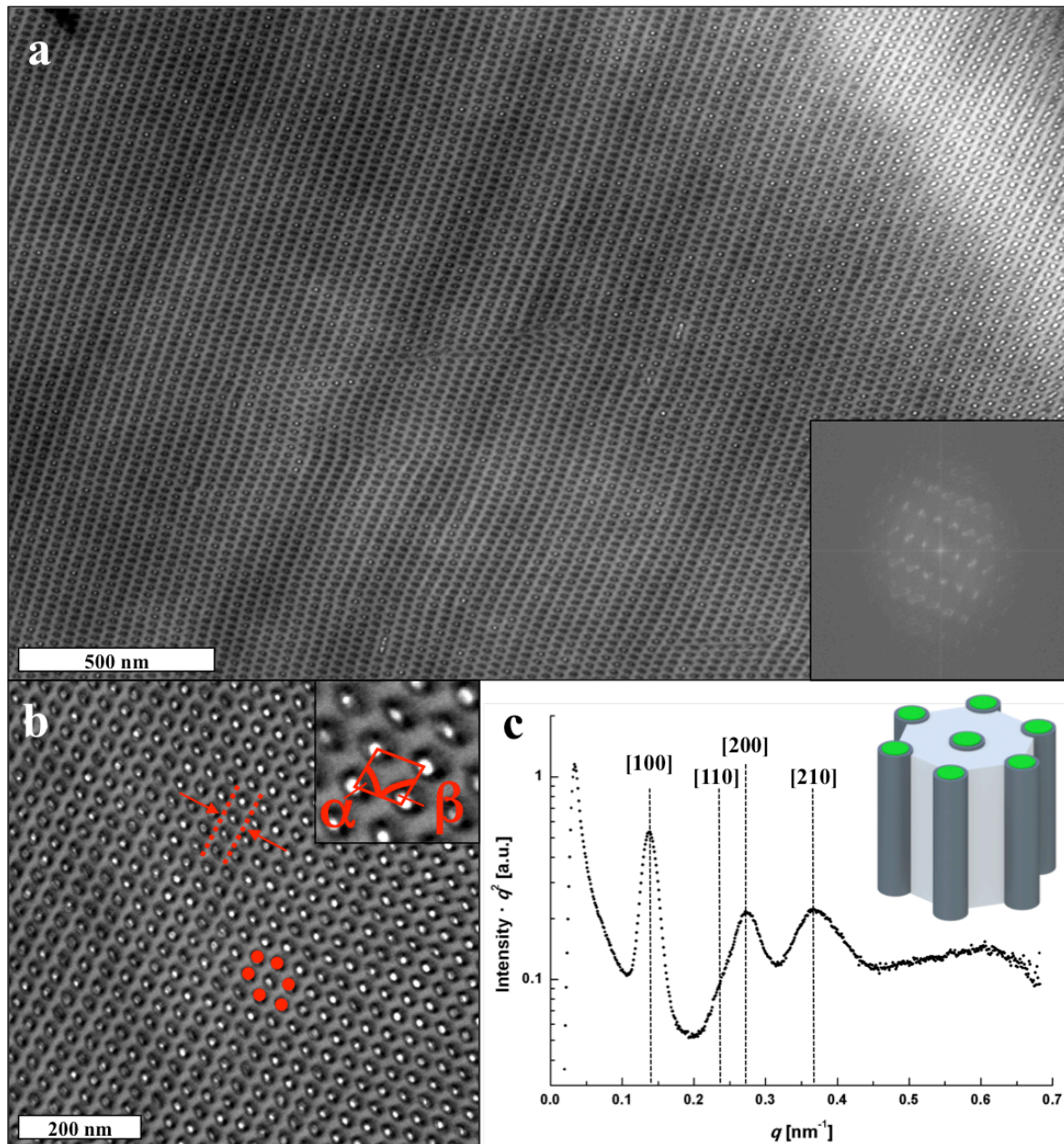


Figure 7.3: Core-shell cylinder morphology. **a)** TEM overview image of $S_{66}B_{11}T_{23}^{85}$ bulk film cast from THF (inset shows FFT of (a)). **b)** Zoom-in on the core-shell morphology with red dots indicating the distorted hexagonal arrangement and red arrows mark the long period L_0 . TEM samples are stained with OsO_4 to enhance the contrast of B phase, which appears dark grey; S is light grey and T appears white due to e-beam degradation. The inset shows the angles α and β of the unit cell. **c)** The Lorentz corrected SAXS pattern shows reflections typical for hexagonal cylinder morphology. The inset shows a scheme of the morphology (S = light grey, B = dark grey, T = green).

The SAXS pattern (Figure 7.3c) shows maxima at relative values of $1 : \sqrt{3} : 2 : \sqrt{7}$ corresponding to typical [100], [110], [200], [210] indices for a hexagonally arranged cylinder morphology. A long period $L_0 = 52.5 \text{ nm} \pm 2.6 \text{ nm}$ was determined from SAXS measurements, which is slightly larger than the value $L_0 = 39.7 \pm 4.9 \text{ nm}$ obtained from TEM. As discussed before, this discrepancy may be explained through underlying inaccuracies in determination of the long period by means of TEM such as shrinkage of the film as a result

of e -beam degradation of T or deformation of the film during cutting. A diameter of $d_{c(S+B)} = 26.7 \pm 1.6$ nm for the core-shell cylinders was determined *via* TEM. This value cannot be measured with SAXS because this method only gives the long period of the entire structure. The SAXS data, the volume fractions of the blocks as well as TEM image analysis suggest core-shell cylinders with a T core and B shell embedded in an S matrix. The structure is illustrated in the inset of Figure 7.3c. Although the B phase is relatively small with only $\phi_B = 0.12$, a homogeneous shell around the T cylinders is formed, which we explain in correspondence to the anomalies discussed for lamella-lamella morphology. The B phase spreads onto T to prevent an S/T interface as a result of $\chi_{ST} > \chi_{BT}$. The cylindrical phase is observed even if the B content increases to $\phi_B = 0.30$ as in the case of $S_{51}B_{28}T_{21}$ ¹⁰⁴. In general, the B phase seems to engulf the T phase irrespective of its volume fraction and we find core-shell cylinders as long as the T block volume fraction remains $\phi_T < 0.25$. The spreading behavior of B suggests that the overall morphology is first and foremost governed by the volume fractions of the end blocks, S and T (especially for B as the minority phase). As long as the T block has a weight fraction corresponding to the cylinder morphology the B volume fraction can adopt a wide range of values without changing the morphology as it only spreads between S and T domains. Hence for SBT, the core-shell cylinder morphology has a high stability region. As shown earlier by Abetz *et al.* for high B content SBT terpolymers, also morphologies are observed with S and T being both spheres or both cylinders within the B matrix when the B phase increases to $\phi_B > 0.50$.⁷³ In these cases, the B phase still separates S from T, which agrees with the assumptions drawn so far.

Cylinder-in-Lamella (CL) Morphology. For SBT triblock terpolymers with $\phi_S \gg \phi_T$ and simultaneously $\phi_B > 0.39$, we observe the formation of a morphology that is best described as hexagonally packed T cylinders exclusively located in B lamellae alternating with “empty” S lamellae. The TEM overview in Figure 7.4a exemplifies this morphology on $S_{46}B_{41}T_{13}$ ⁶⁹, where the light grey S phase forms continuous, undulated lamellae and the dark B lamellae accommodate white T cylinders. The T phase thereby still arranges in slightly distorted hexagonal long-range order as indicated by the FFT pattern and the red dots in Figure 7.4b. The long period $L_0 = 38.5 \pm 1.7$ nm determined from TEM image analysis is small as compared to the previously discussed morphologies, which is expected given the rather low molecular weight of $M_w = 69$ kg/mol. The long period of $L_0 = 57.1 \text{ nm} \pm 2.9$ nm obtained from SAXS is again more reliable and larger than that from TEM. This morphology also has a relatively large stability region and is found for block compositions ranging from $\phi_T = 0.05$ -0.13, while $\phi_B > 0.39$ (Table 7.1, entries 8-11). This morphology was previously described for a block ter-/copolymer blend⁷⁵ and for polystyrene-*block*-poly(2-vinylpyridine)-*block*-poly(*tert*-butyl methacrylate),³⁷ and denoted as undulated lamellae (UL). Although the S and B phases are clearly undulating, the UL terminology does not fully capture the complex geometrical arrangement of all phases. The SAXS pattern in Figure 7.4c shows peaks at relative positions $1 : \sqrt{3} : 2 : \sqrt{7} : 3$ and thus contains characteristics of both the lamella and the cylinder morphology, and is best de-

scribed as cylinder-in-lamella (CL) morphology. TEM in combination with SAXS suggests the following block arrangement as according to the inset in Figure 7.4c: as the minority phase, T (green) forms cylinders within the B lamellae phase (dark grey) alternating with continuous S lamellae (light grey).

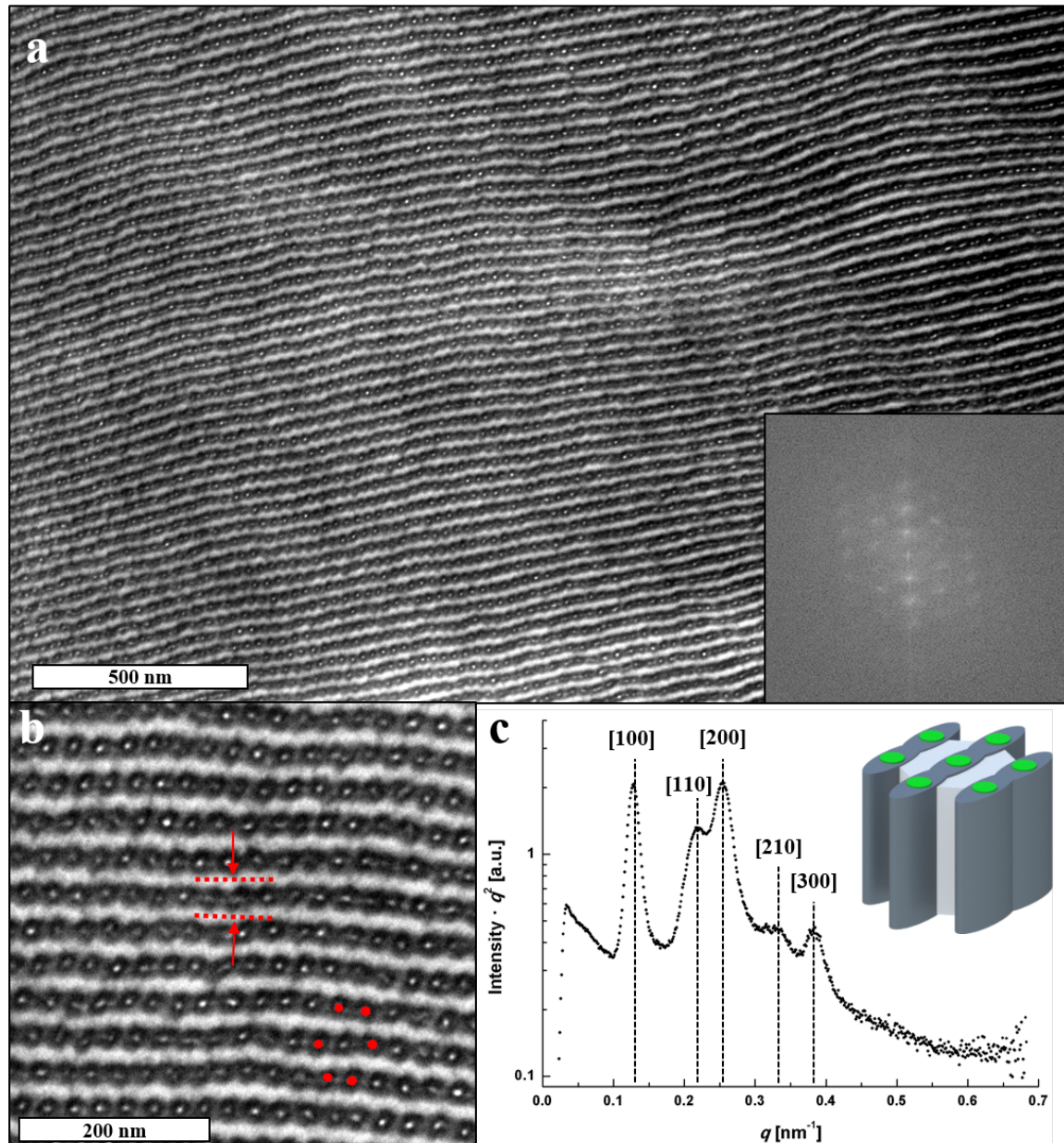


Figure 7.4: Cylinder-in-lamella morphology. a) TEM overview with inset showing the FFT of this image and b) zoom-in on $S_{46}B_{41}T_{13}$ bulk film cast from THF. The B phase is stained with OsO_4 to enhance contrast (S is light grey and T appears white due to e-beam degradation). The S phase forms an undulated lamellar phase, while B lamellae contain T cylinders (red spots indicate hexagonal arrangement of T cylinders). The red arrows mark the long period L_0 . c) Lorentz corrected SAXS pattern show typical reflexes for lamellar and cylindrical morphologies. The schematic in (c) shows the block arrangement for the cylinder-in-lamella morphology: S = light grey, B = dark grey, T = green.

Despite the seemingly complex positioning of the blocks, we can derive its origin rather easily with the help of our previous discussions. Figure 7.5 illustrates the evolution from

core-shell cylinders to cylinder-in-lamella morphology in dependence of the B volume fraction. First a core-shell morphology can be observed as long as the B volume fraction does not exceed $\phi_B = 0.30$ (Figure 7.5a, Table 7.1, entry 6). The rather large $\phi_B = 0.3$ for $S_{51}B_{28}T_{21}^{104}$ in Figure 7.5a still forms a continuous shell, yet already here the core and the shell of the cylinders experience a noticeable elliptic deformation in one direction. With increasing $\phi_B = 0.4$, the shell grows relative to the core and the high incompatibility χ_{SB} causes anisotropic deformation of the B shell. Similar to the core-shell cylinder morphology, we find hexagonally arranged T cylinders (Figure 7.5b), yet with the marked difference that the much larger B shells (in relation to T) start merging into a lamella. The overlapping B volume at $\phi_B = 0.5$ then fuses into a lamellar phase that incorporates the T cylinders (Figure 7.5c). The hexagonal arrangement of the cylinders is thereby preserved.

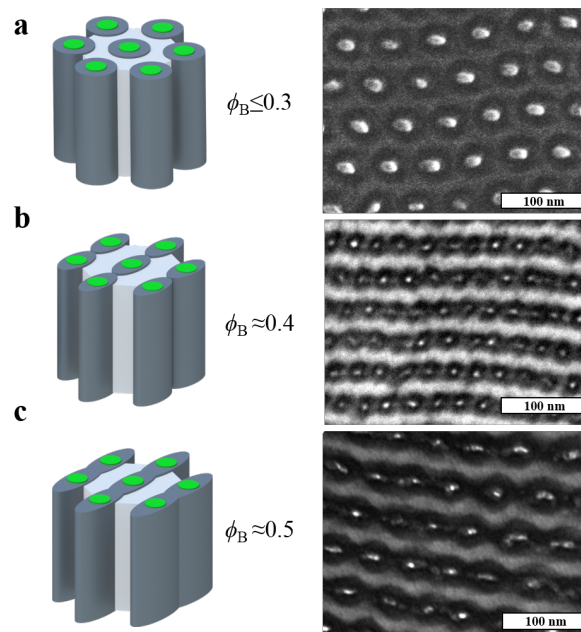


Figure 7.5: Morphological evolution from core-shell cylinder to cylinder-in-lamella morphology. **a)** Core-shell cylinder morphology for volume fractions $\phi_B \leq 0.3$. The corresponding TEM image shows a bulk film of the $S_{51}B_{28}T_{21}^{104}$ triblock terpolymer. **b)** For $S_{46}B_{41}T_{13}^{69}$ with $\phi_B \approx 0.4$, the B shell becomes thicker (relative to T) developing connection points reminiscent of pearl-necklaces. **c)** Further increase to $\phi_B \approx 0.5$ leads to fusion of B into undulated lamellae incorporating T cylinders. The corresponding TEM image shows the $S_{39}B_{51}T_{10}^{80}$ bulk film (S = light grey, B = dark grey, T = green).

Core-Shell Gyroid Morphology. At a certain composition range, we identify the core-shell gyroid morphology in TEM and SAXS. In case of $S_{33}B_{43}T_{24}^{94}$ (Table 7.1, entry 12), a mixture of lamella-lamella and gyroid morphology was found, which changes to exclusive gyroid morphology upon decreasing the T volume fraction. Figure 7.6a,b shows the TEM overview image of the $S_{53}B_{34}T_{13}^{61}$ bulk morphology as well as the zoom-in of most likely the [112] projection of the gyroid morphology.⁷⁶ From this projection a long period of $L_0 = 98.7 \pm 3.1$ nm was determined from TEM. Similar motifs that are characteristic for the core-shell gyroid morphology can also be found for SBT triblock terpolymers with compositions of $S_{45}B_{40}T_{15}^{71}$, $S_{36}B_{47}T_{17}^{87}$ and $S_{50}B_{32}T_{18}^{64}$ (Table 7.1, entries 13-16). This broad

stability region of the gyroid is rather unusual for triblock terpolymers, but is again a consequence of the B phase that spreads as shell on the T gyroid, even at high $\phi_B = 0.35-0.50$.

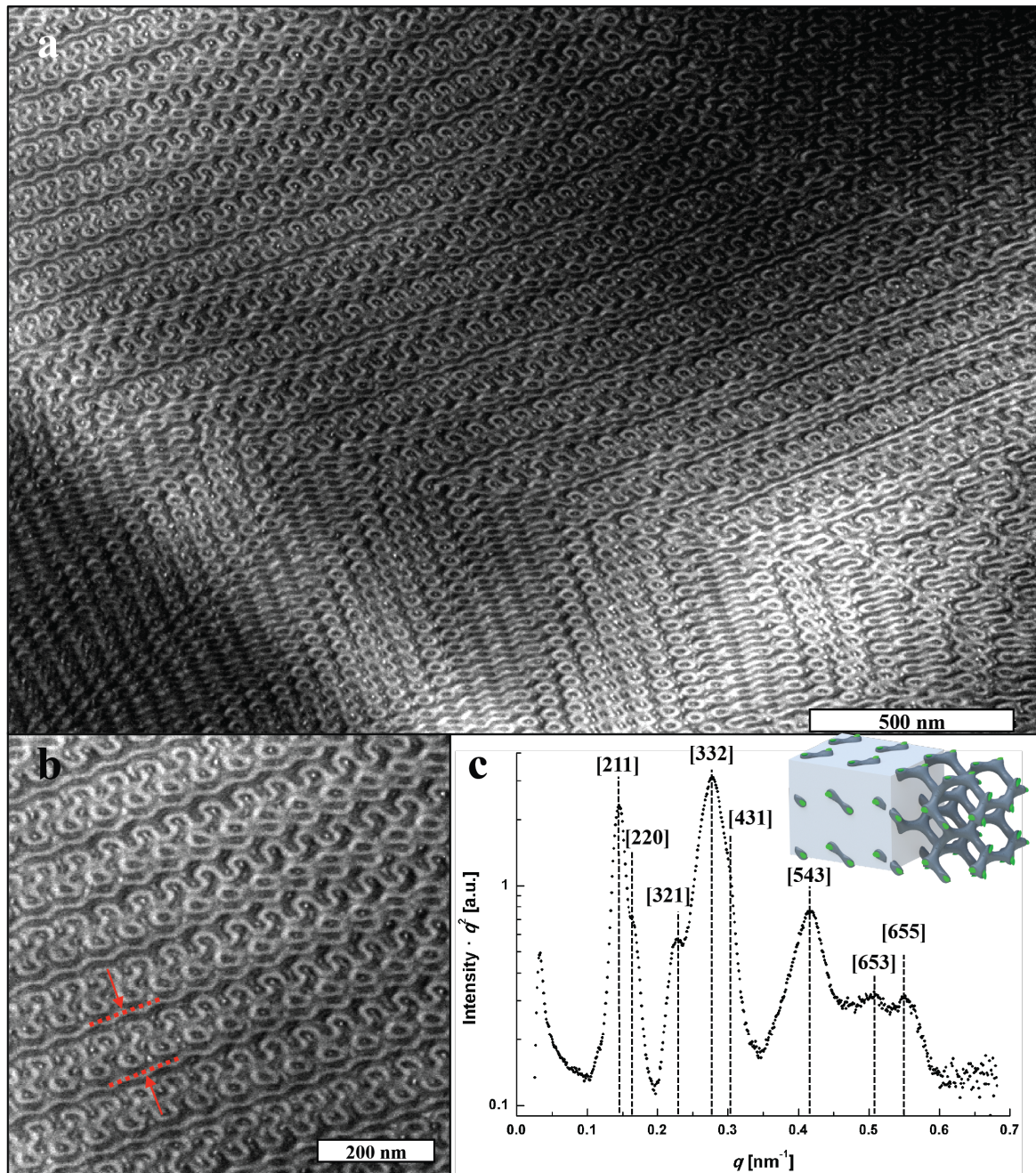


Figure 7.6: Core-shell gyroid morphology. **a)** TEM overview and **b)** zoom-in of $S_{45}B_{40}T_{15}^{71}$ bulk film cast from THF. In the images, S is light grey, B dark grey (stained with OsO_4) and T appears white due to e-beam degradation. The red arrows in (b) mark the long period L_0 . **c)** The Lorentz corrected SAXS pattern depicts reflex positions typical for the gyroid morphology. The schematic in c) illustrates the arrangement of the blocks for the core-shell gyroid morphology: S = light grey, B = dark grey, T = green.

The SAXS pattern in Figure 7.6c shows maxima at relative positions $\sqrt{3} : \sqrt{4} : \sqrt{7} : \sqrt{11} : \sqrt{13} : \sqrt{25} : \sqrt{35} : \sqrt{43}$ that are typical for the gyroid morphology, although peak broadening complicates indexing of all reflections.⁷⁷ The relative peak at $\sqrt{3}$ is

assumed to correspond to the [211] direction. A long period of $L_0 = 106 \text{ nm} \pm 2 \text{ nm}$ was determined from SAXS measurement and is in good agreement with TEM measurements. The inset in Figure 7.5c shows a schematic drawing of the core-shell gyroid with S in light grey, B in dark grey and T in green. All measured gyroid samples have in common that T and B form the core-shell gyroid, which is embedded in an S matrix.

Phase diagram. Figure 7.7 summarizes the discussed morphologies of SBT triblock terpolymers in a comprehensive ternary phase diagram. SBTs with the lowest volume fractions of the T block $\phi_T = 0.05\text{-}0.13$ and high $\phi_B > 0.39$, phase separate to cylinder-in-lamella (CL, or undulated lamella) morphology (Figure 7.7 orange area).

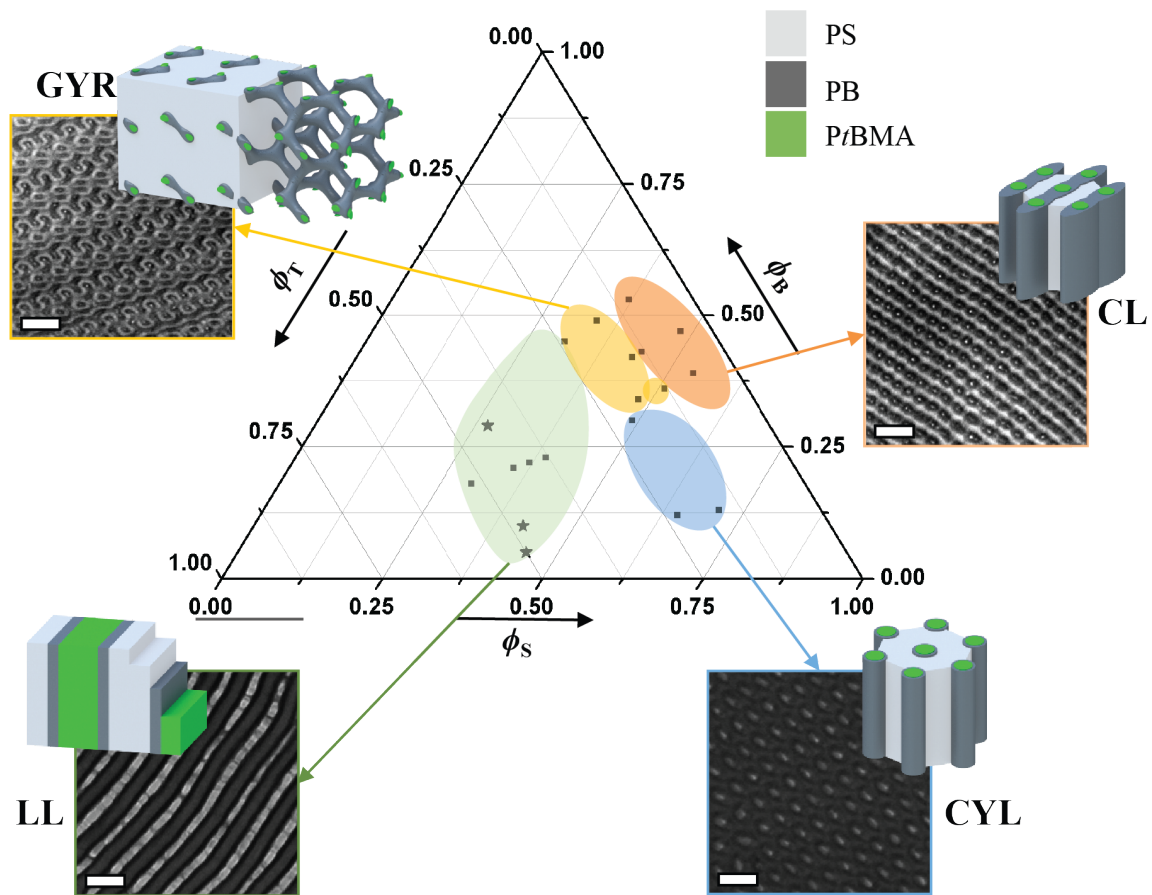


Figure 7.7: Ternary phase diagram of SBT. The colored areas mark regions of the same morphology: blue: core-shell cylinder; green: lamella-lamella (stars denote literature values from ref. [55,73]); orange: cylinder-in-lamella; yellow: core-shell gyroid. All phases are exemplified in TEM images with frames in corresponding colors. The scale bars are 100 nm.

Asymmetric SBT triblock terpolymers with $\phi_S \geq 0.49$ and T fractions between $\phi_T = 0.15\text{-}0.25$ form T core, B shell cylinders in S matrix (CYL, Figure 7.7 blue area). When the S and B blocks are in the range of $\phi_S \approx \phi_B \approx 0.35\text{-}0.50$ with T fractions of $\phi_T \approx 0.15$ the core-shell gyroid (GYR) morphology is present (Figure 7.7 yellow area). The lamella-lamella (LL) phase (Figure 7.7 green area) is observed in a rather large region including literature values (displayed as stars in the phase diagram).^{55,73} The large stability region is attributed to the fact that the B phase always spreads on T and forms lamellae as

long as the S and T block are of similar volume fractions and form lamellae themselves ($\phi_S \approx \phi_T$). Due to $\chi_{ST} > \chi_{BT}$, the B phase tends to spread on T and complex morphologies such as sphere-on-cylinder, helix-on-cylinder or lamellar-sphere as observed for polystyrene-*block*-polybutadiene-*block*-poly(methyl methacrylate) (SBM) are absent.¹ The stability regions over relatively large block copolymer compositions simplify the phase behavior of SBT and the resultant morphologies are easier-to-target synthetically.

Conclusions

Bulk morphologies of 16 SBT triblock terpolymers were investigated *via* TEM and SAXS, and comprise: the core-shell cylinder (CYL), lamella-lamella (LL), undulated lamella or cylinder-in-lamella (CL) and core-shell gyroid (GYR) morphology. Whereas CYL, LL and GYR represent core-shell analogs of known diblock copolymer morphologies, the CL morphology is the result of merging shells of core-shell cylinders in a linear fashion. The rather simple phase behavior of SBT as compared to, *e.g.*, the more complex phase diagram of SBM, might be explained by comparing the χ -parameters of the participating blocks. Since the χ_{ST} as well as χ_{SB} is higher than χ_{BT} , a B/T interface is favored over S/T. To prevent the unfavorable S/T interface the B phase spreads onto T resulting in core-shell structures. Consequently, we observe stability regions of the core-shell analogs of diblock copolymer morphologies over a broader range of block copolymer compositions, because the middle block plays only a minor role in structure evolution. The length of the S and T end blocks mostly determine the final morphology. On the one hand, the simple phase behavior of B reduces the number of possible morphologies to only a few, but on the other hand, it teaches us that proper combinations of χ -parameters (in multiblock copolymers) gives control over phase behavior with minor influence of block volume fractions. In view of applications, this example highlights the importance of knowledge of the block-block interactions, because morphologies that are challenging to target (*e.g.* gyroid) might become easier accessible by reducing the complexity of triblock terpolymer phase behavior through proper choice of monomers.

Acknowledgements

The authors thank Annika Pfaffenberger for ultramicrotoming thin films. The authors acknowledge the Deutsche Forschungsgemeinschaft (DFG) for supporting this work within DFG Mu896/40-1 and SFB 840 (Project A2). This work was carried out under the Academy of Finland's Centre of Excellence Programme (2014-2019) and supported by ERC-2011-AdG (291364-MIMEFUN).

References

1. Abetz V, Simon PFW. *Adv. Polym. Sci.* 2005; 189:125–212.
2. Leibler L. *Macromolecules* 1980;13:1602–17.
3. Matsen M, Schick M. *Phys Rev Lett* 1994;72:2660–3.
4. Matsen MW, Bates FS. *Macromolecules* 1996;29:7641–4.
5. Schmidt SC, Hillmyer MA. *J Polym Sci Part B Polym Phys* 2002;40:2364–76.
6. Ryan AJ, Mai S-M, Patrick A, Fairclough J, Hamley IW, Booth C. *Phys Chem Chem Phys* 2001;3:2961–71.
7. Khandpur AK, Förster S, Bates FS, Hamley IW, Ryan AJ, Bras W, et al. *Macromolecules* 1995;28:8796–806.
8. Floudas G, Vazaiou B, Schipper F, Ulrich R, Wiesner U, Iatrou H, et al. *Macromolecules* 2001;34:2947–57.
9. Hashimoto T, Tanaka H, Hasegawa H. *Macromolecules* 1990;23:4378–86.
10. Abetz V, Goldacker T. *Macromol Rapid Commun* 2000;21:16–34.
11. Warren SC, Messina LC, Slaughter LS, Kamperman M, Zhou Q, Gruner SM, et al. *Science* 2008;320:1748–52.
12. Ruokolainen J, Mäkinen R, Torkkeli M, Mäkelä T, Serimaa R, ten Brinke G, et al. *Science* 1998;280:557–60.
13. Ruokolainen J, ten Brinke G, Ikkala O. *Adv Mater* 1999;11:777–80.
14. Valkama S, Kosonen H, Ruokolainen J, Haatainen T, Torkkeli M, Serimaa R, et al. *Nat Mater* 2004;3:872–6.
15. Vukovic I, ten Brinke G, Loos K. *Macromolecules* 2012;45:9409–18.
16. Kimishima K, Koga T, Hashimoto T. *Macromolecules* 2000;33:968–77.
17. Shi L-Y, Hsieh I-F, Zhou Y, Yu X, Tian H-J, Pan Y, et al. *Macromolecules* 2012;45:9719–26.
18. Fredrickson GH. *J Rheol* 1994;38:1045–67.
19. Gupta VK, Krishnamoorti R, Chen Z-R, Kornfield JA, Smith SD, Satkowski MM, et al. *Macromolecules* 1996;29:875–84.
20. Morkved T, Lu M, Urbas A, Ehrichs E, Jaeger H, Mansky P, et al. *Science* 1996;273:931–3.
21. Schmidt K, Schoberth HG, Ruppel M, Zettl H, Hänsel H, Weiss TM, et al. *Nat Mater* 2008;7:142–5.
22. Böker A, Elbs H, Hänsel H, Knoll A, Ludwigs S, Zettl H, et al. *Phys Rev Lett* 2002;89:135502.
23. Bates FS, Fredrickson GH. *Phys Today* 1999;52:32–8.
24. Ruzette A-V, Leibler L. *Nat Mater* 2005;4:19–31.
25. Hückstädt H, Abetz V, Stadler R. *Macromol Rapid Commun* 1996;17:599–606.
26. Hückstädt H, Göpfert A, Abetz V. *Macromol Chem Phys* 2000;201:296–307.

27. Hadjichristidis N, Iatrou H, Pitsikalis M, Pispas S, Avgeropoulos A. *Prog Polym Sci* 2005;30:725–82.
28. Hirao A, Matsuo Y, Oie T, Goseki R, Ishizone T, Sugiyama K, et al. *Macromolecules* 2011;44:6345–55.
29. Hückstädt H, Göpfert A, Abetz V. *Polymer* 2000;41:9089–94.
30. Müller AHE, Matyjaszewski K. *Controlled and Living Polymerizations*, Weinheim: Wiley-VCH, 2009.
31. Stadler R, Auschra C, Beckmann J, Krappe U, Voigt-Martin I, Leibler L. *Macromolecules* 1995;28:3080–91.
32. Zheng W, Wang Z. *Macromolecules* 1995;28:7215–23.
33. Krappe U, Stadler R, Voigt-Martin I. *Macromolecules* 1995;28:4558–61.
34. Breiner U, Krappe U, Abetz V, Stadler R. *Macromol Chem Phys* 1997;198:1051–83.
35. Breiner U, Krappe U, Stadler R. *Macromol Rapid Commun* 1996;17:567–75.
36. Tschierske C. Non-conventional Soft Matter. *Annu Rep Prog Chem, Sect C*, 2001;97:191–267.
37. Ludwigs S, Böker A, Abetz V, Müller AHE, Krausch G. *Polymer* 2003;44:6815–23.
38. Schacher F, Yuan J, Schoberth HG, Müller AHE. *Polymer* 2010;51:2021–32.
39. Zhang K, Gao L, Chen Y. *Polymer* 2010;51:2809–17.
40. Müllner M, Lunkenbein T, Miyajima N, Breu J, Müller AHE. *Small* 2012;8:2636–40.
41. Lunkenbein T, Kamperman M, Li Z, Bojer C, Drechsler M, Förster S, et al. *J Am Chem Soc* 2012;134:12685–92.
42. Darling SB. *Energy Environ Sci* 2009;2:1266–73.
43. Hsueh H-Y, Chen H-Y, She M-S, Chen C-K, Ho R-M, Gwo S, et al. *Nano Lett* 2010;10:4994–5000.
44. Orilall MC, Wiesner U. *Chem Soc Rev* 2011;40:520–35.
45. Kim E, Vaynzof Y, Sepe A, Guldin S, Scherer M, Cunha P, et al. *Adv Funct Mater* 2014;24:863–72.
46. Son JG, Gwyther J, Chang J-B, Berggren KK, Manners I, Ross CA. *Nano Lett* 2011;11:2849–55.
47. Schacher FH, Rupar PA, Manners I. *Angew Chem Int Ed* 2012;51:2–25.
48. Vukovic I, ten Brinke G, Loos K. *Polymer* 2013;54:2591–605.
49. Crossland EJW, Kamperman M, Nedelcu M, Ducati C, Wiesner U, Smilgies D-M, et al. *Nano Lett* 2009;9:2807–12.
50. Vukovic I, Punzhin S, Vukovic Z, Onck P, De Hosson JTM, ten Brinke G, et al. *ACS Nano* 2011;5:6339–48.
51. Du Sart GG, Vukovic I, Vukovic Z, Polushkin E, Hiekkataipale P, Ruokolainen J, et al. *Macromol Rapid Commun* 2011;32:366–70.

52. Li Z, Hur K, Sai H, Higuchi T, Takahara A, Jinnai H, et al. *Nat Commun* 2014;5:3247.
53. Erhardt R, Böker A, Zettl H, Kaya H, Pyckhout-Hintzen W, Krausch G, et al. *Macromolecules* 2001;34:1069–75.
54. Liu Y, Abetz V, Müller AHE. *Macromolecules* 2003;36:7894–8.
55. Walther A, André X, Drechsler M, Abetz V, Müller AHE. *J Am Chem Soc* 2007;129:6187–98.
56. Walther A, Müller AHE. *Chem Rev* 2013;113:5194–261.
57. Ruhland TM, Gröschel AH, Walther A, Müller AHE. *Langmuir* 2011;27:9807–14.
58. Ruhland TM, Gröschel AH, Ballard N, Skelton TS, Walther A, Müller AHE, et al. *Langmuir* 2013;29:1388–94.
59. Walther A, Hoffmann M, Müller AHE. *Angew Chemie Int Ed* 2008;47:711–4.
60. Gröschel AH, Löblich TI, Petrov PD, Müllner M, Kuttner C, Wieberger F, et al. *Angew Chemie Int Ed* 2013;52:3602–6.
61. Walther A, Matussek K, Müller AHE. *ACS Nano* 2008;2:1167–78.
62. Bahrami R, Löblich TI, Gröschel AH, Schmalz H, Müller AHE, Altstädt V. *ACS Nano* 2014;8:10048-56.
63. Schubert DW, Stamm M, Müller AHE. *Polym Eng Sci* 1999;39:1501–7.
64. Hanisch A, Gröschel AH, Förtsch M, Löblich T, Schacher FH, Müller AHE. *Polymer* 2013;54:4528-37.
65. Goldacker T, Abetz V, Stadler R, Erukhimovich I, Leibler L. *Nature* 1999;398:137–9.
66. Schrage S, Sigel R, Schlaad H. *Macromolecules* 2003;36:1417–20.
67. Han D, Li X, Hong S, Jinnai H, Liu G. *Soft Matter* 2012;8:2144-51.
68. Williams DB, Carter BC. *Transmission Electron Microscopy*, Heidelberg: Springer, 2009.
69. Ah Toy A, Reinicke S, Müller AHE, Schmalz H. *Macromolecules* 2007;40:5241–4.
70. Lanzendörfer MG, Schmalz, H, Abetz, V, Müller A.H.E. in : “In-situ Spectroscopy of Monomer and Polymer Synthesis”, J.E. Puskas, R. Storey, Eds., New York/Dordrecht 2002: Kluwer Academic/Plenum Publishers, pp. 67-82.
71. Mark JE. *Physical Properties of Polymers Handbook*, Woodbury: American Institute of Physics Press; 2007.
72. Sperschneider A, Hund M, Schoberth HG, Schacher FH, Tsarkova L, Müller AHE, et al. *ACS Nano* 2010;4:5609–16.
73. Abetz V, Markgraf K, Rebizant V. *Macromol Symp* 2002;177:139–45.
74. Neumann C, Loveday DR, Abetz V, Stadler R. *Macromolecules* 1998;31:2493-500.
75. Jiang S, Göpfert A, Abetz V. *Macromol Rapid Commun* 2003;24:932–7.
76. Hückstädt H, Goldacker T, Göpfert A, Abetz V. *Macromolecules* 2000;33:3757–61.

77. Hajduk DA, Harper PE, Gruner SM, Honeker CC, Kim G, Thomas EL, et al. *Macromolecules* 1994;27:4063–75.

Chapter 8

The Impact of Janus Nanoparticles on the Compatibilization of Immiscible Polymer Blends under Technologically Relevant Conditions

Ronak Bahrami,^{†,‡} Tina I. Löbling,^{†,‡} André H. Gröschel,[§] Holger Schmalz,[‡] Axel H. E. Müller^{*,‡,¶} and Volker Altstädt^{*,†}

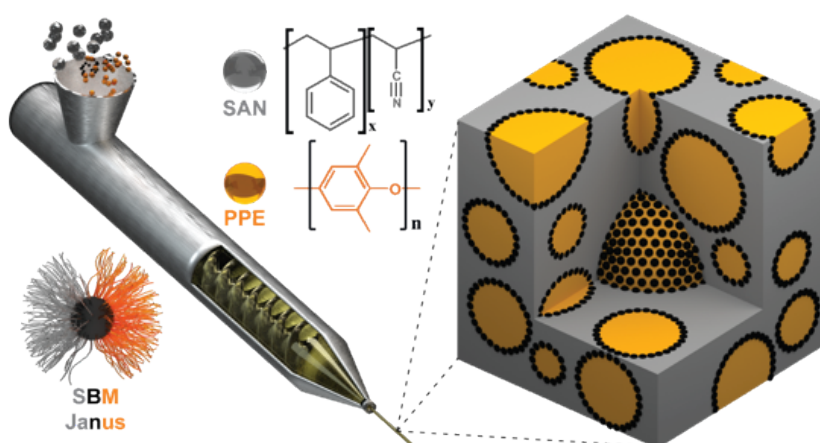
[†] Fakultät für Ingenieurwissenschaften, [‡] Makromolekulare Chemie II, Universität Bayreuth, 95440 Bayreuth, Germany.

[§] Molecular Materials, Department of Applied Physics, School of Science, Aalto University, 02150 Espoo, Finland

[¶]Institut für Organische Chemie, Johannes Gutenberg-Universität Mainz, D-55099 Mainz, Germany

E-Mail: altstaedt@uni-bayreuth.de ; axel.mueller@uni-mainz.de

[‡] Both authors contributed equally to this work



Published in: *ACS Nano*, **2014**, 8, 10048-10056

ABSTRACT

Several hundred grams of Janus nanoparticles ($d \approx 40$ nm) were synthesized from triblock terpolymers as compatibilizers for blending of technologically relevant polymers, PPE and SAN, on industry-scale extruders. The Janus nanoparticles (JPs) demonstrate superior compatibilization capabilities compared to the corresponding triblock terpolymer, attributed to the combined intrinsic properties, amphiphilicity and the Pickering effect. Straightforward mixing and extrusion protocols yield multiscale blend morphologies with “raspberry-like” structures of JPs-covered PPE phases in a SAN matrix. The JPs densely pack at the blend interface providing the necessary steric repulsion to suppress droplet coagulation during processing. We determine the efficiency of JP-compatibilization by droplet size evaluation and find the smallest average droplet size of $d \approx 300$ nm at 10wt.-% of added compatibilizer, whereas at 2wt.-%, use of JPs is most economically with reasonable small droplets and narrow dispersity. In case of excess JPs, rheological properties of the system is changed by a droplet network formation. The large-scale synthesis of JPs, the low required weight fractions and their exceptional stability against extensive shear and temperature profiles during industrial extrusion process make JP promising next generation compatibilizers.

Introduction

The blending of polymers is a well-established and versatile concept to economically unify desirable material properties of multiple components within new materials and builds the foundation of an entire industry.¹⁻³ The inherent immiscibility of polymers usually demands the careful design of blend recipes, processing conditions and/or the addition of compatibilizers to control the blend morphology.^{4,5} Compatibilizers may add further functionality and range from organic molecules to block and graft copolymers,^{6,7} nanoparticles⁸⁻¹¹ and carbon based reinforcements.^{12,13} Thereby, nanoparticle reinforced composites have evolved into a vivid research field owing to the selective localization of particles and thus functional matter at the blend interface.¹⁴⁻¹⁷ In that regard, Janus nanoparticles (JPs) have received much less attention, despite their known exceptional performance in applications that specifically rely on the minimization of interfacial energies (emulsions, suspensions, melts).¹⁸⁻²¹ JPs are the colloidal analogue of surfactants and amphiphilic block copolymers and feature different physical properties on opposing hemispheres.²²⁻²⁴ The combination of amphiphilicity and particulate character (Pickering effect) favors strong and selective adsorption to interfaces. Among others, this is considered challenging when applying nanoparticle compatibilizers in polymer melts.^{25,26} Previous work on polystyrene/poly(methyl methacrylate) (PS/PMMA) blends compatibilized by JPs with matching PS and PMMA hemispheres served as an ideal small-scale model for comprehensive studies on JP location, blending efficiency and morphological evolution.²⁷ Since then, only a handful of theoretical works advanced this prospective research field.²⁸⁻³⁰ Studies involving JPs mostly focus on polymer blends that allow convenient handling (in experiments and calculations) as to understand underlying mechanisms, while studies on blends with material properties appealing for practical applications have remained beyond laboratories' reach.

Poly(2,6-dimethyl-1,4-phenylene ether) (PPE) blended with poly(styrene-*co*-acrylonitrile) (SAN) is such a system of technological relevance. PPE is usually blended with PS, since they are fully miscible, to facilitate its processability. Yet, the need for a modified system, preferably based on PS or its copolymers, with better chemical stability and higher T_g (like SAN) is of high scientific interest. The new blend would combine the heat resistance and dimensional stability of PPE with the stiffness and easy processability of SAN; however, the miscibility of the system depends strongly on the acrylonitrile content of the SAN phase. Almost all commercially available SAN polymers have AN contents between 18-35 wt.-%, whereas above 12.4 wt.-% the PPE/SAN system is immiscible.³¹ In this case, the high surface energy and the low tendency of PPE to form interfaces with SAN cause PPE droplets to rapidly coagulate during extrusion, rendering compatibilizers an essential part of the blend recipe. In earlier studies, we showed that the ABC triblock terpolymer polystyrene-*block*-polybutadiene-*block*-poly(methyl methacrylate) (SBM) efficiently compatibilizes this blend since PS is compatible with PPE and PMMA with SAN.³²⁻³⁴ The soft PB middle block forms low modulus droplets located at the interface and may serve to dissipate energy. We hypothesize that the use of JPs made

from SBM triblock terpolymers could distinctly improve the blend microstructure and outperform the triblock terpolymer due to the superior interfacial activity of amphiphilic particles. So far, JPs have not been studied as compatibilizers in industry-scale blend systems due to severe challenges in the up-scaling of particle production (typically solved for μg to mg amounts).^{21,36} In general, there is a lack of available JP types that are able to operate on the relevant size scale, *i.e.*, particles should be considerably smaller (< 100 nm) than the to-stabilize blend polymer droplets (< 1 μm). It is thus not surprising that JPs are still considered an exotic class of material, merely suited for specialized research and not appropriate for large-scale applications.

Here, we present the first studies on the performance of Janus nanoparticles in technologically relevant polymer blend systems in industry-scale blending equipment using 200 g of SBM JPs for the compatibilization of several kilograms of PPE and SAN (Figure 8.1). We show that despite high shear rates during melt processing JPs quantitatively adsorb at the blend interface and we derive mechanistic explanations for the morphological impact of JPs on the studied polymer blend system. Both are key aspects for the implementation of JPs as compatibilizers in industry-scale processes.

Results and Discussion

We recently reported a solution-based synthesis of nanosized JPs, which opens the way to significantly larger quantities of JPs.³⁷ The JPs for this study were prepared from a triblock terpolymer of the composition $\text{S}_{40}\text{B}_{20}\text{M}_{40}^{108}$ (subscripts denote block weight fractions and superscript overall molecular weight in kg/mol) according to a modified recipe from ref 37 (see Supporting Information) yielding 100 g JPs in a single batch (Supporting Information Figure S8.1). The JPs feature a cross-linked PB core and equally sized PS/PMMA hemispheres (Supporting Information Figures S8.2 and S8.3). The polymer chains of the hemispheres are above the critical entanglement lengths, M_c , with $M_{n,\text{PS}} = 42$ kg/mol ($M_{c,\text{PS}} = 34$ kg/mol)³⁸ and $M_{n,\text{PMMA}} = 42$ kg/mol ($M_{c,\text{PMMA}} = 18$ kg/mol),³⁹ ensuring sufficient interaction between JPs and the blended polymers. In a typical blend experiment, 540 g PPE powder and 360 g SAN polymer pellets were dry-mixed together with 100 g JPs to yield a blend ratio of PPE/SAN 60:40 (w/w) containing 10 wt.-% JPs as compatibilizer. This particular blend ratio has a well-processable medium viscosity and demonstrated convincing blend performance in earlier studies.^{13,32,33,40} After optimizing process parameters such as screw speed on the neat blend, all mixtures were extruded on a Brabender DSE twin-screw extruder at fixed nozzle temperature of 245 $^{\circ}\text{C}$, at constant screw speed of 85 rpm and constant throughput of 1 kg/h (details are given in the Experimental Section).

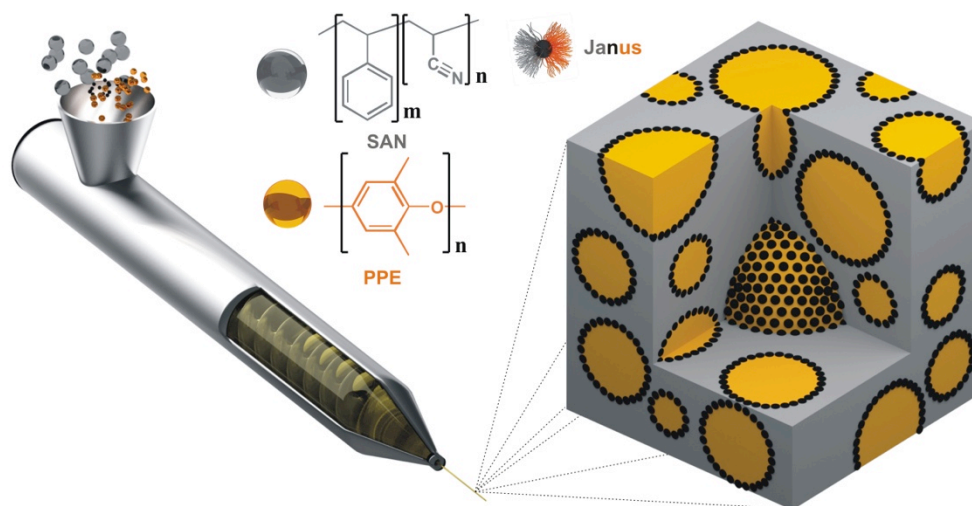


Figure 8.1. Processing of polymer blends using Janus nanoparticles (JPs) as compatibilizer. During extrusion of the polymer melt, JPs (black dots) compatibilize and stabilize PPE droplets (yellow) within the SAN matrix (grey).

To analyze the blend morphology, scanning electron microscopy (SEM) and transmission electron microscopy TEM were used. For TEM imaging, ultrathin sections (thickness < 100 nm) were cut from the blend granules after extrusion (Figure 8.2). We find a substantial improvement of the blend homogeneity after addition of 10 wt.-% JPs (Figure 8.2b) compared to the neat blend system (Figure 8.2a). The neat blend shows elongated, ill-shaped droplets that frequently coagulate and resemble a co-continuous phase (parallel to extrusion direction), whereas the JP blend shows an entirely different morphology of small droplets. The morphology in Figure 8.2b shows small PPE droplets (dark) embedded in a continuous SAN matrix (bright). Strikingly, the droplets are able to pack densely without coagulation despite the harsh processing conditions (temperature, pressure, high viscosity) and the strong arising shear forces. Although the PPE droplets collide and deform as evident from their nonspherical shape, the JPs at the interface provide efficient stabilization and repulsion for the droplets. The size of most droplets is well below $1 \mu\text{m}$ as a direct result of efficient reduction of interfacial energy. Despite the excess of PPE in the feed, we still find PPE droplets in a SAN matrix, because the high viscosity ratio, $\eta_{\text{PPE}}/\eta_{\text{SAN}} > 10$, shifts phase inversion far from a feed ratio of 50:50 (w/w). This peculiarity is well-known for PPE/SAN, where the less viscous SAN always forms the matrix.^{32,33} On closer inspection of the droplet morphology in Figure 8.2b, we frequently observe brighter SAN droplets inside the darker PPE droplets, suggesting a double emulsion morphology, usually found close to phase inversion,⁴¹ *i.e.*, SAN droplets in PPE matrix (see also Supporting Information Figures S8.4 and S8.5). The TEM close-up in Figure 8.2c corroborates the double emulsion morphology. Here, the larger PPE droplet engulfs smaller SAN droplets, while all interfaces are densely covered with JPs visible as black dots (OsO_4 staining of remaining PB double bonds). We will discuss the origin of this morphology and the narrow droplet size distribution in more detail later.

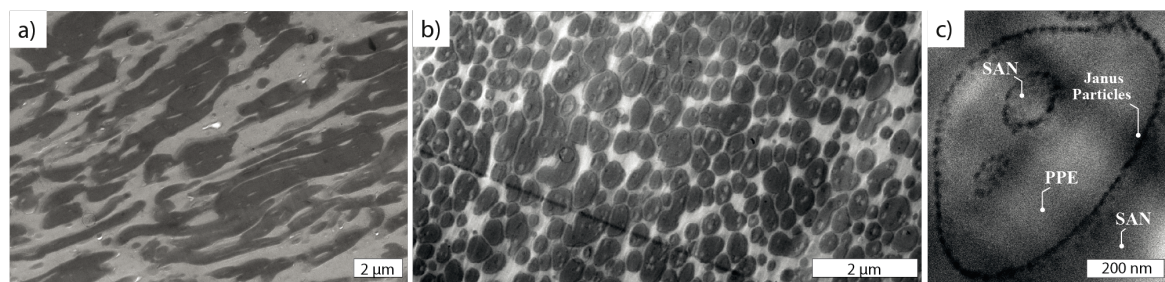


Figure 8.2. Droplet morphology of the PPE (dark)/SAN (bright) blend (60/40 w/w), as neat blend and compatibilized with 10 wt.-% of SBM JPs. **a)** TEM overview of the PPE/SAN (60/40 w/w) blend without and **(b and c)** with compatibilization. The neat blend system shows irregular, elongated and fused droplets, whereas small drop morphology occurs with 10 wt.-% JPs **(b)**. The TEM magnification **(c)** of one PPE droplet shows JPs as black dots exclusively located at the PPE/SAN blend interface. PB cores of JPs were selectively stained with OsO_4 to increase the contrast.

To get a better overview of the blend structures, SEM images of the neat and JP compatibilized blends are shown in Figure 8.3, panels a and b, respectively. Here again the difference in blend structures shows a clear transition from a random co-continuous structure to a homogenous droplet structure. The morphological difference is also clearly demonstrated when comparing horizontal (parallel to extrusion direction) and vertical (perpendicular to extrusion direction) fractures of the blends to evaluate the homogeneity throughout the samples (Supporting Information Figure S8.6). The JP blend displays sub-micrometer features in both directions proving isotropic distribution of the blend components. Compared to that, the neat blend contains micron-sized elliptical domains in the horizontal, but distinctly different elongated cylindrical domains in the vertical cross section attributed to anisotropic shearing of the PPE phase. This difference in morphological homogeneity should have profound effects on the stability of the blend when subjected to stress. We find the droplet morphology also in SEM as a random distribution of dents and bumps corresponding to droplets and holes left behind by detached PPE droplets (Figure 8.3b; red and blue arrows). The droplets show a multiscale structure as they are fully covered with JPs, forming raspberry-like structures in a SAN matrix. We clearly identify the JPs at the blend interface in SEM (Figure 8.3c). After cryo-fracturing of the blend, the droplet surface is fully decorated with small spherical particles corresponding to points of adhesion between PPE and SAN mediated by JPs. The inset in Figure 8.3c shows a tendency for hexagonal close packing with interparticle distances of 30 nm attributed to the JP size in the collapsed state (Supporting Information Figure S8.3).³⁷

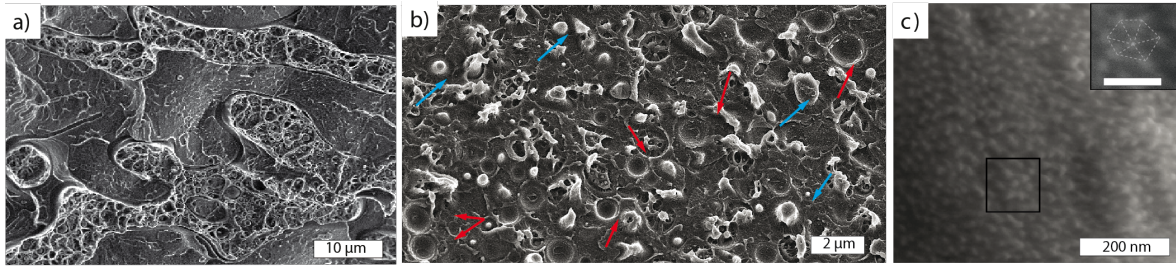


Figure 8.3. SEM overview of cryo-fractured blends. Irregular shaped neat (a) and compatibilized blend interface with small drop morphology (b). Red and blue arrows point to dents left behind by pulled-out droplets and remaining droplets, respectively. c) SEM magnification of a PPE droplet interface fully covered by JPs (raspberry-like structure). The inset is a further magnification of the region marked by the black square and illustrates the hexagonal packing tendency of the JPs at the interface (scale bar in inset is 100 nm).

Although very similar packing was observed previously with a PS/PMMA blend,²⁷ the PPE/SAN blend inherits a set of entirely different physical properties. The fact that JPs still selectively locate at the interface is remarkable and explained by the energy, ΔE_{desorb} , required to desorb the JPs from the blend interface. According to eq 8.1 (see Supporting Information),

$$\Delta E_{\text{desorb}} \approx 3\pi R_{\text{JP}}^2 \gamma_{\text{PPE/SAN}} \quad (8.1)$$

increases with the square of the particle radius, R_{JP} , and the interfacial tension between the blend components, $\gamma_{\text{PPE/SAN}}$.^{25,27} The interfacial tension between two polymers can be estimated from the Flory-Huggins polymer-polymer interaction parameter, χ , applying the relation $\gamma \propto \chi^{1/2}$ (for $\chi > 0$). In the studied system all parameters favor JP location at the interface,⁴⁰ *i.e.*, high incompatibility of the blend components, $\chi_{\text{PPE/SAN}} > 0.5$, and good compatibility between blend components and the respective JP corona blocks, $\chi_{\text{PPE/PS}} = -0.044$ and $\chi_{\text{SAN/PMMA}} = -0.008$ ³¹ (for 19 wt.-% AN in SAN). To further increase ΔE_{desorb} , we chose JPs to be considerably larger than the radius of gyration of the blended polymers ($R_{\text{g,polymer}} < 10$ nm *vs.* $R_{\text{JP,TEM}} = 19$ nm; $V_{\text{JP}}/V_{\text{polymer}} \geq 7$). Although an exact calculation of ΔE_{desorb} is elusive, the quantitative adsorption of JP to the blend interface suggests that ΔE_{desorb} must be sufficiently high to overcome the thermal energy impacting the particles at 260°C during extrusion.

Figure 8.4 summarizes the efficiency with which the JPs compatibilize this blend system. Here, we compare the morphology without additive, compatibilized with 10 wt.-% $\text{S}_{32}\text{B}_{36}\text{M}_{32}$ ⁹³ triblock terpolymer and with 10 wt.-% JPs made from $\text{S}_{40}\text{B}_{20}\text{M}_{40}$ ¹⁰⁸. All other processing parameters were kept constant to allow reliable comparison. The JPs considerably reduce the droplet size as compared to the neat blend and also significantly outperform the SBM terpolymer (Figure 8.4a).

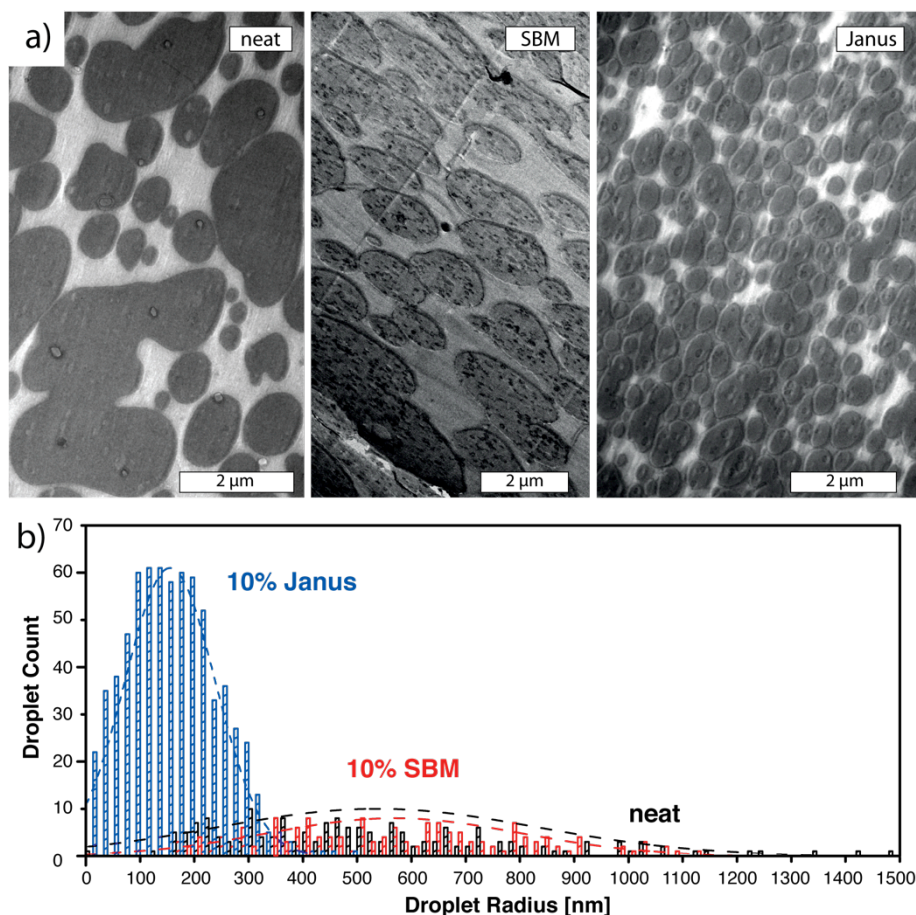


Figure 8.4. Impact of compatibilizer on blend morphology. a) TEM images of the neat blend (without additive, perpendicular to the extrusion direction), compatibilized with 10 wt.-% SBM terpolymer and with 10 wt.-% SBM JPs (slight contrast differences originate from varying film thicknesses). b) Histogram of 500 droplet radii for all blend systems.

For each system we analyzed the radii of 500 PPE droplets in TEM micrographs of ultrathin cuts. The radius of each droplet is calculated from the cross-sectional area (determined using ImageJ software), assuming spherical shape (Figure 8.4b). The average droplet radius, R_{PPE} , and standard deviation strongly decrease from $R_{PPE;SBM} = 670 \pm 230$ nm to $R_{PPE;JP} = 155 \pm 85$ nm underlining the superior stabilization capabilities of JPs as compared to the SBM terpolymer. Both compatibilizers are amphiphilic in nature and exhibit the same interactions with the blend polymers, which is why we consider the Pickering effect and the accompanying high interfacial activity of the JPs mostly responsible for the significant improvement. The droplet radius for the neat blend, $R_{PPE-neat} = 540 \pm 300$ nm, was determined for the sake of completeness, but does not adequately reflect the occasional multi micron-sized droplets. Without any additive the neat blend yields entirely unpredictable and irreproducible morphologies that may change at any given point even within the same extrusion experiment. In addition, reasonable droplet evaluation was complicated by excessive droplet coagulation, commonly observed for insufficient or missing surface stabilization (compare also Figure 8.2a and 8.3a). The difference between the SBM terpolymer and the neat blend is surprisingly small: both show broad distributions without significant shift of the average radius. We believe that a

considerable fraction of the SBM terpolymer is actually present as micelles or micelle clusters that manifest as black spots inside PPE droplets in Figure 8.4b (SBM terpolymer-stabilized blend). These micelles in the SBM compatibilized blends are the reason for reduced efficiency of SBM during compatibilization (probably due to lower activity compared to JPs). These trapped SBM polymer chains in PPE do not contribute to the stabilization of interfaces. Therefore, the difference between neat and SBM blends is only a more homogeneous morphology without smaller droplet sizes.

Figure 8.5 and Table 8.1 illustrate the morphological evolution of the blend as a function of the Janus particle content, *i.e.* at weight fractions of $f_{JP} = 0, 1, 2, 5$ and 10 wt.-%. The histograms in Figure 8.5a show a distinct trend for the evolution of droplet radius in dependence of JP content. The addition of only 0.5 (not shown) and 1 wt.-% JPs is not able to provide the necessary coverage to stabilize the interface and besides irregular droplet shape and large average droplet radii, droplets still partly coagulate into the co-continuous PPE/SAN morphology (Figure 8.2a). Figure 8.5b shows that by increasing the JP content, not only the PPE domain size gets smaller, but also the homogeneity of the blend morphologies improves.

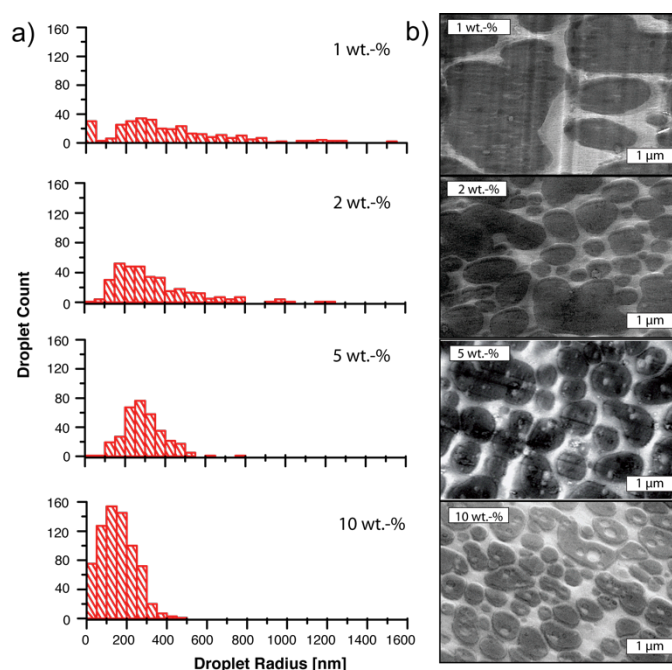


Figure 8.5. Dependence of droplet size on JP content. **a)** Histograms of 500 droplet radii and **(b)** TEM image series of the corresponding morphologies.

Table 8.1. Dependence of average droplet size and stabilization efficiency on the JP content.

f_P [wt%]	R_{PPE} [nm] ^{a)}	$s(R_{PPE})$ [nm] ^{b)}	$R_{PPE}\sqrt{f_{JP}}$ [nm]
0	540	300	---
1	440	350	440
2	340	190	480
5	270	100	600
10	150	80	474

^{a)}Average of 500 droplets; ^{b)}Standard deviation

Therefore, the occasional too large or too small particles visible in the blends with 1 and 2 wt.-% JPs are not visible in blends with 5 and 10 wt.-% JPs. The homogeneity of the blend morphology would result in homogenous macro mechanical properties and is of great industrial interest. As already discussed, at $f_{JP} = 10$ wt.-% (and at a lower extent in the blend with 5wt.-% JP) the morphology is reminiscent of a double emulsion with SAN inclusions inside PPE droplets. We hypothesize that the system creates additional interface due to excess stabilization capability of the large amount of JP added. The second interface also suggests that the droplet already reached its optimum curvature considering the given interfacial energies. Assuming a dense packing of the JPs on the interface area, A_{PPE} , simple geometric relations show that the radius of the PPE droplets should scale with the inverse square root of the JP content, f_{JP} :

$$\begin{aligned}
 A_{PPE} &= 4\pi R_{PPE}^2 \propto f_{JP}^{-1} \\
 \therefore R_{PPE} &\propto f_{JP}^{-1/2} \quad \text{or} \quad R_{PPE} \cdot f_{JP}^{1/2} = \text{const.}
 \end{aligned}
 \tag{8.2}$$

Table 8.1 shows that (with the exception of $f_{JP} = 5\%$) the product $R_{PPE} \cdot f_{JP}^{1/2}$ is indeed constant, confirming our assumption that the JPs densely pack at the interface, irrespective of the JP content.

The SAN inclusions are only visible in the blends with 5 wt.-% JP or more and are less frequent compared to the significant micelle and micellar cluster formation observed in the SBM compatibilized blend. To understand the formation of the SAN inclusions in the 5 and 10 wt.-% blends, shear rheology measurements were performed on the neat and the JP compatibilized blends (Figure 8.6).

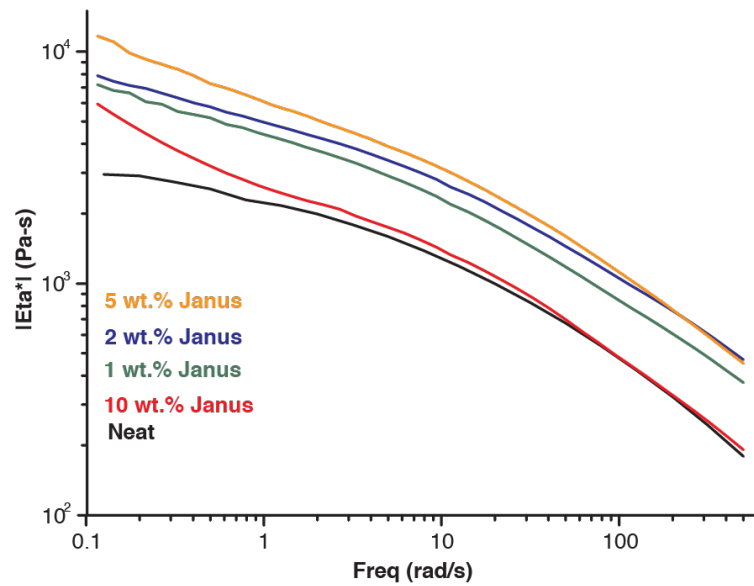


Figure 8.6. Absolute zero shear viscosities of the PPE/SAN blends compatibilized with 1, 2, 5, and 10 wt.-% JPs.

The increase in viscosity after the addition of JPs indicates effective compatibilization as a result of enhanced stress transfer between the phases in the blends with $f_{JP} = 1, 2,$ and 5 wt.-%. In case of the blend with 10 wt.-% JPs, the viscosity does not change significantly in the high frequency range as compared to the neat blend. However, at lower frequencies, an increase in the viscosity is visible, indicating some network-like structure formations. The 3D network forms through structure buildup of the PPE droplets in the matrix once their sizes drop below a critical value.⁴² We assume that at high JP concentration during extrusion, at first the particles cover all PPE droplet interface and minimize droplet size, while excess JPs are still present as clusters in one of the phases (for equal hemispheres cluster formation is equally probable in both phases). These excess JPs which form clusters (super-micelles) are freely dispersed in the blend, and since they are small spherical particles, they can facilitate low friction sliding between the PPE droplets and the overall viscosity of the blend is reduced to that of the neat blend. In case of the blend with 5 wt.-% JPs, we observe a similar phenomenon at smaller scale (Figure 8.5), also corroborating that the most economic amount of Janus particles to realize full compatibilization of the blend is indeed $f_{JP} = 2-5$ wt.-%. Another consequence of the excess amounts of JPs in the 5 and 10 wt.-% blend is that the system tries to build up extra surface to accommodate excess JPs and hence, SAN inclusions form within the PPE droplets. In addition, lower the viscosity of the blend at higher shear rates further facilitates the formation of such SAN inclusions.

Although the effect of processing parameters on the blend morphology has been comprehensively studied in the past, many works conclude that the mechanisms of morphology development and the final morphology would be similar for batch mixers and twin-screw extruders. However, one should always keep in mind that the shear field generated is unique to the equipment and may have different, even dramatic effects on the polymer blend. To study the effect of different shear rates, two processing machines, one with high and one with low shear forces have been chosen to compare the effect of processing condi-

tions on the blend material. At first, all other processing conditions including residence time, temperature profile, and screw speed were kept constant and only the effect of different shear fields was investigated. We blended PPE/SAN with JP on a lab-scale mini-compounder which produces low shear forces and obtained a co-continuous morphology compared to the industry-scale extruder which has much higher shear forces, demonstrating the profound effect of forces accompanied to the used machinery (Figure 8.7). The measured torque values during the process were 5 and 45 Nm for mini-compounder and extruder, respectively, which confirm low and high shear forces during the process. Since it is here proven that low shear forces in the mini compounder cannot break up the high viscous PPE phase into droplets, another experiment was performed with higher mixing (residence) time. From the results (Supporting Information Figure S8.7), one can conclude that the effect of shear forces produced by the machine is much higher than that of processing conditions (such as residence time), since the blend with double residence time in the compounder still shows co-continuous morphology. This is because mechanisms leading to PPE droplet break up need high shear forces and, within the steady state regime, are independent of residence time. This knowledge is of particular interest when designing and testing lab-scale prototype materials or working with special blend systems (*i.e.* with high viscosity ratios). In case of some polymer blends with special viscosity ratios, extensional flows are needed to provide the desired morphologies and therefore, other compounding devices such as co-kneader twin-screw extruders would be needed. To predict morphologies in blends, the underlying mechanisms need to be understood more clearly, which is why we are convinced that large-scale studies establish an invaluable basis for the application-oriented development of designer materials (such as JPs) and likewise for the advancement of existing theoretical models.

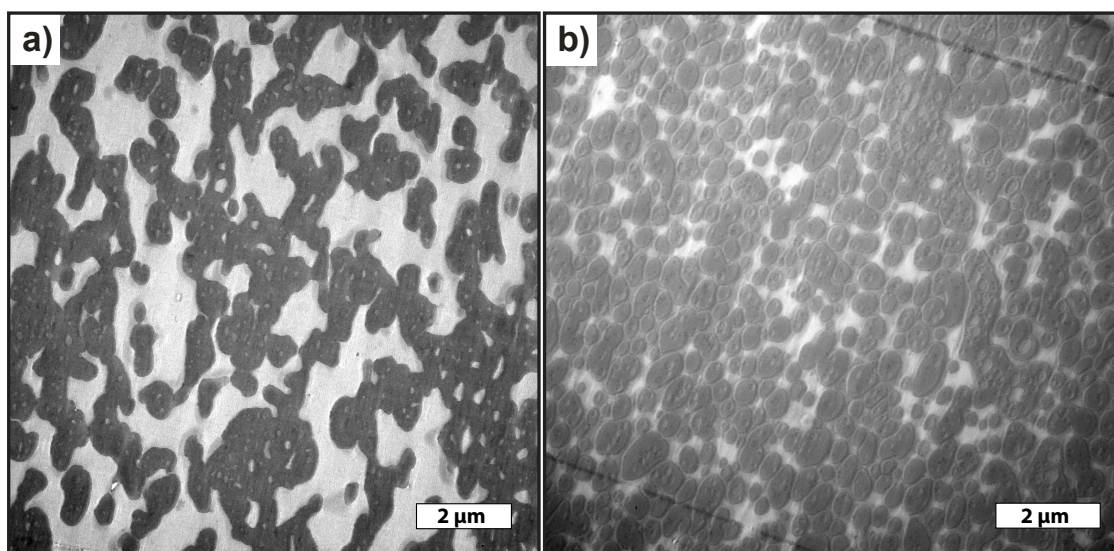


Figure 8.7. Morphologies obtained for lab- and large-scale compounding of PPE/SAN blends compatibilized with 10 wt.-% JPs. a) Co-continuous morphology produced with mini-compounder under low shear conditions and **(b)** nanosized drop morphology of the same blend composition produced with industry-scale extruder with high shear forces.

Conclusions

We demonstrated the efficient compatibilization of PPE/SAN blends using Janus nanoparticles in industry-scale blending equipment. The combination of strong interfacial affinity and the Pickering effect promote quantitative adsorption of JPs to the blend interface irrespective of the harsh processing conditions. The Pickering effect significantly contributes to particle adsorption by overcoming the high thermal energy of the particles in the polymer melt. The optimum fraction of JPs necessary for sufficient droplet stabilization without formation of double emulsion morphology was determined to be in the range of 2–5 wt.-%. A more economic use of the Janus nanoparticles may be realized by admixing specific amounts of SBM triblock terpolymer. Preliminary results show synergetic stabilization capabilities of SBM JPs/triblock terpolymer mixtures. Entirely different morphologies were obtained for lab-scale and industry-scale processing underlining the importance of large-scale studies on systems involving specialized materials. Ongoing work comprises comprehensive studies on mechanical properties, the use of Janus nanoparticles with unequal-sized volume ratios of the corona hemispheres (Janus balance), and synergetic effects of JPs in combination with other conventional compatibilizers. Especially JPs with Janus balance in favour of the stabilizing patch could result in even smaller droplet radii than the ones reported.

Experimental Section

Materials

All solvents used were of analytical grade. Dialysis tubes of regenerated cellulose with a MWCO of 12,000 – 14,000 g/mol were purchased from Roth, equilibrated in deionized water for 30 min and washed with excess dioxane before use. The photo-cross-linker, 2,4,6-trimethylbenzoyldiphenyl-phosphineoxide ($I_{\max} \approx 360$ nm) was obtained from BASF AG, Ludwigshafen, Germany (Lucirin TPO[®]). Commercial-grade poly(2,6-dimethyl-1,4-phenylene ether) (PPE; PX100F) was obtained as powder from Mitsubishi Engineering Plastics Europe, Düsseldorf, Germany. The weight average molecular weight $M_w = 12.9$ kg/mol and the polydispersity index $PDI = 1.63$ of PPE was determined by size exclusion chromatography (SEC) with THF as eluent at a flow rate of 1.0 ml/min (columns at 40 °C) using an UV detector and polystyrene standards for calibration. The commercially available poly(styrene-*co*-acrylonitrile) (SAN) with a acrylonitrile content of 19 wt.% was purchased as pellets, from BASF AG, Ludwigshafen, Germany (SAN VLL 19100). The $M_w = 97.1$ kg/mol and $PDI = 2.13$ of SAN was determined the same way as mentioned above. The low acrylonitrile content of the polymer ensures homogenous miscibility of the SAN with the PMMA blocks of the compatibilizers at the relevant processing conditions. Irganox 1010 and Irgafos 168 (BASF, Germany) were used as stabilizers to prevent polymer heat degradation during the process.

Synthesis of SBM Janus Nanoparticles. The SBM triblock terpolymers were synthesized *via* sequential living anionic polymerization of styrene, butadiene and methyl methacrylate, as reported elsewhere in detail.³² The Janus nanoparticles were prepared according to a recipe modified from the earlier report to satisfy the requirements of industry blending equipment.³⁷ In a typical experiment, 100 g of SBM triblock terpolymer was dissolved in 1 L THF to yield a concentration of $c = 100$ g/L. After complete dissolution, the concentrated polymer solution was dialyzed against 10 L acetone/isopropanol (60:40 v/v) (selective solvent for PMMA). The solvent mixture was changed twice to generate JPs clusters (spherical multicompartment micelles that consist of JPs). After dialysis, the phase-separated state of the micelles was permanently fixed by cross-linking of the PB block. Therefore, 0.25 equiv (compared to the PB double bonds) of photo-cross-linker, 2,4,6-trimethylbenzoyldiphenyl-phosphineoxide (Lucirin TPO[®]; $\lambda_{max} \approx 360$ nm) was dissolved in 1 L acetone/isopropanol (60:40 v/v) and added to the dispersion of the JPs clusters to dilute the highly viscous dispersion from 100 g/L to 50 g/L. The sample was then irradiated for 24 h using a UV-lamp with a cut-off filter of $\lambda = 300$ nm. Continuous stirring ensured homogeneous cross-linking of the opaque solution. The Janus micelles were recovered by precipitation into 20 L methanol.

Pre-blending of Dry Polymer Powders. Before melt blending of the homopolymers, the PPE powder and the SAN pellets were dried at 80 °C for at least 12 h under vacuum. For SBM triblock terpolymers and JPs a lower temperature of 40 °C was chosen due to sensitivity of the PB block to degradation when longer exposed to oxygen atmosphere at elevated temperatures. In addition, the SBM and Janus compatibilizers were cryo-grinded into a powder. Prior to melt blending, PPE and SAN were dry blended with SBM or JPs using powder mixers. The PPE/SAN ratio was kept constant at 60:40; however, for each blend the amount of compatibilizer (SBM or Janus particles) was varied to 0.5, 1.0, 2.0, 5.0 and 10 wt.-%. To prevent thermal degradation, 0.1 wt.-% of stabilizer (mixture of Irganox 1010 and Irgafos 168) was added to the compounds.

Instrumentation

Lab-scale melt processing. Melt blending of the compounds was performed on a microcompounder (Xplore DSM) with co-rotating conical twin-screw setup and volume capacity of 15 ml. This process is comparable to a batch mixing process. The temperature inside the microcompounder was kept constant at 260 °C, the screw speed at 85 rpm and the mixing time was 5 minutes (similar to the residence time in the extruder). The melt strands were cooled and cut into pellets.

Industry-scale melt processing. A continuous scale, co-rotating twin-screw extruder (Brabender DSE 20/40) with $L/D=30$ was used to compound the polymer blends. The maximum barrel and nozzle temperature were fixed at 250 °C and 245 °C, respectively, and the screw speed was kept constant at 85 rpm with a constant throughput of 1 kg/h. Therefore, the mean residence time of the blends in the extruder was around 5 min.

Transmission electron microscopy (TEM). Ultrathin sections (60 nm) were cut of the blended materials at room temperature using an ultra-microtome (Reichert-Jung Ultracut E microtome) equipped with a diamond knife. Micellar samples were prepared by placing one drop of the polymer solution (0.01 g/L) onto carbon-coated copper grids. Excess solvent was instantly absorbed by a filter paper. To ensure sufficient contrast between the phases, the particles and ultrathin sections were stained with OsO_4 for 30 s in vacuum in case of SBM compatibilized blends and 3 h at ambient conditions in case of Janus particle compatibilized blends. Due to this staining method, SAN appears as the brighter and PPE as the darker phase, while the PB block (or core) of SBM (JPs) appears black (selectively stained with OsO_4). Bright field transmission electron microscopy at an acceleration voltage of 80 kV was carried out using a Zeiss CEM 902 electron microscope. Number average diameter of the PPE droplets and their distribution were obtained by measuring 500 droplets in TEM micrographs using ImageJ software. First, the area of each PPE droplet was measured using the software; then, assuming that droplets are fully sphere particles and the TEM cuts have gone through middle of each droplet, the radius corresponding to the area was back calculated. Of course these assumptions cannot be 100% fulfilled, hence resulting in the relatively large standard deviations in Table 8.1.

Field emission scanning electron microscopy (FESEM) was conducted on a Leo 1530 Gemini from Zeiss using a secondary electron detector and an acceleration voltage of 15 kV. For a better contrast the samples were sputtered with a 1.3 nm thick Platinum layer.

Dynamic light scattering (DLS) was performed at a scattering angle of 90° on an ALV DLS/SLS-SP 5022F equipment consisting of an ALV-SP 125 laser goniometer, an ALV 5000/E correlator, and a He–Ne laser operating at a wavelength of $\lambda = 632.8$ nm. The CONTIN algorithm was applied to analyze the obtained correlation functions. Apparent hydrodynamic radii were calculated according to the Stokes–Einstein equation. All CONTIN plots are intensity-weighted. Prior to the light scattering measurements, all sample solutions were filtered twice through a $5 \mu\text{m}$ PTFE-filter.

Rheological investigations. Rheological properties were investigated by a stress controlled dynamic-mechanical rheometer RDA III from Rheometric Scientific with plate-plate geometry under nitrogen atmosphere. The pressed samples had a diameter of 25 mm and thickness of 1.5 mm and were analyzed isothermally at 260°C . The storage modulus, the loss modulus, and the complex viscosity of blend systems were measured as a function of frequency within the range of 0.01–500 rad/s at 260°C . Prior to each measurement, the linear viscoelastic region was determined by carrying out an amplitude sweep at a deformation range of 0.1–100 %, at frequencies of 1 and 50 rad/s. Subsequently, the deformation applied for the frequency sweeps was set to be within the linear viscoelastic region. Each measurement was repeated at least three times to minimize the experimental errors.

ASSOCIATED CONTENT

Conflict of Interest

The authors declare no competing financial interest.

Supporting Information

Additional experimental data; SEC and TEM characterization of SBM; additional TEM and SEM images of blends; supporting calculations and Figures S8.1-S8.7. This material is available free of charge *via* the Internet at <http://pubs.acs.org>.

AUTHOR INFORMATION

Corresponding Authors

altstaedt@uni-bayreuth.de ; axel.mueller@uni-mainz.de;

Notes

RB and TIL contributed equally to this work.

Acknowledgments

This work was supported by the Deutsche Forschungsgemeinschaft within grants AL 474/21-1 and Mu 896/39-1. The authors acknowledge BASF for donating SAN and Mitsubishi for PPE polymer.

REFERENCES

1. Leibler, L. Nanostructured Plastics: Joys of Self-Assembling. *Prog. Polym. Sci.* **2005**, *30*, 898–914.
2. Paul, D. R.; Bucknall, C. B. *Polymer Blends*; Wiley: New York, 2000.
3. Utracki, L. A. *Commercial Polymer Blends*; 1st ed.; Chapman and Hall: London, 1998.
4. Pernot, H.; Baumert, M.; Court, F.; Leibler, L. Design and Properties of Co-Continuous Nanostructured Polymers by Reactive Blending. *Nat. Mater.* **2002**, *1*, 54–58.
5. Kietzke, T.; Neher, D.; Landfester, K.; Montenegro, R.; Güntner, R.; Scherf, U. Novel Approaches to Polymer Blends Based on Polymer Nanoparticles. *Nat. Mater.* **2003**, *2*, 408–412.
6. Macosko, C. W.; Gue, P.; Khandpur, A. K.; Nakayama, A.; Marechal, P.; Inoue, T. Compatibilizers for Melt Blending: Premade Block Copolymers. *Macromolecules* **1996**, *29*, 5590–5598.
7. Cerclé, C.; Favis, B. D. Generalizing Interfacial Modification in Polymer Blends. *Polymer* **2012**, *53*, 4338–4343.
8. Cai, X.; Li, B.; Pan, Y.; Wu, G. Morphology Evolution of Immiscible Polymer Blends as Directed by Nanoparticle Self-Agglomeration. *Polymer* **2012**, *53*, 259–266.
9. Kim, B. J.; Bang, J.; Hawker, C. J.; Chiu, J. J.; Pine, D. J.; Jang, S. G.; Yang, S.-M.; Kramer, E. J. Creating Surfactant Nanoparticles for Block Copolymer Composites through Surface Chemistry. *Langmuir* **2007**, *23*, 12693–12703.
10. Jang, S. G.; Kramer, E. J.; Hawker, C. J. Controlled Supramolecular Assembly of Micelle-like Gold Nanoparticles in PS-*b*-P2VP Diblock Copolymers *via* Hydrogen Bonding. *J. Am. Chem. Soc.* **2011**, *133*, 16986–16996.
11. Zhao, Y.; Thorkelsson, K.; Mastroianni, A. J.; Schilling, T.; Luther, J. M.; Rancatore, B. J.; Matsunaga, K.; Jinnai, H.; Wu, Y.; Poulsen, D.; *et al.* Small-Molecule-Directed Nanoparticle Assembly towards Stimuli-Responsive Nanocomposites. *Nat. Mater.* **2009**, *8*, 979–985.
12. Cao, Y.; Zhang, J.; Feng, J.; Wu, P. Compatibilization of Immiscible Polymer Blends Using Graphene Oxide Sheets. *ACS Nano* **2011**, *5*, 5920–5927.
13. Du, B.; Handge, U. a.; Majeed, S.; Abetz, V. Localization of Functionalized MWCNT in SAN/PPE Blends and Their Influence on Rheological Properties. *Polymer* **2012**, *53*, 5491–5501.
14. Balazs, A. C.; Emrick, T.; Russell, T. P. Nanoparticle Polymer Composites: Where Two Small Worlds Meet. *Science* **2006**, *314*, 1107–1110.
15. Kao, J.; Thorkelsson, K.; Bai, P.; Rancatore, B. J.; Xu, T. Toward Functional Nanocomposites: Taking the Best of Nanoparticles, Polymers, and Small Molecules. *Chem. Soc. Rev.* **2013**, *42*, 2654–2678.
16. Duin, V. A. N.; Jerome, R. Strategies for Compatibilization Polymer Blends. *Prog. Polym. Sci.* **1998**, *23*, 707–757.

17. Li, G.; Shrotriya, V.; Huang, J.; Yao, Y.; Moriarty, T.; Emery, K.; Yang, Y. High-Efficiency Solution Processable Polymer Photovoltaic Cells by Self-Organization of Polymer Blends. *Nat. Mater.* **2005**, *4*, 864–868.
18. Walther, A.; Hoffmann, M.; Müller, A. H. E. Emulsion Polymerization Using Janus Particles as Stabilizers. *Angew. Chemie Int. Ed.* **2008**, *47*, 711–714.
19. Gröschel, A. H.; Löbbling, T. I.; Petrov, P. D.; Müllner, M.; Kuttner, C.; Wieberger, F.; Müller, A. H. E. Janus Micelles as Effective Supracolloidal Dispersants for Carbon Nanotubes. *Angew. Chemie Int. Ed.* **2013**, *52*, 3602–3606.
20. Kim, S.-H.; Lee, S. Y.; Yang, S.-M. Janus Microspheres for a Highly Flexible and Impregnable Water-Repelling Interface. *Angew. Chemie Int. Ed.* **2010**, *49*, 2535–2538.
21. Hirsemann, D.; Shylesh, S.; Souza, R. a De; Diar-Bakerly, B.; Biersack, B.; Mueller, D. N.; Martin, M.; Schobert, R.; Breu, J. Large-Scale, Low-Cost Fabrication of Janus-Type Emulsifiers by Selective Decoration of Natural Kaolinite Platelets. *Angew. Chemie Int. Ed.* **2012**, *51*, 1348–1352.
22. Walther, A.; Müller, A. H. E. Janus Particles: Synthesis, Self-Assembly, Physical Properties, and Applications. *Chem. Rev.* **2013**, *113*, 5194–5261.
23. Wurm, F.; Kilbinger, A. F. M. Polymeric Janus Particles. *Angew. Chemie Int. Ed.* **2009**, *48*, 8412–8421.
24. Jiang, S.; Chen, Q.; Tripathy, M.; Luijten, E.; Schweizer, K. S.; Granick, S. Janus Particle Synthesis and Assembly. *Adv. Mater.* **2010**, *22*, 1060–1071.
25. Binks, B. P.; Fletcher, P. D. I. Particles Adsorbed at the Oil - Water Interface: A Theoretical Comparison between Spheres of Uniform Wettability and “ Janus ” Particles. *Langmuir* **2001**, 4708–4710.
26. Kim, J.; Matsen, M. Positioning Janus Nanoparticles in Block Copolymer Scaffolds. *Phys. Rev. Lett.* **2009**, *102*, 078303.
27. Walther, A.; Matussek, K.; Müller, A. H. E. Engineering Nanostructured Polymer Blends with Controlled Nanoparticle Location Using Janus Particles. *ACS Nano* **2008**, *2*, 1167–1178.
28. Xu, K.; Guo, R.; Dong, B.; Yan, L.-T. Directed Self-Assembly of Janus Nanorods in Binary Polymer Mixture: Towards Precise Control of Nanorod Orientation Relative to Interface. *Soft Matter* **2012**, *8*, 9581–9588.
29. Yan, L.-T.; Popp, N.; Ghosh, S.-K.; Böker, A. Self-Assembly of Janus Nanoparticles in Diblock Copolymers. *ACS Nano* **2010**, *4*, 913–920.
30. Huang, M.; Li, Z.; Guo, H. The Effect of Janus Nanospheres on the Phase Separation of Immiscible Polymer Blends *via* Dissipative Particle Dynamics Simulations. *Soft Matter* **2012**, *8*, 6834–6845.
31. Merfeld, G. D.; Karim, A.; Majumdar, B.; Satija, S. K.; Paul, D. R. Interfacial Thickness in Bilayers of Poly(phenylene oxide) and Styrenic Copolymers. *J. of Polym. Sci.* **1998**, *36* 3115-3125.
32. Ruckdäschel, H.; Sandler, J. K. W.; Altstädt, V.; Rettig, C.; Schmalz, H.; Abetz, V.; Müller, A. H. E. Compatibilisation of PPE/SAN Blends by Triblock Terpolymers: Correlation between Block Terpolymer Composition, Morphology and Properties. *Polymer* **2006**, *47*, 2772–2790.

33. Ruckdäschel, H.; Sandler, J. K. W.; Altstädt, V.; Schmalz, H.; Abetz, V.; Müller, A. H. E. Toughening of Immiscible PPE/SAN Blends by Triblock Terpolymers. *Polymer* **2007**, *48*, 2700–2719.
34. Ruckdäschel, H.; Gutmann, P.; Altstädt, V.; Schmalz, H.; Müller, A. H. E. Foaming of Microstructured and Nanostructured Polymer Blends. In *Adv. Polym. Sci.*; Springer-Verlag: Berlin Heidelberg, 2010.
35. Kirschnick, T.; Gottschalk, A.; Ott, H.; Abetz, V.; Puskas, J.; Altstädt, V. Melt Processed Blends of Poly(styrene-co-Acrylonitrile) and Poly(phenylene Ether) Compatibilized with Polystyrene-*b*-Polybutadiene-*b*-Poly(methyl Methacrylate) Triblock Terpolymers. *Polymer* **2004**, *45*, 5653–5660.
36. Loget, G.; Roche, J.; Kuhn, A. True Bulk Synthesis of Janus Objects by Bipolar Electrochemistry. *Adv. Mater.* **2012**, *24*, 5111–5116.
37. Gröschel, A. H.; Walther, A.; Löbbling, T. I.; Schmelz, J.; Hanisch, A.; Schmalz, H.; Müller, A. H. E. Facile, Solution-Based Synthesis of Soft, Nanoscale Janus Particles with Tunable Janus Balance. *J. Am. Chem. Soc.* **2012**, *134*, 13850–13860.
38. Dobkowski, Z. Determination of Critical Molecular Weight for Entangled Macromolecules Using the Tensile Strength Data. *Rheol. Acta* **1995**, *34*, 578–585.
39. Wool, R. P. *Polymer Interfaces*; 1st ed.; Carl Hanser: Munich, 1995.
40. Stadler, R.; Auschra, C.; Beckmann, J.; Krappe, U.; Voigt-Martin, I.; Leibler, L. Morphology and Thermodynamics of Symmetric Poly (A-block-B-block-C) Triblock Copolymers. *Macromolecules* **1995**, *28*, 3080–3091.
41. Macosko, C. W. Morphology Development and Control in Immiscible Polymer Blends. *Macromol. Symp.* **2000**, *149*, 171–184.
42. Münstedt, H. Rheology of Rubber-Modified Polymer Melts. *Polym. Eng. Sci.* **1981**, *21*, 259–270.

Supporting Information

to

The Impact of Janus Nanoparticles on the Compatibilization of Immiscible Polymer Blends under Technologically Relevant Conditions

by Ronak Bahrami, Tina I. Löblich, André H. Gröschel, Holger Schmalz,

Axel H. E. Müller* and Volker Altstadt*

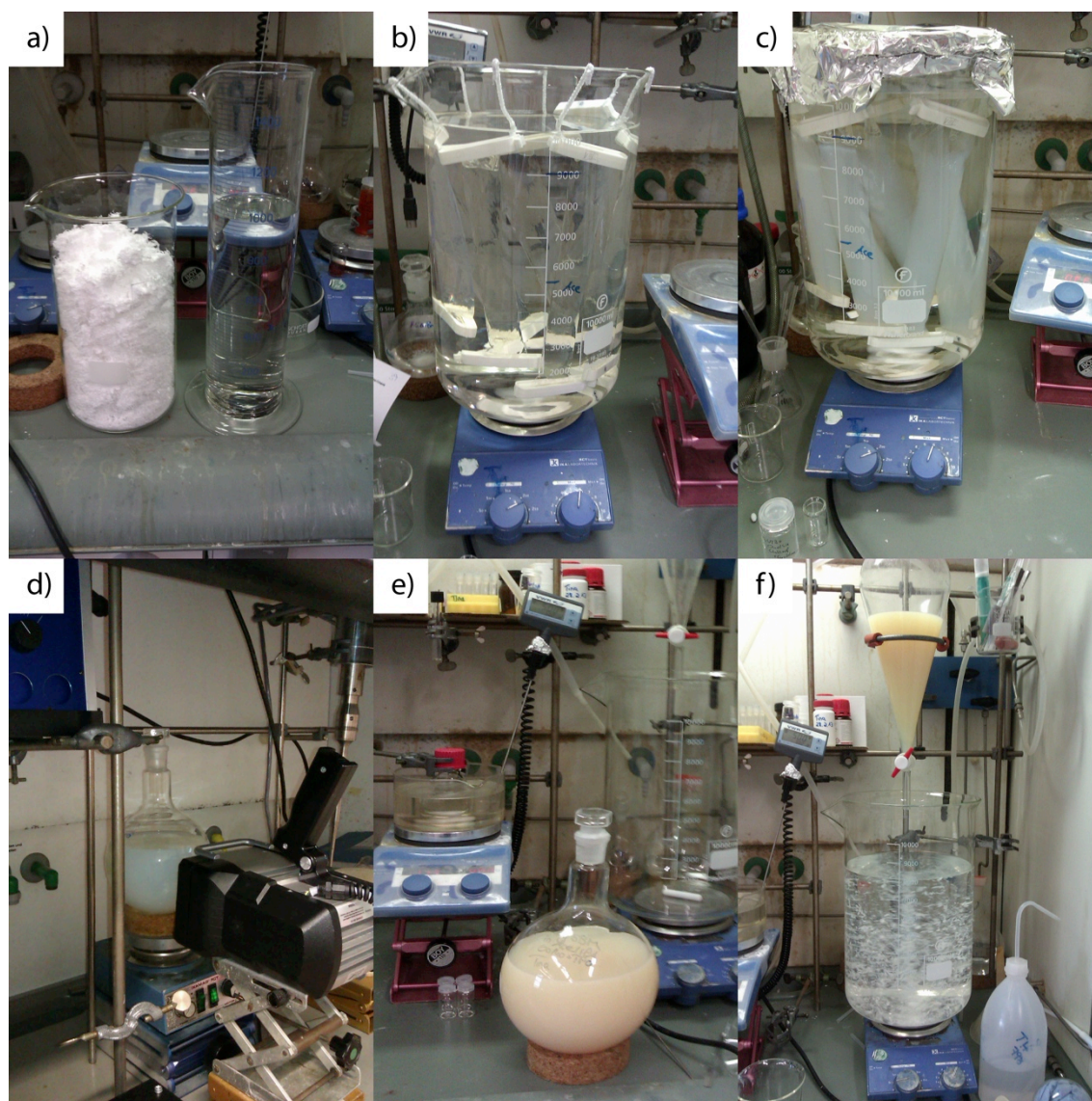


Figure S8.1: Illustration of the preparative steps synthesizing 100 g SBM JPs. **a)** Dissolution of 100 g $S_{40}B_{20}M_{40}^{108}$ triblock terpolymer (108 kg/mol) in 1 L THF yields a polymer concentration of 10 wt.-%. **b)** Dialysis into acetone/isopropanol (60/40 v/v) as selective solvent for PMMA forms patchy multicompart ment micelles (JP clusters). **c)** Turbid colloidal dispersion of JP cluster of defined size. **d)** Addition of 0.25 equiv. Lucirin TPO™ photo-cross-linker ($\lambda_{\max} = 360$ nm) and UV irradiation (cut-off $\lambda = 300$ nm) for 24 h. **e)** Dispersion after cross-linking. **f)** Purification of JPs *via* precipitation into excess methanol.

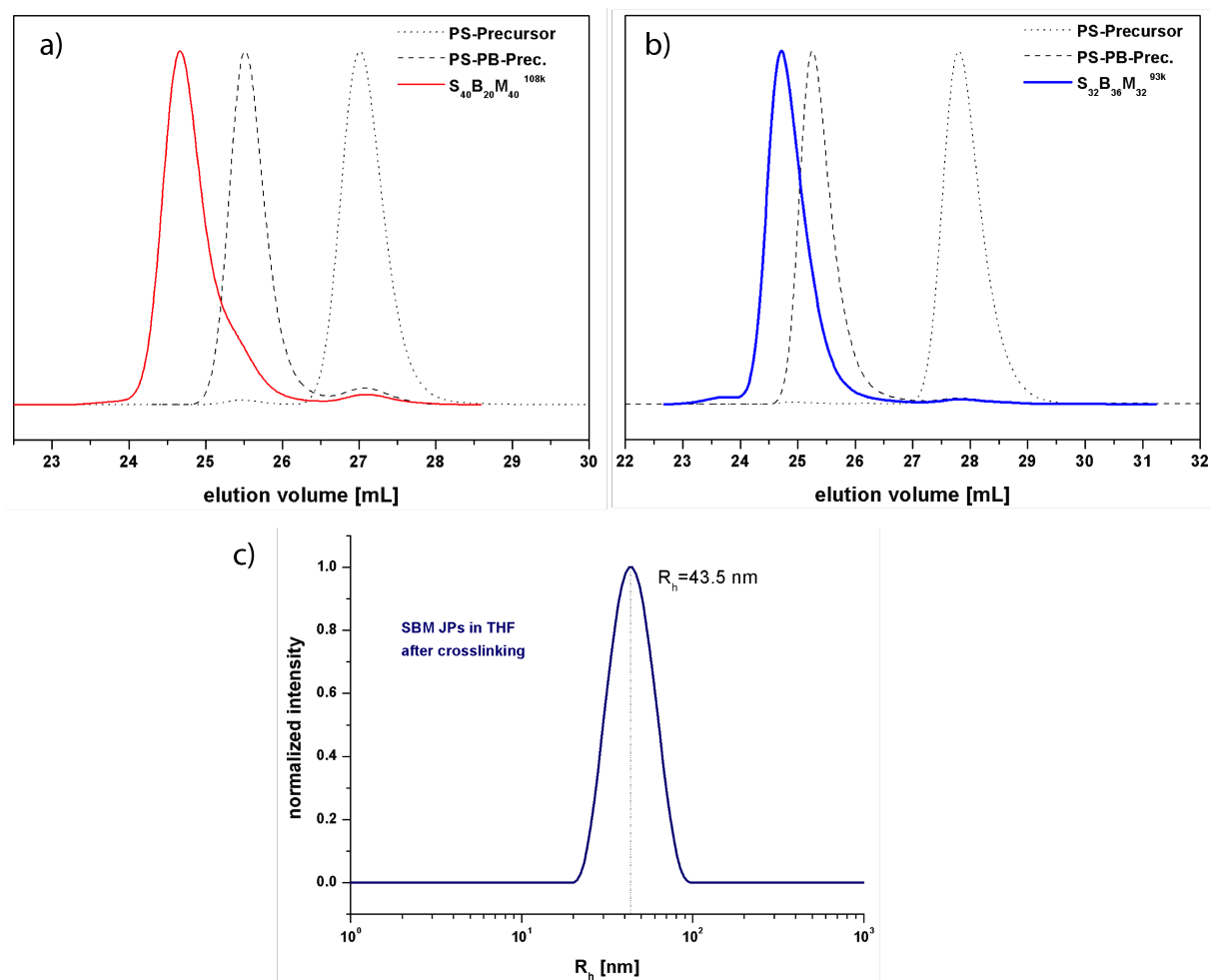


Figure S8.2: Characterization of $S_{32}B_{36}M_{32}^{93}$ and $S_{40}B_{20}M_{40}^{108}$ triblock terpolymers and JPs derived from $S_{40}B_{20}M_{40}^{108}$. a) THF-SEC traces of the SBM triblock terpolymer that is transformed to JPs and b) of the reference SBM triblock terpolymer. c) DLS of JPs in THF after cross-linking and purification ($c = 1$ g/L).

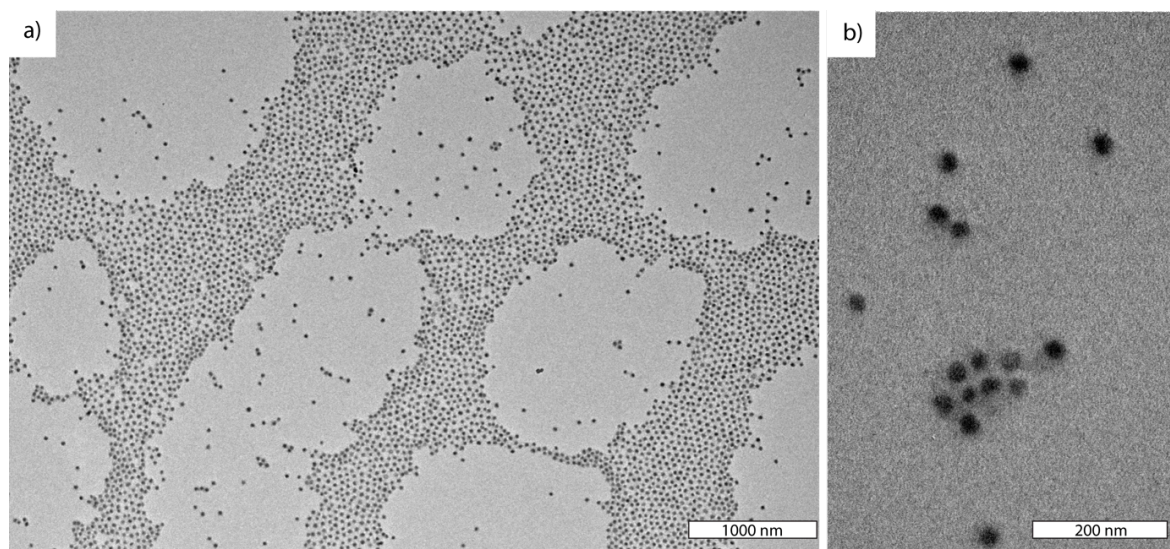


Figure S8.3: TEM of $S_{40}B_{20}M_{40}^{108}$ JPs. **a)** Overview of concentrated areas with hexagonal packing indicating low particle size dispersity. **b)** Magnification of JPs with radius of $R_{TEM} = 19$ nm. Samples were drop-cast from THF solution onto carbon coated copper grids and stained with OsO_4 .

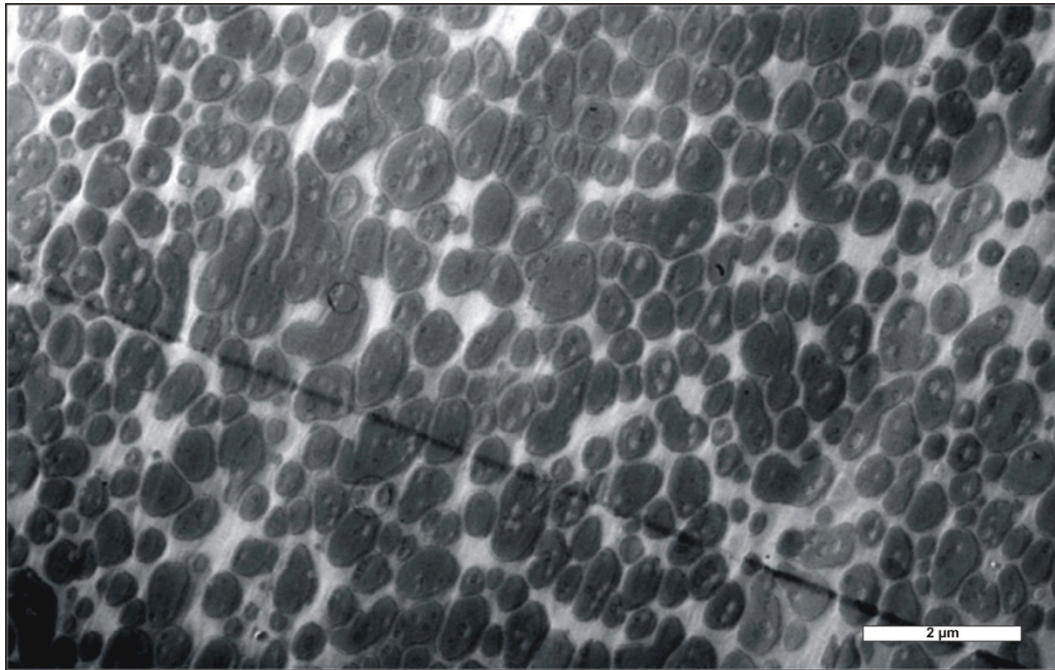


Figure S8.4: TEM overview of PPE/SAN blend (60:40 w/w) compatibilized with 10 wt.-% JPs showing double emulsion morphology.

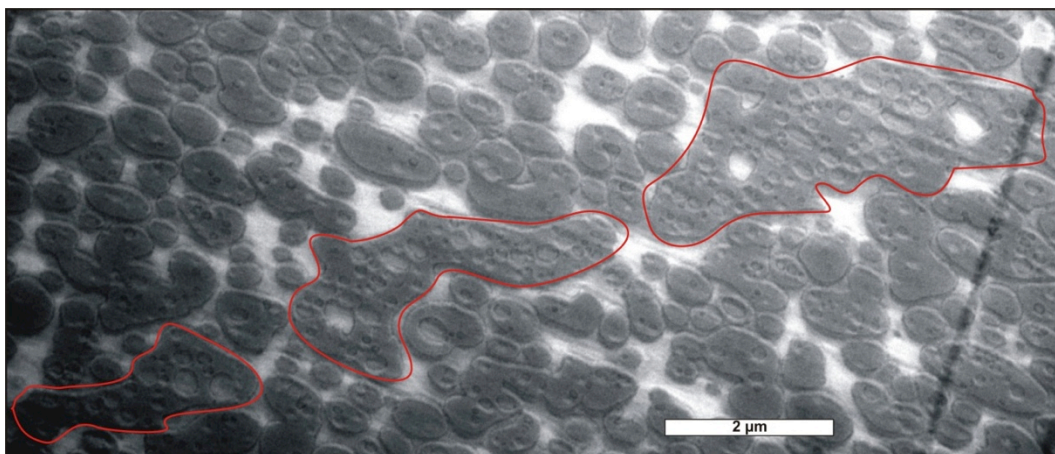


Figure S8.5: Evidence for onset of phase inversion to SAN droplets in a continuous PPE matrix (PPE/SAN (60:40 w/w), 10 wt.-% JPs).

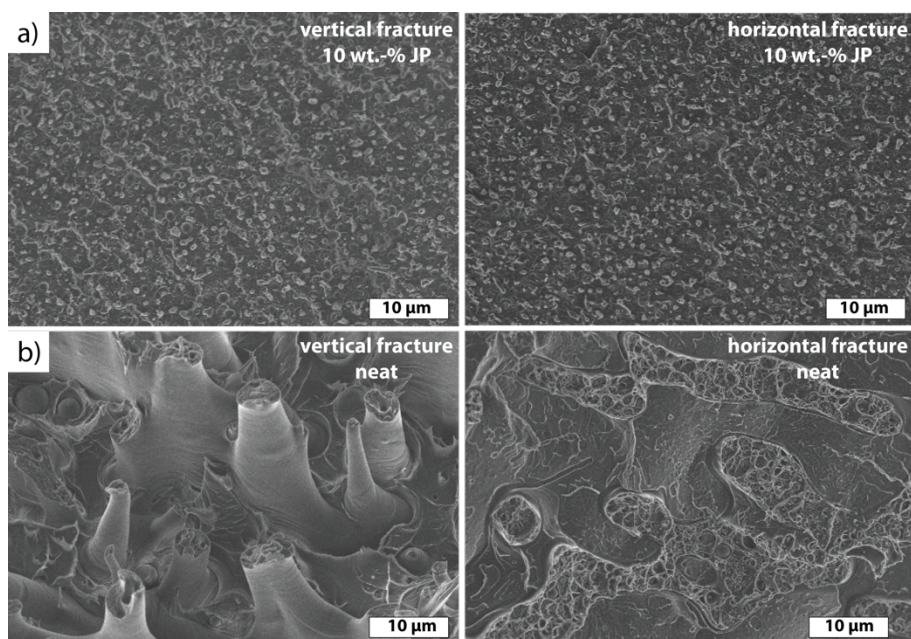


Figure S8.6: SEM images of horizontal and vertical fractures (with respect to extrusion) of (a) PPE/SAN (60:40 w/w) blends with 10 wt.-% JPs added and (b) without any additive. The blend containing JPs shows the same small drop morphology in both cross-sections (directions) with sub-micron features, whereas the neat blend shows much larger and highly anisotropic domains.

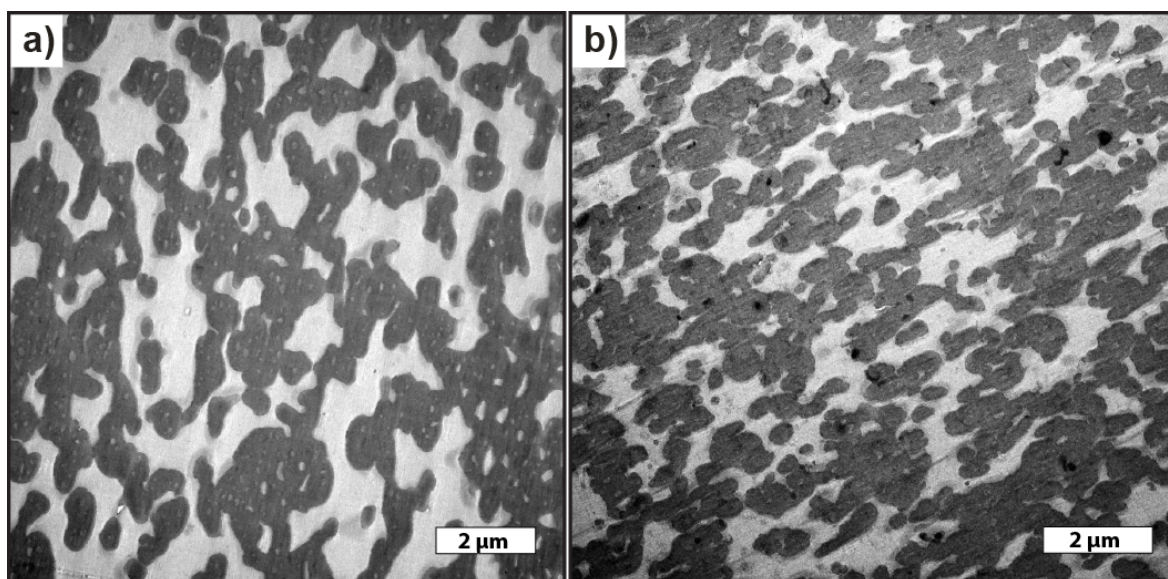


Figure S8.7: TEM images of PPE/SAN (60/40 w/w), 10 wt.-% JPs produced in lab scale compounder with (a) 5 minutes mixing (residence) time (b) 10 minutes mixing (residence) time.

Supporting Calculations:

Interfacial energies for quantitative adsorption

Desorption energy:

$$E(\beta) = 2\pi R_{JP}^2 \left[\begin{aligned} &\gamma_{(S_{JP}/PPE)}(1 + \cos \alpha) + \gamma_{(MMA_{JP}/PPE)}(\cos \beta - \cos \alpha) \\ &+ \gamma_{(MMA_{JP}/SAN)}(1 - \cos \beta) - \frac{1}{2}\gamma_{(PPE/SAN)}(\sin^2 \beta) \end{aligned} \right] \quad (8.1.1)$$

Considering negligible $g_{(S/PPE)}$ and $g_{(MMA/SAN)}$ ($c_{(S/PPE)} < 0$ and $c_{(MMA/SAN)} < 0$), the equation for symmetric particles $a = 90^\circ$ (a = relative areas of the PS/PMMA surface regions) and at (quasi-) planar interfaces $b = 90^\circ$ (b = immersion depth of the particle in the PPE/SAN interface) simplifies to:

$$E(\beta) = -\pi R_{JP}^2 \gamma_{(PPE/SAN)} \quad (8.1.2)$$

The energy of the particle in the SAN phase:

$$E(SAN) = 2\pi R_{JP}^2 \left[\begin{aligned} &\gamma_{(S_{JP}/PPE)} + \gamma_{(MMA_{JP}/PPE)}(\cos \beta) \\ &+ \gamma_{(MMA_{JP}/SAN)}(1 - \cos \beta) - \frac{1}{2}\gamma_{(PPE/SAN)}(\sin^2 \beta) \end{aligned} \right] \quad (8.1.3)$$

The energy required to desorb the particle from that interface and push it into SAN reads:

$$\Delta E_{\text{desorb.}} = E(SAN) - E(\beta) = 2\pi R_{JP}^2 \gamma_{(MMA_{JP}/PPE)} + \pi R_{JP}^2 \gamma_{(PPE/SAN)} \quad (8.1.4)$$

We can assume $\gamma_{(MMA/PPE)} \approx \gamma_{(SAN/PPE)}$ and therefore:

$$\Delta E_{\text{desorb.}} \approx 3\pi R_{JP}^2 \gamma_{(PPE/SAN)} \quad (8.1.5)$$

List of Publications:

17. **Löbbling, T.I.**, Ikkala, O., Gröschel, A.H., Müller, A.H.E.: „Control of Multicompartment Nanostructures of Linear Triblock Terpolymers by Post-Polymerization Processes”, *submitted to ACS Macro Letters*
16. Hiekkataipale, P., **Löbbling, T.I.**, Poutanen, M., Priimägi, A., Ikkala, O., Gröschel, A.H.: “Controlling the shape of Janus nanostructures through supramolecular modification of ABC terpolymer bulk morphologies“, *Polymer*, 2016, *accepted*
15. **Löbbling, T.I.**, Borisov, O., Haataja, J.S., Ikkala, O., Gröschel, A.H., Müller, A.H.E.: “Rational Design of ABC Triblock Terpolymer Solution Nanostructures“, *Nature Communications*, 2016, *accepted*
14. Köhn-Serrano, M.S., König, T.A.F., Haataja, J.S., **Löbbling, T.I.**, Schmalz, H., Agarwal, S., Fery, A., Greiner, A.: “Self-Organization of Gold Nanoparticle Assemblies with 3D Spatial Order and Their External Stimuli Responsiveness“, *Macromolecular Rapid Communications*, 2015, 37, 215-220
13. Bahrami, R., **Löbbling, T.I.**, Schmalz, H., Müller, A.H.E., Altstädt, V.: „Micromechanics of “raspberry” morphology in PPE/SAN polymer blends compatibilized with linear ABC triblock terpolymers“, *Polymer*, 2015, 80, 52-63
12. Bärwinkel, S., Bahrami, R., **Löbbling, T.I.**, Schmalz, H., Haataja, J.S., Müller, A.H.E., Altstädt, V.: „Polymer Foams Made of Immiscible Polymer Blends Compatibilized by Janus Particles – Effect of Compatibilization on Foam Morphology“, *Advanced Engineering Materials*, 2015, DOI: 10.1002/adem.201500387
11. Bryson, K.C., **Löbbling, T.I.**, A.H., Müller, A.H.E., Russell, T.P., Hayward, R.C.: „Using Janus Nanoparticles to Trap Polymer Blend Morphologies during Solvent-Evaporation-Induced Demixing“, *Macromolecules*, 2015, 48, 4220-4227
10. Schieder, M., Lunkenbein, T., Bojer, C., Dulle, M., vom Stein, J., Auffermann, G., **Löbbling, T.I.**, Schmalz, H., Breu, J.: „Access to molybdenum oxycarbide nanotubes – A stepwise template removal approach“, *Zeitschrift für allg. und anorg. Chemie*, 2015, 641, 1829-1834
9. **Löbbling, T.I.**, Hiekkataipale, P., Hanisch, A., Bennet, F., Schmalz, H., Ikkala, O., Gröschel, A.H., Müller, A.H.E.: „Bulk morphologies of polystyrene-*block*-polybutadiene-*block*-poly(*tert*-butyl methacrylate) (SBT) triblock terpolymers“, *Polymer*, 2015, 72, 479-489

8. Gegenhuber, T., Gröschel, A.H., **Löbbling, T.I.**, Drechsler, M., Ehlert, S., Förster, S., Schmalz, H.: „Non-Covalent Grafting of Carbon Nanotubes with Triblock Terpolymers: Toward Patchy 1D Hybrids“, *Macromolecules*, **2015**, 48, 1767-1776
Front Cover, *Macromolecules*, Volume 48, Issue 6, **2015**
7. **Löbbling, T.I.**, Haataja, J., Synatschke, C.V., Schacher, F.H., Müller, M., Hanisch, A., Gröschel, A.H., Müller, A.H.E.: „Hidden Structural Features of Multicompartment Micelles Revealed by Cryogenic Transmission Electron Tomography“, *ACS Nano*, **2014**, 8, 11330-11340
Highlighted as main topic in a perspective article: Tsang, B., Yu, C., Granick, S., *ACS Nano*, **2014**, 8, 11030-11034
6. Bahrami, E., **Löbbling, T.I.**, Gröschel, A.H., Schmalz, H., Müller, A.H.E., Altstädt, V.: „The Impact of Janus Nanoparticles on the Compatibilization of Immiscible Polymer Blends under Technologically Relevant Conditions“, *ACS Nano*, **2014**, 8, 10048-10056
Editor's Choice in Science, **2014**, Vol. 346, Issue 6208
5. Gröschel, A.H., Walther, A., **Löbbling, T.I.**, Schacher, F.H., Schmalz, H., Müller, A.H.E.: „Guided Hierarchical Co-Assembly of Soft Patchy Nanoparticles“, *Nature* **2013**, 503, 247-251
4. Hanisch, A., Gröschel, A.H., Förtsch, M., **Löbbling, T.I.**, Schacher, F.H., Müller, A.H.E.: „Hierarchical Self-Assembly of Miktoarm Star Polymer Systems Containing a Polycationic Segment: A General Concept“, *Polymer* **2013**, 54, 4528-4537
3. Synatschke, C.V., **Löbbling, T.I.**, Förtsch, M., Hanisch, A., Schacher, F.H., Müller, A.H.E.: “Micellar Interpolyelectrolyte Complexes with a Compartmentalized Shell”, *Macromolecules* **2013**, 46, 6466-6474
2. Gröschel, A.H., **Löbbling, T.I.**, Petrov, P.D., Müllner, M., Kuttner, C., Wieberger, F., Müller, A.H.E.: „Janus Micelles as Effective Supracolloidal Dispersants for Carbon Nanotubes“, *Angew. Chem.* **2013**, 125, 3688-3693; *Angew. Chem. Int. Ed.* **2013**, 52, 3602-3606
Frontispiece Cover, *Angew. Chem. Int. Ed.*, Volume 52, Issue 13, **2013**
1. Gröschel, A.H., Walther, A., **Löbbling, T.I.**, Schmelz, J., Hanisch, A., Schmalz, H., Müller, A.H.E.: „Facile, Solution-Based Synthesis of Soft, Nanoscale Janus Particles with Tunable Janus Balance“, *J. Am. Chem. Soc.* **2012**, 134, 13850-13860

List of Conference Contributions:

Oral Presentations

1. March **2013** in Ebermannstadt, Germany at the **1. Polymer Science Doktoranden-symposium**: Hierarchical Self-& Co-Assembly of Soft Particles with Controlled Patchiness
2. September **2013** in Indianapolis, USA at the **246th ACS National Meeting**: Directed Self-Assembly of Soft Compartmentalized Nanoparticles
“Excellent Student Speaker” in the Division “Anisotropic Particles”
3. July **2014** in Chiang Mai, Thailand at the **IUPAC World Polymer Congress (MACRO 2014)**: Cryo-Electron Tomography Study of Complex Compartmentalized Nanostructures
4. June **2015** in Dresden, Germany at the **European World Polymer Congress (EPF 2015)**: Self-Assembly of Complex Triblock Terpolymer Solution Morphologies
5. June **2015** in Aachen, Germany at the **DWI/RWTH Aachen Summer School / LANXESS Talent Award**: Exploring the Structural Complexity of ABC Triblock Terpolymers in Solution
Winner of the “Lanxess Talent Award” for outstanding achievements in the category “Advances in Polymer Materials”

Poster Presentations

1. May **2013** in Sitges, Spain at the **Third International Symposium: Frontiers in Polymer Science**: Shape-Anisotropic Interpolyelectrolyte Complexes in Multicompartment Micelles of Triblock Terpolymers
2. February **2014** in Freiburg, Germany at the **Makromolekulares Kolloquium Freiburg**: Directed Co-Assembly of Soft Compartmentalized Nanoparticles

Danksagung

Eigentlich war für mich klar, dass ich nach dem Abitur auf keinen Fall studieren werde, sondern sofort in den Beruf übergehe. Chemie hat mich jedoch schon seit der Schulzeit interessiert und so habe ich mich in Bayreuth für ein Chemiestudium eingeschrieben („um mal zu schauen“). Während des Studiums wurde mir schnell klar, dass mich die Welt der Makromoleküle am meisten fasziniert. Als studentische Hilfskraft fand ich dann bereits Mitte 2009 den Weg in den Lehrstuhl Makromolekulare Chemie II unter Leitung von Prof. Axel Müller. Und seitdem bin ich auch nicht wieder gegangen! Nach erfolgreicher Masterarbeit habe ich die vorliegende Dissertation im Zeitraum von Februar 2012 bis März 2015 angefertigt. Während der gesamten Zeit des Studiums als auch der Doktorarbeit wurde ich dabei von vielen interessanten Menschen begleitet, die mein Leben bereichert und mich unterstützt haben. Ohne sie würde es die vorliegende Arbeit in dieser Form nicht geben und deshalb möchte ich mich im nachfolgenden bei diesen Menschen zutiefst bedanken.

Zuerst möchte ich meinem Doktorvater Prof. Axel Müller danken. Er hat mir nicht nur die Möglichkeit gegeben diese Doktorarbeit als letzte Doktorandin an seinem Lehrstuhl anzufertigen, sondern vielmehr hat er es mir und auch allen anderen Doktoranden in seinem Arbeitskreis ermöglicht, eigenständig zu forschen und sich geistig frei zu entfalten. Das mir dabei entgegengebrachte Vertrauen, meine Doktorarbeit größtenteils frei zu gestalten ehrt mich sehr und spornte mich auch in Phasen an, in denen die Ergebnisse auf sich warten ließen. Ich bin unendlich dankbar für die Erfahrungen die ich auf internationalen Konferenzen sammeln durfte und es mir somit gleichzeitig ermöglicht wurde, einen Teil der Welt zu sehen, den ich ansonsten wahrscheinlich nie kennengelernt hätte.

Die inspirierende und familiäre Atmosphäre in der ich arbeiten durfte kam natürlich auch durch die einzigartige Zusammensetzung des Arbeitskreises zustande. Ich würde die Mitarbeiter der „alten“ mc^2 nicht als meine Mitarbeiter oder Kollegen bezeichnen, sondern vielmehr als Freunde, die ich über die Zeit kennenlernen durfte. Besonderer Dank geht an die beste Sekretärin die man sich vorstellen kann: Gaby Oliver. Nicht nur bestritt sie allen bürokratischen „Kram“ der zu Erledigen war und erinnerte an vergessene Unterschriften auf wichtigen Dokumenten, sondern dank ihres erstaunlichen Durchsetzungsvermögens gelang es ihr auch sehr oft die bürokratischen Mühlen der Verwaltung etwas zu beschleunigen wenn es darauf ankam. Danke auch an das Anionik-Team Holger Schmalz, Kerstin Küspert, Andreas Hanisch und Dane Blasser, die mir jederzeit mit Rat und Tat zur Seite standen, mich in die wundervolle Welt der kontrollierten, lebenden, sequentiellen, anionischen Polymerisation einweichten und auch meine Depression nach gescheiterten Versuchen teilten. Danke auch an die Engel des Lehrstuhls, die alles am Laufen gehalten haben und immer ein offenes Ohr für Sorgen und Probleme hatten: Unsere technischen Angestellten Melanie Müller, Annika Pfaffenberger, Marietta Böhm und Annette Krökel. Es gab in der mc^2 immer einen Grund zu feiern und unzählige Barbecues, Feierabend-Bierchen und Brückenpausen trugen zum harmonischen Miteinander bei. Im Folgenden möchte ich mich bei den Leuten bedanken die dazu stets ihren Beitrag geleistet haben: Meine Laborkollegen Thomas Ruhland und Stephan Weiss, die Sängergemeinschaft

Joachim Schmelz und Francesca Bennet, Sandrine Tea, André Pfaff, Zhicheng Zheng, IT-Verantwortlicher Alexander Schmalz, Alexander Majewski, Andrea Wolf, Eva Betthausen, Stefan Reinicke, Marina Krekhova, TEM-Experte Markus Drechsler, Markus Müllner, Christopher Synatschke, Stefan Döhler, Mikheil Doroshenko, Tobias Rudolph und natürlich nicht zu vergessen unsere russische Division Dmitry (Dima) Pergushov, Alexander (Sascha) Yakimansky und Oleg Borisov sowie die spanische Gemeinschaft Ramón Novoa-Carballal, Lourdes Pasteur-Pérez und Ainhoa Tolentino Chivite.

Interdisziplinär geht mein Dank an die Ingenieure Ronak Bahrami und Amir Fathi, an Kollegen der MCI Andreas Ringk, Florian Wieberger, Katharina Neumann, Klaus Kreger, Christian Neuber, Tristan Kolb und Anne Neubig; Bär und Sandra sowie Jessica Goller aus der OC und Moritz Tebbe, Munish Chanana, Mareen Müller, Sascha Ehlert sowie Tobias Güttler aus der PC. Ich danke auch meinen Praktikanten Carina Bojer und Kirsten Volk die fachlich als auch menschlich überzeugten.

Ein ganz besonderer Dank geht an drei sehr wichtige Personen die mich während meiner Doktorandenzeit unterstützt haben und stets ein offenes Ohr hatten. Viele Diskussionen wurden geführt -manche einmal, viele sehr oft- es wurde geweint aber besonders viel gelacht: Danke Daniela Pirner, Melissa Köhn-Serrano und Viola Buchholz für die wertvolle Zeit die ich mit euch hatte und hoffentlich auch noch haben werde, egal wo es uns später auf dem Erdball hinzieht.

Während meiner Doktorandenzeit durfte ich an vielen Veränderungen teilnehmen und so kam es, dass ich insgesamt drei Arbeitsgruppen kennenlernen durfte. Dies war unter anderem die „neue“ MC2 unter Leitung von Prof. Greiner und Prof. Agarwal. Beiden gilt mein Dank, dass sie es mir ermöglichten meine Doktorarbeit weiterhin in Bayreuth anzufertigen. Ich war beeindruckt wie herzlich ich in den neuen Arbeitskreis aufgenommen wurde und so möchte ich mich auch bei den Mitgliedern der „neuen“ MC2 bedanken: Meine Laborkollegen Holger Pletsch, Florian Käfer, Pin Hu, Yinfeng Shi, Payal Tyagi und Li Liu, die Kicker-Experten Judith Schöbel und Fangyao Liu, die Filmabend-Gruppe Amanda Pineda mit Dido, Viola, Melissa, Lisa Hamel und Hui Wang sowie Paul Pineda, Matthias Burgard, Amir Reza-Bagheri, Lu Chen, Oliver Hauenstein, Tobias Moss, Markus Langner, Arne Lerch, Peter Ohlendorf, Fabian Mitschang, Alexander Vogelsang und der Mann mit einer Allgemeinbildung wie ein Lexikon Roland Dersch.

Ich bin im April 2014 nach Finnland in die Gruppe von Prof. Olli Ikkala gegangen um dort etwas über Transmissionselektronentomographie zu lernen und habe das Angebot bekommen zu bleiben. Im November 2014 habe ich dann meine Zelte in Deutschland abgebrochen um einen neuen Lebensabschnitt in Finnland zu beginnen. I want to thank Prof. Olli Ikkala for giving me the opportunity to work in his group and for being such an inspiring person. I'm very much looking forward to work in your group and enjoy the enthusiastic and imaginative atmosphere. Of course, the members of *Molecular Materials* group made it very easy for me to get settled in Finland and integration was so easy. Special thanks goes to Johanna Majoinen and Panu Hiekkataipale for being so patient, translating the mysterious Finnish language both work-related and for the private life, be it the chemical training course, the electricity contract or the manual of the washing machine.

The support, the willingness to discuss any kind of topics and that everyone is treated with such respect impressed me deeply and I want to thank you all in no particular order: Jukka Hassinen, Mikko Poutanen, Riikka Koski, Jenni Koskela, Tuukka Verho, Ville Liljeström, Juuso Korhonen, Marjo Kettunen, Juhana Sorvari, Maria Morits, Mika Latikka, Maja Vuckovac, Pegah Khanjani, Xiaotao Zhu, Lahja Martikainen, Jani-Markus Malho, cryo-Tomo-Magician Johannes Haataja, Mikael Henny, Henrikki Mertaniemi, Robin Ras, Teemu Myllymäki, Angel Sanchez-Sanchez, Nonappa, Nikolay Houbenov, Timo Kajava, Orvokki Nyberg, Marita Halme, Janne Ruokolainen, Matti Toivonen, Jason McKee and Henna Rosilo.

Das Beste kommt immer zum Schluss:

Ich bin zutiefst dankbar während meiner Studienzeit mit André Gröschel den wundervollsten Menschen kennengelernt zu haben den ich mir vorstellen kann. Die Zeit mit dir ist die wertvollste meines Lebens und jeder Tag wird durch dich bereichert. Ohne deine stete Unterstützung, Motivation und natürlich die unzähligen Diskussionen wäre ich jetzt nicht an dem Punkt an dem ich jetzt stehe. Du bist mein Fels in der Brandung und egal was die Zukunft bringen wird, sie wird wunderbar weil wir sie gemeinsam bestreiten werden.

Das gesamte Studium und diese Dissertation wären auch ohne die grenzenlose Unterstützung meiner Familie nicht möglich gewesen. Es war finanziell oft nicht einfach und deshalb möchte ich nicht nur meinen Eltern, sondern auch meinem Bruder Peter und meinen Tanten Angie und Susi für ihren finanziellen Beitrag an diesem Projekt danken. Es gab viele Erfolge aber auch Niederlagen zu bestreiten und meine Eltern sowie meine gesamte Familie haben mich dabei immer aufgefangen, mich wieder aufgebaut und das wichtigste: Sie haben nie an mir gezweifelt! Sie haben Das aus mir gemacht was ich jetzt bin.

DANKE!

(Eidesstattliche) Versicherungen und Erklärungen

(§ 8 S. 2 Nr. 6 PromO)

Hiermit erkläre ich mich damit einverstanden, dass die elektronische Fassung meiner Dissertation unter Wahrung meiner Urheberrechte und des Datenschutzes einer gesonderten Überprüfung hinsichtlich der eigenständigen Anfertigung der Dissertation unterzogen werden kann.

(§ 8 S. 2 Nr. 8 PromO)

Hiermit erkläre ich eidesstattlich, dass ich die Dissertation selbständig verfasst und keine anderen als die von mir angegebenen Quellen und Hilfsmittel benutzt habe.

(§ 8 S. 2 Nr. 9 PromO)

Ich habe die Dissertation nicht bereits zur Erlangung eines akademischen Grades anderweitig eingereicht und habe auch nicht bereits diese oder eine gleichartige Doktorprüfung endgültig nicht bestanden.

(§ 8 S. 2 Nr. 10 PromO)

Hiermit erkläre ich, dass ich keine Hilfe von gewerblichen Promotionsberatern bzw. -vermittlern in Anspruch genommen habe und auch künftig nicht nehmen werde.

.....

Ort, Datum, Unterschrift

Tina I. Löbling